Measurements of neutral particles and simulations of plasma-neutral dynamics in the HIT-SI3 experiment

Derek A. Sutherland

A dissertation
submitted in partial fulfillment of the
requirements for the degree of

Doctor of Philosophy

University of Washington

2019

Reading Committee:

Thomas Jarboe, Chair

Uri Shumlak

Brian Nelson

Program Authorized to Offer Degree:
Department of Aeronautics and Astronautics

University of Washington

Abstract

Measurements of neutral particles and simulations of plasma-neutral dynamics in the HIT-SI3 experiment

Derek A. Sutherland

Chair of the Supervisory Committee:
Professor Thomas Jarboe
Department of Aeronautics and Astronautics

Clean, safe, and reliable energy sources are needed to displace those harmful to people and the environment. Fusion energy is such an energy source, provided it is both technically and economically viable. The HIT-SI3 experiment at the University of Washington seeks to develop a pathway towards commercially viable, economical fusion energy based on compact, toroidal (CT) magnetic confinement of fusion plasmas. This experiment makes use of a novel inductive helicity injection scheme that both forms and sustains CT plasma configurations known as spheromaks for confinement of high temperature fusion plasmas. This work details measurements of neutral particles and simulations of plasma-neutral dynamics in the HIT-SI3 experiment that is of interest for optimizing sustained spheromak performance for fusion energy applications. In particular, a two-photon absorption laser induced fluorescence (TALIF) diagnostic system measured monatomic, ground state deuterium neutral densities and temperatures in HIT-SI3 spheromak plasmas. These data were compared to dynamic plasma-neutral simulations performed with the PSI-Tet code. The plasma-neutral fluid model implemented in PSI-Tet includes an magnetohydrodynamic (MHD) plasma fluid and a monatomic, deuterium neutral fluid with electron impact ionization, radiative recombination, and resonant charge exchange plasma-neutral reactions. Plasma-neutral PSI-Tet simulations of decaying spheromaks in the HIT-SI3 flux conserver geometry are used to compare to experimental TALIF neutral density and temperature measurements. Validation results are presented that exhibit varying degrees of agreement that are strongly dependent on the choice of boundary conditions and limiting the usage of stabilizing artificial diffusivity. The observed levels of agreement between experimental TALIF measurements and plasma-neutral simulations, though promising, motivate the collection of additional data concerning the neutral particle composition and parameters in HIT-SI3 spheromak plasmas and an expansion of the currently implemented plasma-neutral model to include a diatomic, molecular fluid to more accurately capture the physical system under consideration.

TABLE OF CONTENTS

Page

LIST OF FIGURES

Figure Number Page

LIST OF TABLES

ACKNOWLEDGMENTS

The work presented herein would not have been possible without the assistance and support of many different people. I would like to thank my advisor Prof. Tom Jarboe for his guidance and providing for a my continued education in the field of plasma physics and fusion energy. Additionally, the foundational work performed by Prof. Uri Shumlak and Dr. Eric Meier, and additional conversations with these individuals have been critical for the success of this project; I thank them for their insights and assistance. Additionally, I would like to thank Dr. Drew Elliott and his colleagues from West Virginia University for enabling the collaboration that led to successful neutral density and temperature measurements on the HIT-SI3 experiment. Lastly, I would like to personally thank the many other people that have contributed to this work in some capacity. Specifically, I would like to thank Dr. Chris Hansen, Dr. Kyle Morgan, Dr. Aaron Hossack, Dr. Brian Nelson, Dr. John O'Bryan, Dr. Cihan Akcay, Dr. Brian Victor, Chris Everson, James Penna, Tom Benedett, Alan Kaptanoglu, John Rogers and Jamie Coyne for their numerous conversations and assistance over the years that is much appreciated. Lastly, I would like to thank my family and friends who I dedicate this work to for their unrelenting support. Words are insufficient to express my gratitude, and so I hope it will suffice to say, thank you all so very much.

This research was supported by the U.S. Department of Energy. Simulations presented in this work were performed at the National Energy Research Computing Center (NERSC) at Lawrence Berkeley National Laboratory (LBNL) and on the Hyak supercomputing cluster at the University of Washington.

DEDICATION

To my family and friends for their unrelenting support

Chapter 1

INTRODUCTION

There is a need for clean, safe, and reliable energy sources to displace those harmful to people and the environment. From decades of data collection and research, it is widely viewed that anthropogenic greenhouse-gas emissions, partly from the usage of fossil fuels to generate electricity, is causing our climate to warm [1]. Though the exact amount of warming, and the impacts such warming will have on human civilization is not certain due to the complexity of climate modeling and the need for more climatological data, there is considerable evidence that anthropogenic climate change could be detrimental to human civilization and measures should be taken now to reduce potentially negative impacts [1]. Though there are many proposed approaches to reduce human-caused climate change, one commonality between the most credible plans is a substantial reduction of greenhouse-gas emissions. In short, there must be widespread adoption of energy sources that do not produce greenhouse gas emissions to displace fossil fuels, such as coal and natural gas, to reduce the impact humans are having on Earth's climate [1, 2, 3].

Beyond the concern of negative impacts of anthropogenic climate change, fossil fuel emissions near large population centers can result in unhealthy air quality, which can result in respiratory illnesses and even premature deaths from ailments that are exacerbated by pollution [4, 5, 6, 7]. Additionally, the consumption of fossil fuels currently exceeds their estimated replenishment rate through natural processes. Though not an immediately pressing matter, future shortages of fossil fuels could lead to prohibitively high fuel costs, which motivates research into alternative energy sources before such scarcity becomes apparent.

One greenhouse gas emission-free energy source that is widely used today is nuclear fission energy. Though the use of this baseload, carbon-free energy source is readily able

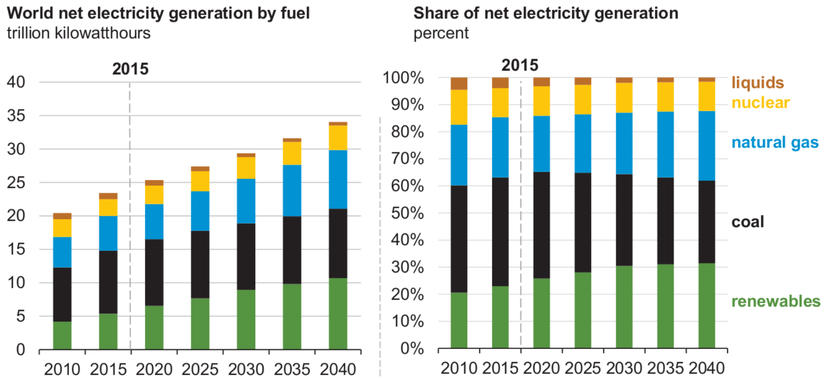

Figure 1.1: Past and projected worldwide electricity generation market shares by source over time [8].

to be expanded, the U.S. Energy Information Administration projects only modest growth through the mid-21st-century due to safety, environmental and other concerns [8]. Instead, robust growth in natural gas and renewable energy sources is projected over the next decades, with the combination of both of these sources reaching an estimated 57% global market share by 2040 [8]. The past and projected variation in electricity generation market shares by source over time is provided in Fig. 1.1. Within the renewable energy sector, hydropower is the dominant energy source with a 71% market share in 2015, which is projected to decline to 53% by 2040 due to strong growth in transient, renewable energy sources such as wind and solar energy [8], as shown in Fig. 1.2.

However, despite these projections of strong growth in the renewable electricity generation sector over the next decades, it is also projected that fossil fuels in the form of coal and natural gas will likely hold a significant market share through 2040 [8], as shown in Fig. 1.1. Renewable electricity generation will likely continue to increase its market share beyond 2040, and with this continued expansion, there will be a greater need for large-scale energy storage [9]. The evolution of electricity markets over the coming decades will likely be dependent on geographical location, as various areas of the world have particular energy sources that are

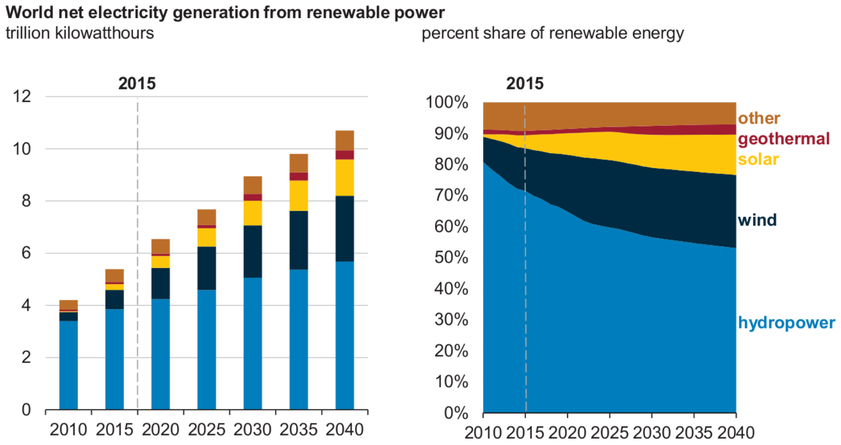

Figure 1.2: Past and projected renewable electricity generation market shares by source over time [8].

naturally more plentiful, such as the widespread usage of hydropower in the Pacific Northwest of the United States [10]. However, until a robust, distributed, renewable electricity grid with sufficient energy storage capacity is realized, there will be a need for flexible power sources to displace those that generate greenhouse-gas and other harmful emissions. Fusion energy is such an energy source, with plentiful amounts of fuel, no long-lived radioactive waste, no risk of an accident leading to a meltdown, and is on-demand. These features motivate the continued research and development of this potentially revolutionary energy source.

1.1 Overview of fusion energy

Fusion is the fundamental energy source of the Universe. It is a nuclear process of combining lighter elements to produce heavier ones through a nuclear process that operates via the strong nuclear force. In changing locations on the binding energy curve, an exothermic release of energy via $\Delta E = \Delta mc^2$ occurs that is more energetic per nucleon involved in the reaction than nuclear fission.

One of the most common fusion reactions considered for first-generation fusion reactors

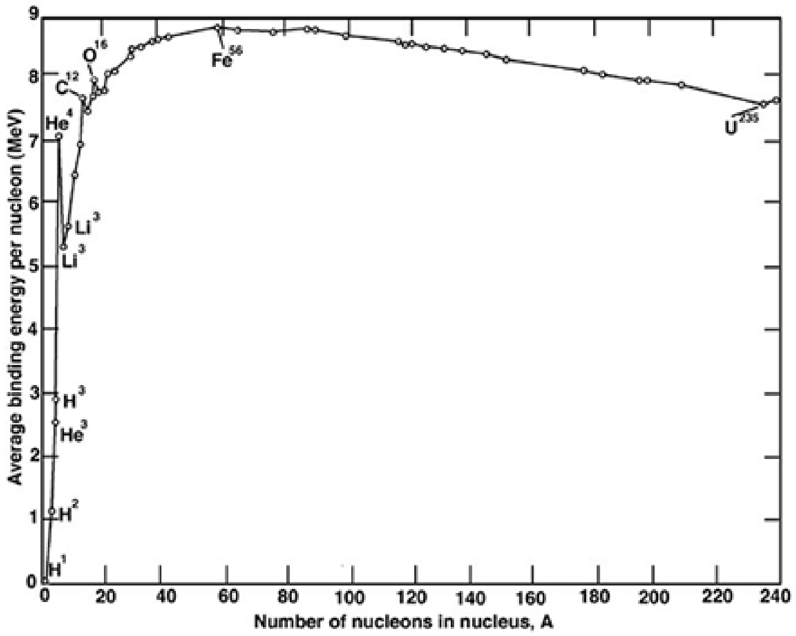

Figure 1.3: The binding energy of nuclei versus nucleon number. Reactions proceeding from the left (light elements) to the right are fusion events, whereas reactions proceeding from the right (heavy) to the left are fission events.

is deuterium-tritium (DT) fusion, which produces an alpha particle and a neutron with 3.5 mega-electronvolts (MeV) and 14.1 MeV of kinetic energy respectively, as shown in Eq. 1.1. DT fusion has the largest cross-section at relatively low plasma temperatures, as shown in Fig. 1.4. But, the pursuit of a DT fusion reactor introduces the difficulties involved with the of use of tritium, which is a radioactive isotope of hydrogen with a half-life of approximately 12.3 years. Due to the short half-life of tritium compared to the age of Earth, there are only trace amounts of naturally occurring tritium in the environment, and so it must be produced artificially. Luckily, nature has provided tritium generating reactions expressed in Eq. 1.2 and Eq. 1.3 which both make use of neutrons interacting with lithium nuclei to produce tritium. These reactions introduce the possibility of a closed, or in other words, self-sufficient fusion fuel cycle with plentiful amounts of naturally occurring deuterium and local production of tritium by surrounding the fusion core with a moderating blanket containing lithium. Thus, the main consumables of a DT fusion reactor system would be deuterium and lithium, with the products of helium, neutrons, and excess energy for the generation of electricity or high-grade process heat.

$$ {}^{2}_{1}\mathrm{H} + {}^{3}_{1}\mathrm{H} \rightarrow {}^{4}_{2}\mathrm{He}\,(3.5\,\mathrm{MeV}) + {}^{1}_{0}\mathrm{n}\,(14.1\,\mathrm{MeV}) \tag{1.1} $$

$$ {}^{6}_{3}\mathrm{Li} + {}^{1}_{0}\mathrm{n} \rightarrow {}^{4}_{2}\mathrm{He}\,(2.05\,\mathrm{MeV}) + {}^{3}_{1}\mathrm{H}\,(2.75\,\mathrm{MeV}) \tag{1.2} $$

$$ {}^{7}_{3}\mathrm{Li} + {}^{1}_{0}\mathrm{n} \rightarrow {}^{4}_{2}\mathrm{He} + {}^{3}_{1}\mathrm{H} + {}^{1}_{0}\mathrm{n}\,(-2.47\,\mathrm{MeV}) \tag{1.3} $$

As is seen in Fig. 1.4, plasma temperatures between 15 – 20 keV are required for large-scale DT fusion power production due to relatively large cross-sections in that temperature regime. In order to maintain fusion plasma temperatures, some method of confinement must be employed to prevent excessive thermal losses that would prevent reaching the temperatures required to generate substantial amounts of fusion power. The two main terrestrial methods of controlled fusion energy is inertial and magnetic confinement. Magnetic confinement fusion (MCF) will be the main method of controlled fusion of interest for this work. MCF relies on the Lorentz force confining charged particles that make up a fusion plasma.

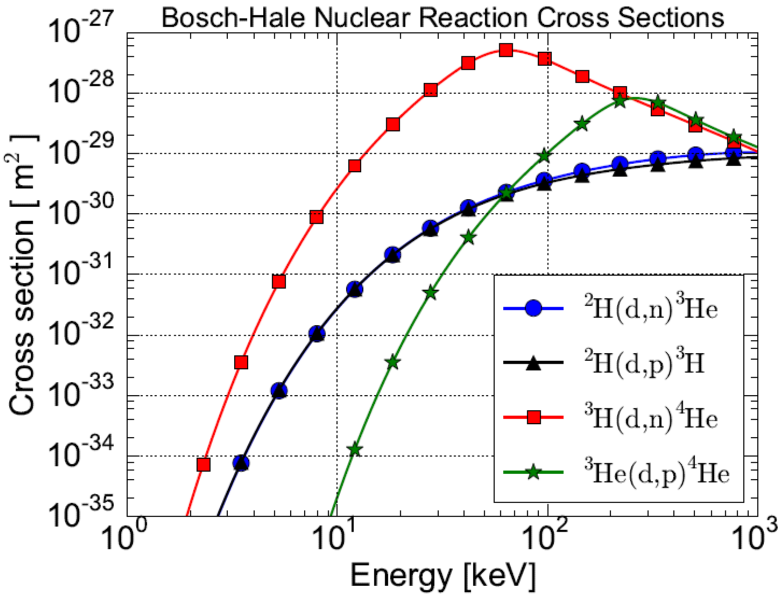

Figure 1.4: The Bosch-Hale parametrization cross-sections for various fusion reactions of interest. Note that the deuterium-tritium (DT) fusion reaction has a considerably higher cross section than the other reactions at modest energies (i.e. $E < 30$ keV) [11].

Charged particles undergo helical motion in a magnetic field, enabling confinement of these particles perpendicular to the direction of the magnetic field, but no confinement along magnetic field lines. By wrapping magnetic fields into a torus, losses resulting from the lack of confinement parallel to magnetic field lines is largely eliminated. This line of reasoning motivates the majority of magnetic fusion approaches pursued today that use a toroidal confinement geometry in some capacity [12].

The magnetic confinement approach to fusion energy is the leading approach to date on an absolute plasma parameter basis [12]. The two leading concepts within this realm of fusion research are the tokamak and stellarator [12, 13]. ITER, a collaborative, international fusion project dedicated to demonstrating the physical viability of tokamak-based MCF is currently under construction in Cadarache, France with first plasma scheduled for December 2025 [14]. This device, shown in Fig. 1.5, is designed to be the first net energy gain fusion experiment by producing 10 times more energy that is consumed for operation. The second best performing magnetic fusion concept is the stellarator, which is an intrinsically steady-state device that uses externally applied magnetic rotational transform to confine a fusion plasma [15, 12]. A flagship stellarator device has begun operations in Griefswald, Germany called W7-X, shown in Fig. 1.6. Both of these experiments are testaments to the sophisticated, worldwide effort in developing magnetic fusion energy.

Though these two approaches to magnetic fusion energy are the leading candidates, there are still several issues to resolve before a commercial fusion reactor based on these concepts can be realized [12]. These issues, such as disruptive plasma instabilities, plasma-material interface concerns, and economic competitiveness motivate continued research and development into alternative approaches to fusion energy that may ameliorate or eliminate some of these issues. One alternative approach to magnetic fusion energy is the spheromak concept, shown in Fig. 1.7. The spheromak is a compact, toroidal plasma configuration with no externally-applied toroidal magnetic flux that is contained within a simply connected vacuum chamber. The spheromak allows for reduced engineering complexity due to the more extensive use of plasma current to provide both confining and stabilizing magnetic fields instead of

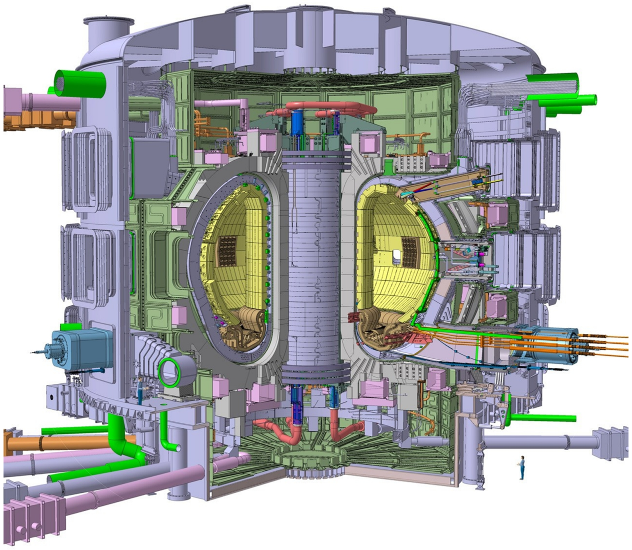

Figure 1.5: The ITER tokamak experiment that is designed to achieve net-gain fusion power production with a plasma gain ($Q_p = 10$). This experiment should produce 500 MW for pulses on the order of 400 seconds, and allow for the study of the burning plasma regime with fusion-generated alpha particles providing the majority of heating power to maintain thermonuclear temperatures [17].

using external, superconducting coil sets [16]. Lesser engineering complexity may translate into economic competitiveness, as is argued in a spheromak-based reactor concept that suggests that overnight capital costs could be competitive with coal-fired power plants at a 1000 mega-watt-electric (MWe) power output level [16]. A poloidal cross section of the Dynomak fusion reactor vision is shown in Fig. 1.8. The possibility of economical spheromak-based fusion reactors is a strong motivator the continued research and development of spheromak configurations.

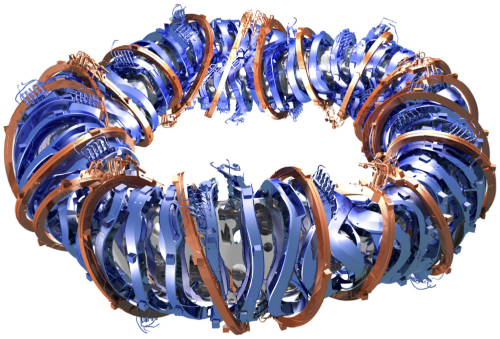

Figure 1.6: The W7-X stellarator experiment (major radius $R = 5.5$ m, minor radius $a = 0.53$ m) which is designed to run up to thirty minutes at a time with keV-scale plasma temperatures [18].

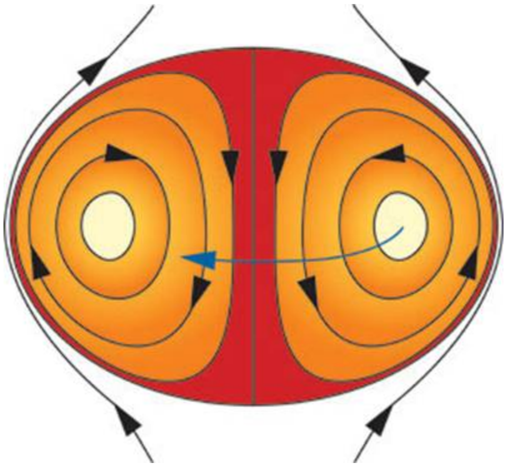

Figure 1.7: A standard spheromak configuration. Poloidal plasma currents produce toroidal magnetic flux to stabilize the plasma configuration, and toroidal plasma currents produce poloidal magnetic flux for confinement of plasma. Only one equilibrium coil set is fundamentally required for steady-state equilibrium [15].

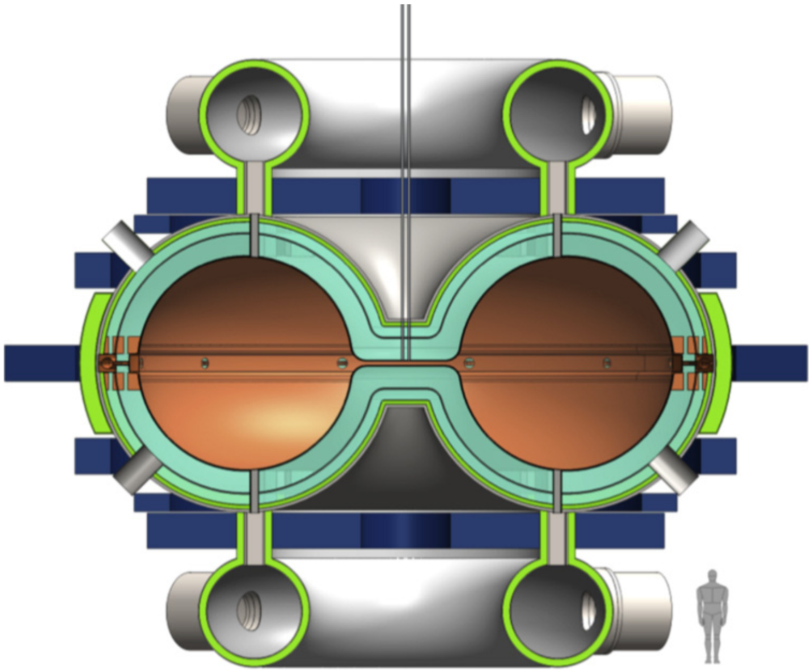

Figure 1.8: A poloidal cross section of the 1000 MWe Dynomak reactor concept. A dumbbell shaped flux conserver contains a high-β sustained spheormak configuration. A turquoise colored molten-salt blanket made of FLiBe moderations fusion neutrons, breeds tritium, and satisfactorily cools the first wall and reactor assemblies. The FLiBe primary coolant will couple to a secondary cycle (not shown) for the production of electricity or high-grade process heat. ITER developed cryopumps and metal hydride fast neutron and gamma shielding are used as well [16].

1.2 Overview of spheromak configurations

1.2.1 Magnetic helicity and Taylor states

Magnetic helicity is often invoked when describing the evolution of magnetized plasma configurations since it is a robust constant of motion with respect to relatively fast dissipative or organizational processes, such as small-scale turbulence or magnetic reconnection[19]. Magnetic helicity is defined via Eq. 1.4 [19],

$$K \equiv \int_V \vec{A} \cdot \vec{B}\, d^3r \tag{1.4}$$

where $\vec{A}$ is the magnetic vector potential, $\vec{B}$ is the magnetic field, and the integral is carried out over a volume V. Magnetic helicity can be understood as the linkage of magnetic flux with magnetic flux. Provided one magnetic flux tube with flux ϕ that is linked with another flux tube of flux ψ, the above equation can be written and evaluated as,

$$K \equiv \int_V \vec{A} \cdot \vec{B}\, d^3r = 2\phi\psi \tag{1.5}$$

If these two flux tubes overlap spatially, then the magnetic field in the overlapping region would be the sum of the magnetic fields present in each flux tube, which would result in twisted magnetic fields in which the amount of helicity corresponds to the degree of twist [19].

It has been established that plasma configurations tend to relax towards minimum energy states subject to any constants of motion during the relaxation process [19, 20], such as conservation of magnetic helicity. It has been shown that for perfectly-conducting plasmas in which field lines are "frozen" into the plasma fluid, all topological properties of the field lines in a magnetic configuration are invariant [20]. For finite electrical resistivity plasmas, for relaxation periods much shorter than the resistive timescale, one withstanding invariant is magnetic helicity, whereas magnetic energy decreases until a minimum energy state is reached [20]. The final state of relaxation for an isolated (i.e. $\vec{B} \cdot \hat{n} = 0$ on the surface inscribing the volume of interest that is integrated over in Eq. 1.4)) spheromak configuration is found to be described by

$$\nabla \times \vec{B} = \lambda \vec{B} \tag{1.6}$$

where $\lambda = \frac{\mu_o \vec{j}}{\vec{B}}$ is a constant having the same value on all field lines (i.e. constant λ within the spheromak volume) [20]. Solutions to Eq. 1.6 are called Taylor states [19] and represent the minimum energy state of a magnetic configuration in which magnetic relaxation processes freely determine the ratio of poloidal to toroidal magnetic flux, in contrast to reversed-field pinches (RFPs), tokamaks or stellarators where some or all of the configuration magnetic fields are externally applied. Axisymmetric, lowest order solutions in a cylindrical geometry, while neglecting toroidal curvature, to Eq. 1.6 are found to be

$$\begin{aligned} B_z &= B_o J_0(\lambda r) \\ B_\theta &= B_o J_1(\lambda r) \\ B_r &= 0 \end{aligned} \tag{1.7}$$

where B_z is the axial (toroidal) field, B_θ is the poloidal field, and B_r is the radial field that is equal to zero in this axisymmetric configuration [19, 20]. J_0 and J_1 are Bessel functions of the first kind of orders 0 and 1, respectively. B_o is the value of the magnetic field on magnetic axis, and r is the minor radius at the point of evaluation of the above functions. Note that in this isolated spheromak equilibrium, the strengths of the poloidal and toroidal field are of the same magnitude (i.e. $B_z \approx B_\theta$). The above solution is often called the Bessel Function Model [19].

1.2.2 Driven spheromak configurations and relative helicity

Spheromak configurations use both poloidal and toroidal plasma currents to produce both stabilizing and confining magnetic fields, respectively. However, due to the finite electrical resistivity of plasma, these plasma currents will tend to decay. Thus, some method of plasma current sustainment must be employed for a spheromak configuration to be maintained for periods longer than its resistive decay time, such as when pursuing steady-state operation for a spheromak-based fusion reactor [16]. Plasma current sustainment can also be viewed as magnetic helicity sustainment. In short, magnetic helicity decays on a resistive timescale, and thus some method of magnetic helicity injection must be employed to enable spheromak lifetimes longer than the resistive decay time.

First, the concept of magnetic helicity injection introduces the issue of defining magnetic helicity gauge invariantly. The definition of magnetic helicity introduced previously, $K = \int_V \vec{A} \cdot \vec{B}\, d^3r$, is gauge invariant for transformations $\vec{A} \to \vec{A} + \nabla\Phi$ in isolated systems ($\vec{B} \cdot \hat{n} = 0$ on surface S inscribing volume V), but not in driven systems [19, 21]. Since all flux tubes are no longer fully enclosed by V while being driven, there are field lines that now penetrate the surface (i.e. $\vec{B} \cdot \hat{n} \neq 0$ on surface S enclosing the volume of interest V), allowing for the injection of magnetic helicity through the boundary S. The definition and use of relative helicity overcomes this flux linkage (gauge invariance) issue, which is defined as

$$K_{rel} = \int_{V_a} (\vec{A} + \vec{A_p}) \cdot (\vec{B} - \vec{P})\, d^3r \tag{1.8}$$

where $\vec{A_p}$ and $\vec{P}$ are arbitrary gauge vector potentials and magnetic fields, respectively [22]. By choosing a gauge vector potential A_p that satisfies the requirements that $\nabla \cdot A_p = 0$ and $\vec{A_p} \cdot \hat{n}|_s = 0$ [21, 23], the relative helicity conservation equation is found to be

$$\frac{dK_{rel}}{dt} = -2 \int_V \vec{E} \cdot \vec{B}\, d^3r + 2 \oint_S \vec{A_p} \times \vec{E} \cdot \hat{n}\, d^2r \tag{1.9}$$

where $\vec{E}$ is electric field [21]. The first term on the right hand side provides helicity dissipation, whereas the second term involves transport of helicity across the bounding surface S. Inspecting the helicity dissipation term more carefully, it can be shown the only term in the Generalized Ohm's law that contributes to the helicity dissipation integral is the resistive term (i.e. $\vec{E} = \eta\vec{j}$) [24]. The integrand in the dissipative portion of Eq. 1.9 is maximized in a force-free state with $\vec{j} \parallel \vec{B}$. Substituting the expression for the resistive electric field, the helicity decay rate is given as

$$\frac{dK_{decay}}{dt} = -2 \int_V \eta\vec{j} \cdot \vec{B}\, d^3r \tag{1.10}$$

Thus, some method of helicity injection through the boundary inscribing a volume V is required to counteract the resistive loss of helicity in order to sustain a spheromak equilibrium [19, 21].

It can be shown that the helicity flux term in Eq. 1.9 can be expressed in terms of the vacuum $\vec{E}$ and $\vec{B}$ fields obtained using the same boundary values of $\vec{B} \cdot \hat{n}$ and $\vec{E} \times \hat{n}$ used in the plasma case [25],

$$\frac{dK_{inj}}{dt} = 2 \int_V \vec{E}_v \cdot \vec{B}_v \, d^3r \tag{1.11}$$

The above expression can be further simplified for geometries like the RFP (reversed-field pinch), the flux core, the coaxial source, and HIT-SI3 to [25]

$$\frac{dK_{inj}}{dt} = 2V\Psi \tag{1.12}$$

where V is the injector voltage and Ψ is the injector flux. In HIT-SI3, V is the applied inductive voltage V_{inj} that drives the helicity injector current I_{inj}. The vacuum flux Ψ is the externally applied injector flux Ψ_{inj}. Thus, the helicity injection rate in HIT-SI3 can be simply put as

$$\frac{dK_{inj}}{dt} = 2V_{inj}\Psi_{inj} \tag{1.13}$$

Given this helicity injection rate, it is clear from Eq. 1.10 and Eq. 1.13 the helicity conservation equation can be written as

$$\frac{dK_{rel}}{dt} = 2V_{inj}\Psi_{inj} - \frac{K_{rel}}{\tau_{K_{rel}}} \tag{1.14}$$

where τ_K is a characteristic helicity decay time that will be related to the magnitude of the plasma resistivity shown in Eq. 1.10.

The last preliminary concept about helicity injection to note is that, for a driven spheromak, $\lambda = \mu_o \vec{j}/\vec{B}$ is no longer constant across the entire configuration as is the case in a fully relaxed isolated spheromak. The quantity λ will tend to vary across the volume with a profile dependent on the method of sustainment and degree of relaxation. It can be shown that for two adjacent, thin, closed flux tubes in a system in which global helicity is conserved, the minimum energy state corresponds to $\lambda_1 = \lambda_2$ where subscripts 1 and 2 denote the λ of each respective flux tube [19]. In the case that $\lambda_1 > \lambda_2$, helicity will tend to flow from the region of high λ (λ_1) to low λ (λ_2) in order to minimize the magnetic energy per unit helicity of the system. At fixed helicity, lower λ indicates lower amounts of magnetic energy in the system since $\lambda = \mu_o W_B/K$ [19]. Thus, in order to "sustain," or inject helicity into a spheromak, λ_{inj} must be greater than $\lambda_{spheromak}$. Otherwise, if $\lambda_{inj} < \lambda_{spheromak}$, it is not energetically favorable to inject helicity into the spheromak, and thus the system will no longer being sustained against resistive dissipation. Another useful quantity to define is the safety factor $q \equiv d\Phi/d\psi$, where Φ is the toroidal flux and ψ is the poloidal flux [19]. This quantity can be viewed as the level of twist of a magnetic field line, and is a useful quantity when attempting to assess the stability of a magnetized plasma configuration to particular instabilities of interest, such as pressure or current driven modes [15]. Lastly, the normalized unit typically used to characterized magnetohydrodynamic (MHD) pressure limits is $\beta \equiv \frac{2\mu_o p}{B^2}$, where p is thermal pressure, B is magnetic field, and μ_o is vacuum permeability.

1.3 The HIT-SI and HIT-SI3 experiments

HIT-SI (Steady Inductive Helicity Injected Torus) is a compact toroidal plasma experiment partly focused on studying advanced current drive methods for magnetic fusion concepts. The HIT-SI experiment, shown in Fig. 1.9, produces spheromaks using fully inductive, non-axisymmetric helicity injection in a copper, bow-tie shaped poloidal magnetic flux conserver. HIT-SI has produced sustained spheromaks with evidence of pressure confinement and current gains ($G \equiv I_{tor}/I_{inj}$) approaching 4, which is a spheromak record [26]. Imposed-dynamo current drive (IDCD) is a leading theory for explaining the observed behavior of sustained spheromak plasmas in HIT-SI [27]. Non-axisymmetric magnetic perturbations, required by Cowling's theorem [28] for steady-state sustainment by an MHD dynamo, are imposed externally instead of being generated by confinement-degrading plasma instabilities seen in previous spheromak experiments sustained by coaxial helicity injection (CHI), such as the Sustained Spheromak Physics Experiment (SSPX) [29].

Measurements made on the HIT-SI experiment suggest electron temperatures in the range

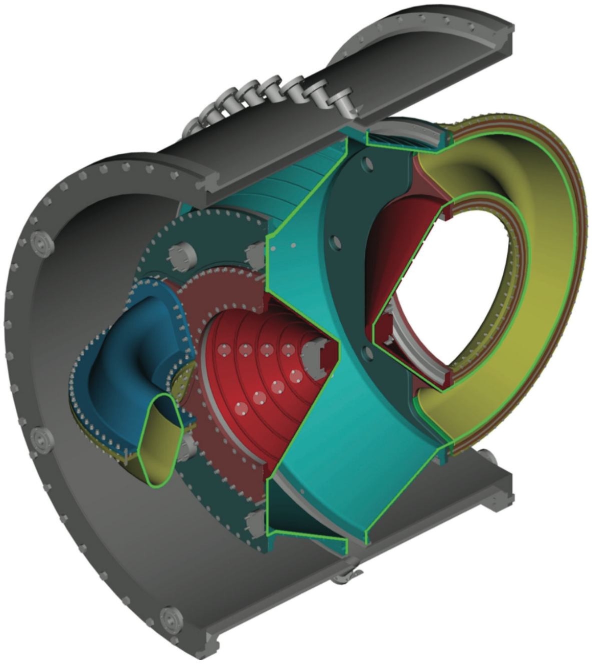

Figure 1.9: A poloidal cross section of the HIT-SI experiment. Two inductive helicity injectors (half-tori) are driven by voltage and flux coils to inject magnetic helicity. These injectors are able to form and sustain a spheromak configuration in a bow-tie shaped copper flux conserver.

of 6–20 eV from a Langmuir triple probe, with ion temperatures upwards of 20–40 eV from measuring impurity spectral lines via ion Doppler spectroscopy (IDS) [30]. A representative time trace from the HIT-SI experiment is shown in Fig. 1.10. In Fig. 1.10, the injector current I_{inj}, toroidal plasma current I_{tor}, and current gain $G \equiv I_{tor}/I_{inj}$ is plotted as a function time during a representative shot while operating at both low (i.e. $f_{inj} \approx$ 14.5 kHz) and high (i.e. $f_{inj} \approx$ 68.5 kHz) injector frequencies. The highest toroidal current shots were produced during low frequency helicity injector operations, primarily due to the ability to couple the most power to the plasma while operating at that frequency. However, as is apparent in Fig. 1.10, the highest current gain G discharges were obtained while operating at high injector frequencies. Interestingly, these highest current gain shots were correlated with an observed Shafranov shift of the magnetic axis, that is likely due to pressure confinement [26]. Thus, these results suggest the ability of sustained spheromak configurations capable of confining plasma pressure at the highest experimental current gains achieved, as shown in Fig. 1.11.

An upgrade of the HIT-SI experiment, called HIT-SI3, is operational at the time of writing. Instead of two helicity injectors located on either side of the flux conserver as shown in Fig. 1.9, three co-planar helicity injectors are used to form and sustain spheromak equilibria in HIT-SI3, as shown in Fig. 1.12 and Fig. 1.13. The use of three injectors provides flexibility in the temporal phasing of the helicity injectors relative to one another, which allows for variations in the imposed magnetic perturbation profile while still providing constant volumetric helicity injection rates like HIT-SI (i.e. with 0-60-120 or 0-120-240 phasing), as shown in Fig. 1.14. Additionally, in Fig. 1.14, it is shown that the injector phasing can be chosen to operate with time varying helicity injection rates. Representative HIT-SI3 data traces are shown in Fig. 1.15 for 0-60-120, 0-120-240, and 0-0-0 helicity injector phasings [31]. Performance on HIT-SI3 has steadily improved as operations are optimized in this new experimental geometry, and current gains exceeding 3.5 have been achieved on this experimental platform. The HIT-SI3 experiment is the experimental platform considered most in this work.

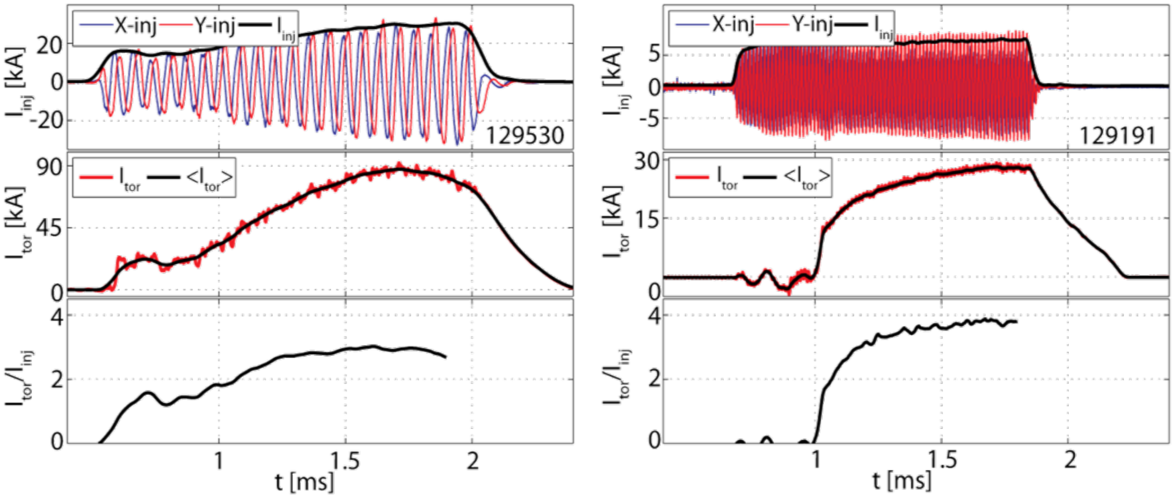

Figure 1.10: Representative time traces from the HIT-SI experiment from low frequency (left) and high frequency (right) helicity injector operations. Plotted are the injector currents I_{inj}, toroidal plasma current I_{tor}, and current gain G $\equiv$ I_{inj}/I_{tor}. Note the highest current gains achieved are during high frequency helicity injector operations (i.e. $f_{inj} \approx$ 68.5 kHz), whereas the largest toroidal currents are achieved during lower frequency operations (i.e. $f_{inj} \approx$ 14.5 kHz).

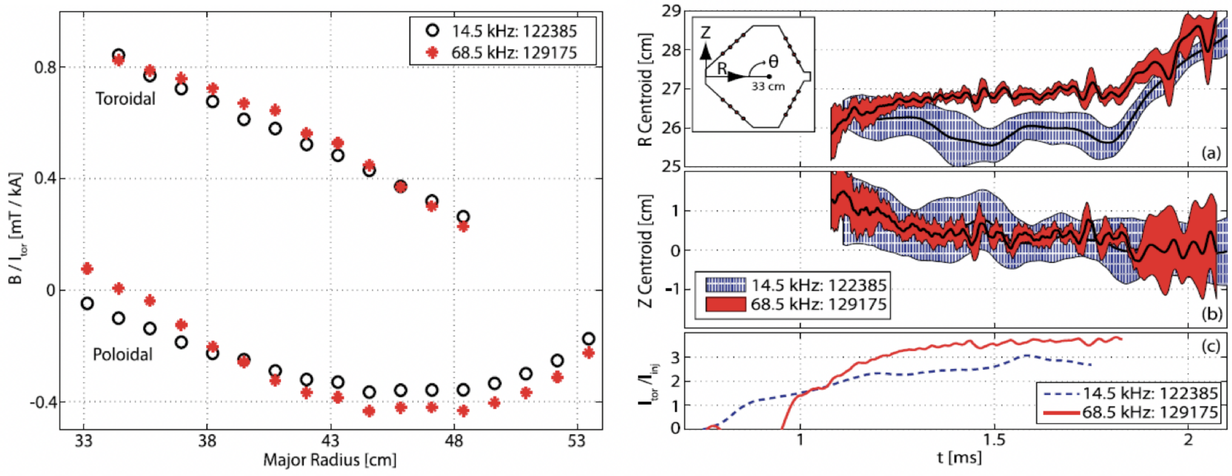

Figure 1.11: Comparisons in magnetic and current centroid data during low and high frequency operation on HIT-SI. *Left*: Internal magnetic probe measurements normalized by the toroidal plasma current. Note the outward shift of the magnetic axis ($B_p = 0$) at high frequency operations compared to low frequency operations. *Right*: Current centroid calculations. R and Z centroids show the mean and standard deviations from the four toroidal locations where the surface probe arrays are located. Note the outward shift of the current centroid measurements at high frequency when compared to low frequency, and improved symmetry of the equilibrium fields while operating at high frequency as well.

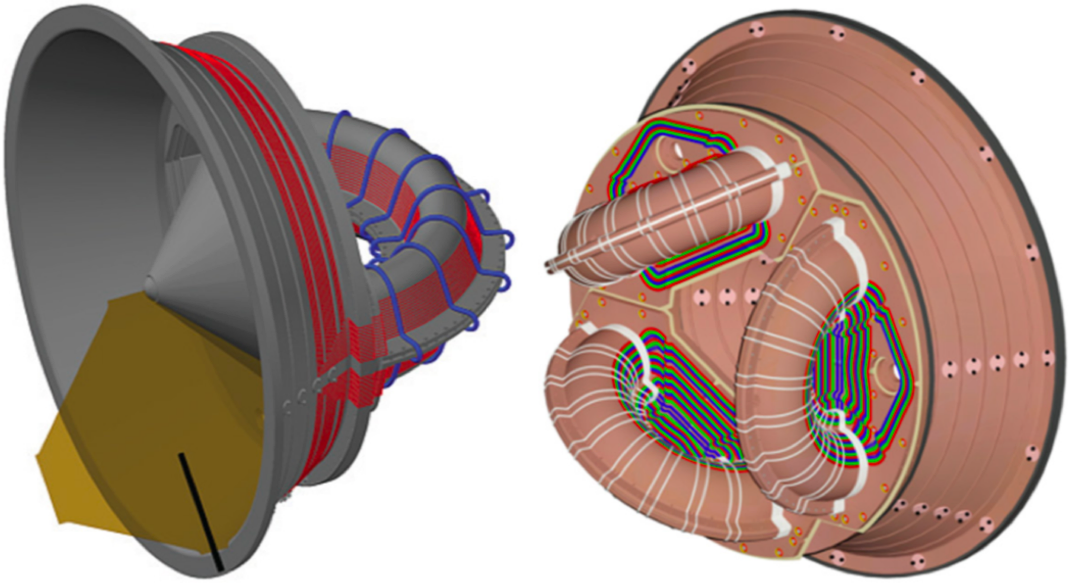

Figure 1.12: A CAD rendering of the HIT-SI and HIT-SI3 experiments for comparison. *Left*: A cross-section of the HIT-SI experiment with a yellow poloidal cross section shown and the location of an inserted internal magnetic probe in black. The magnetic flux coils (blue) and voltage coils (red) provides injection of magnetic helicity and power into the bow-tie shaped flux conserver. *Right*: The three inductive helicity injectors on the HIT-SI3 experiment. The magnetic flux coils (white) and voltage coils (multicolored) are shown.

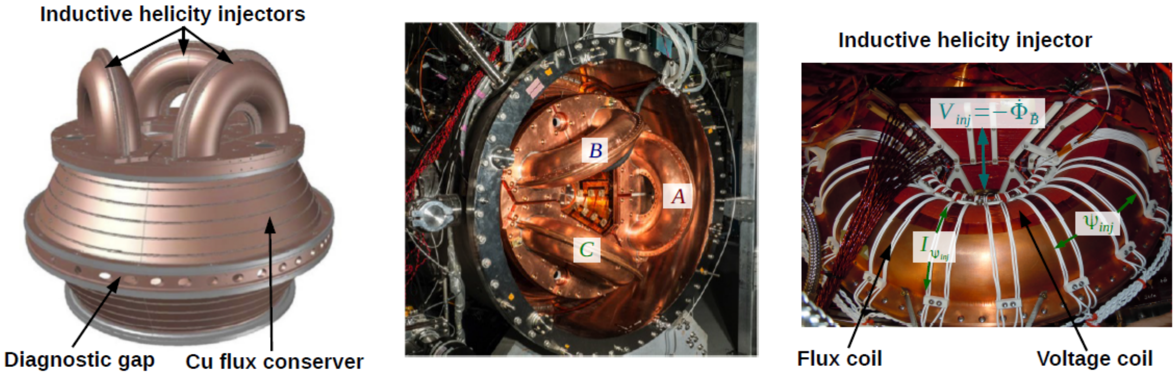

Figure 1.13: The HIT-SI3 flux conserver and injector geometry. Note the usage of three coplanar helicity injectors (A-B-C) located on a single side of the machine to form and sustain a spheromak plasma. Varying the phasing of these helicity injectors changes the imposed magnetic perturbation profile while injecting helicity at a constant or variable rate. A close-up of an inductive helicity injector is shown on the right, depicting the injector voltage V_{inj} and flux Ψ_{inj} required for helicity injection.

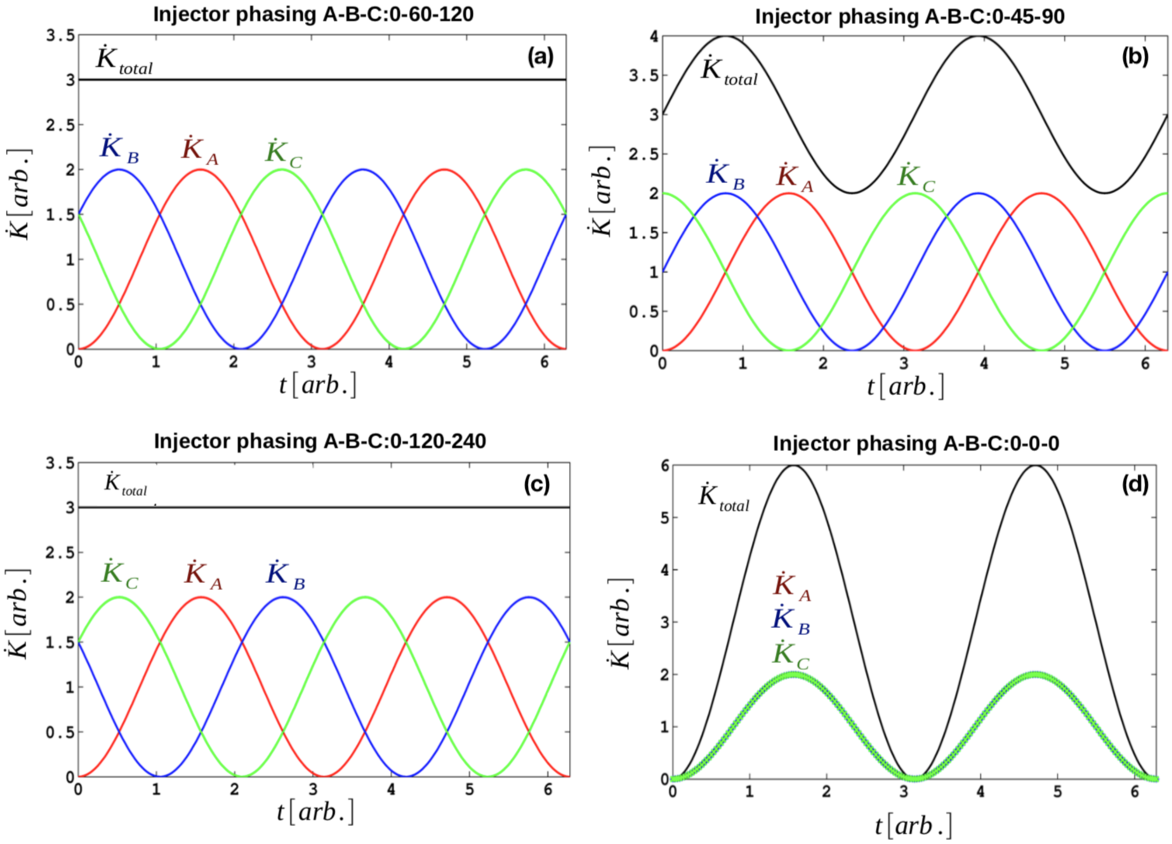

Figure 1.14: A comparison of helicity injection rates at varying injector phasing in HIT-SI3. Images (a) and (c) show the two phasings on HIT-SI3 that provide steady volumetric helicity injection rates. Images (b) and (d) show two example phasings (0-45-90) and (0-0-0) which have time varying helicity injection rates. Though spheromak performance appears to be maximized with constant helicity injection rate injector phasing, in all injector phasings tried led to the formation and sustainment of spheromak configurations, showing the operational flexibiity of this experimental platform.

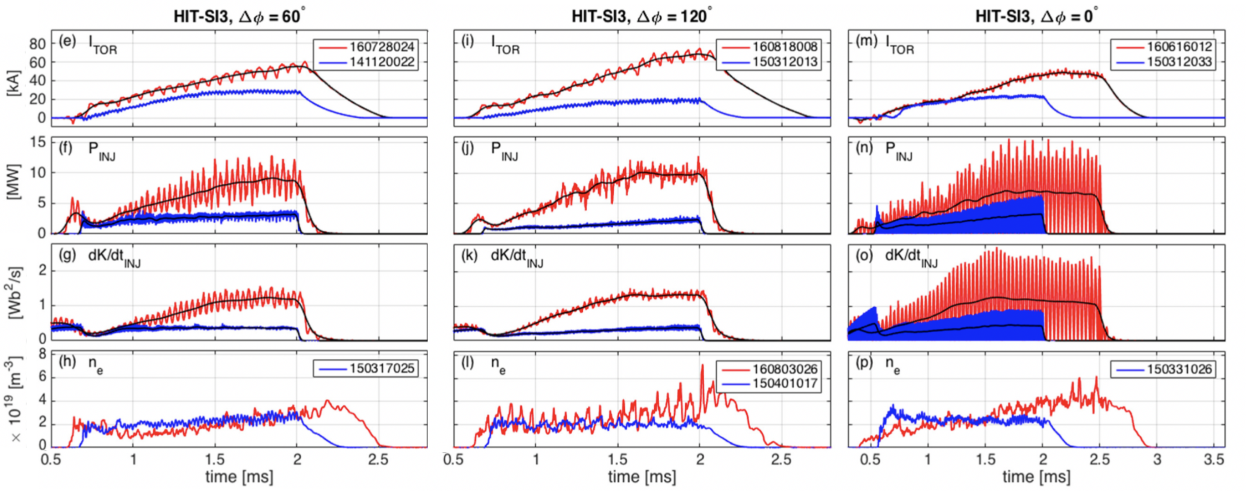

Figure 1.15: Representative time traces from the HIT-SI3 experiment using three different injector phasings and frequencies. Blue traces are for high frequency operations (i.e. $f_{inj} \approx 50$ kHz), and red traces are for low frequency operations (i.e. $f_{inj} \approx 4.5$ kHz). Plotted in each column from top to bottom is the toroidal plasma current I_{TOR}, helicity injector power P_{INJ}, helicity injection rate $\frac{dK_{INJ}}{dt}$, and far-infrared (FIR) interferometer measured electon density n_e. Note for both 60 and 120 degree phasing (left and center) the helicity injection rate is always non-zero, whereas for 0 degree phasing (right) the helicity injection rate varies much more in time [31].

Chapter 2

NEUTRAL DYNAMICS IN FUSION PLASMAS

2.1 Background and Motivation

Neutral particle dynamics can play important roles in plasma experiments, such as the HIT-SI and HIT-SI3 spheromak experiments described previously. Even in high-temperature fusion devices, such as tokamak configurations, neutral dynamics can have pronounced effects on the overall performance of the device, power exhaust, and in other areas to be described in the next subsections.

2.1.1 Gas and pellet Injection

Gas injection is often used for initial startup and continuous plasma fueling in many plasma physics experiments around the world. For example, in the HIT-SI and HIT-SI3 experiments, deuterium or helium gas is injected with gas puff valves that are capable of rapid actuation [30]. Gas injection occurs in the inductive helicity injectors, and through the helicon antenna that is used as a pre-ionizer on HIT-SI and HIT-SI3. [32]. After plasma breakdown occurs from applying sufficiently large voltages with the inductive helicity injectors, gas is continuously fed into the helicity injectors to avoid termination of the injector currents, which is commonly referred to as injector starvation. Thus, gas injection into the helicity injectors and the helicon pre-ionizer both are sources of neutral particles in the system.

Another example of the importance of fuel injection in plasma physics experiments is provided in the ITER tokamak experiment currently under construction in Cadarache, France, shown in Fig. 1.5. In ITER, cryopumps will be used to remove impurities from the plasma, such as helium ash produced from fusion reactions [12, 33]. After being produced via a fusion reaction, He-4 nuclei do not undergo subsequent fusion reactions and will tend to displace hydrogen in the core due to quasineutrality conditions (i.e. $n_e = \sum\limits_i Z_i n_i$). Above a particular helium population fraction ($\approx 3-5\%$), core hydrogen isotope dilution can jeopardize fusion power balance [16]. Thus, helium ash must be promptly removed from the core plasma after production, and typically helium-cooled cryopumps are the method of choice for removal of this material [16]. However, due to operation of cryopumps near the boiling point of helium ($\approx$ 4.2 K) and the higher boiling temperature for hydrogen ($\approx$ 20 K), these devices tend to more effectively pump hydrogen isotopes when compared to helium. As a result, fusion systems making use of cyropumps will tend to remove a considerable amount of the fuel from the system before it fuses in attempt to maintain an acceptable helium population in the core fusion plasma. Due to this extraction of fuel from the system, fuel injection methods such as gas injection [34] and frozen pellet fueling [35] are used to counteract the removal of fuel from fusion plasmas, thereby maintaining approximately constant plasma density during steady-state operations.

In short, since some method of fueling that involves the introduction of neutral particles into fusion plasmas is needed, this underpins the need for measuring and simulating plasma-neutral dynamics. It is important to ensure the underlying plasma-neutral dynamics governing the efficacy of these methods are well understood.

2.1.2 Edge Recycling

Most plasmas produced in the laboratory are created within a vacuum chamber, which introduces a plasma-material boundary in some capacity. The existence of a plasma-material boundary, which most commonly is an interface between plasma and a solid material, introduces sources of neutral particles and complex dynamics near the plasma-material boundary in a region colloquially referred to as the plasma edge. Considerable amounts of research has been performed to better understand the plasma-material boundary in magnetic fusion systems, and [36] provides a thorough discussion of this subject matter. However, for completeness, a simple basis for understanding the plasma-material interface in magnetic fusion devices is provided to serve as a physical foundation for this work.

As one of the simplest models for understanding the plasma-material interface in a laboratory experiment, consider an unmagnetized, quasineutral plasma in thermodynamic equilibrium, such that the velocity distribution function for both the ion and electron species is well described by a Maxwellian distribution. Then, assume this plasma contacts a solid material surface. Under the assumption of no net-electric current being drawn by the wall, or in other words, assuming ambipolar flow of ions and electrons to the wall, an electrostatic sheath is generated. Within the sheath region, aforementioned quasineutrality conditions are violated, and there is significant electrostatic potential that forms that is commonly referred to as the sheath voltage. This electrostatic potential tends to accelerate ions toward and repel electrons away from the plasma-facing wall. Only the faster electrons in the velocity distribution function impact the wall since slower electrons are reflected by negative surface charge that is responsible for generating the electrostatic potential. Fig. 2.1 provides an illustration of the electrostatic sheath, which can be shown to have a characteristic length on the order of few Debye lengths ($\lambda_{De} = (\frac{\epsilon_o k T_e}{n_e e^2})^{1/2}$ [11]). Sheath physics will not be addressed in detail in this doctoral work since accurately capturing sheath dynamics is beyond a MHD plasma model that will be used extensively throughout this work. However, considerations of sheath dynamics will be made in some areas of this work, in particular, when choosing boundary conditions for MHD plasma-neutral simulations to be described in subsequent sections.

Provided with the understanding that both plasma ions and electrons impact a solid surface after interacting with an electrostatic sheath region within a few Debye lengths of the wall, it is discussed by Stangeby in [36] that plasma and solid materials do not coexist since ions and electrons tend to stick to, or embed themselves into material surfaces and subsequently recombine into neutral particles. In general, two categories of interactions of ions and electrons with the wall is that of prompt backscatter and absorption/desorption, as shown in Fig. 2.2. The primary difference between these two processes is the dwell time of the ions and electrons while interacting with a material boundary. In the case of prompt backscatter, an incident ion and electron quickly recombine on the material surface, and

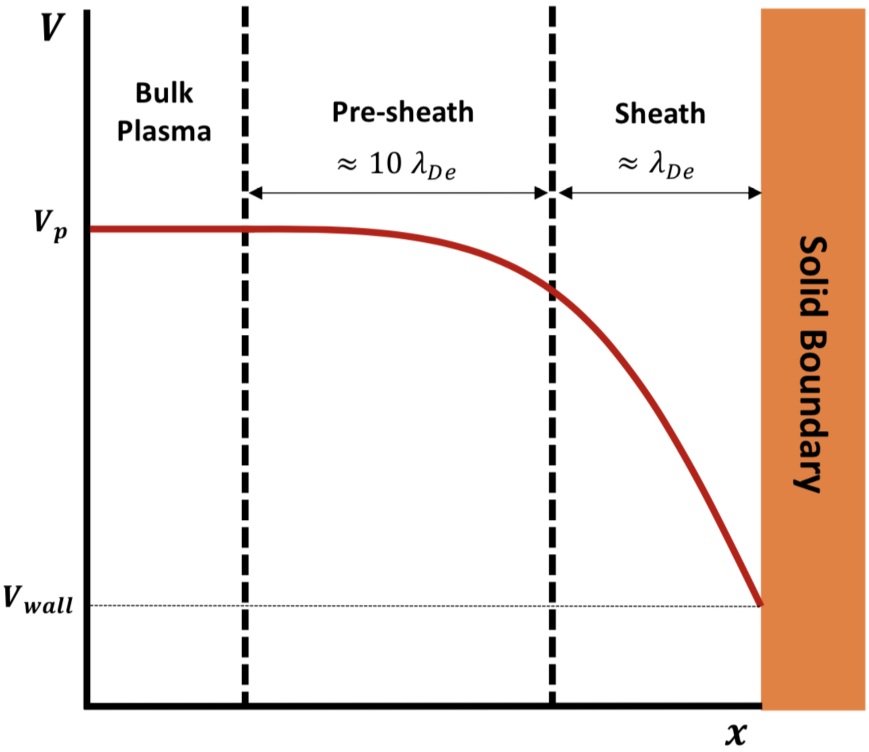

Figure 2.1: An illustration of the electrostatic sheath that is produced at plasma-solid interfaces. Note the negative voltage of the wall relative to the plasma voltage, which tends to accelerate ions that enter the sheath region toward the wall, and repel slower electrons away from the wall, thereby achieving ambipolar flow.

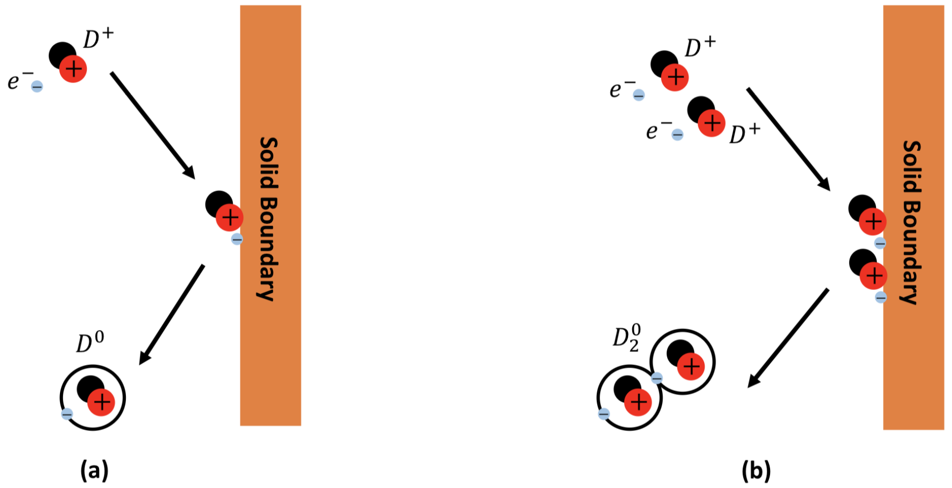

Figure 2.2: An illustration of the two primary categories of interaction of plasma with a solid boundary. Image (a) depicts prompt backscattering, whereas image (b) depicts the process of absorption and desorption where neutral particles are desorbed from the wall as thermalized molecules.

re-enter the plasma region as a monatomic atom with a significant fraction of the incident ion kinetic energy. In the case of absorption/desorption, a longer dwell time enables the recombination and thermalization of ions and electrons into neutral particles at the wall temperature, which then are desorbed from the surface as thermal neutral particles, such as diatomic deuterium molecules shown in Fig. 2.2(b). The process described, where ions and electrons interact with a solid wall which subsequently gives rise to neutral particles, is often referred to as edge recycling [36]. This process is important for understanding edge plasma dynamics and can have dramatic effects on the performance of a fusion device as a whole, as will be described in subsequent sections.

Following the production of neutral particles via edge recycling through the processes shown in Fig. 2.2, these neutral particles are once again in the presence of plasma ions and electrons. In effect, the production of these neutral particles via recycling can be thought of as a source of gas injection described in the previous section at any plasma-material interface. Neutral particles will interact with the ion and electron species in the plasma. In Fig. 2.3, multiple pathways for the dissociation and ionization of diatomic deuterium molecules are shown: one-step electron-impact ionization (EI) of a deuterium molecule in (a), Frank-Condon dissociation and subsequent EI of monatomic deuterium atoms (b), and two-step EI of a deuterium molecule [36]. In the description of images (a) and (c), the number of steps for EI to occur refers to the the number of steps required to produce the first, monatomic deuterium ion in the respective process. In Fig. 2.4, additional interactions of interest for plasma species interactions with monatomic deuterium atoms are shown, such as resonant charge exchange (CX) in (a), and EI in (b).

It should be noted that two important processes, electron-impact ionization (EI) and resonant charge exchange (CX) have been identified in this section that are of interest for this work. Due to edge recycling at plasma-material interfaces, the process of EI of these edge recycled neutral particles represents a continuous expenditure of plasma energy. Additionally, any gas or pellet injection for fueling as described in the previous section will result in plasma energy losses due to EI. Lastly, resonant charge exchange (CX) reactions can play an important role in fusion plasmas as well. Relatively cold, monatomic neutral atoms can undergo CX with relatively hot plasma ions. Thus, the products of such a CX reaction is a relatively hot neutral atom and relatively cold plasma ions, and shown in Fig. 2.4(a). Since the two particles involved in this CX reaction have changed species (i.e. the ion became a neutral atom, and vice versa) without any energy input, this reaction provides a net transfer of energy from the plasma species to the neutral species. Since neutral particles are no longer confined by magnetic fields, large amounts of CX reactions of hot plasma ions and cool neutral atoms can result in significant plasma energy and momentum losses from a fusion plasma back to the plasma-material interface if the CX hot neutral atoms are not reionized before exiting the system.

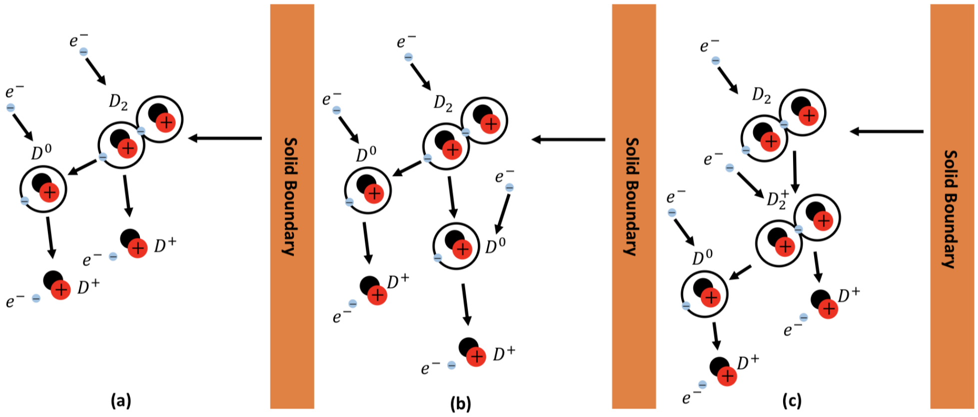

Figure 2.3: An illustration of different molecular dissociation and ionization processes for deuterium molecules that are desorbed from a solid plasma-facing surface. In Image (a), the two-step dissociation and ionization of a deuterium molecule is shown. Image (b) shows the generation of two neutral deuterium atoms after the dissociation of molecular deuterium, and the subsequent ionization of these atoms. This process is commonly refered to as Frank-Condon dissociation. Lastly, image (c) shows the two-step dissociation and ionization of a deuterium molecule via the intermediate generation of D_2^+ in the process. Note the primary ionizing electrons are not shown in the final products towards the lower section of the figure.

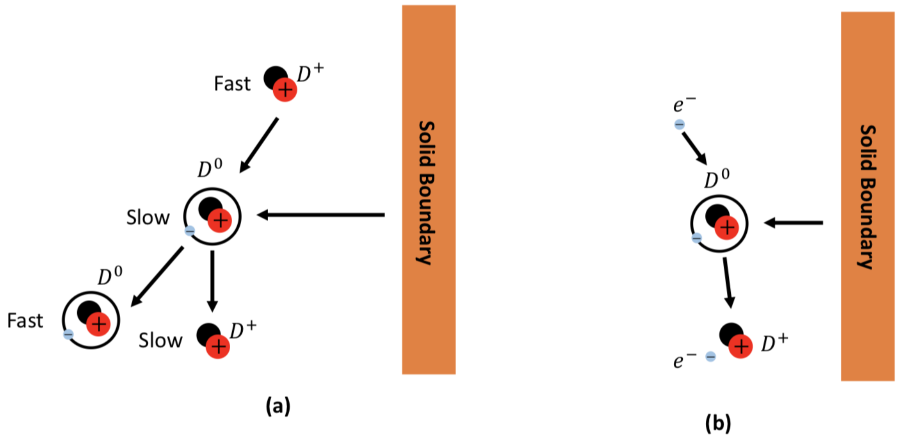

Figure 2.4: An illustration of different interactions of interest for deuterium atoms that are backscattered from the wall, or produced during intermediate molecular dissociation steps shown in Fig. 2.3. Image (a) depicts the resonant charge exchance interaction, which can give rise to very energetic neutral atoms after charge exchanging with hotter plasma ions. Lastly, image (b) depicts EI of an monatomic deuterium atom.

2.1.3 Gas-box divertors and detachment

As is mentioned in the previous sections, neutral particles are introduced into fusion systems via gas injection, pellet injection, and edge recycling in regions where there is a plasma-material interface. Two important plasma-neutral reactions of interest, namely, electron-impact ionization (EI) and resonant charge exchange (CX) have been identified thus far. Another plasma-neutral reaction of interest, radiative recombination (RR), can play an important role in magnetic fusion devices, primarily in the cooler regions of the plasma edge. An example of such a region where radiative recombination is important is in the divertor region of tokamak fusion experiments [13]. Historically, the boundary of tokamak fusion experiments was defined by a limiting surface, such as the vacuum chamber or a inserted piece of solid material, shown in Fig. 2.5(a) and Fig. 2.5(b). Using the understanding that solid materials are sinks for plasma, a movable limiter allowed for control over the location of the edge of magnetically confined plasma. However, as described in the previous section, any solid plasma-material interface will introduce a source of neutral particles into the system due to edge recycling, which can have deleterious effects on plasma performance via EI and CX losses as described previously. As suggested in [37], is it favorable to have low neutral densities immediately outside of the core plasma region to reduce the negative impacts of EI and especially CX that can lead to considerable plasma energy and momentum losses from multiple-generation charge exchange events [37].

Motivated by the favorable impact of moving recycling neutral particles further away from the core fusion plasma, most modern tokamaks make use of a diverted magnetic topology instead of a limiter, shown in Fig. 2.5(b) and Fig. 2.5(c). External shaping coils are used to modify the poloidal cross section of the tokamak plasma, and allows for the generation of an "x-point" where the poloidal magnetic field is locally zero but with non-zero toroidal magnetic field [36]. The location and number of x-points in a tokamak configuration characterizes the type of diverted magnetic topology being employed. In Fig. 2.5(c) and Fig. 2.5d, a lower single null (LSN) and upper single null (USN) are shown, respectively. Additionally, a LSN and USN can be generated simultaneously, which gives rise to a double null (DN) diverted magnetic topology [13]. The commonality between these diverted topologies is moving the location of the primary plasma-material interface, and therefore the location of the majority of edge recycling, further away from the core plasma. This modification to the location of plasma-material boundary allows for a reduction in EI and CX losses from the core plasma, and instead attempt to localize these plasma-neutral interactions to within the divertor region.

Beyond improved core plasma performance through the use of a diverted magnetic topology, the concentration of particle and heat exhaust through the scrape-of-layer (SOL) onto the divertor assemblies introduces new challenges and opportunities [36]. First, a diverted magnetic topology concentrates plasma heat flux onto a surface area that is a relatively small fraction of the total first wall surface area facing the plasma, as can be seen when comparing Fig. 2.5(a), Fig. 2.5(c) and Fig. 2.5(d). As a result, the divertor assemblies can be subject to relatively large heat fluxes (i.e. $q'' \geq 10$ MWm^{-2}) [12, 13]. In short, it is challenging to design an effective cooling system that removes these large heat fluxes in steady-state. Also, periodic edge plasma phenomena, such as edge localized modes (ELMs), or other transient plasma dynamics introduce the possibility of time varying heat fluxes that can exceed operational limits of the heat removal systems. As a result, there is concern that excessively large heat fluxes on the divertor plates can permanently damage these assemblies and jeopardize the successful operation of a magnetic fusion reactor.

Luckily, with the concentration of plasma heat exhaust on the divertor plates, there is also a concentration of plasma particle exhaust on these assemblies as well. Due to this relatively high plasma particle flux on the divertor plates, edge recycling leads to correspondingly high neutral particle densities in the divertor region as well. High neutral densities are welcomed in the divertor region because the previously described process of EI can remove energy from the incoming plasma heat flux thereby reducing the surface heat flux on the divertor assemblies. Additionally, through the introduction of additional neutral gas through gas injection ports in the divertor region, which may be the same species as the core plasma, or

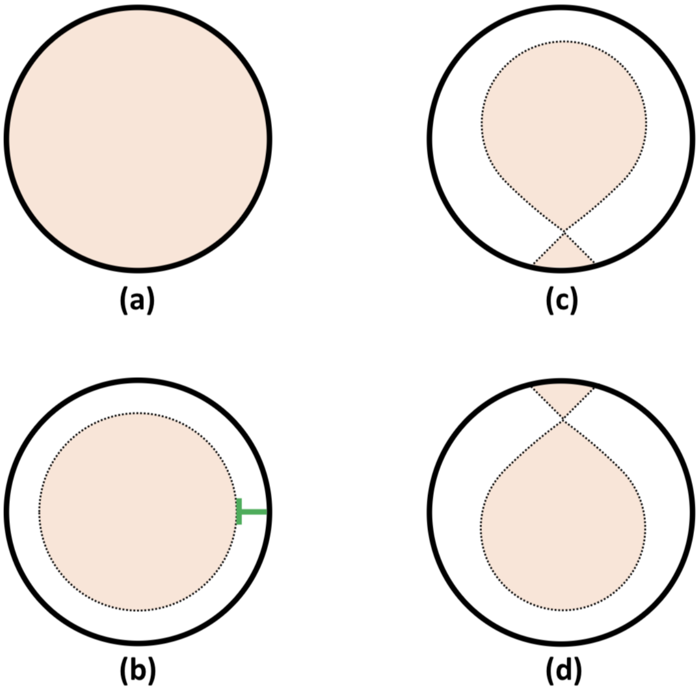

Figure 2.5: A illustration of both limited and diverted tokamak plasmas. Image (a) shows a wall-limited plasma, whereas image (b) depicts the use of a bumper limiter (shown in green) to move the plasma boundary further away from the wall. Image (c) depicts a LSN diverted topology, whereas image (d) depicts an USN diverted topology. Note the fine dashed black line indicates the location of the magnetic separatrix of the tokamak plasma, which is located at the wall in image (a).

a higher Z impurity, more plasma heat flux can be expended on EI until the plasma above the divertor plates becomes relatively cool (i.e. $T \leq 1$ eV for hydrogen plasmas [36, 38]). Below this plasma temperature, the reaction rate for radiative recombination becomes significant, which is the process when an ion and electron recombine into a monatomic atom while simultaneously emitting a photon with energy $E_\gamma = h\nu$ [38, 36]. Then, since magnetic fusion plasmas are optically thin [37], these photons will eventually impact the wall and be absorbed. Thus, the process of radiative recombination in advanced divertors is paramount to handling high plasma heat fluxes since it efficiently converts plasma heat flux that would have impinged onto the divertor plates into photons, which are then distributed over a larger plasma-facing wall surface area than just the divertor assemblies, thereby lowering the plasma heat flux to the divertor plates considerably. A desired state for the operation of a high power density, high plasma heat flux tokamak plasma is with so-called fully detached state, which allows for high performance diverted operation well within operational limits of the divertor cooling system [36]. Advanced methods of feedback control for plasma heat exhaust using the principles described in this section have been studied extensively in Alcator C-Mod [39].

2.2 *Prior works and defined needs*

2.2.1 Neutral density and temperature measurements

Prior to this work, limited information regarding neutral densities and temperatures in sustained spheromak plasmas produced in the HIT-SI3 experiments was available. Prior to this work, optical diagnostics were capable of measuring volumetric emission from the plasma, specifically for the $D_\alpha \approx 656$ nm or for particular wavelength ranges viewed with the SPRED (Survey, Poor Resolution, Extended Domain) spectrometers [40]. These diagnostics do not provide spatially resolved information regarding atomic emission from the plasma. Thus, the deficiency of spatially resolved neutral density and temperature information in HIT-SI3 sustained spheromak plasmas motivate measurements of these parameters for this work. Such measurements would provide meaningful information concerning plasma-neutral interactions occurring in this system, and provide data for comparisons with simulations to be described in the next section.

2.2.2 Simulation of plasma-neutral dynamics

There has been a multitude of efforts in simulating plasma-neutral dynamics in plasma physics and fusion experiments. The most sophisticated attempts to simulate plasma-neutral dynamics in magnetic fusion devices are codes that make use of Monte Carlo (MC) methods for simulating the neutral species. Typically, kinetic MC neutral codes are coupled to a plasma fluid code to simulate plasma-neutral reactions of interest. Simulations of plasma-neutral mixtures have been conducted in the scrape-off-layer (SOL) and divertor regions of tokamak devices using a multitude of codes. One widely used code is SOLPS (Scrape-Off Layer Plasma Simulation), which is a hybrid 2D code featuring a multifluid model for ions and electrons in the edge coupled to a 3D, kinetic MC code for the neutral species [41]. Another example is the UEDGE code, based on a set of multifluid, multispecies transport equations for the plasma coupled to a reduced set of Navier-Stokes transport equations for hydrogen isotope atoms [42, 43]. Also, both EDGE2D and EMC3, which is a 2D plasma fluid code and a 3D plasma fluid MC code, respectively, have been coupled with EIRENE, a 3D, kinetic MC code for the neutrals [44, 45, 46, 47]. Lastly, another code used for simulating plasma-neutral interactions is NIMRAD, which has been used to simulate MGI during disruptions on tokamaks, which is of importance to ITER and other future burning plasma experiments [48, 49]. NIMRAD is a code based on NIMROD, which is coupled to the KPRAD atomic physics code for the neutral species [49].

Many of the aforementioned computational efforts to capture relevant plasma-neutral dynamics invoke a kinetic treatment of neutral species primarily because they can exhibit significant deviations from Maxwellian velocity distributions, with marginal collisionality to justify a highly collisional, fluid model in the plasma edge [36]. Additionally, assuming a sufficiently collisional plasma, the complexity of plasma-neutral interactions in the edge can become increasingly difficult to capture with a fluid model due to the need to introduce separate evolution equations for each species of interest (e.g. molecules, charge states, etc.). Thus, when simulating complex physical systems, MC simulations are sometimes preferred as it becomes intractable to define and evolve separation equations with appropriate closures needed for each species to be included in a multifluid model.

However, with the above arguments for a kinetic treatment of neutral species, in systems with short mean-free-paths (i.e. $\lambda_{mfp} \ll L_{system}$), it is physically justifiable to capture the primary plasma-neutral reactions of interest using a multifluid model, which can be incorporated into existing MHD codes used for simulating highly collisional plasmas. Of particular interest to this study, a general nonlinear fluid model has been derived by Meier and Shumlak, which will be described in detail in subsequent sections [50]. This model has been implemented in the HiFi code by Meier and Shumlak at the University of Washington, and used for simulating various 2-D systems, such as coaxial plasma acceleration, and rotating magnetic field driven FRC ion spin-up [38]. This work will serve as the theoretical foundation for the simulations performed in this study, with the focus of simulating plasma-neutral dynamics in the HIT-SI3 experiment using a 3D Extended-MHD code called PSI-Tet.

2.2.3 Dynamic plasma-neutral fluid models

After reviewing prior works in this subject area, there is a need for a 3D Extended-MHD code that captures key plasma-neutral dynamics of interest in magnetized plasma configurations. Many of the codes, such as SOLPS, NIMRAD, UEDGE, EDGE2D are 2D codes for use in largely axisymmetric devices such as tokamaks. HIT-SI3 is a non-axisymmetric sustained spheromak experiment, and thus a 3D MHD code capable of performing calculations with a non-axisymmetric simulation volume is of unique interest. A fully 3D, unstructured, tetrahedral mesh Extended-MHD code called PSI-Tet is currently being used to simulate relevant plasma dynamics in both HIT-SI and HIT-SI3 experimental geometries, and is used in parallel with the more established NIMROD code [51, 52, 53] to enhance understanding of plasma dynamics in these systems. PSI-Tet is able to capture the non-axisymmetric geometry of HIT-SI and HIT-SI3, which cannot be done with the NIMROD code since it requires an

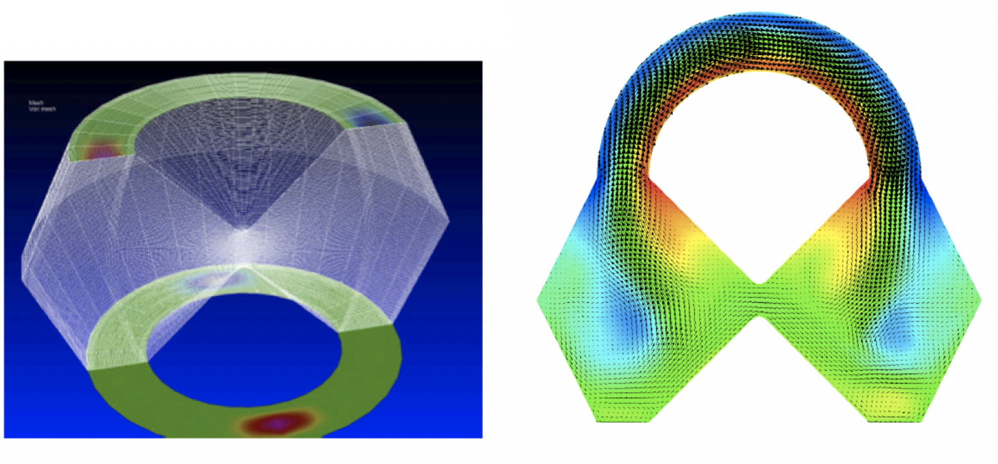

Figure 2.6: A comparison of the NIMROD and PSI-Tet simulation domains. *Left*: Axisymmetric NIMROD mesh used for simulating HIT-SI, with helicity injectors modeled as boundary conditions on axisymmetric simulation domain. *Right*: An example of a PSI-Tet simulation, showing the ability to simulate plasma dynamics within the bow-tie shaped confinement volume and within non-axisymmetric magnetic helicity injectors.

axisymmetric meshed solution domain [54]. Instead, the injectors are modeled as boundary conditions on the axisymmetric flux conserver domain in NIMROD as an approximation to the experimental geometry [54]. A comparison of the simulation domains between NIMROD and PSI-Tet is shown in Fig. 2.6.

For a complete description of plasma-neutral interactions of interest, a kinetic model based on a Boltzmann equation for each species is required, shown in Eq. 2.1.

$$\frac{\partial f_\alpha}{\partial t} + \vec{v} \cdot \frac{\partial f_\alpha}{\partial \vec{x}} + \frac{q_\alpha}{m_\alpha}(\vec{E} + \vec{v} \times \vec{B}) \cdot \frac{\partial f_\alpha}{\partial \vec{v}} = \frac{\partial f_\alpha}{\partial t}|_{col} = \sum_\beta C_{\alpha\beta} \tag{2.1}$$

where f_α is the distribution function for a species α, $\vec{v}$ is bulk velocity of the species, $\vec{E}$ and $\vec{B}$ are electric and magnetic fields, respectively, and $C_{\alpha\beta}$ is an operator for quantifying the impact of collisions between species α and β.

With a multitude of different states, species, and collision types in magnetic fusion plasmas, a completely descriptive kinetic model can quickly becomes computationally intractable for use in simulating these systems. Instead, multifluid equations can be derived from the kinetic equation by taking velocity moments of Eq. 2.1. Simplified, multifluid plasma-neutral models have been developed using this approach that have varying degrees of validity provided collisional mean-free-paths are short compared to the characteristic system size [50, 55, 56, 57, 58]. The neutral model provided in [50] captures the primary plasma-neutral reactions of interest within a multifluid framework: electron-impact ionization (EI), radiative recombination (RR), and resonant charge exchange (CX), as shown below.

$$
\begin{gathered}
e^- + n \rightarrow i^+ + 2e^- - \phi_{ion} \\
e^- + i^+ \rightarrow n + h\nu \\
i^+ + n \rightarrow n + i^+
\end{gathered}
$$

This model is derived following the approach carried out by Braginskii in [59], with the addition of the plasma-neutral reactions of interest. The model derives closed-form expressions for the reaction terms by only considering the Maxwellian component of the reacting species; this process is consistent with the multifluid formulation of the model, which includes an electron, plasma, and neutral species.

This model includes self-consistent density, momentum, and energy evolution equations for each species considered. From the three-fluid model, a two-fluid model can be derived by taking the appropriate asymptotic limits to yield an MHD formulation for the plasma fluid interacting with a neutral fluid. The process for deriving the two-fluid (plasma-neutral) model from the general three-fluid model of the system is provided in Appendix A. With the MHD formulation of the plasma fluid, this model can be implemented into existing MHD codes by adding in neutral fluid equations, closures, and the appropriate plasma-neutral reaction terms. In this study, plasma-neutral Extended-MHD model is implemented in PSI-Tet to simulate plasma-neutral dynamics in the non-axisymmetric HIT-SI3 experiment.

2.3 Focus of work

In the previous subsections, chosen topics have been discussed topics that highlight the important roles neutral particles can play in magnetic fusion devices, but it should be noted that this is not an exhaustive list. More complicated interactions involving molecules, such as rotational or vibrational modes, have not been discussed but can also play important roles in magnetic fusion plasmas [60, 61]. Such effects could be captured in more sophisticated plasma-neutral formulations as a subject of future work. Nevertheless, three main reactions of interest have been identified: electron impact ionization (EI), resonant charge exchange (CX), and radiative recombination (RR). These identified plasma-neutral interactions while considering only a monatomic neutral fluid interacting with a MHD plasma fluid will be considered for this study.

The main topics included in this work is the measurement and simulation of plasma-neutral dynamics in the HIT-SI3 experiment. These topics are of particular importance in smaller plasma devices such as HIT-SI3 due to a relatively low plasma surface area to volume ratio, and a relatively short length from the material wall to the core of the spheromak configurations produced in this device (i.e. $a \approx 0.25$ m). Additionally, gas injection occurs in both the inductive helicity injectors and helicon pre-ionizer, which provides another source of neutrals into the system. As was mentioned previously, spatially-localized information concerning the neutral particle density and temperature in HIT-SI3 was not known, and Extended-MHD simulations including effects from plasma-neutral reactions had not been performed of the HIT-SI3 device. Thus, the focus of this work is on remedying these deficiencies with experimental data and enhance computational capability by measuring both the neutral particle densities and temperatures in the HIT-SI3 experiment, implementing a two-fluid (plasma-neutral) MHD model [50] into the 3D Extended-MHD code PSI-Tet [51], and then attempt to validate the implemented plasma-neutral model with measurements of neutral parameters in HIT-SI3 spheromak plasmas. Provided with a validated Extended-MHD code that can capture relevant plasma-neutral dynamics of interest, this computational tool could be used on other plasma physics and fusion experiments of interest, or expanded to include additional plasma-neutral dynamics that have not been included in current implementation

Chapter 3

RESEARCH OBJECTIVES AND METHODS

3.1 Neutral measurements on HIT-SI3 with TALIF

3.1.1 Overview of TALIF diagnostic

It is desired to measure neutral particle densities and temperatures in sustained spheromaks on the HIT-SI3 experiment. Through a collaboration with West Virginia University, a two-photon absorption laser induced fluorescence (TALIF) diagnostic is used to measure absolute monatomic deuterium neutral density and temperature as a function of position and time in the HIT-SI3 experiment.

The TALIF diagnostic derives its name from the simultaneous absorption of two $\lambda \approx 205$ nm photons by atomic hydrogen in its ground state (i.e. principal quantum number $n = 1$), which excite bound electrons from the $n = 1$ to the $n = 3$ energy level (Lyman-β (Ly-β) transition) [62]. After this excitation, and an excited state lifetime of 16 ns [63], a known fraction of the hydrogen atoms decay to the $n = 2$ quantum level and emit photons with wavelength $\lambda \approx 656.3$ nm. The photon absorption rate, which is determined by measurement of Balmer-α (i.e. D_α) emission, is proportional to the number of neutral atoms with a given velocity in the region illuminated by the focused beam. In measuring the TALIF emission as a function of scanned laser wavelength, one can determine the neutral hydrogen density, temperature, and flow from this diagnostic system.

An illustration of the TALIF diagnostic system implemented on the HIT-SI3 experiment in provided in Fig. 3.1. The TALIF emission, $S(\lambda)$, from neutral hydrogen atoms of velocity space density $n(v)$ is given by Eq. 3.1 [64],

$$S(\lambda) = \frac{\Delta\Omega}{4\pi} n(v) I^2 \sigma \alpha G \tag{3.1}$$

where $\Delta\Omega$ is the solid angle over which the emitted light is collected, I is the laser intensity, σ is the absorption cross section from the initial state (i.e. n = 1) to the excited state (i.e. n = 3), α is a coefficient between 0 and 1 that includes the effects of the branching ratio from the excited state to the final state of fluorescence, the transmission efficiency of optical filters, and the quantum efficiency of the photodetector, and G is the gain of the photomultiplier tube shown in Fig. 3.1.

An important dependency of the TALIF emission to note is that to the square of the laser intensity, instead of the linear proportionality for laser induced fluorescence (LIF) [62, 64]. This feature allows for the better localization of ground state hydrogen density and temperature measurements around the focal point of the focused $\lambda \approx 205$ nm laser beam. For this diagnostic system, the resolution along the beam path (i.e. on-axis) is less than 1 cm using the beam waist and quadratic dependence of TALIF on incidient laser intensity. Off-axis resolution is sub-millimeter.

Additionally, it is possible to make a Doppler-free measurement by employing two counter-propagating beams, where the energy of a photon from each beam sums to the transition energy for all atom velocities. In practice, for this type of measurement the time resolution of density measurements is increased as there is no need to scan the laser frequency with this setup [62]. Due to collaboration time constraints, only confocal measurements are made on the HIT-SI3 experiment, as shown in Fig. 3.1.

Experimental Materials

The experimental materials used for this diagnostic system are as follows. The lasers used in this study was a frequency-tripled, pulsed dye laser (Sirah Cobra-Stretch$^{\text{TM}}$) pumped with a frequency-doubled Nd:YAG laser, operating at 20 Hz. The output of the Nd:YAG laser was up to 750 mJ of 532 nm light in a 10 ns pulse. The output of the Nd:YAG laser pumped the dye laser, which contained a mixture of Rhodamine B and Rhodamine 101. The dye laser is optimized to operate in the 612 – 630 nm wavelength range up to 120 mJ per 12 ns pulse. The 615 nm output of the dye laser was frequency tripled by first passing through a SHG-250 BBO crystal (i.e. frequency doubled to 308 nm), mixing it with the 615 nm fundamental beam, and then passing it through another SHG-206 BBO crystal to generate a third harmonic beam at 205 nm in a 6 – 8 ns pulse with a 5 mm beam diameter. The 205 nm beam is at the desired UV wavelength to be incident on neutral atoms present during plasma discharges in the HIT-SI3 experiment to cause the desired excitation. All measurements made during this study were acquired using less than 2 mJ of UV energy.

The confocal measurement scheme shown in Fig. 3.1 requires that both the emitted and injected photons pass through the same focusing/collecting lens. This diagnostic setup uses a mirror with a 1 cm diameter hole cut through the center at a 45^o angle, which allows for the full passing of the 5 mm diameter laser beam while still reflecting the majority of the collected fluorescent emission toward the PMT. The localized measurement location within the HIT-SI3 flux conserver is changed by only moving the final focusing lens closest to the optical view point shown in Fig. 3.1. Collected 656.3 nm emitted photons are filtered with a 656.3 ± 0.5 nm band-pass filter prior to being collected by the PMT to ensure the measured signal was the desired D_α wavelength of interest for this diagnostic, as shown in Fig. 3.1.

Calibration and measurement method

Using the known relative TALIF absorption cross sections between Kr and D ($\frac{\sigma_{\mathrm{D}}}{\sigma_{\mathrm{Kr}}} = 0.62$) [65, 66, 67], the TALIF diagnostic system can be absolutely calibrated by comparing separate TALIF measurements perform on Kr gas and D plasmas with known fill pressure of Kr. Absolute measurements of the integrated deuterium ground state (i.e. $n = 1$) density are obtained via Eq. 3.2,

$$n_{\mathrm{D}} = \int n_{\mathrm{D}}(v)\, dv = n_{\mathrm{Kr}} \left(\frac{S_{\mathrm{D}}}{S_{\mathrm{Kr}}}\right) \left(\frac{\sigma_{\mathrm{Kr}}}{\sigma_{\mathrm{D}}}\right) \tag{3.2}$$

where n_{Kr} is the Kr number density, and S_{D} and S_{Kr} are the measured TALIF signals for measurements performed on deuterium plasmas and Kr gas, respectively. Kr calibration are made on HIT-SI3 using a 0.2 – 0.4 mTorr Kr fill measured with a convectron calibrated to N_2 and the known correction for Kr gas measurements. For each new measurement location in the HIT-SI3 chamber, a new Kr calibration is performed.

After the TALIF emission photons are collected by the PMT shown in Fig. 3.1, the output current from the PMT is integrated over a short interval centered on the laser pulse time. The choice of integration window is constrained by the rise and fall time of the PMT, the laser pulse length (10 ns), and the excited state lifetime (16 ns [63]). To determine the amount of the measured D_α emission is from TALIF, the background D_α signal must be subtracted. For background subtraction, the PMT current immediately before and after the laser pulse is sampled for a time interval set by the observed signal peak. As a result, the TALIF signal as a function of scanned dye laser wavelength is as follows,

$$S(\lambda) = \int_{t_0}^{t_0+\Delta t_m} A(t)\,dt - \frac{\Delta t_m}{2\Delta t_{BG}} \int_{t_0-\Delta t_{BG}}^{t_0} A(t)\,dt - \frac{\Delta t_m}{2\Delta t_{BG}} \int_{t_0+\Delta t_m}^{t_0+\Delta t_m+\Delta t_{BG}} A(t)\,dt \qquad (3.3)$$

where $A(t)$ is the PMT current, t_0 is the start of the laser pulse, and $\Delta t_m = 50$ ns is the integration time window used in this study. Equal background sampling measurement times are used, such that $\Delta t_{BG} = \Delta t_m$. The most significant observed plasma density oscillations for TALIF measurements on HIT-SI3 were at the helicity injector operation frequency of 55.25 kHz, or a period of 18 microseconds. Additionally, the fastest characteristic time in the system is expected to be the radial Alfvén time $\tau_a = \frac{a}{v_{alf}} = \frac{a}{\frac{B}{\sqrt{\mu_o \rho}}} \approx 1.5\,\mu\text{s}$. Since the sampling time is much shorter than the characteristic oscillation and transit times in the HIT-SI3 spheromak plasmas, the background contributions are assumed to be constant throughout the sampling interval. A representative PMT time trace is shown in Fig. 3.4.

The PMT signals are recorded and integrated using process described. The wavelength of the dye laser is scanned to determine the spectral width of the measured TALIF emission. For each wavelength scanned, a minimum of six shots and similar plasma conditions are used and averaged to obtain reported values. The scanned wavelength of the $\lambda \approx 615$ nm dye laser is measured wavelength of the beam obtained with a High Finesse WS7 wavelength meter that has a precision of 0.075 pm. An example of a measured TALIF signal on the HIT-SI3 experiment is shown in Fig. 3.3. Note that a Maxwellian distribution is fitted to the measured TALIF emission data. The area under the fitted Maxwellian, normalized by the laser intensity, PMT gain, and quantum efficiency of various filters and PMT yields the number density of ground state deuterium atoms. The spectral width of the Maxwellian fit $\Delta\lambda$ provides the ground state deuterium atom temperature via Eq. 3.4 using the full-width-half-maximum (FWHM) of the fitted Maxwellian distribution,

$$T = \frac{\Delta\lambda^2 m_{\mathrm{D}} c^2}{2\lambda_0^2 \ln(2)} \tag{3.4}$$

where m_{D} is the mass of the deuterium atom, λ_0 is the nominal wavelength of the centroid of the Maxwellian fit.

The focal point of the laser is adjusted for localized measurements of the neutral density and temperatures across the poloidal cross-section of HIT-SI3. By adjusting the time of the laser pulse at a given location, the temporal evolution of neutral densities and temperatures can be determined as well. Provided with a spatial profile of the neutral density and temperature in HIT-SI3 with TALIF, this information will be compared with the results from PSI-Tet, the Extended-MHD code described previously, once the complete neutral dynamics physics module has been added. This project is a portion of the larger effort of using HIT-SI3 as an experimental platform for verifying and validating Extended-MHD codes like PSI-Tet and NIMROD.

3.2 Simulating neutral dynamics in HIT-SI3

3.2.1 Implementing a dynamic plasma-neutral model into PSI-Tet

As was mentioned previously, the self-consistent, multifluid plasma-neutral models provided in [50] serves as the theoretical foundation for the computational portion of this work. In particular, the two-fluid (plasma-neutral) model that provides separate density, velocity, and temperature evolution equations for each species is desired to be implemented in the Extended-MHD PSI-Tet code. The strong form equations and relevant closures of the two-fluid plasma-neutral model implemented in PSI-Tet are provided in Eq. 3.8 - 3.19. The derivation of these strong form equations starting from the three fluid (ion, electron, and neutral) formulation presented in [50] is provided in Appendix A, including many of the

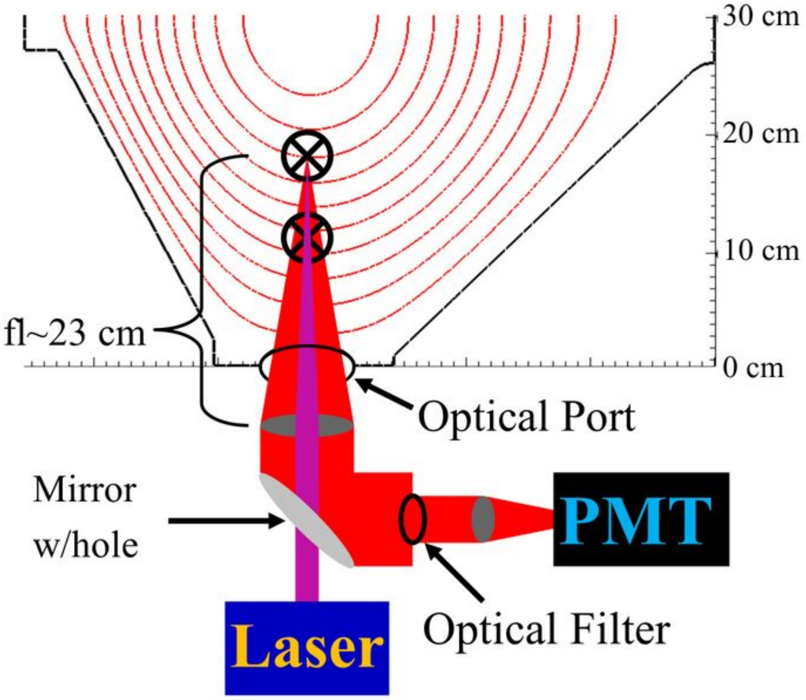

Figure 3.1: The confocal TALIF experimental setup on the HIT-SI3 experiment used for measuring neutral densities and temperatures in spheromak plasmas.

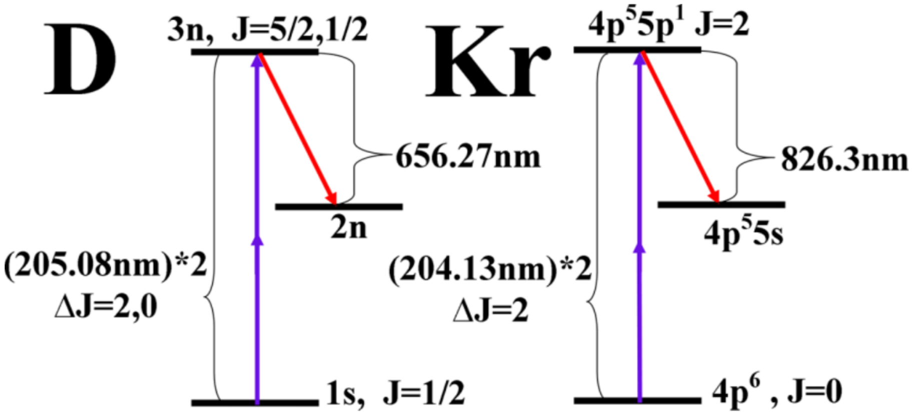

Figure 3.2: Energy levels for both D and Kr of interest for the calibration of the TALIF diagnostic system. Two 205.08 nm photons excite atomic deuterium from the n = 1 to n = 3 energy levels. A fraction of these excited atoms decay to the n = 2 level while emitting 656.27 nm photons, which are collected confocally. For Kr, two 204.13 nm photons excite ground state Kr to an excited state. A fraction of these excited atoms decay to a lower energy state, emitting 826.3 nm photons in the process.

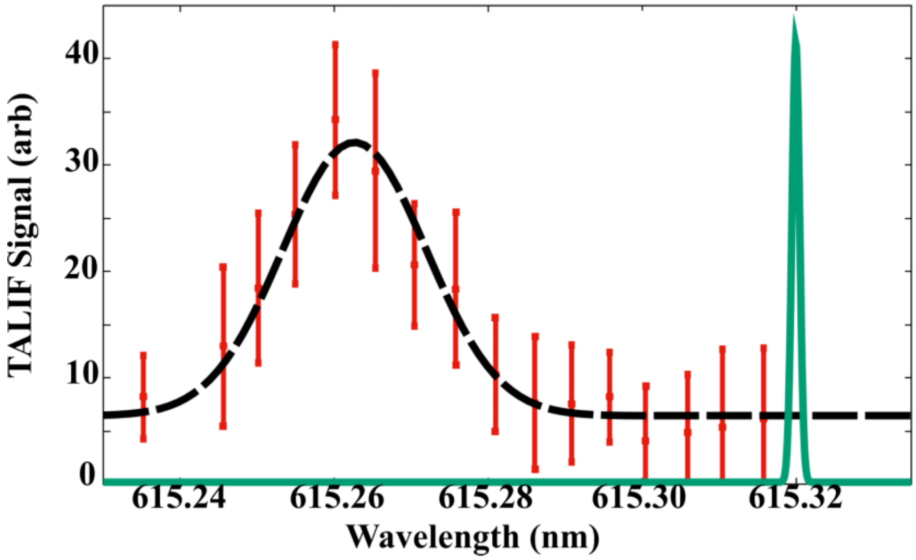

Figure 3.3: A representative normalized TALIF signal as a function of scanned dye laser wavelength ($\lambda \approx 615$ nm). Note the width of the laser line shown in green compared to measured TALIF signal. The amplitude of the TALIF signal is directly related to the measured ground state deuterium density in HIT-SI3 plasmas. The spectral width of the signal provides the neutral temperature. Lastly, any shift of the centroid of the signal would indicate a red-shift or blue-shfit, suggesting a bulk neutral flow.

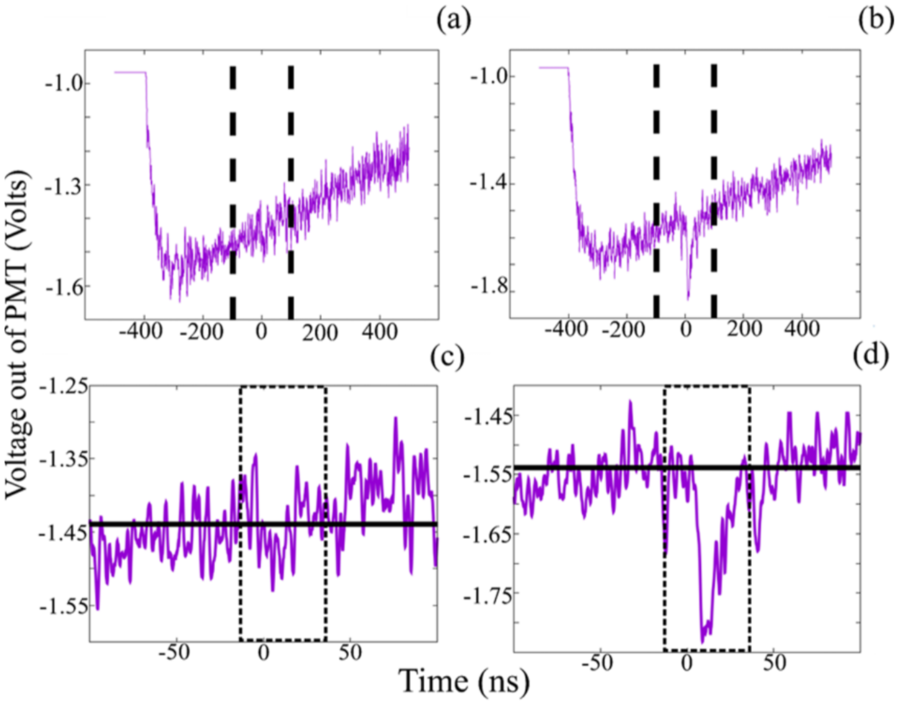

Figure 3.4: A representative PMT current time traces for TALIF measurements on HIT-SI3 for the PMT gate "on" interval for (a) a laser pulse tuned to a wavelength outside of the absorption line width and (b) with the laser on resonance. The integration windows intervals are magnified in (c) and (d). The solid lines in (c) and (d) provide the averaged background during the integration time.

assumptions made in this version of the implementation. As shown in Eq. 3.16, Braginskii anisotropic thermal conduction is used in this implemented model [59]. For neutral thermal conduction, Eq. 3.17 provides the ad-hoc neutral thermal conduction that is inversely dependent on the charge-exchange and hard sphere collisional frequencies is used, in line with previous work [38]. The current version of PSI-Tet provides three different plasma viscosity formulations, kinematic, isotropic, and anisotropic. The majority of simulations performed in this work have used isotropic plasma viscosity. Lastly, simple, fixed coefficient kinematic neutral viscosity is used for the majority of simulations in this work, as shown in Eq. 3.19. These closures for the neutral fluid could be modified and refined as a subject of future work, as needed.

These strong form equations must be converted into weak form for the finite element method (FEM) used in PSI-Tet for solving systems of partial differential equations (PDE). For finite element methods, an approximate solution S is represented as a set of basis functions ϕ_i multiplied by appropriate weights W_i, as shown in Eq. 3.5.

$$S(\vec{x}) \approx \sum W_i \phi_i(\vec{x}) \tag{3.5}$$

In the version of PSI-Tet at the time of writing, tetrahedral finite elements are used to discretize the solution domain, and basis functions ϕ_i are defined within each FEM cell. The FEM, instead of solving the strong form equations of interest provided in Eq. 3.8 - 3.19, solve for the minimum of a equivalent weak formulation, with respect to a set of suitable test functions ϕ_j^T. The PSI-Tet code makes use of the Galerkin method, which selects the test function space to be the same as the basis set used to expand the solution in Eq. 3.5 [68]. Using the Galerkin method for selecting test functions, one can derive weak formulations of systems of equations that can be readily solved numerically. The derivation of weak formulations of the strong form equations are provided in Appendix B.

Lastly, it should be noted that PSI-Tet makes use of the Crank-Nicolson (CN) time-centered implicit scheme for evolving all equations of interest in time [51, 68]. This method assumes a general PDE form as expressed in Eq. 3.6, where U is the quantity of interest to evolve (e.g. n, T, v, ...). The strong from PDEs are discretized for the CN scheme as expressed in Eq. 3.7.

$$\frac{\partial U}{\partial t} = F(U, x, t, \frac{\partial U}{\partial x}, ...) \tag{3.6}$$

$$\frac{U^{n+1} - U^{n}}{\Delta t} = \frac{1}{2}\left[F^{n+1}(U, x, t, \frac{\partial U}{\partial x}, ...) + F^{n}(U, x, t, \frac{\partial U}{\partial x}, ...)\right] \tag{3.7}$$

As detailed in Appendix B, the nonlinear metrics derived in variational form are provided in a compliant form for use with this time stepping scheme. Since the CN scheme is implicit, the nonlinear metrics provided in Appendix B must be solved for the solution at the next time step. In PSI-Tet, a Newton-Rhapson method is used to solve the system of nonlinear equations with a Krylov space iterative method (i.e. GMRES [69]) which provides an approximate inverse of the system Jacobian. The general process for calculating the weak formulations of the Jacobians used for the Newton-Rhapson method with a complete example of the calculation of Jacobians for the density advances are provided in Appendix B. Please note that exact Jacobians are not implemented in PSI-Tet since they are not required for rapid convergence of the Newton-Rhapson method. Please review the most recent version of the PSI-Tet plasma-neutral code in Appendix D for the currently implemented Jacobian terms in the plasma-neutral model. If efficient convergence is not observed for the Newton-Rhapson method during a given simulation, it may be required to add in additional terms in the order of importance for plasma and neutral quantities of interest. In short, the philosophy taken for the implementation of the Jacobians for the plasma-neutral model should be that of the simplest implementation to provide efficient convergence.

Continuity

$$\frac{\partial n}{\partial t} + \nabla \cdot (n\vec{v}) = \Gamma_i^{ion} - \Gamma_n^{rec} + D\nabla^2 n \tag{3.8}$$

$$\frac{\partial n_n}{\partial t} + \nabla \cdot (n_n\vec{v}_n) = -\Gamma_i^{ion} + \Gamma_n^{rec} + D_n\nabla^2 n_n \tag{3.9}$$

Momentum

$$\rho\left[\frac{\partial \vec{v}}{\partial t} + \vec{v} \cdot \nabla v\right] = \vec{J} \times \vec{B} - \nabla(2nT) - \nabla \cdot \mathbf{\Pi} + \Gamma_i^{ion} m_i(\vec{v}_n - \vec{v}) + \Gamma^{cx} m_i(\vec{v}_n - \vec{v}) \tag{3.10}$$

$$+ \vec{R}_{in}^{cx} - \vec{R}_{ni}^{cx}$$

$$\rho_n\left[\frac{\partial \vec{v}_n}{\partial t} + \vec{v}_n \cdot \nabla \vec{v}_n\right] = -\nabla(n_n T_n) - \nabla \cdot \mathbf{\Pi_n} + \Gamma_n^{rec} m_i(\vec{v} - \vec{v}_n) + \Gamma^{cx} m_i(\vec{v} - \vec{v}_n) \tag{3.11}$$

$$+ \vec{R}_{ni}^{cx} - \vec{R}_{in}^{cx}$$

Energy

$$\frac{n}{\gamma - 1}\left[\frac{\partial T}{\partial t} + \vec{v} \cdot \nabla T\right] = -nT\nabla \cdot \vec{v} - \nabla \cdot \vec{q} + \frac{1}{2}\left(\eta \vec{J}^2 - \mathbf{\Pi} : \nabla \vec{v}\right) \tag{3.12}$$

$$+ \frac{1}{2}[(\vec{v}_n - \vec{v}) \cdot \vec{R}_{in}^{cx} + (\Gamma_i^{ion} + \Gamma^{cx})\frac{m_i}{2}(\vec{v} - \vec{v}_n)^2 - \Gamma_i^{ion}\left(\phi_{ion} + \frac{2T}{\gamma - 1}\right) + \Gamma_n^{rec}\left(\frac{2T}{\gamma - 1}\right)$$

$$+ Q_n^{ion} - Q_i^{rec} + Q_{in}^{cx} - Q_{ni}^{cx}]$$

$$\frac{n_n}{\gamma - 1}\left[\frac{\partial T_n}{\partial t} + \vec{v}_n \cdot \nabla T_n\right] = -n_n T_n \nabla \cdot \vec{v}_n - \nabla \cdot \vec{q}_n - \mathbf{\Pi_n} : \nabla \vec{v}_n + (\vec{v} - \vec{v}_n) \cdot \vec{R}_{ni}^{cx} \tag{3.13}$$

$$+ (\Gamma_n^{rec} + \Gamma^{cx})\frac{m_i}{2}(\vec{v} - \vec{v}_n)^2 - (\Gamma_n^{rec} - \Gamma_i^{ion})\left(\frac{T_n}{\gamma - 1}\right) + Q_i^{rec} - Q_n^{ion} + Q_{ni}^{cx} - Q_{in}^{cx}$$

Maxwell's Equations

$$\frac{\partial \vec{B}}{\partial t} = -\nabla \times \left[-\vec{v} \times \vec{B} + \eta \vec{J} + \frac{1}{ne}\left(\vec{J} \times \vec{B} - \nabla(nT)\right) + \frac{m_e}{ne^2}\frac{\partial \vec{J}}{\partial t}\right] \tag{3.14}$$

$$\nabla \times \vec{B} = \mu_o \vec{J} \tag{3.15}$$

Thermal conduction

$$\vec{q} = -n\left[\chi_{\parallel}\hat{e_b}\hat{e_b} + \chi_{\perp}\left(\mathbf{I} - \hat{e_b}\hat{e_b}\right)\right]\cdot\nabla T \tag{3.16}$$

$$\vec{q_n} = -\kappa_n \nabla T_n = -\left(\frac{5}{2}\frac{k_b}{m_n}\frac{n_n k_b T_n}{\nu_{cx} + \nu_{hs}}\right)\nabla T_n \tag{3.17}$$

Viscosity

$$\mathbf{\Pi} = \begin{cases} -\nu\nabla\vec{v} & \text{Kinematic} \\ -\nu\left[\nabla\vec{v} + (\nabla\vec{v})^T - \frac{2}{3}\left(\mathbf{I}\nabla\cdot\vec{v}\right)\right] \equiv -\nu\mathbf{W} & \text{Isotropic} \\ -\left[\nu_{\parallel}\hat{e_b}\hat{e_b} + \nu_{\perp}\left(\mathbf{I} - \hat{e_b}\hat{e_b}\right)\right]\cdot\mathbf{W} & \text{Anisotropic} \end{cases} \tag{3.18}$$

$$\mathbf{\Pi_n} = -\nu_n \nabla\vec{v}_n \tag{3.19}$$

3.2.2 Two-fluid (plasma-neutral) PSI-Tet simulations

Verification with test problems

A series of verification test problems are performed to ensure the plasma-neutral model has been implemented correctly in PSI-Tet. Each test problems seeks to verify the density, velocity, and temperature advances for both the plasma and neutral species. All verification test problems are performed in a rectangular simulation domain that is periodic in all three directions.

Density advance verification

To verify the implemented density advance provided in strong form in Eqs. 3.8 – 3.9, a test problem to ensure the plasma-neutral system evolves towards an expected coronal equilibrium is considered [36]. One can derive the expected equilibrium of the plasma-neutral system by considering Eq. 3.8 - 3.9 in the limit that the time derivatives of both species are zero (i.e. $\frac{\partial n}{\partial t} = \frac{\partial n_n}{\partial t} = 0$), and with no bulk velocity for either species, as expressed in

Eq. 3.2.2.

$$0 = \Gamma_i^{ion} - \Gamma_n^{rec}$$

$$0 = -\Gamma_i^{ion} + \Gamma_n^{rec}$$

Thus, the expected equilibrium solution is $\Gamma_i^{ion} = \Gamma_n^{rec}$, where the ionization rate exactly balances the recombination rate, resulting in no net change of the plasma or neutral number densities in time. Expanding this expression out in terms of relevant variables in Appendix C, one obtains Eq. 3.6.

$$n_e n_n \left\langle \sigma_{ion} v_e \right\rangle = n_e n_i \left\langle \sigma_{rec} v_e \right\rangle$$

Recalling the assumption of quasineutrality made for deriving an MHD plasma model, as presented in Appendix A, $n_e = n_i \equiv n$, such that the expression in Eq. 3.2.2 can be reduced to the fraction listed in Eq. 3.2.2.

$$\frac{n_e}{n_n} = \frac{\left\langle \sigma_{ion} v_e \right\rangle}{\left\langle \sigma_{rec} v_e \right\rangle}$$

Lastly, one can define an ionization fraction $f_{ion} \equiv \frac{n}{n+n_n}$ which represents the relative composition of ionized particles relative to the total number of ionized and neutral particles in a plasma-neutral mixture. Using Eq. 3.2.2 and the definition of ionization fraction, one can represent the ionization fraction in the form of interest in Eq. 3.2.2.

$$f_{ion} = \frac{n_n}{n + n_n} \frac{\left\langle \sigma_{ion} v_e \right\rangle}{\left\langle \sigma_{rec} v_e \right\rangle}$$

Provided with the definition of expected equilibrium ionization fractions in terms of the evolved quantities of interest n and n_n, one must define functional forms of the ionization and recombination rates for Eq. 3.2.2 to be solved.

The functional forms for the ionization and recombination rates presented in [38] are used for this work, expressed in Eqs. 3.20 – 3.21, noting that electron temperatures T_e are in units of electron-volts (eV). Since the majority of plasmas of interest in the HIT-SI3 experiment make use of deuterium, Z = 1 is assumed consistently with assumptions made in Appendix A.

$$\left\langle \sigma_{ion} v_e \right\rangle \approx 2.9 \times 10^{-14} \left(\frac{(\frac{\phi_{ion}}{T_e})^{0.39}}{0.232 + (\frac{\phi_{ion}}{T_e})} \right) e^{-\phi_{ion}/T_e} \ [\mathrm{m^3 s^{-1}}] \tag{3.20}$$

$$\langle \sigma_{rec} v_e \rangle \approx 2.6 \times 10^{-19} \frac{Z^2}{T_e^{1/2}} \ [\mathrm{m^3 s^{-1}}] \tag{3.21}$$

Alternative expressions for ionization and recombination rates are also available in Goldston [37], which are provided in Eqs. 3.22 – 3.23. Again, note that temperatures T are in units of electron-volts (eV). These functions are plotted as a function of electron temperature T_e in Fig. 3.5.

$$\langle \sigma_{ion} v_e \rangle = \frac{2.0 \times 10^{-13}}{6 + \left(\frac{T}{13.6}\right)} \left(\frac{T}{13.6}\right)^{1/2} e^{-13.6/T} \ [\mathrm{m^3 s^{-1}}] \tag{3.22}$$

$$\langle \sigma_{rec} v_e \rangle = 0.7 \times 10^{-19} \left(\frac{13.6}{T}\right)^{1/2} \ [\mathrm{m^3 s^{-1}}] \tag{3.23}$$

When comparing the Goldston ionization and recombination expressions in Eqs. 3.22 – 3.23 to Eqs. 3.20 – 3.21 [38], the recombination reaction rates $\langle \sigma_{rec} v_e \rangle$ are nearly identical. However, when comparing the ionization reaction rates $\langle \sigma_{ion} v_e \rangle$, there is a slight difference between the two expressions in that Goldston's relation appears to predict larger ionization rates than that of one used in [38]. Though this is a small difference, using Goldston's expression for ionization rates would lead to slightly larger ionization fractions within the electron temperature range of 1 – 2 eV, as shown in Fig. 3.6.

Should simulation results deviate from the measured data, it may be worthwhile to consider other functional forms of the ionization rate, including the alternative expression above, as a potential modification to the neutral physics module. Even so, the differences between the expressions are quite small and likely unimportant, and so for consistency with past work in [38], the expressions for ionization and recombination expressed in Eq. 3.20 and 3.21 are presently used in the PSI-Tet implementation.

For these density evolution verification simulations, only the densities and velocities for each species are evolved in time, whereas the temperature of each species is chosen to be a non-zero constant in time. The velocities of each species is chosen to be equal and opposite (i.e. $\vec{v} = -\vec{v}_n$), with equal initial number densities (i.e. $n_n = n$). This choice of initial conditions ensures that the system is initialized with zero momentum, which allows for a test

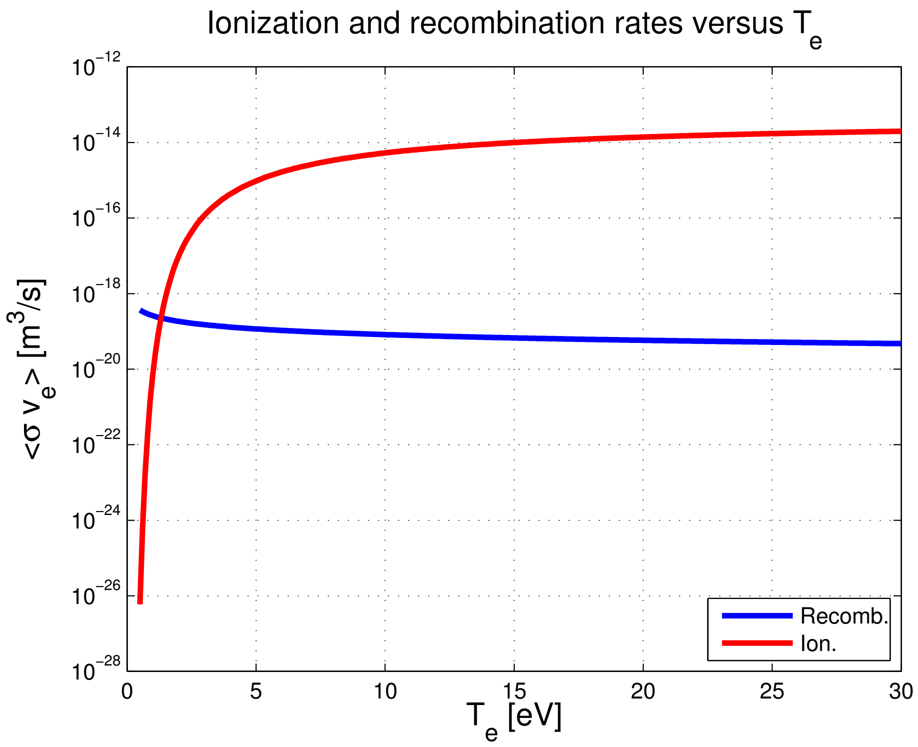

Figure 3.5: Ionization and recombination rates implemented in PSI-Tet from [38] versus electron temperature T_e.

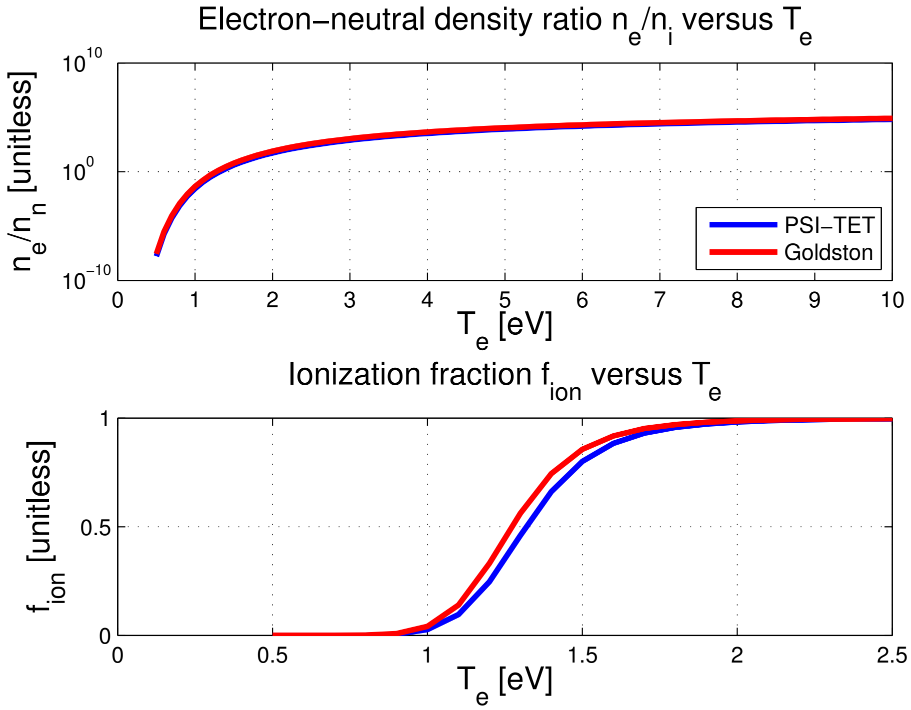

Figure 3.6: Coronal equilibrium $\frac{n_e}{n_n}$ values and ionization fractions as a function of temperature for a hydrogenic plasma using both the PSI-Tet implemented and Goldston forms for ionization and recombination reaction rates.

of the flux quantities in Eqs. 3.8 – 3.9 (i.e. $\nabla \cdot (n\vec{v})$ and $\nabla \cdot (n_n \vec{v}_n)$) with an expected end state of both species tending to zero velocity. Lastly, the artificial stabilizing diffusivities present in Eqs. 3.8 – 3.9 are set to zero for these test problems. The elimination of artificial diffusivities while maintaining run stability for these test problems is possible due to the choice of solution volume and boundary conditions. There are no appreciable spatial gradients in either the plasma or neutral densities in the system as the system is chosen to be isotropic with periodic boundary conditions.

Velocity advance verification

For the verification of the velocity advances for both species, the same rectangular simulation domain with periodic boundary conditions is used as was used for density advance verification. When considering Eqs. 3.10 – 3.11, a test problem is chosen to simplify the evolution equations to better isolate the newly added plasma-neutral terms. The test problem assumes an unmagnetized ($|\vec{J}| = |\vec{B}| = 0$), isothermal ($T = T_n$) plasma-neutral mixture with equal and opposite initial velocities with equal initial number densities $n_n = n$, as was done for verification of the density advances. Since this test problem seeks to demonstrate conservation of momentum, and Eqs. 3.10 – 3.11 include both ionization and recombination Γ_i^{ion} and Γ_n^{rec} terms, both the velocities and densities of each species must be evolved, while the chosen temperatures for each fluid are chosen and held fixed in time for a self-consistent simulation. In short, the chosen test problem, along with the chosen initial conditions for all evolved variables used for verifying the density advance are similar for verifying the velocity advance.

Thus, using the aforementioned test problem and assumptions, the strong form expressions for the velocity advances considered are given in Eqs. 3.24 – **??** while noting that the density is advanced for each species, still setting artificial diffusivity to zero for both species. Since the total momentum of the system is initialized to be zero (i.e. equal and opposite bulk velocity of plasma and neutral species each with the same number density), as the plasma and neutral fluids interact via reaction terms expressed in Eqs. 3.10 – 3.11, the system should evolve towards each species having zero velocity as $t \rightarrow \infty$. Closures for all plasma-neutral reaction terms are provided in Appendix C in line with previous work presented in [38].

$$\rho\left[\frac{\partial\vec{v}}{\partial t}+\vec{v}\cdot\nabla v\right]=-\nabla\cdot\mathbf{\Pi}+\Gamma_i^{ion}m_i(\vec{v}_n-\vec{v})+\Gamma^{cx}m_i(\vec{v}_n-\vec{v})+\vec{R}_{in}^{cx}-\vec{R}_{ni}^{cx} \tag{3.24}$$

$$\rho_n\left[\frac{\partial\vec{v}_n}{\partial t}+\vec{v}_n\cdot\nabla\vec{v}_n\right]=-\nabla\cdot\mathbf{\Pi_n}+\Gamma_n^{rec}m_i(\vec{v}-\vec{v}_n)+\Gamma^{cx}m_i(\vec{v}-\vec{v}_n)+\vec{R}_{ni}^{cx}-\vec{R}_{in}^{cx}$$

Temperature advance verification

For the verification of the temperature advances for both species, the same rectangular simulation domain with periodic boundary conditions is used as was used for density and velocity advance verification. When considering Eqs. 3.12 – 3.13, a few assumptions are made to simplify the system of equations to better isolate the newly added plasma-neutral reaction terms. The test problems to be describe all assume an unmagnetized ($|\vec{J}|=|\vec{B}|=0$) plasma. Additionally, the heat flux for both the plasma and neutral species is assumed to be zero, for simplicity (i.e. $\vec{q}=\vec{q_n}=0$). Lastly, the viscosity coefficients for both species are set to zero for simplicity as well (i.e. $\nu=\nu_n=0$). Thus, the reduced temperature evolution equations of interest are expressed in Eqs. 3.28 – 3.29.

The introduction of an ionization energy loss ϕ_{ion} in Eq. 3.12 represents an continuous expenditure of plasma energy on ionizing neutral atoms. Thus, when considering constructing test problems to demonstrate conservation of energy, one notes that the total thermal energy of the system is expected to decrease in time so long as a non-zero ionization rate is present. This leads to a more complicated evolution of the plasma and neutral temperatures that does not provide as clear of a demonstration of conversation energy since one must keep track of the energy being lost from the system.

Instead, one can modify the implementation to provide a clear demonstration of conservation of energy without a structural change to the implemented equations. First, a test problem that assumes the ionization energy loss per event is zero (i.e. $\phi_{ion}=0$) eliminates the continuous expenditure of plasma energy on ionizing neutral particles. However, since ionization and recombination are still allowed to occur in this test problem, these plasma-neutral reactions will naturally lead to a change in the plasma and neutral densities as a function of time via Eqs. 3.8 – 3.9. Additionally, for self-consistency, both the plasma and neutral velocities should be advanced as well since these variables interact with the density advances via the flux terms. However, even with the evolution of all three variables of interest for both species, the assumption of zero ionization energy loss should result in the total thermal energy of the system being constant in time, if energy conservation is obeyed even though the evolution of all three variables for each species still may be complex. Thus, the reduced set of equations being evolved using the assumption that $\phi_{ion} = 0$ are given in Eqs. 3.30 – 3.31.

Lastly, as a method to isolate the resonant charge-exchange terms from the ionization and recombination terms, one can construct a test problem that assumes both the ionization and recombination rates are zero (i.e. $\langle \sigma_{ion} v_e \rangle = \langle \sigma_{rec} v_e \rangle = 0$). Thus, all terms in Eqs. 3.28 – 3.29 that are multiplied by either Γ_i^{ion} or Γ_n^{rec} are now zero. This dramatically reduces the complexity of these equations, as shown in Eqs. 3.32 – 3.33.

Having only resonant charge exchange terms active in this test problem results in any zero net expenditure of plasma energy, unlike when ionization energy loss is included. Additionally, due to the symmetry of resonant charge exchange interactions, such that there is no net conversion of plasma to neutrals or vice versa, without the ionization and recombination reactions, there is no change of the plasma or neutral densities as a function of time. With the same chosen initial conditions of the plasma and neutral densities equal (i.e. $n = n_n$) and the initial velocities of each species equal and opposite (i.e. $\vec{v}_n = -\vec{v}$) one can demonstrate conversation of energy as follows.

From the equipartition theorem [12], each component of a plasma-neutral mixture (i.e. electrons, ions, and neutrals) contributes $E_{x/y/z} = \frac{1}{2}kT$ for each x,y,z direction of movement. Thus, since particles are permitted to move in all three directions, each species contributes $E_\alpha = \frac{3}{2}kT_\alpha$, such that the total initial thermal energy of the system is given by Eq. 3.25.

$$E_{th}|_{initial} = \frac{3}{2}n_i kT_i + \frac{3}{2}n_e kT_e + \frac{3}{2}n_n kT_n \tag{3.25}$$

Using the same assumptions required for an MHD plasma model, as described in Appendix A, the quasineutrality condition necessitates that $n_e = n_i \equiv n$. Additionally, a single temperature model of the plasma fluid has been assumed, such that $T_e = T_i = T$. And, assuming equal initial number densities for both the plasma and neutral species $n = n_n$, the initial thermal energy of the system is given by Eq. 3.26.

$$E_{th}|_{initial} = 3nkT + \frac{3}{2}nkT_n \tag{3.26}$$

As the system evolves in time, energy is conserved, and all species in the plasma-neutral mixture will equilibrate in temperature toward T_{final} as $t \to \infty$ via the plasma-neutral charge exchange terms. Since resonant charge exchange does not lead to a net change in the plasma or neutral densities, one expects the initial condition of $n = n_n$ to be maintained throughout system evolution. The system will evolve towards $T = T_n = T_{final}$, which using the end state expectation of $n = n_n$ and conservation of energy $E_{th}|_{initial} = E_{th}|_{final}$, the expected final temperature T_{final} is given in terms of the initial plasma temperature T and neutral temperature T_n in Eq. 3.27.

$$T_{final} = \frac{1}{3}(2T + T_n) \tag{3.27}$$

.

Simplified temperature advances

$$\frac{n}{\gamma-1}\left[\frac{\partial T}{\partial t} + \vec{v}\cdot\nabla T\right] = -nT\nabla\cdot\vec{v} + \frac{1}{2}\left[(\vec{v}_n - \vec{v})\cdot\vec{R}^{cx}_{in} + (\Gamma^{ion}_i + \Gamma^{cx})\frac{m_i}{2}(\vec{v}-\vec{v}_n)^2\right. \tag{3.28}$$
$$\left. -\Gamma^{ion}_i\left(\phi_{ion} + \frac{2T}{\gamma-1}\right) + \Gamma^{rec}_n\left(\frac{2T}{\gamma-1}\right) + Q^{ion}_n - Q^{rec}_i + Q^{cx}_{in} - Q^{cx}_{ni}\right]$$

$$\frac{n_n}{\gamma-1}\left[\frac{\partial T_n}{\partial t} + \vec{v}_n\cdot\nabla T_n\right] = -n_nT_n\nabla\cdot\vec{v}_n + (\vec{v}-\vec{v}_n)\cdot\vec{R}^{cx}_{ni} \tag{3.29}$$
$$+ (\Gamma^{rec}_n + \Gamma^{cx})\frac{m_i}{2}(\vec{v}-\vec{v}_n)^2 - (\Gamma^{rec}_n - \Gamma^{ion}_i)\left(\frac{T_n}{\gamma-1}\right) + Q^{rec}_i - Q^{ion}_n + Q^{cx}_{ni} - Q^{cx}_{in}$$

Temperature advances with $\phi_{ion} = 0$

$$\frac{n}{\gamma - 1}\left[\frac{\partial T}{\partial t} + \vec{v}\cdot\nabla T\right] = -nT\nabla\cdot\vec{v} + \frac{1}{2}\Big[(\vec{v}_n - \vec{v})\cdot\vec{R}^{cx}_{in} + (\Gamma^{ion}_i + \Gamma^{cx})\frac{m_i}{2}(\vec{v} - \vec{v}_n)^2 \tag{3.30}$$

$$-\Gamma^{ion}_i\left(\frac{2T}{\gamma - 1}\right) + \Gamma^{rec}_n\left(\frac{2T}{\gamma - 1}\right) + Q^{ion}_n - Q^{rec}_i + Q^{cx}_{in} - Q^{cx}_{ni}\Big]$$

$$\frac{n_n}{\gamma - 1}\left[\frac{\partial T_n}{\partial t} + \vec{v}_n\cdot\nabla T_n\right] = -n_nT_n\nabla\cdot\vec{v}_n + (\vec{v} - \vec{v}_n)\cdot\vec{R}^{cx}_{ni} \tag{3.31}$$

$$+ (\Gamma^{rec}_n + \Gamma^{cx})\frac{m_i}{2}(\vec{v} - \vec{v}_n)^2 - (\Gamma^{rec}_n - \Gamma^{ion}_i)\left(\frac{T_n}{\gamma - 1}\right) + Q^{rec}_i - Q^{ion}_n + Q^{cx}_{ni} - Q^{cx}_{in}$$

Temperature advances with $\langle\sigma_{ion/rec}v_e\rangle = 0$

$$\frac{n}{\gamma - 1}\left[\frac{\partial T}{\partial t} + \vec{v}\cdot\nabla T\right] = -nT\nabla\cdot\vec{v} + \frac{1}{2}\Big[(\vec{v}_n - \vec{v})\cdot\vec{R}^{cx}_{in} + \Gamma^{cx}\frac{m_i}{2}(\vec{v} - \vec{v}_n)^2 \tag{3.32}$$

$$+Q^{cx}_{in} - Q^{cx}_{ni}]$$

$$\frac{n_n}{\gamma - 1}\left[\frac{\partial T_n}{\partial t} + \vec{v}_n\cdot\nabla T_n\right] = -n_nT_n\nabla\cdot\vec{v}_n + (\vec{v} - \vec{v}_n)\cdot\vec{R}^{cx}_{ni} + \Gamma^{cx}\frac{m_i}{2}(\vec{v} - \vec{v}_n)^2 \tag{3.33}$$

$$+ Q^{cx}_{ni} - Q^{cx}_{in}$$

Boundary condition analysis

When performing simulations of systems of partial differential equations, the choice of boundary conditions is an important topic since it can have a meaningful impact on computed solutions. When attempting to validate any simulation with experimental data [70, 71], one is testing the validity of a physical model of explaining phenomena being observed. However, if a simulation cannot be validated with experimental data, it can be challenging to determine whether disagreement is due to a faulty physical model or poorly chosen boundary conditions.

In an attempt to reduce the uncertainty of whether the physical model, its discretized implementation, and/or chosen boundary conditions are the source of disagreement between simulation and experimental data, it is often desired for chosen boundary conditions to be physically motivated in some capacity. Of particular interest for this work, when considering the plasma-material boundary present in many plasma physics experiments as described in Chapter 2, one encounters an environment that is not well described by an MHD plasma model, such as the one used in the implemented plasma-neutral model in PSI-Tet. Namely, within the region of an electrostatic sheath that is generated near the plasma-material interface, shown in Fig. 2.1, the conditions of quasineutrality are violated ($n_e \neq n_i$) [36]. Additionally, the characteristic length scale of the sheath is on the order of a Debye length λ_{De}, where $\lambda_{De} = \sqrt{\frac{\epsilon_0 k T_e}{e^2 n}} \approx 7\,\mu\text{m}$ for HIT-SI3 plasma parameters. When deriving an MHD plasma model, as is presented in Appendix A, the asymptotic assumptions made to proceed from a two-fluid (i.e. ions and electrons) plasma model to a single-fluid MHD plasma model implies that the characteristic length scales over which the model is valid are much longer than the electron gyroradius r_{Le}, where $r_{Le} = \frac{m_e v_\perp}{eB} \approx 360\,\mu\text{m}$ for HIT-SI3 plasma parameters. Thus, with both the quasineutrality violation and a characteristic scale length smaller than the electron gyroradius, the sheath region is not readily captured by an MHD plasma model.

However, though the implemented plasma-neutral model in PSI-Tet is not able to capture the sheath near the plasma-material interface, it is possible to use information concerning plasma-material interactions and sheath physics to motivate the choice of boundary conditions for a subset of the experimental volume within which an MHD plasma model is better justified. In particular, as seen in Fig. 2.1, there is a natural boundary between sheath dominated edge and interior, bulk plasma region. This boundary, which is often referred to as the sheath “entrance” or sheath “edge” region [36], is better suited as the boundary of validity for an MHD plasma-neutral fluid model since it physically represents the end of the bulk, quasineutral plasma region when proceeding from the core of the plasma towards the plasma-material interface. Thus, it is proposed to study the relationship between the plasma and neutral parameters of interest (i.e. density, velocity, and temperature) at the sheath entrance to derive more physically motivated boundary conditions for use when performing plasma-neutral simulations with PSI-Tet of the HIT-SI3 experiment.

The complexity of the plasma-material interface is extensive [36], and without a significant amount of information about the edge plasma or neutral species, it is challenging to garner meaningful information from physical models of the edge plasma region. However, for this work, some of the simplest models of the sheath region are considered to develop more physically-informed boundary conditions even in the absence of edge plasma or neutral experimental data. Should validation with experimental data be achieved using more physically-informed boundary conditions, this would provide a higher degree of confidence that the chosen physical model is satisfactory for explaining observed phenomena. However, if validation is not achieved, both the physical model and/or boundary conditions remain suspect as potential sources for disagreement.

As described in Section 2.1.2., edge recycling provides a source of neutral particles at plasma-material interfaces. When bulk plasma ions and electrons enter the sheath region, they are in the presence of an electric field, as shown in Fig. 2.1. This electric potential tends to accelerate ions towards the surface and repel electrons due to the presence of a negative surface charge required to maintain ambipolar (i.e. zero-net electric current) flow. When accelerated ions impact the material surface, they can be either promptly backscattered or absorbed by the material surface, as shown in Fig. 2.2. Particles that are promptly backscattered tend to be monatomic atoms with a significant fraction of the incident ion energy, whereas absorbed ions recombine with free electrons, thermalize with the wall, and then desorb from the surface largely as thermal atoms or molecules. Both of these processes introduce neutral particles into the system and are forms of edge recycling. When considering a solid plasma-material interface, it is desirable to know the fraction of incident plasma ions that are either promptly backscattered or absorbed/desorbed as a function of incident ion energy and the composition of the plasma-material interface. Additionally, it is desirable to know the kinetic energy of promptly backscattered neutral particles. Such information would allow for self-consistent relationships between chosen boundary conditions for both the plasma and neutral fluid variables of interest.

Consider the sheath region shown in Fig. 3.7, where a sheath entrance is defined as the boundary between the nearly quasineutral pre-sheath region and sheath region near a solid plasma-material interface. This boundary is located approximately one Debye length off the plasma-material interface, as shown in Fig. 2.1 [36]. Assuming steady-state conditions (i.e. $\frac{\partial}{\partial t} \to 0$), mass conservation requires the total particle flux into the sheath control volume must be zero, as expressed in Eq. 3.34.

$$\Gamma_i|_{SE} + \Gamma_{desorb} = \Gamma_{pump} + \Gamma_n|_{SE} \tag{3.34}$$

Thus, the total incoming particle flux through the sheath entrance $\Gamma_i|_{SE}$ and desorption from the solid wall Γ_{desorb} is balanced with neutral particles exiting the sheath region through the sheath entrance $\Gamma_n|_{SE}$, or are being absorbed, or "pumped" Γ_{pump} by the wall.

A few important points must be made when considering this model. This model introduces the concept of recycling fraction $f_{re} = \frac{\Gamma_n|_{SE}}{\Gamma_i|_{SE}}$ which is directly related to the flux terms Γ_{pump} and Γ_{desorb} via Eq. 3.34. As described previously, sheath-accelerated ions that are absorbed into a solid wall recombine into thermal atoms or molecules, and then are subsequently desorbed from the wall. The steady-state expectation of this system is for the pumping particle flux Γ_{pump} to be equal to the desorption particle flux Γ_{desorb} such that there is no further mass accumulation in the solid boundary once the wall becomes saturated with neutral gas [36]. Under this circumstance, the recycling fraction $f_{re} = 1$ and Eq. 3.34 reduces to Eq. 3.35,

$$\Gamma_i|_{SE} = \Gamma_n|_{SE} \tag{3.35}$$

Thus, the total incoming plasma flux into the sheath entrance $\Gamma_i|_{SE}$ must be balanced by the particle flux of neutral particles exiting the sheath entrance $\Gamma_n|_{SE}$.

However, many plasma physics experiments, such as the HIT-SI3 experiment, make use of wall conditioning to improve the performance of discharges. In short, wall conditioning modifies the relationship between Γ_{pump} and Γ_{desorb} by allowing for the net accumulation of mass in the solid boundary (i.e. $\Gamma_{pump} \neq \Gamma_{desorb}$) until the wall reaches its saturation point. Thus, the reduction in desorption of thermalized neutral particles back into the bulk plasma region under these transient conditions is favorable for core plasma performance since it reduces the impact of plasma-neutral reactions described in previous sections with a smaller amount of cool, thermal neutral particles reentering the bulk plasma region.

In the limit that all plasma absorbed into the wall is not desorbed as thermalized neutrals during a given discharge, the mass conservation equation for the sheath control volume reduces to Eq. 3.36.

$$\Gamma_i|_{SE} = \Gamma_{pump} + \Gamma_n|_{SE} \tag{3.36}$$

Thus, in this scenario, assuming no other species conversion occurring in the sheath control volume due to its short length compared to the estimated characteristic ionization and charge exchange length scales in HIT-SI3 (i.e $\lambda_{mfp} \approx 2 - 5$ cm), the only neutral particles exiting through the sheath entrance surface $\Gamma_n|_{SE}$ will be those that are not absorbed and retained by the solid wall, or in other words, are promptly backscattered as energetic neutral atoms. In the limit that there are no promptly backscattered neutral particles, and all absorbed particles are retained, $\Gamma_n|_{SE} = 0$ and correspondingly the recycling fraction $f_{re} = 0$.

This simple example has highlighted needed information for deriving more physically motivated boundary conditions based on analysis of PMI and sheath physics. First, functional forms of $\Gamma_i|_{SE}$ and $\Gamma_n|_{SE}$ are needed to relate plasma and neutral boundary condition values to respective particle fluxes. One can express these fluxes simply as follows, neglecting the mass contribution of electrons,

$$\Gamma_i|_{SE} = nc_s \tag{3.37}$$

$$\Gamma_n|_{SE} = n_n c_{s,n} \tag{3.38}$$

where n and n_n are the plasma and neutral densities at the sheath entrance, respectively, and c_s and $c_{s,n}$ are the characteristic speeds of the plasma and neutral species at the sheath entrance, respectively.

For this work, a simple Bohm model of the sheath region is assumed [36]. Saturating the inequality in the Bohm criterion for an equilibrated (i.e. $T_i = T_e$) plasma, plasma ions enter the sheath region at their sound speed $c_s = \sqrt{\frac{kT}{m}}$. Using an assumed sheath entrance plasma density n_{SE} and temperature T_{SE}, the plasma flux into the sheath region is defined as $\Gamma_i|_{SE} = n_{SE}\sqrt{\frac{kT_{SE}}{m}}$. To determine the self-consistent neutral parameters at the sheath entrance, one must consider Eq. 3.34. Additional required information is (1) the wall pumping rate Γ_{pump} that is directly related to the recycling fraction f_{re}, (2) the relative fraction of incident plasma ions that are promptly backscattered as neutral particles or are absorbed by the wall, and the kinetic energy of promptly backscattered neutral particles, and (3) the functional form of the neutral particle flux at the sheath entrance $\Gamma_n|_{SE}$. To address (1), it is assumed that $f_{re} = 1$ for this work since the majority of TALIF neutral density and temperature measurements were taken while running in pulsed discharge cleaning (PDC) mode with deuterium on HIT-SI3. In general, when PDC is used with helium plasmas to condition the walls of HIT-SI3 for high performance deuterium shots, the favorable impact of helium wall conditioning is usually lost after approximately 10, 2 ms long discharges in HIT-SI3. Thus, since TALIF measurements were taken during PDC deuterium operations with many more than 10 shots after a consistent D_α background was obtained, the assumption of $f_{re} = 1$ is likely justified. Correspondingly, Eq. 3.35 applies for the assumption of $f_{re} = 1$, which still requires additional information regarding the composition and kinetic energy of neutral particles exiting through sheath entrance $\Gamma_n|_{SE}$.

To address (2), the Stopping Power and Range of Ions in Matter (SRIM) code is used to gain insight on the aforementioned topics regarding the plasma-material interface [72]. This code calculates the stopping and range of incident ions of varying initial energy using a quantum-mechanical treatment of ion-atom collisions. Of interest for developing physically motivated boundary conditions, this code is used to calculate the fraction of incident ions that are either promptly backscattered or implanted into the material surface and provides the kinetic energy of the promptly backscattered atoms as well.

To address (3), it is assumed that the particle flux of neutrals at the sheath entrance $\Gamma_n|_{SE}$ takes a similar form as flux of plasma into the sheath $\Gamma_i|_{SE}$, such that $\Gamma_n|_{SE} = n_{n,SE}\sqrt{\frac{kT_{n,SE}}{m}}$. With a recycling fraction $f_{re} = 1$ assumption, and using Eq. 3.35 and the aforementioned functional forms for the expressions, the relationship between the plasma and neutral parameters at the sheath entrance are given by Eqs. 3.39 – 3.41. These relationships will be used with SRIM calculations and assumed edge plasma conditions to determine self-consistent neutral fluid boundary conditions should they wish to be used for plasma-neutral simulations with PSI-Tet.

$$n_{n,SE}\sqrt{\frac{kT_{n,SE}}{m}} = n_{SE}\sqrt{\frac{kT_{SE}}{m}} \tag{3.39}$$

$$v = c_s = \sqrt{\frac{kT_{SE}}{m}} \tag{3.40}$$

$$v_n = c_{s,n} = \sqrt{\frac{kT_{n,SE}}{m}} \tag{3.41}$$

Lastly, it should be noted that this section is focused on developing more physically-informed boundary conditions for use in plasma-neutral simulations with PSI-Tet. A simple sheath model and analysis of PMI in HIT-SI3 with SRIM with provide a basis for setting boundary conditions, which may still prove to be incorrect. Without experimental data from the edge plasma region, it is difficult to determine whether this simple sheath model and PMI analysis includes sufficiently complex physics to accurately motivate chosen sheath entrance boundary conditions for plasma-neutral simulations with PSI-Tet. Thus, more sophisticated analyses for choosing physically motivated boundary conditions for MHD plasma-neutral fluid simulations is a topic of future work, which should be guided by experimental data from a given plasma physics experiment of interest.

Validation with TALIF measurements

A central goal for this work is the successful validation of the implemented plasma-neutral code in PSI-Tet with experimental TALIF measurements of the monatomic, deuterium neutral density and temperature in HIT-SI3 spheromak plasmas. Of course, attempts of validation between simulation and experiment is fundamentally driven, and limited by the available data to compare to simulation. The data acquired from a TALIF diagnostic system, described in Section 3.1, and information concerning the plasma-material and sheath physics to provide physically informed boundary conditions, as described in Section 3.2, will moti-

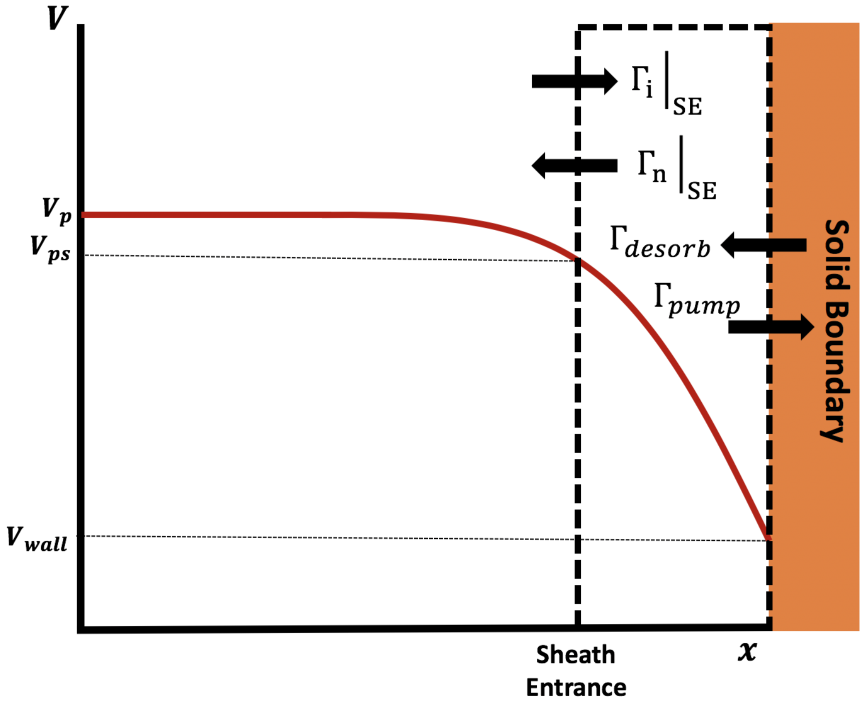

Figure 3.7: Model of sheath region with relevant particle fluxes labeled. An incoming plasma flux $\Gamma_i|_{SE}$ into the sheath control volume is balanced by neutral particles exiting the sheath region through the sheath entrance $\Gamma_n|_{SE}$, being "pumped" by the wall Γ_{pump} and subsequently desorbed by the wall Γ_{desorb}. Note that the pre-sheath voltage V_{ps} and sheath voltage V_{wall} are negative relative to the plasma potential V_p.

vate particular plasma-neutral simulations being performed for comparison to experimental data.

Should validation between simulation and experiment be achieved, this result would suggest a physical model and/or chosen boundary conditions that are capable of reproducing observed physical phenomena in the experiment, which is a desired result for this effort. However, if validation is not achieved, this provides useful information concerning both the physical model and chosen boundary conditions as being suspect for accurately capturing reality. Such a result would motivate continued exploration of methods to improve agreement through modifications to the physical model and/or boundary conditions. Additionally, such a result also motivates acquiring additional experimental data should certain areas be determined to be deficient.

Chapter 4

RESEARCH RESULTS

4.1 TALIF neutral density and temperature measurements

The TALIF diagnostic system shown in Fig. 3.1 was installed on the HIT-SI3 experiment, and both monatomic, ground state neutral deuterium number density and temperature measurements were successfully made. Results from this study have been published in *Review of Scientific Instruments* [64]. In an effort to improve statistics of the neutral density and temperature measurements, the HIT-SI3 experiment was operated in pulsed discharge cleaning (PDC) mode, which allowed for a discharge every 20 – 30 seconds rather than one every 5 – 10 minutes. This shorter inter-shot period is possible while operating in PDC mode since the capacitors that are charged over a multi-minute charging period are not fully discharged after each PDC shot like they are during a regular discharge, and only a subset of data generated during the shot is downloaded and saved, reducing data download times. As mentioned previously, HIT-SI3 typically produces helium spheromak plasmas while operating in PDC mode for wall conditioning purposes, and then a sequence 5 – 10 deuterium discharges are taken before beginning a wall conditioning PDC cycle again. This process of wall conditioning allows for significant amounts of transient pumping by the solid plasma-material interface, as described previously. However, due to collaboration time constraints with West Virginia University scientists, it was elected to operate with deuterium while running in PDC mode to enable a greater number of deuterium plasmas on which to perform TALIF measurements in a shorter amount of time. The decision to operate in PDC mode with deuterium for TALIF measurements led to lower performing shots than those produced while making use of wall conditioning, with peak toroidal currents of 10 – 12 kA. Nevertheless, operating in PDC mode provided a fairly repeatable, extensive set of deuterium discharges on which TALIF measurements were performed.

TALIF measurements were attempted both during the driven phase (i.e. when the helicity injectors were active) and decay phase (i.e. when the helicity injectors were inactive after the driven phase) of discharges in HIT-SI3 at multiple radial depths across a poloidal cross section. Statistically significant, non-zero TALIF measurements were only able to be acquired in the HIT-SI3 experiment during the decay period of discharges. In particular, TALIF measurements were acquired at two different measurement locations during a 180 microsecond interval during spheromak decay. Representative toroidal current traces from deuterium PDC shots TALIF measurements were made in are shown in Fig. 4.1. These TALIF measurements were made at t = 2.10, 2.16 and 2.18 ms at depths d = 11 and 18 cm from the optical viewport shown in Fig. 3.1. Monatomic, ground state neutral deuterium number densities $n_n \approx 3 - 7 \times 10^{15}$ m^{-3} were measured during this time interval. At a depth of d = 11 cm, it is observed that the neutral density n_n increases monotonically in time, as shown in Fig. 4.2. Spatially, a relatively flat netural density profile is observed between a depth d = 11 − 18 cm, as shown in Fig. 4.4. Neutral deuterium temperatures $T_n \approx 0.7{-}1.8$ eV were measured with the TALIF diagnostic system. An increase in measured neutral temperatures is observed in the latter 20 μs of the measurement interval, between $t = 2.16 - 2.18$ ms, as shown in Fig. 4.3. Spatially, the neutral temperature increases from a depth of d = 11 cm to d = 18 cm when proceeding from the measurement location closer to the optical viewport toward the spheromak core, shown in Fig. 4.5.

4.2 Two-fluid (plasma-neutral) PSI-Tet simulations

4.2.1 Verification with test problems

Density advance verification

A series of density advance test simulations were performed as described in Chapter 3. For these simulations, the initial plasma and neutral densities are set equal to other another (i.e. $n = n_n = 1 \times 10^{19}$ m^{-3}), with equal and opposite velocities (i.e. $\vec{v} = -\vec{v}_n$) at a value of

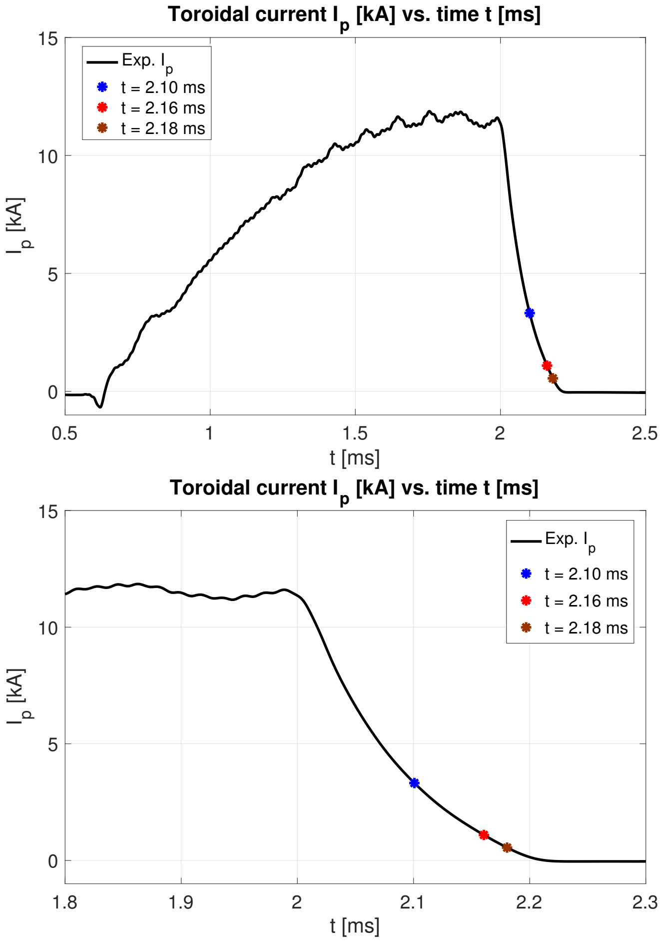

Figure 4.1: A representative toroidal current trace from a discharge in HIT-SI3 and TALIF measurement timepoints. Note that non-zero TALIF neutral density and temperature measurements were made at t = 2.10, 2.16, and 2.18 ms at depths d = 11 and 18 cm, shown in Fig. 3.1. **Top**: The spheromak forms at approximately t = 0.6 ms via steady, inductive helicity injection. A maximum toroidal current of $I_{tor} \approx 11.5$ kA. At t = 2 ms, the helicity injectors are shut off, and the spheromak resistively decays over approximately a 200 μs period. **Bottom**: The same toroidal current trace centered on the spheromak decay period.

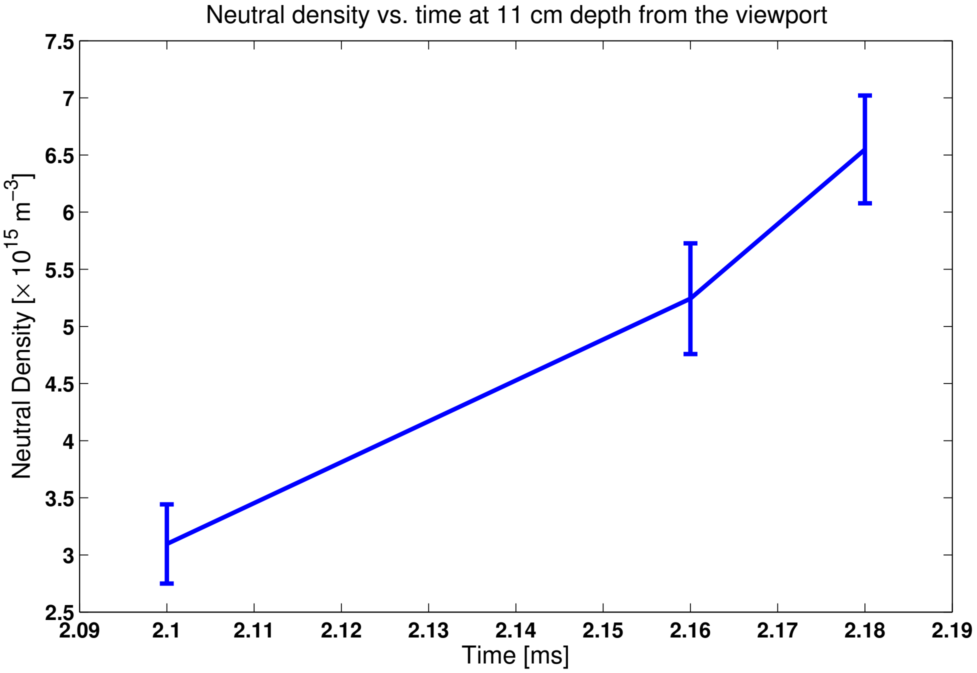

Figure 4.2: The measured neutral density at d = 11 cm depth from the viewport as a function of time from t = 2.10 – 2.18 ms. Note the monotonically increasing neutral density versus time.

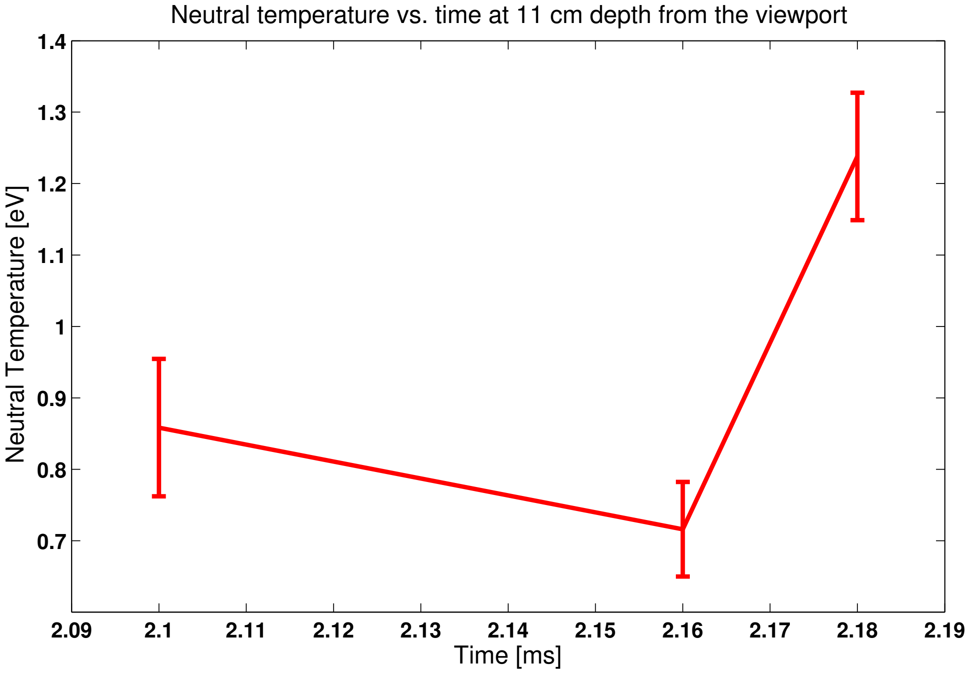

Figure 4.3: The measured neutral temperature at d = 11 cm depth from the optical viewport as a function of time from t = 2.10 – 2.18 ms. Note the increase in neutral temperature observed from t = 2.16 – 2.18 ms.

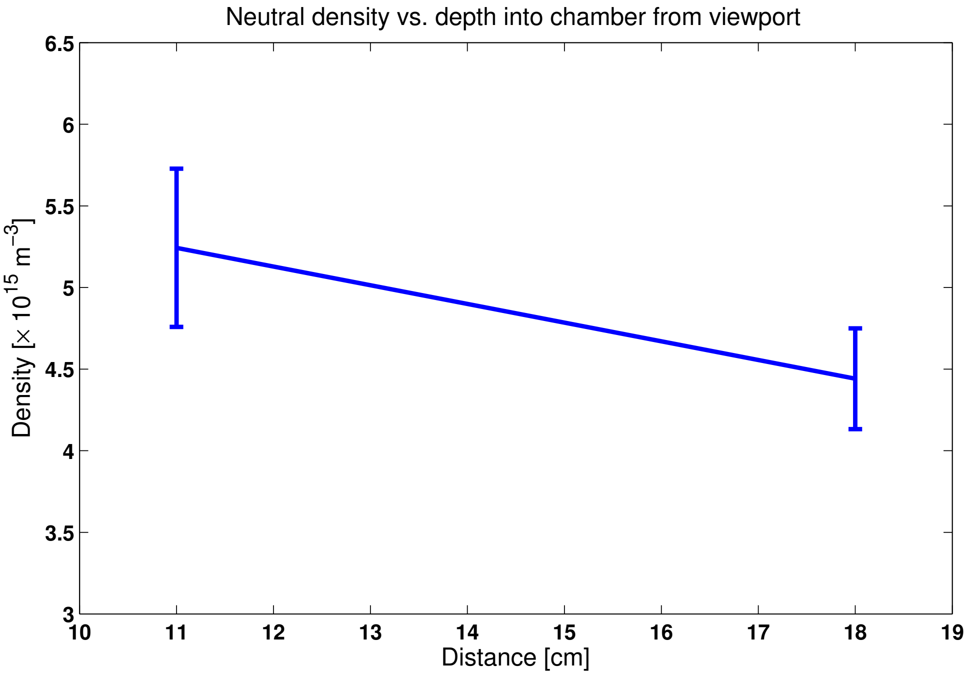

Figure 4.4: The measured neutral density n_n at d = 11 and 18 cm in from the optical viewport. Note the flat profile, to within uncertainties, observed at t = 2.16 ms.

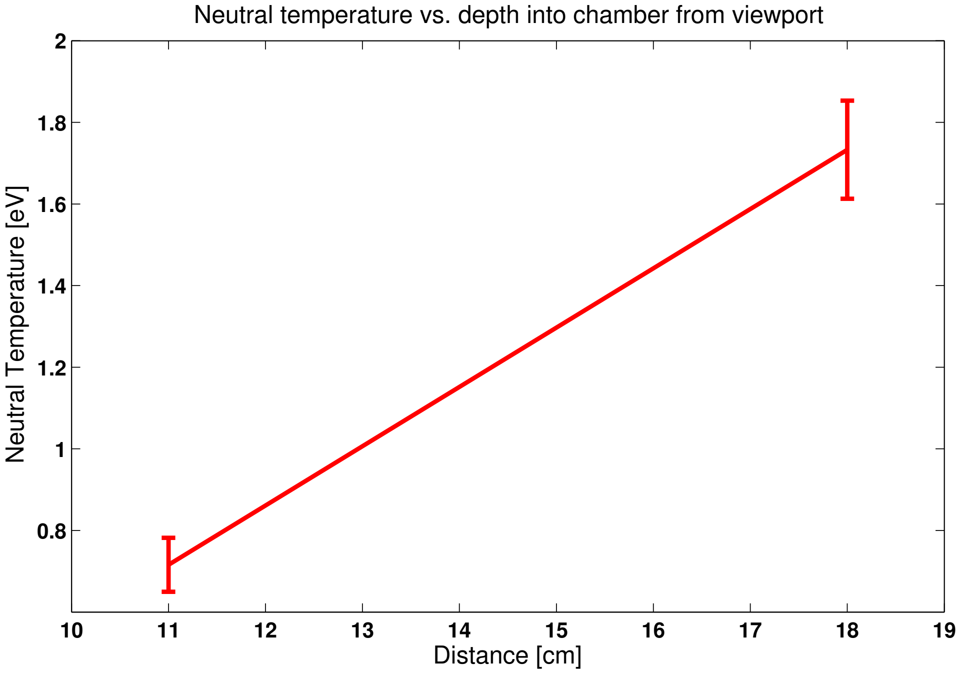

Figure 4.5: The measured neutral temperatures T_n at d = 11 and 18 cm in from the viewport at t = 2.16 ms. Note the monotonically increasing neutral temperature from the outer to inner regions of the spheromak configuration.

$|\vec{v}| = 1000$ m/s. A range of different plasma temperatures are chosen, which are not evolved during these simulations, along with a fixed neutral temperature $T_n = 1$ eV. Since the EI and RR reaction rates are purely a function of electron, or in an MHD plasma model, plasma temperature, the chosen neutral temperature does not affect the evolution of the system towards coronal equilibrium in a meaningful way.

In Fig. 4.6, the evolution of both the plasma and neutral density as a function of time is shown. Starting with an ionization fraction of 50% (i.e. $n = n_n$), the neutral number density rapidly declines as EI dominates over RR at a fixed plasma temperature $T = 12$ eV, as seen in Fig. 3.5. Using the prediction for the $\frac{n_e}{n_n}$ ratio from Fig. 3.6 at this plasma temperature, the expected plasma and densities in coronal equilibrium is plotted as a function of time. It is clear in Fig. 4.6 that the system is far from being in coronal equilibrium early in time, but as the system evolves toward steady-state conditions, the computed values for plasma density n and neutral density n_n converge towards the predicted coronal equilibrium values.

The same test simulations were performed assuming a plasma temperature $T = 10$ eV and $T = 5$ eV, as shown in Figs. 4.7 and 4.8. Note that in these additional cases the time required to reach coronal equilibrium is longer than for a plasma temperature $T = 12$ eV. This longer time requirement to reach steady-state conditions is due to the smaller ionization reaction rates at lower plasma temperatures, shown in Fig. 3.5. Noting these differences in characteristic time scales to reach coronal equilibrium between the test cases, all cases tried exhibit convergence of both the plasma and neutral densities towards their expected coronal equilibrium values late in time. Thus, these simulations suggest that both the plasma and neutral density advances have been implemented successfully in PSI-Tet by producing expected physical results.

Velocity advance verification

A velocity advance test simulation was performed as described in Chapter 3. The test problem is initialized with equal plasma and neutral number densities (i.e. $n = n_n = 1 \times 10^{19}$ m^{-3}), with equal and opposite velocities (i.e. $\vec{v} = -\vec{v}_n$) at a value of $|\vec{v}| = 1000$ m/s.

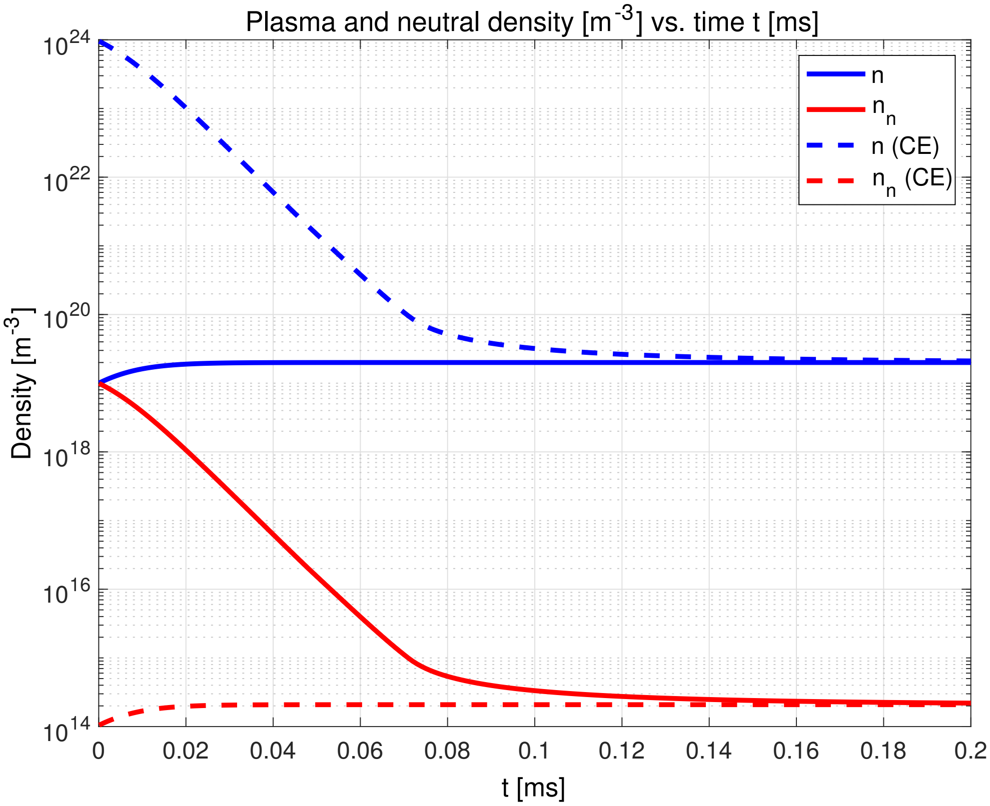

Figure 4.6: The depletion of neutrals starting with a 50% ionization fraction at $n = n_n = 1 \times 10^{19}$ m^{-3} initial densities as a function of time with a plasma temperature $T = 12$ eV. Dashed lines indicate the predicted coronal equilibrium (CE) values of the densities. The plasma and neutral densities in this test simulation evolve towards their expected coronal equilibrium values, as desired. Note the neutral density plateau of approximately $\approx 2 \times 10^{14}$ m^{-3} reached when assuming an plasma temperature $T = 12$ eV.

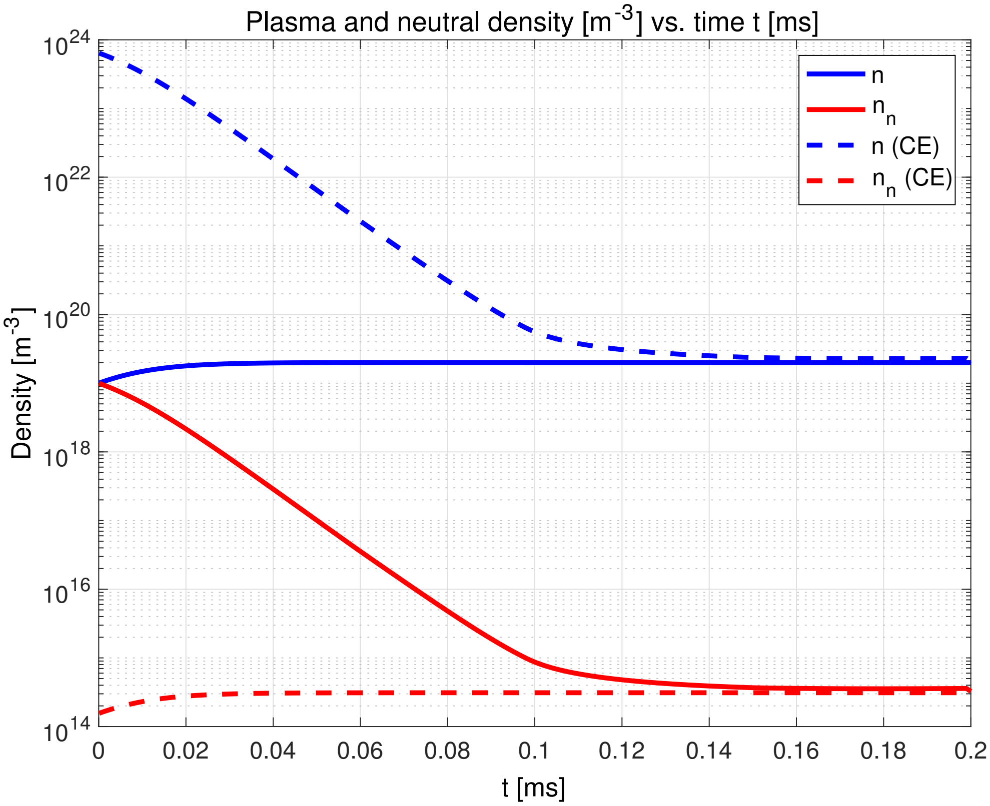

Figure 4.7: The depletion of neutrals starting with a 50% ionization fraction at $n = n_n = 1 \times 10^{19}$ m^{-3} initial densities as a function of time with a plasma temperature $T = 10$ eV. Dashed lines indicate the predicted coronal equilibrium (CE) values of the densities. The plasma and neutral densities in this test simulation evolve towards their expected coronal equilibrium values, as desired. Note the neutral density plateau of approximately $\approx 3.1 \times 10^{14}$ m^{-3} reached when assuming an plasma temperature $T = 10$ eV.

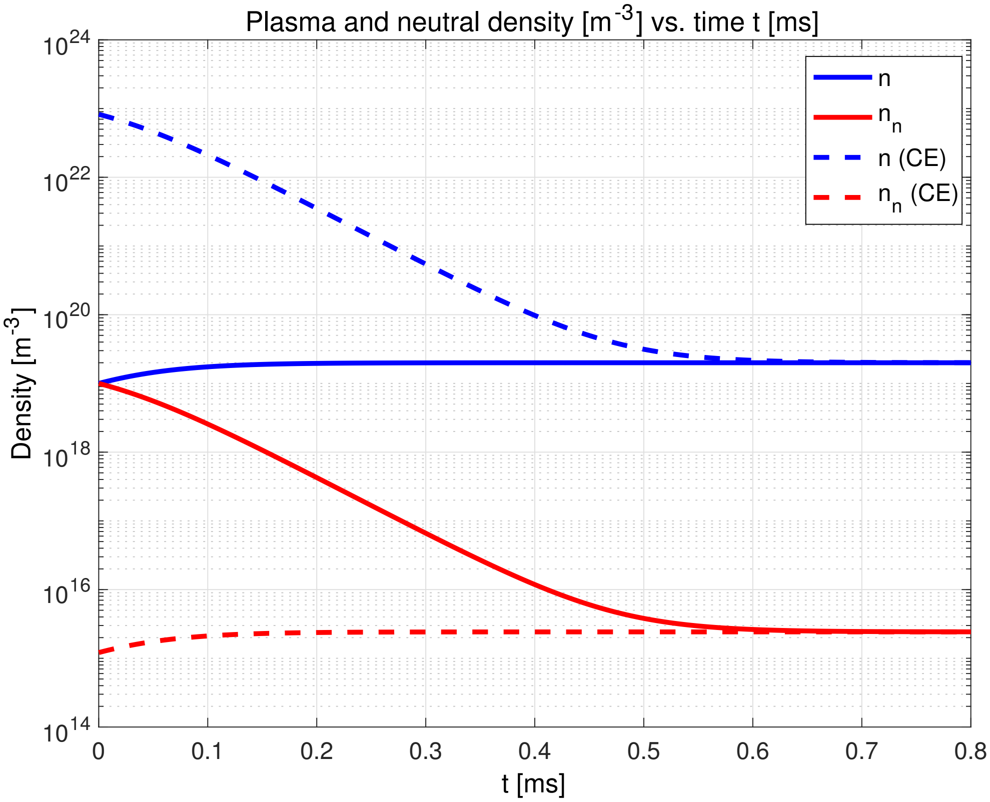

Figure 4.8: The depletion of neutrals starting with a 50% ionization fraction at $n = n_n = 1 \times 10^{19}$ m^{-3} initial densities as a function of time with a plasma temperature $T = 5$ eV. Dashed lines indicate the predicted coronal equilibrium (CE) values of the densities. The plasma and neutral densities in this test simulation evolve towards their expected coronal equilibrium values, as desired. Note the neutral density plateau of approximately $\approx 2.4 \times 10^{15}$ m^{-3} reached when assuming an plasma temperature $T = 5$ eV.

Additionally, it is assumed that the plasma-neutral mixture is isothermal and fixed, such that $T = T_n = 5$ eV. Both the densities and velocities of both species are evolved in time for the self-consistent demonstration of conservation of momentum. The result of this test simulation is shown in Fig. 4.9. In this simulation, the densities of both species are free to evolve, which is required for the self-consistent demonstration of conservation of momentum with non-zero ionization and recombination reaction rates. Thus, these simulations suggest that both the plasma and neutral velocity advances have been implemented successfully in PSI-Tet by producing expected physical results.

Temperature advance verification

A series of temperature advance test simulations were performed as described in Chapter 3. Three different test simulations were performed to verify the temperature advances implemented in PSI-Tet. All simulations assume an unmagnetized ($|\vec{J}| = |\vec{B}| = 0$) plasma, no heat flux for both the plasma and neutral species (i.e. $\vec{q} = \vec{q}_n = 0$), sets the viscosity coefficients for both species are set to zero (i.e. $\nu = \nu_n = 0$). Also, all simulations use an initial conditions of equal plasma and neutral number densities (i.e. $n = n_n = 1 \times 10^{19}$ m^{-3}), equal and opposite velocities (i.e. $\vec{v} = -\vec{v}_n$) with a magnitude of $|\vec{v}| = 1000$ m/s, and a plasma temperature $T = 10$ eV and a neutral temperature of $T = 1$ eV. In these simulations, all three variables of interest are evolved for each species.

The first test simulation is performed while evolving the temperature advances expressed as Eqs. 3.28 – 3.29. This simulation includes the ionization energy loss from electron impact ionization, with all variables evolving for both species for a self-consistent simulation. Plasma and neutral variables of interest are plotted in Fig. 4.10. This simulation exhibits a continuous decrease in plasma thermal energy from the system, as a result of the continuous expenditure of plasma energy on ionization events. This expenditure of plasma energy on ionization is also reflected in the temperature evolution plot in Fig. 4.10, which exhibits a continuous decrease of both the plasma and neutral temperature after equilibration occurs early in time via charge-exchange collisions. The rate of energy loss from the system decreases in time

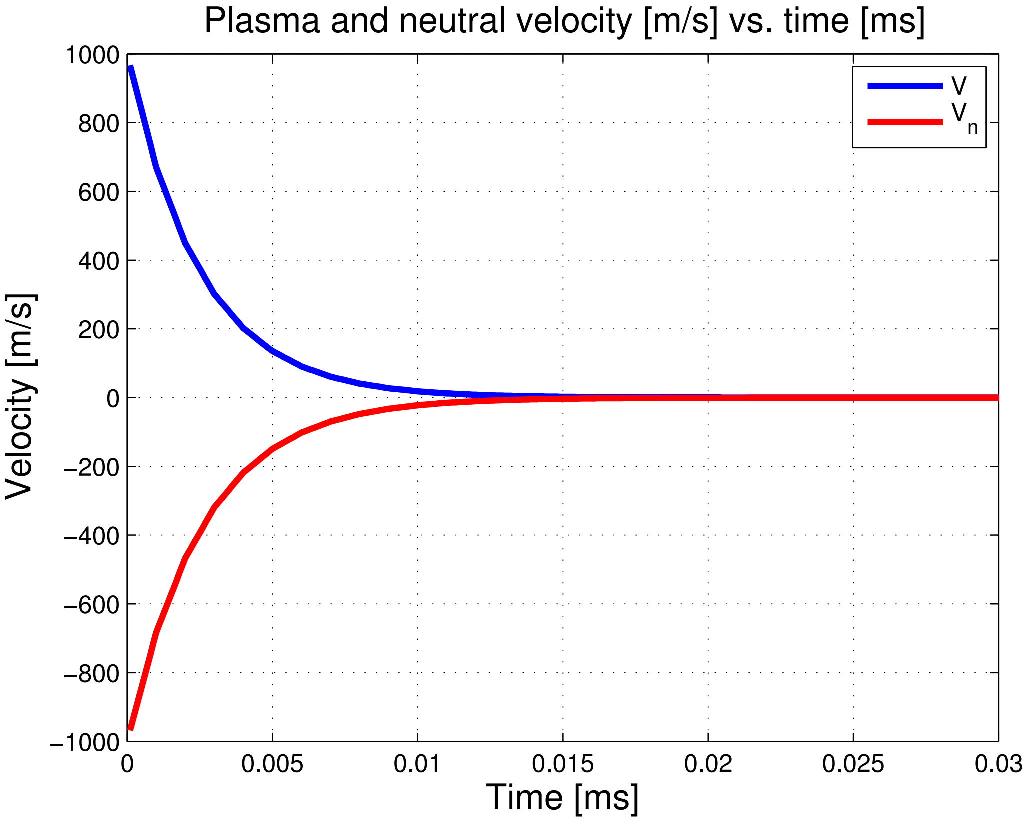

Figure 4.9: Demonstration of conservation of momentum in PSI-Tet. Both the velocities and densities of both species is allowed to evolve, assuming the same initial number densities, fix temperatures of 5 eV, and equal and opposite initial velocities. Since the initial momentum of the system is zero, the final state also has zero momentum, with the velocities of both species tending to zero.

due to the lower plasma temperatures later in time, which correspond to a lower ionization reaction rate as seen in Fig. 3.5.

The second test simulation is performed while evolving the temperature advances expressed as Eqs. 3.30 – 3.31, assuming that the ionization energy loss $\phi_{ion} = 0$. This simulation involves no structural changes to the plasma-neutral PSI-Tet code beyond changing the value of this assumed constant. The result of this simulation is shown in Fig. 4.11. It is clear that the evolution of the thermal energy densities, temperatures, and densities have changed notably from the previous test simulation shown in Fig. 4.10. First, and most importantly for verification of the temperature advances, it is observed that the total thermal energy of the system remains constant in time, instead of decreasing in time as observed in Fig. 4.10. This change is the result of the plasma no longer expending energy to ionize neutral particles, as expected. As a result of this change, the temperature evolution of both the plasma and neutral species has changed as well. The two species equilibrate early in time via CX collisions as before, but do so at a higher equilibrated temperature than in Fig. 4.10. This higher equilibration temperature is due to the elimination of plasma thermal energy loss from ionization. Due to this higher plasma temperature for the duration of the simulation than shown in Fig. 4.10, and a corresponding larger ionization reaction rate in Fig. 3.5, the neutral density is depleted more quickly than in Fig. 4.10, as expected.

The final test simulation is performed while evolving the temperature advances expressed as Eqs. 3.32 – 3.33 assuming the ionization and recombination reaction rates are zero (i.e. $\left\langle \sigma_{ion/rec} v_e \right\rangle = 0$). In making this assumption, this isolates the CX reaction terms from both EI and RR reaction terms. The result of this simulation in shown in Fig. 4.12. In this simulation, just as the one shown in Fig. 4.11, the total thermal energy density of the system is constant in time, as expected due to no mechanism being present that results in a net-loss of plasma thermal energy from the system. However, the evolution of individual thermal energy densities, temperature, and densities have changed considerably when compared to Fig. 4.10 and Fig. 4.11. This difference is driven by the marked change in the density evolution of both species. Since ionization and recombination reactions have been excluded from this simulation, and CX reactions do not lead to a net conversion of species, the densities of both species remain constant in time at their initial value of $n = n_n = 1 \times 10^{19}$ m^{-3}. As a result, once the two species equilibrate in temperature early in time from CX reactions, all variables no longer change as a function of time. As a quantitative test of energy conservation, using Eq. 3.27 and the initial plasma temperature $T = 10$ eV and initial neutral temperature $T = 1$ eV, the expected final temperature of the plasma-neutral mixture $T_{final} = 7$ eV. As seen in Fig. 4.12, both the plasma and neutral temperatures equilibrate to 7 eV, as expected. Thus, these simulations suggest that both the plasma and neutral temperature advances have been implemented successfully in PSI-Tet by producing expected physical results.

4.2.2 Boundary condition analysis

The SRIM code is used to calculate the fraction of incident ions that are either promptly backscattered or absorbed into an aluminum oxide target, and also provides the kinetic energy of promptly backscattered neutral particles. For these SRIM calculations, aluminum oxide at 100% theoretical density is used with zero surface roughness. In reality, the alumina plasma-material interface likely has a lower mass density and a finite surface roughness that tends to reduce the prompt backscattering fraction [73]. Thus, these SRIM simulations serve as a bounding case that maximizes the prompt backscattering fraction. Nevertheless, this analysis is focused on this bounding case of a pure aluminum oxide plasma facing component that has a completely smooth surface.

The choice of incident ions for these simulations are deuterium nuclei, which have a +1 positive charge and a atomic mass of $m_u \approx 2.014$ amu. This choice of incident ions is driven by the TALIF measurements of ground state, monatomic neutral densities and temperatures that were made in deuterium spheromak plasmas. An illustration of the simulated system is shown in Fig. 4.13. An incident ion beam of a chosen kinetic energy impacts an aluminum oxide sample that is nominally chosen to be 30 Å thick.

Using the simple Bohm model described in previous sections to relate plasma and neutral

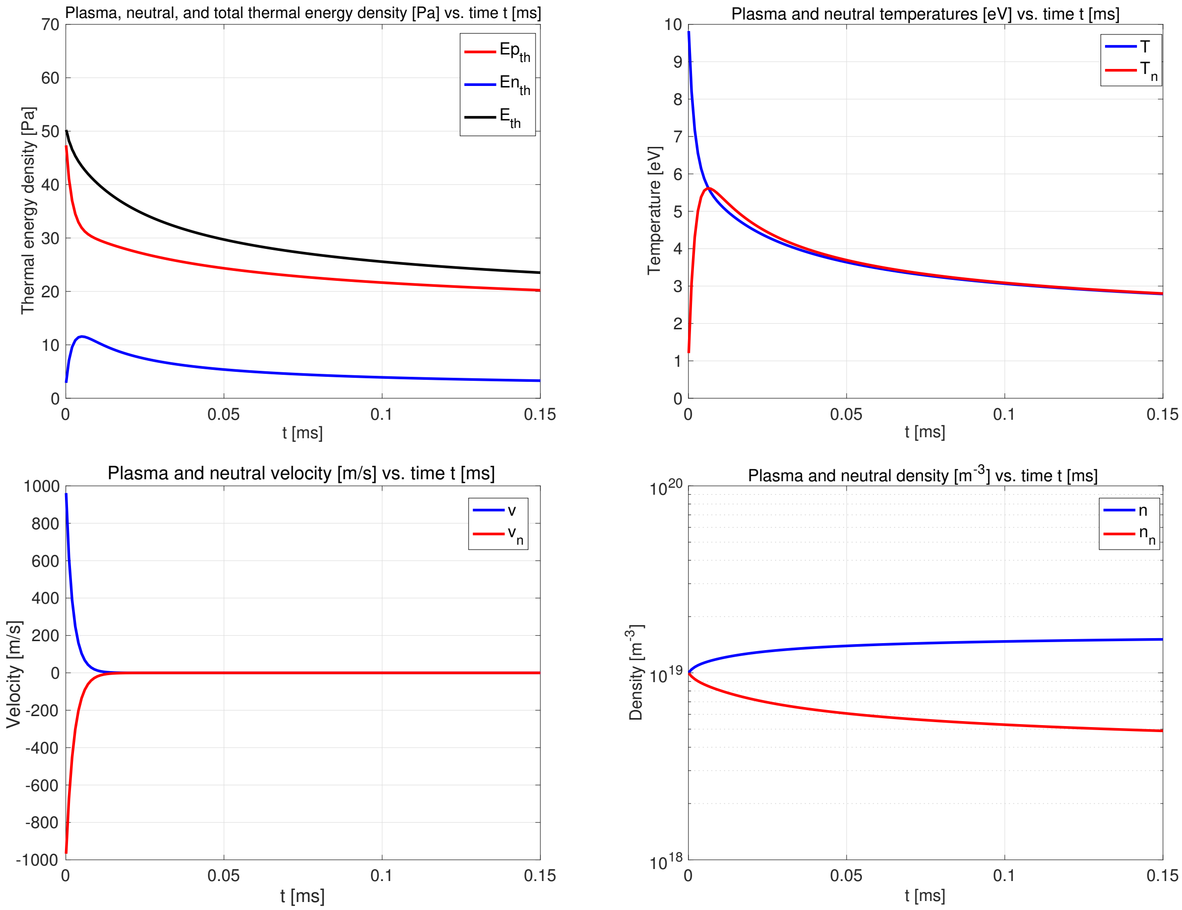

Figure 4.10: Plasma and neutral variables vs. time all plasma-neutral reaction terms active. **Top left**: Plasma Ep_{th} and neutral En_{th} thermal energy densities, and their sum plotted vs. time. Note that the total thermal energy of the system decreases in time due to the continuous expenditure of plasma thermal energy on ionizing neutral particles. **Top right**: Plasma T and neutral T_n temperatures vs. time. Note that both the plasma and neutral fluid temperatures equilibrate early in time, and track one another well during the remainder of the simulation primarily via charge-exchange collisions. The temperature continuously decreases in time due to the expenditure of plasma energy on ionization. **Bottom left**: Plasma $\vec{v}$ and neutral $\vec{v}_n$ velocities vs. time. Note that the counter-propagating fluids quickly come to rest in the simulation, as is consistent with the velocity verification simulation. **Bottom right**: Plasma n and neutral n_n densities vs. time. Note there is an increase in plasma density and a corresponding decrease in neutral density as a function of time from ionization events.

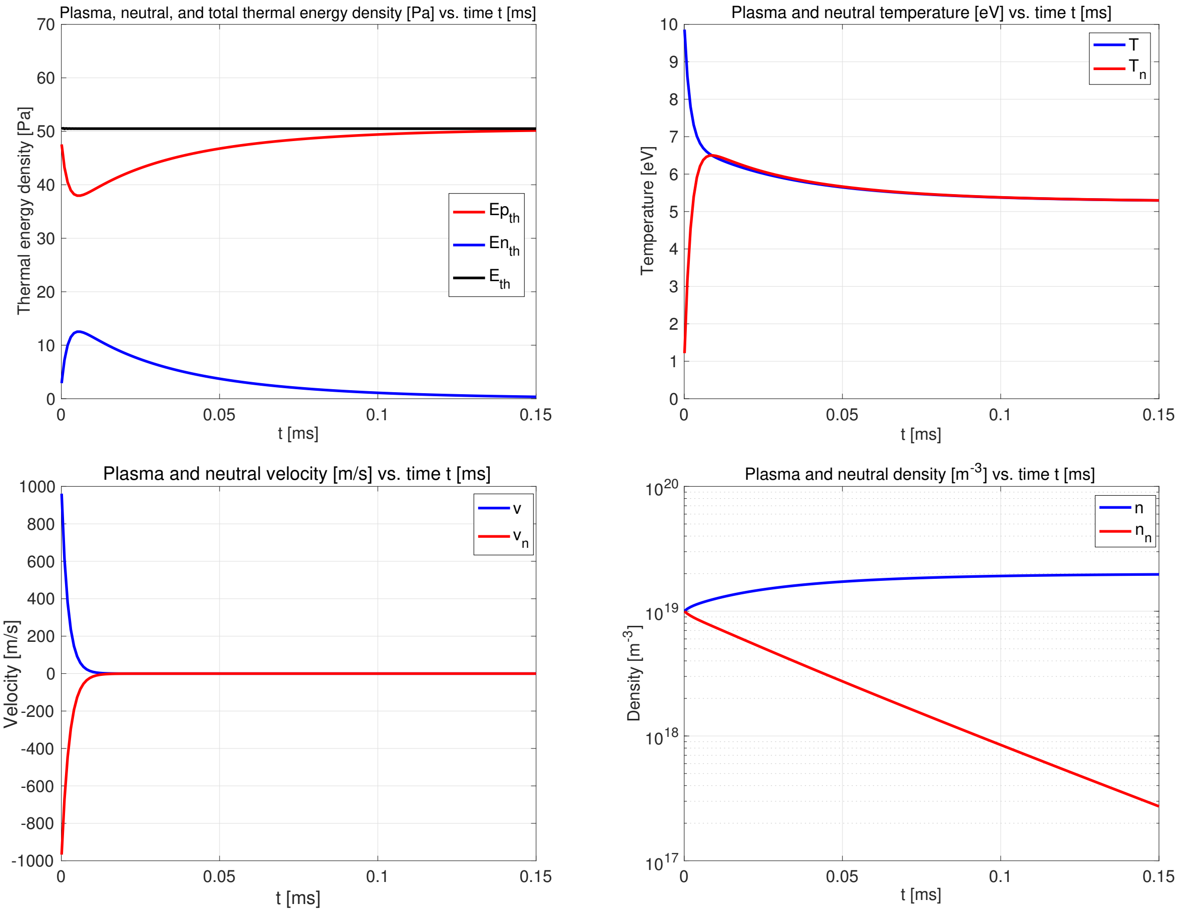

Figure 4.11: Plasma and neutral variables vs. time with ionization energy loss $\phi_{ion} = 0$. **Top left**: Plasma Ep_{th} and neutral En_{th} thermal energy densities, and their sum E_{th} plotted vs. time. Note that the total thermal energy of the system is constant in time the ionization energy loss has been set to zero. **Top right**: Plasma T and neutral T_n temperatures vs. time. Note that both the plasma and neutral fluid temperatures equilibrate early in time, and track one another well during the remainder of the simulation primarily via charge-exchange collisions. The temperature begins to approach steady-state conditions late in time as both fluids equilibrate. **Bottom left**: Plasma $\vec{v}$ and neutral $\vec{v}_n$ velocities vs. time. Note that the counter-propagating fluids quickly come to rest in the simulation, as is consistent with the velocity verification simulation. **Bottom right**: Plasma n and neutral n_n densities vs. time. Note there is an increase in plasma density and a corresponding decrease in neutral density as a function of time from ionization events, though the plasma is not expending energy during ionization.

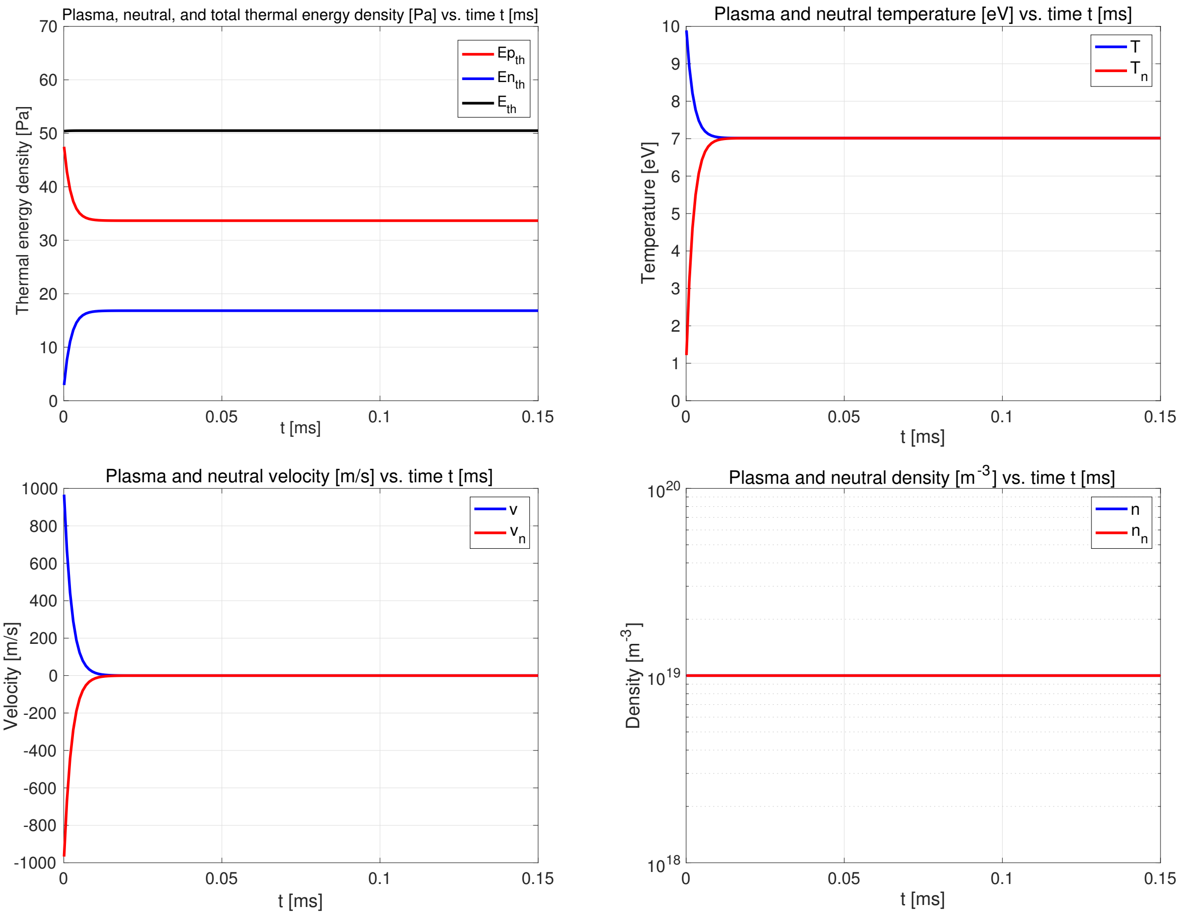

Figure 4.12: Plasma and neutral variables vs. time with only charge-exchange reaction terms active. **Top left**: Plasma Ep_{th} and neutral En_{th} thermal energy densities, and their sum plotted vs. time. Note that the total thermal energy of the system is constant in time, as expected. **Top right**: Plasma T and neutral T_n temperatures vs. time. Note that both the plasma and neutral fluid temperatures equilibrate early in time via charge-exchange collisions, and stay constant at $T_{final} = 7$ eV for the remainder of the simulation. **Bottom left**: Plasma $\vec{v}$ and neutral $\vec{v}_n$ velocities vs. time. Note that the counter-propagating fluids quickly come to rest in the simulation, as is consistent with the velocity verification simulation. **Bottom right**: Plasma n and neutral n_n densities vs. time. Note that since the ionization and recombination reactions have been excluded in these terms, there is no net conversion of plasma into neutrals or vice versa from CX alone. Thus, the densities of both species are constant in time at their initial values.

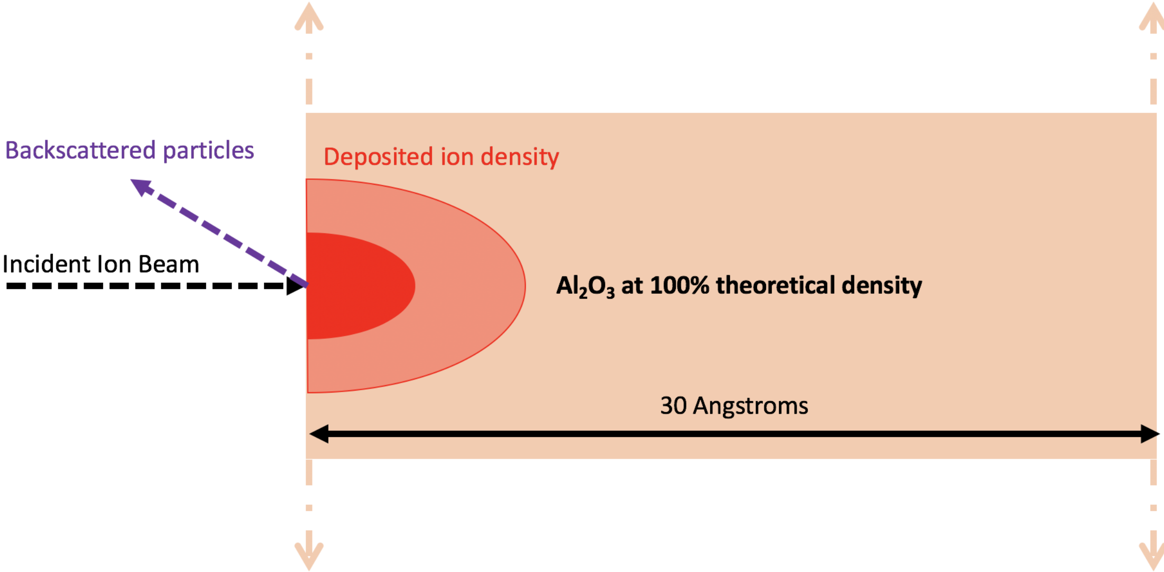

Figure 4.13: An illustration of the system being simulated with SRIM. An aluminum oxide (Al_2O_3) sample at 100% theoretical density and with a thickness of 30 Å is impacted by an incident ion beam. SRIM provides the prompt backscattered particle fraction, their kinetic energy, and the deposited ion density in the solid material as a function of incident ion energy.

parameters of interest at the sheath entrance, it is known for an equilibrated (i.e. $T_i = T_e$) hydrogen plasma, the sheath accelerates ions entering the sheath region to approximately three times its sheath entrance kinetic energy [36]. More specifically, starting in the bulk, quasineutral plasma region without significant plasma flow, ions enter the presheath region that has a total electric potential drop $V_{ps} \approx -\frac{0.7kT}{e}$ below the plasma potential V_p as shown in Fig. 3.7 [36]. Then, entering the sheath at approximately the ion sound speed c_s, the ions experience an additional potential drop of $V_s \approx -\frac{3kT}{e}$ [36]. Thus, the total potential drop in both the presheath and sheath regions is the wall potential $V_{wall} \approx -\frac{4kT}{e}$, which is negative relative to the plasma potential V_p for these assumed hydrogen plasma conditions. Knowing for electrostatic fields, $\vec{E} = -\nabla V$ and from Lorentz force law $\vec{F} = q\vec{E}$, this electrostatic potential tends to accelerate ions towards the wall while repelling electrons, as described previously.

For this work, the sheath entrance (i.e. the interface between the sheath and presheath regions) is chosen as a suitable boundary for an MHD plasma-neutral fluid simulation with PSI-Tet. As a result, it is assumed that ions exiting the MHD simulation domain at the presheath-sheath interface will be accelerated by the sheath voltage $V_s = -\frac{3kT}{e}$ to approximately 3 times its kinetic energy at the sheath entrance. Thus, a sheath entrance plasma temperature of between $T_{SE} = 1.67 - 8.33$ eV corresponds to sheath accelerated ion kinetic energies $E_{inc} = 5 - 25$ eV. Note that if a different boundary is chosen for the MHD plasma-neutral fluid simulation volume, such as the interface between the bulk plasma and presheath entrance, the relationship between plasma and neutral parameters will be modified at this chosen boundary. However, the range of incident ion energies E_{inc} simulated in SRIM has been chosen to span the likely space of expected edge plasma temperatures in HIT-SI3.

Using the range of incident deuterium ion kinetic energies $E_{inc} = 5 - 25$ eV, SRIM is used to calculate the desired quantities of interest. The deposited ion density is shown in Fig. 4.14, which shows a broader and deeper implantation of incident ions within the aluminum oxide sample as the incident energy increases. An additional plot assuming an incident ion energy of $E_{inc} = 50$ eV is included in Fig. 4.14 to show implanted ions spanning the entire 30 Å thick aluminum oxide sample. However, for incident ion energies $E_{inc} = 5 - 25$ eV, nearly no incident ions are fully transmitted through the 30 Å-thick alumina layer, which motivated the chosen thickness for these simulations. The alumina layer in HIT-SI3 is on the order of ≈100s μm or more, and so no ions are expected to fully penetrate the alumina plasma facing coating in the HIT-SI3 experiment.

These SRIM simulations suggest a weak dependence of the promptly backscattered fraction as a function of incidient ion energy in aluminum oxide, shown in Fig. 4.15. These calculations suggest a promptly backscattered fraction $f_{bs} \approx 21 - 26\%$ with incident ion energies $E_{inc} = 5 - 25$ eV. Thus, a significant majority of incident, sheath accelerated ions are deposited in the solid material instead of being promptly backscattered.

These SRIM simulations also indicate a weak dependence of the fractional kinetic energy of prompt lybackscattered neutral particles f_e as a function of incidient ion energy E_{inc}, as shown in Fig. 4.16. Over the range of incident ion energies simulated, the average fractional kinetic energy of promptly backscattered neutral particles $f_e \approx 36.5\%$ for this system. As an example, for an incident ion with a kinetic energy of 10 eV, corresponding to an assumed sheath entrance plasma temperature of ≈ 3.33 eV, it can be either promptly backscattered as an energetic neutral particle with approximately 3.65 eV of kinetic energy or implanted into the surface. Interestingly, the backscattered energy fraction nearly cancels with the sheath acceleration of the ion such that the kinetic energy of promptly backscattered neutral particles correspond to the assumed plasma temperature at the sheath entrance. In short, this relationship is due to the elastic scattering efficiency considerations for deuterium ions impacting a solid target made of aluminum oxide.

4.2.3 Validation of simulations with experimental data

As mentioned in previous sections, non-zero TALIF measurements of monatomic, ground state deuterium neutral densities and temperatures were only made during the decay period of spheromak discharges in the HIT-SI3 experiment. In particular, these TALIF measurements were made in a 180 μs time interval during spheromak decay following a 2 ms driven

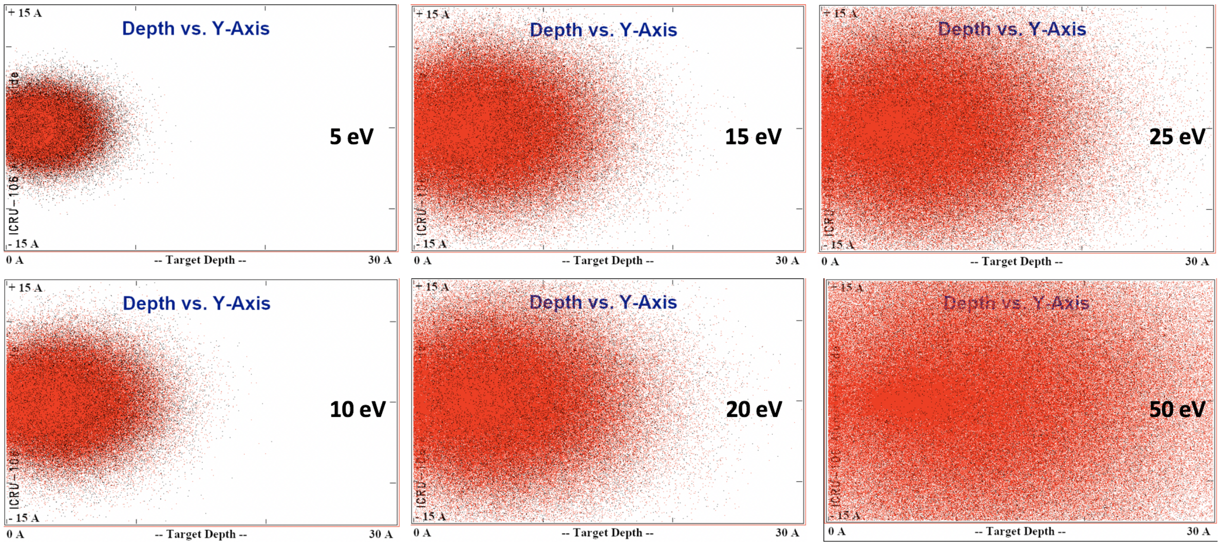

Figure 4.14: SRIM calculated deposited ions in aluminum oxide as a function of incident ion energy $E_{inc} = 5 - 50$ eV. Note the broader, deeper deposition of incident ions as the incidient kinetic energy of ions increases, as expected.

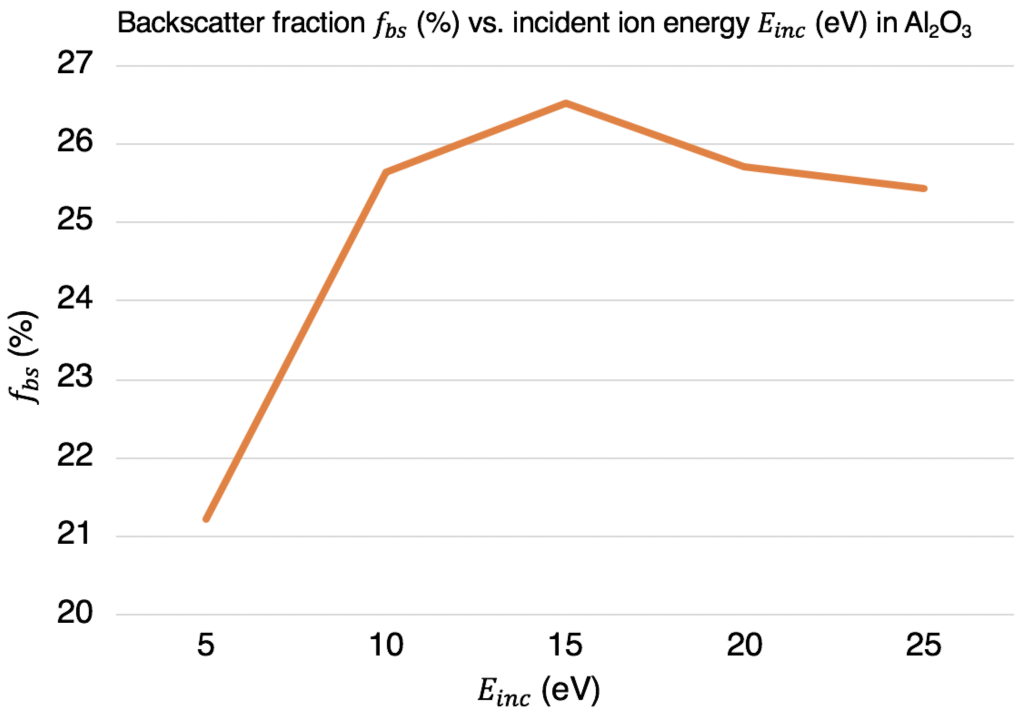

Figure 4.15: Prompt backscattered fraction f_{bs} (%) as a function of incident ion energy E_{inc} impacting aluminum oxide (Al_2O_3). Note the relatively weak dependence of the prompt backscattered fraction with incident ion energy over the energy range analyzed.

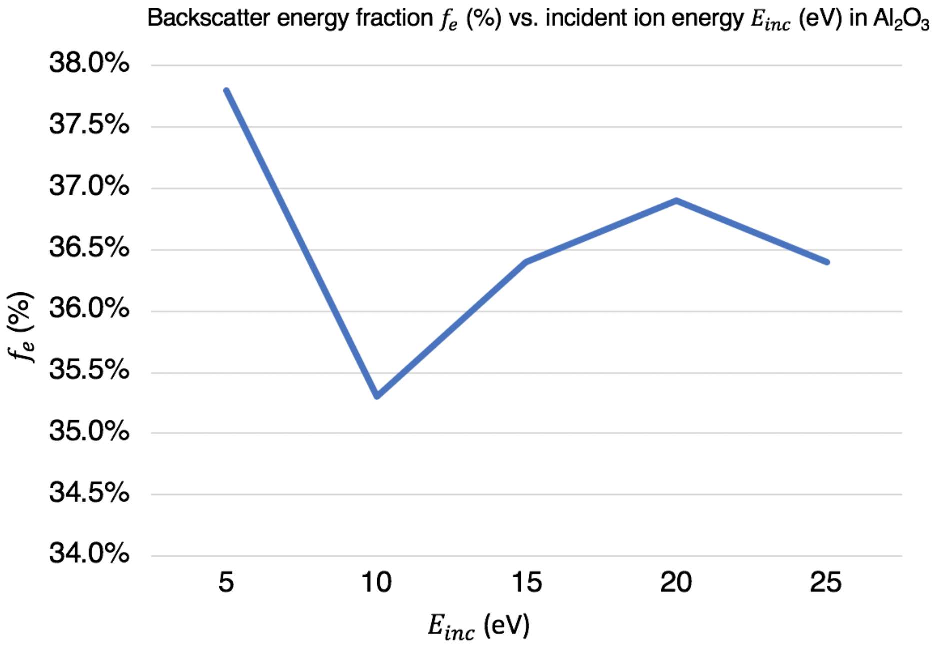

Figure 4.16: Backscattering energy fraction f_e (%) as a function of incident ion energy E_{inc} impacting aluminum oxide (Al_2O_3). Note the weak dependence of f_e as a function of incident ion energy over the energy range analyzed, with an average backscattered energy fraction $f_e \approx 36.5\%$.

period. A representative toroidal current trace from shot 150625006 is shown in Fig. 4.1. Ideally, it would be desired to peform a plasma-netural simulation that captures the entirety of the spheromak discharge period, both the helicity injector driven and spheromak decay periods for comparisons with TALIF measurements. Such a simulation would help ensure the spheromak conditions at the start of decay are most similar to those in experimental discharges. However, a 2 ms driven HIT-SI3 simulation is computationally expensive due to complex helicity injector and spheromak dynamics, which limits the ability to quickly iterate with different boundary conditions to observe their impact on simulations. Additionally, since TALIF measurements made during the driven phase of spheromak discharges on HIT-SI3 yielded null results, there are no experimental data to compare plasma-neutral simulations to for this period of the discharge. Thus, due to the lack of non-zero TALIF measurements during the driven phase of the discharge, the usefulness of performing plasma-neutral simulations that capture the driven period of operation of HIT-SI3 for validation purposes is limited.

Instead, to enable less computationally-expensive simulations while still allowing for meaningful comparisons to TALIF data acquired during the spheromak decay period of HIT-SI3 discharges, it was elected to perform plasma-neutral simulations of only decaying spheromak configurations in the HIT-SI3 flux conserver geometry as a focus of this work. For these simulations, a spheromak Taylor state equilibrium, described by Eq. 1.6, with a chosen toroidal plasma current is used as the initial toroidal magnetized plasma object contained within the HIT-SI3 flux conserver for decaying spheromak plasma-neutral simulations. The amplitude of these initial Taylor states are chosen such that their toroidal currents are much larger than those measured of spheromaks in which TALIF measurements were made. With an assumed set of boundary conditions, the spheromak undergoes resistive decay with all variables of interest being evolved for both the plasma and neutral fluids.

Since a Taylor state equilibrium is used as the initial condition for the spheromak configuration to undergo resistive decay, which requires $\vec{J} \parallel \vec{B}$ from Eq. 1.6, this type of spheromak equilibrium does not support a pressure gradient when considering steady-state force balance

$\nabla p = \vec{J} \times \vec{B} = 0$. Thus, though this initial equilibrium is assumed, since these plasma-neutral PSI-Tet simulations allow for non-zero plasma pressure and plasma pressure gradients, the initialized spheromak is not in equilibrium at the time of initialization (i.e. $t = 0$). As a result, after beginning evolution of the plasma-neutral fluid variables of interest, the spheromak equilibrium quickly evolves towards a new equilibrium that contains non-zero pressure gradients, as shown in Fig 4.17.

After the pressure confining spheromak reaches its new equilibrium, finite Spitzer electrical resistivity η appearing in Eq. 3.14 causes the toroidal current to decay as time progresses since the helicity injectors are not actively driving the equilibrium. This behavior can be readily understood when considering Eq. 1.14 with both $V_{inj} = 0$ and $\Psi_{inj} = 0$. Without helicity injection into the HIT-SI3 confinement volume, magnetic helicity decays on a resistive timescale via Eq. 1.10, which is directly related to the decay of the toroidal plasma current. As the spheromak configuration decays, it will resistively heat the plasma fluid via Eq. 3.12 which interacts with the neutral fluid via the plasma-neutral reactions included in the plasma-neutral model. After sufficient time, the spheromak will decay to a similar amplitude toroidal plasma current as the decaying spheromaks in which TALIF measurements were made, providing a basis for comparison between experimental data and plasma-neutral simulations.

A key limitation worthy of note for this approach in comparing TALIF measurements and decaying spheromak plasma-neutral simulations is whether the simulation system is sufficiently representative of the experimental system under consideration. Though both the experimental period in which TALIF measurements were made and decaying spheromak plasma-neutral simulations share that they are undriven systems, the initial condition assumed for simulations is quite different from the system at the beginning of the spheromak decay period in the experiment. In experimental discharges for TALIF measurements, the helicity injectors form and sustained $I_p \approx 10 - 12$ kA spheromak configurations during a 2 ms period before the decay period begins after helicity injectors are shut off. Thus, both the equilibrium, and also the plasma and neutral fluid parameters of interest, likely deviate

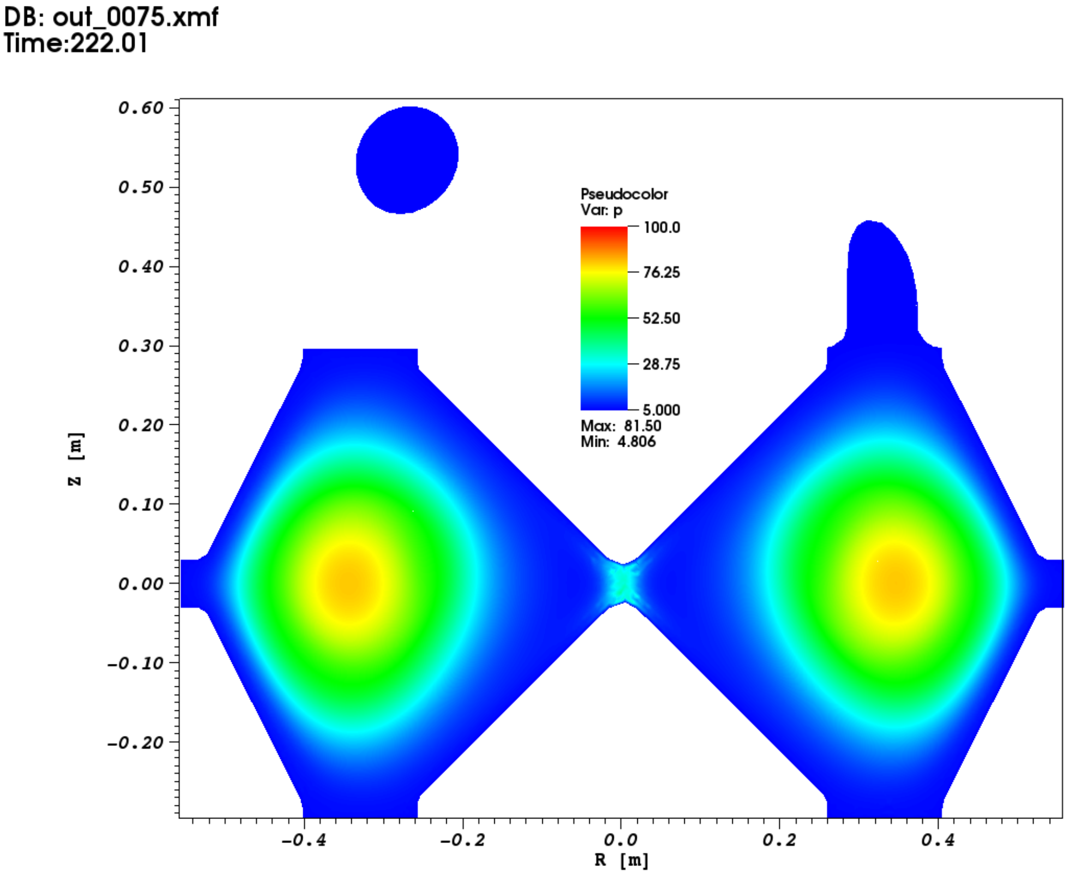

Figure 4.17: A poloidal cross-section plot of the plasma pressure. Note the non-uniform plasma pressure across the simulation domain, with local maxima of plasma pressure located near the magnetic axis of the spheromak region. The locally higher plasma pressure observed near the geometric axis is to due the presence of relatively high plasma density that is the result of two boundaries held at high plasma density in close proximity to one another.

from the assumed initial and boundary conditions for PSI-Tet simulations as described previously. However, in choosing a sufficiently large amplitude Taylor state for initialization, and acknowledging non-zero TALIF measurements were made more than 100 μs into spheromak decay or later in the experiment, it is argued that potential impacts from significant differences resulting from variations between chosen initial conditions for plasma-neutral PSI-Tet simulations and experimental discharges will be reduced or eliminated during the period of comparison between simulations and experimental data. However, should experimental data disagree with simulation, it may become necessary to perform a full driven HIT-SI3 simulation that precedes the decay period to ensure the simulation conditions at the start of decay are more likely to be representative of experimental conditions.

Beyond potential discrepancies between the chosen initial conditions for plasma-neutral simulations of decaying spheromaks and experimental discharges, the choice of boundary conditions can significantly impact the level of agreement between experimental data and simulations. The impact of chosen boundary conditions on calculations will be discussed at length in the next chapter, but key results will be presented in this section for context with validation results. Dirichlet boundary conditions for both the plasma and neutral fluid variables were used for plasma-neutral simulations presented in this work. The use of Dirichlet boundary conditions is motivated by previous work performed with PSI-Tet that made extensive use of this type of boundary condition for HIT-SI simulations [51]. In particular for this work, chosen boundary conditions were partially guided using results from SRIM simulations and a simple sheath model described previously to self-consistently choose values for n, n_n, T, T_n at the boundary of the simulation domain. However, due to the uncertainty in the plasma density and temperature at the sheath entrance, and the recycling fraction during a typical TALIF discharge, and whether the simple sheath model applies sufficiently well to the HIT-SI3 experimental system, SRIM results and a simple sheath model are used more as bounding guidelines for acceptable boundary conditions to choose for PSI-Tet plasma-neutral simulations. Using these physically informed bounds, boundary conditions are chosen with the intent of reaching the best agreement with experimental data possible.

Before presenting validation results, representative simulation parameters are given in Tab. 4.1 detailing key choices for boundary condition values for the plasma and neutral fluids, along with chosen viscosities and diffusivity coefficients. As mentioned in previous paragraphs, Dirichlet boundary condition are used for all plasma-neutral variables of interest, including the no-slip boundary conditions assumed for both the plasma and neutral velocities. For the representative simulation parameters presented in Tab. 4.1, it is important to note the main quantities being varied in simulations to be presented. First, the neutral density at the boundary is varied between $n_n = 10^{17} - 10^{18}$ m^{-3} for presented results since this choice led to the closest agreement with TALIF measurements and is consistent with a simple sheath model with a recycling fraction $f_{re} < 1$ (i.e. net wall pumping occurs). Additionally, these varied neutral densities at the boundary were simultaneously varied with the assume plasma temperature at the boundary T. The plasma temperature T in presented results was varied between $T = 0.75 - 1.5$ eV at the boundary. The chosen neutral temperautre at the boundary is varied $T_n = 0.025eV - 1.5$ eV, though the majority of presented simulation results made use $T_n = 0.025$ eV. This choice of neutral temperature boundary condition is motivated by SRIM results that indicated the majority of incident ions within the energy range analyzed implant into the wall rather than being promptly backscattered with a significant fraction of the sheath-accelerated incident ion energy. As mentioned previously, presented SRIM results made use of an incident ion beam on an aluminum oxide target with zero surface roughness. Finite surface roughness tends to decrease the prompt backscatter fraction of incident ions on most material surfaces [36, 74, 73], and thus it is assumed that the majority of neutrals produced via edge recycling at the plasma-material interface are thermal desorbed deuterium molecules, thus motivating the assumed room temperature neutral temperature boundary condition. The full implications of the important result that the majority of edge recycled neutral particles are likely thermalized molecules will be discussed in subsequent sections as a subject of future work, but it should be noted that this model does not include a diatomic fluid at the time of writing. Plasma and neutral viscosity coefficients are held constant for

Parameter	Symbol	Value	Units
Plasma density	n	1×10^{19}	m^{-3}
Neutral density	n_n	1×10^{18}	m^{-3}
Plasma temperature	T	1.5	eV
Neutral temperature	T_n	0.025	eV
Plasma viscosity	ν	400	m^2/s
Neutral viscosity	ν_n	400	m^2/s
Plasma diffusivity	D	1	m^2/s
Neutral diffusivity	D_n	1	m^2/s

Table 4.1: Table of representative simulation parameters for decaying spheromak plasma-neutral simulations with PSI-Tet for comparison with TALIF experimental measurements.

all simulations presented, though this quantity should be varied to determine its impact on solutions in future work. Lastly, the plasma and neutral diffusivity coefficients are held equal $D = D_n = 1$ m^2/s to ensure this artificial stabilizing term is not having a significant impact on computed solutions. This consideration of the impact of artificial diffusivity on plasma-neutral simulations is discussed in subsequent sections in detail. Using the chosen boundary condition values shown in Tab. 4.1, a plasma-neutral PSI-Tet simulation is initialized with a spheromak Taylor state equilibrium with a toroidal current of approximately $I_p = 36$ kA for all simulations presented in this section. The fixed boundary conditions values for the plasma and neutral densities, temperatures and velocities are uniform throughout the simulation domain at the time of initialization. After initialization, PSI-Tet evolves all parameters of interest forward in time to observe plasma-neutral dynamics.

For these plasma-neutral simulations, a few common behaviors are observed for all simulations presented. First, as the relatively high toroidal current spheromak configuration resistively decays, it tends to ohmically-heat the plasma fluid via Eq. 3.12 to higher plasma temperatures than its initialization value. These higher plasma temperatures result in a substantially larger electron-impact ionization rate when compared to the radiative recombination rate, which tends to deplete the starting neutral density that interacts with the Ohmically heated spheromak plasma. Additionally, resonant charge-exchange reactions tend to result in an exchange of energy between the plasma and neutral fluids, which then tends to increase the neutral fluid temperature substantially higher than its starting value. For most of the simulations results presented in this section, the characteristic decay time for the simulated spheromak is $t_{decay} \approx 800\,\mu$s, which is substantially longer than the observed experimental decay time $t_{decay} \approx 200\,\mu$s, shown in Fig. 4.24.

At $t = 222$ μs into spheromak decay for the simulation performed using chosen parameters shown in Tab. 4.1, minimum neutral densities $n_n < 10^{14}$ m^{-3} are observed, which is more than 4 orders of magnitude lower than its starting value of $n_n = 1 \times 10^{18}$ m^{-3}, as seen in Fig. 4.18. Additionally, a maximum neutral temperature at this time point in the simulation $T_n \approx 16.5$ eV, much higher than its starting value of $T_n = 0.025$ eV, as shown in Fig. 4.18. Higher plasma temperatures are observed in Fig. 4.19, with a maximum plasma temperature at this time point $T \approx 27.5$ eV, which is much higher than its starting value of $T = 1.5$ eV. Lastly, due to the conversion of the starting neutral fill into plasma via electron-impact ionization, a non-uniform plasma density profile is observed in Fig. 4.19, with a locally higher plasma density observed in the spheromak core where the neutral density has been depleted the most, as seen in Fig. 4.18.

As the spheromak continues to resistively decay, an expected $n = 2$ kink mode [25] is observed that begins at $t \approx 288$ μs into the simulation, as seen in Figs. 4.20 – 4.21. Note the non-axisymmetric, $n = 2$ distortion of the plasma density and temperature in Fig. 4.21 from its nominally axisymmetric structure in Fig. 4.19. Additionally, it is clear in Fig. 4.19 that though the maximum plasma temperature observed at this time point in the simulation is comparable to that observed at the earlier time point, the volume of plasma appearing at this higher temperature has been notably reduced due to this instability event. This non-axisymmetric distortion of the spheromak equilibrium from this instability also propagates, to a less pronounced extent, into the neutral fluid variables, as seen Fig. 4.20.

After this instability saturates and decays away during the simulation, and subsequently allowing for the nearly complete decay of the toroidal plasma current, the behavior shown in Figs. 4.22 – 4.23 is observed. Even at the end of spheromak decay, the observed minimum neutral density $n_n \approx 1.3\times10^{15}$ m^{-3} with a corresponding maximum neutral temperature $T_n \approx$ 0.62 eV. This result suggests overall higher neutral densities and lower neutral temperatures at the end of decay when compared to earlier time points shown in Fig. 4.18 and Fig. 4.20. A boundary condition dominated plasma density profile is observed in Fig. 4.23 at this time point in the simulation, with higher plasma densities observed near the geometric axis due to the close proximity of two simulation boundaries being held at $n = 1 \times 10^{19}$ m^{-3}. Lastly, a maximum plasma temperature $T \approx 1.8$ eV is observed in Fig. 4.23, which is only 0.3 eV higher than the boundary condition value $T = 1.5$ eV.

Validation results are presented for decaying spheromak plasma-neutral simulations as a series of figures for each comparison. It should be noted that for all validation results presented in this section, the available set of TALIF data contains spatial profile information at an experimental time $t = 2.16$ ms. But, spatial profile simulation results at the other equivalent TALIF experimental measurement times $t = 2.10$ ms and $t = 2.18$ ms are plotted for completeness. The available set of TALIF data contains temporal evolution information at all time points, but only at a single depth $d = 11$ cm. But, temporal evolution simulation results at the other TALIF measurement depth $d = 18$ cm is provided for completeness. In short, when comparing simulation results to experimental data, for spatial profiles one should compare the experimental data to simulation results at the experimental time $t = 2.16$ ms as indicated on the plot. For temporal evolution, one should compare the experimental data to simulation results at a depth $d = 11$ cm.

The set of Figs. 4.24 – 4.28 details results from a decaying spheromak plasma-neutral simulation using the set of simulation parameters listed in Tab. 4.1. As will be the case for all validation results presented, the representative experimental toroidal current trace shown in

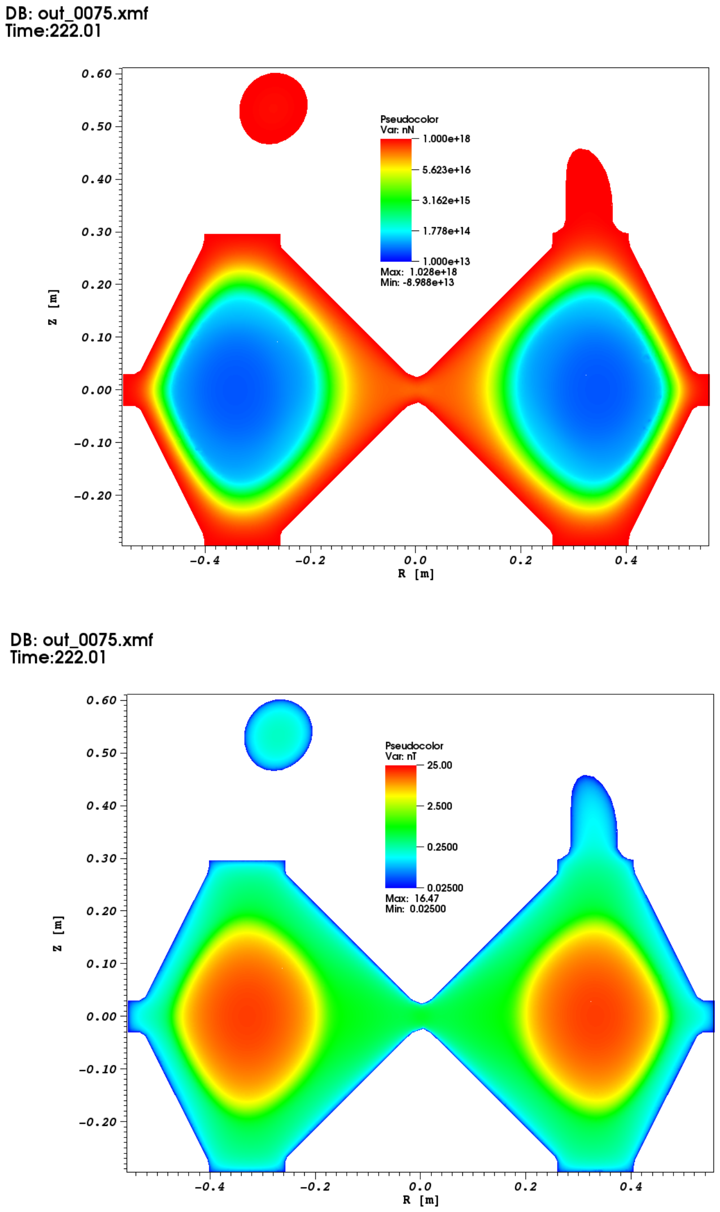

Figure 4.18: A poloidal cross-section plot of the neutral density (**Top**) and temperature (**Bottom**) at $t \approx 222\,\mu$s during the simulation. **Top**: Note the depletion of the neutral density within the core spheromak region to values $n_n < 1 \times 10^{14}$ m^{-3}, well below its starting value of $n_n = 1 \times 10^{18}$ m^{-3}. **Bottom**: Note the increase in neutral temperature throughout the simulation domain above its starting value of $T_n = 0.025$ eV. The strongest heating is observed in the spheromak core region, where the neutral density is also at its lowest values.

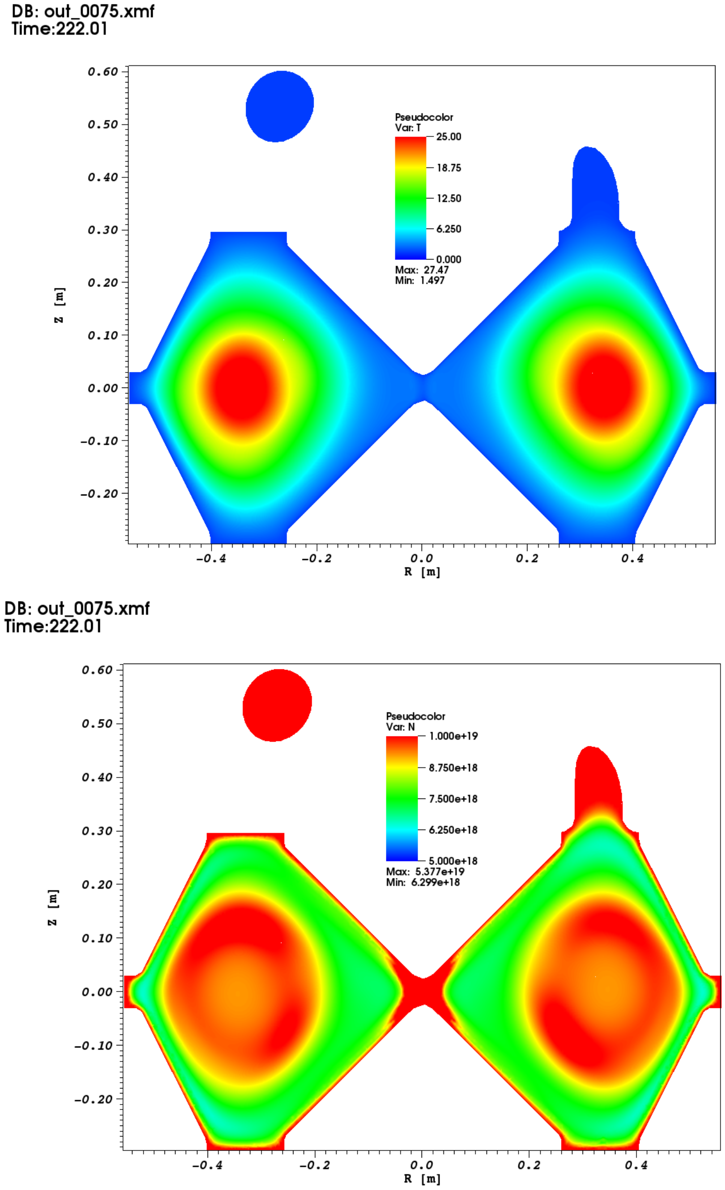

Figure 4.19: A poloidal cross-section plot of the plasma density (**Top**) and temperature (**Bottom**) at $t \approx 222\,\mu$s in the simulation. **Top**: Note the locally higher plasma density in the spheromak core region due to the species conversion of the starting neutral fill into plasma. **Bottom**: Note the increase in plasma temperature above its starting value of $T_n = 1.5$ eV. The strongest heating is observed in the spheromak core region.

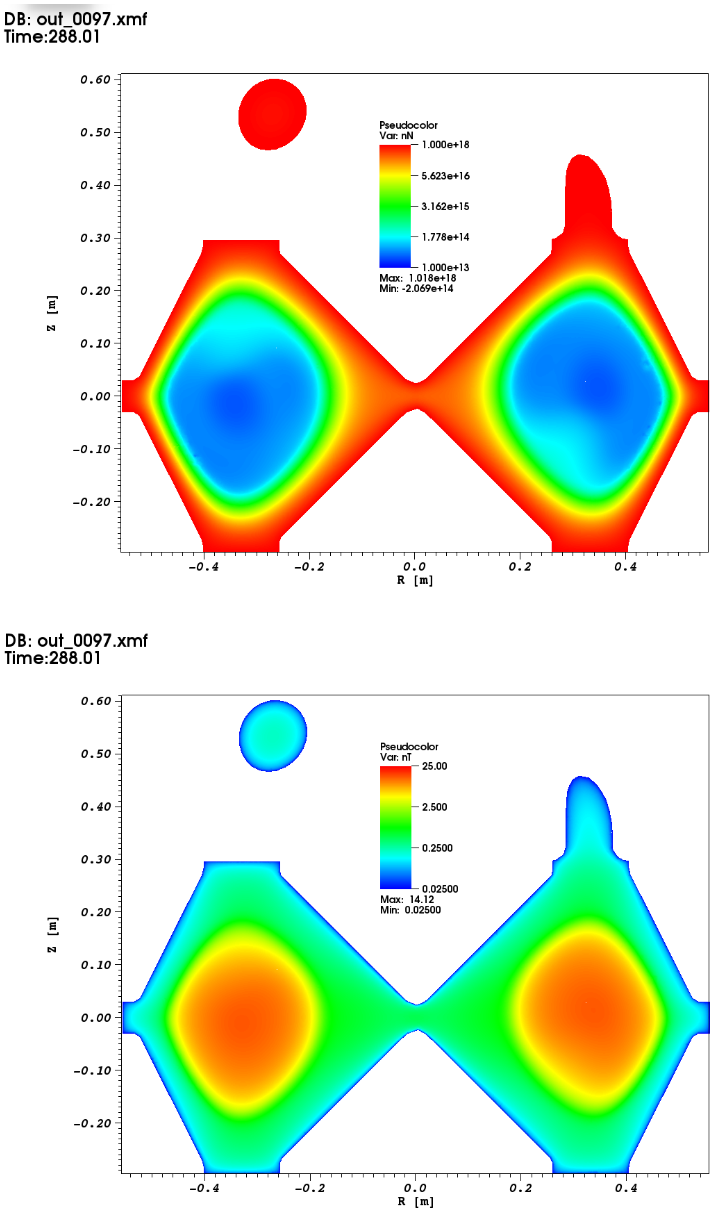

Figure 4.20: A poloidal cross-section plot of the neutral density (**Top**) and temperature (**Bottom**) at $t \approx 288\,\mu$s in the simulation. **Top**: Note the non-axisymmetric distortion of the neutral density that is driven by a distortion of the plasma density appearing in Fig. 4.21. **Bottom**: Note the the maximum neutral temperature observed at this time point $T_n \approx 14$ eV, which is orders of magnitude larger than its starting value of $T_n = 0.025$ eV.

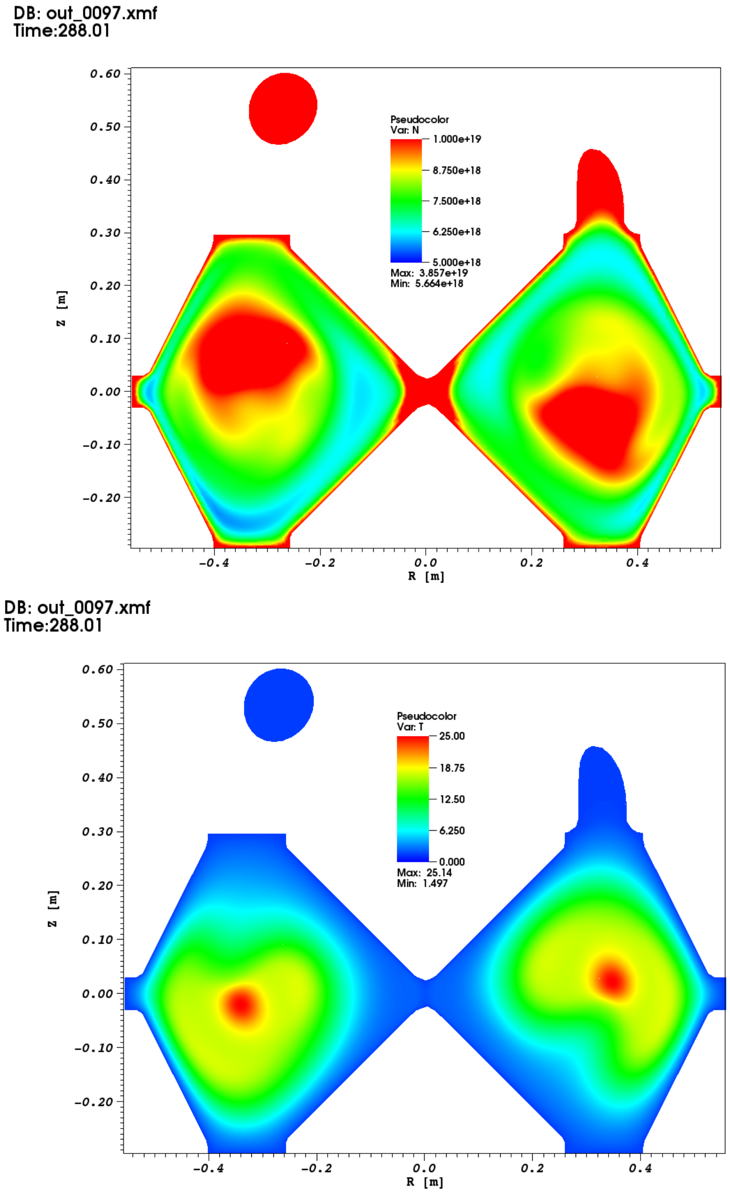

Figure 4.21: A poloidal cross-section plot of the plasma density (**Top**) and temperature (**Bottom**) at $t \approx 288\,\mu$s in the simulation. **Top**: Note the pronounced non-axisymmetric distortion of the plasma density profile due to an $n = 2$ kink instability occurring at this time in the simulation. **Bottom**: Note the overall cooling of the plasma temperature compared to Fig. 4.19 during this kink-instability event.

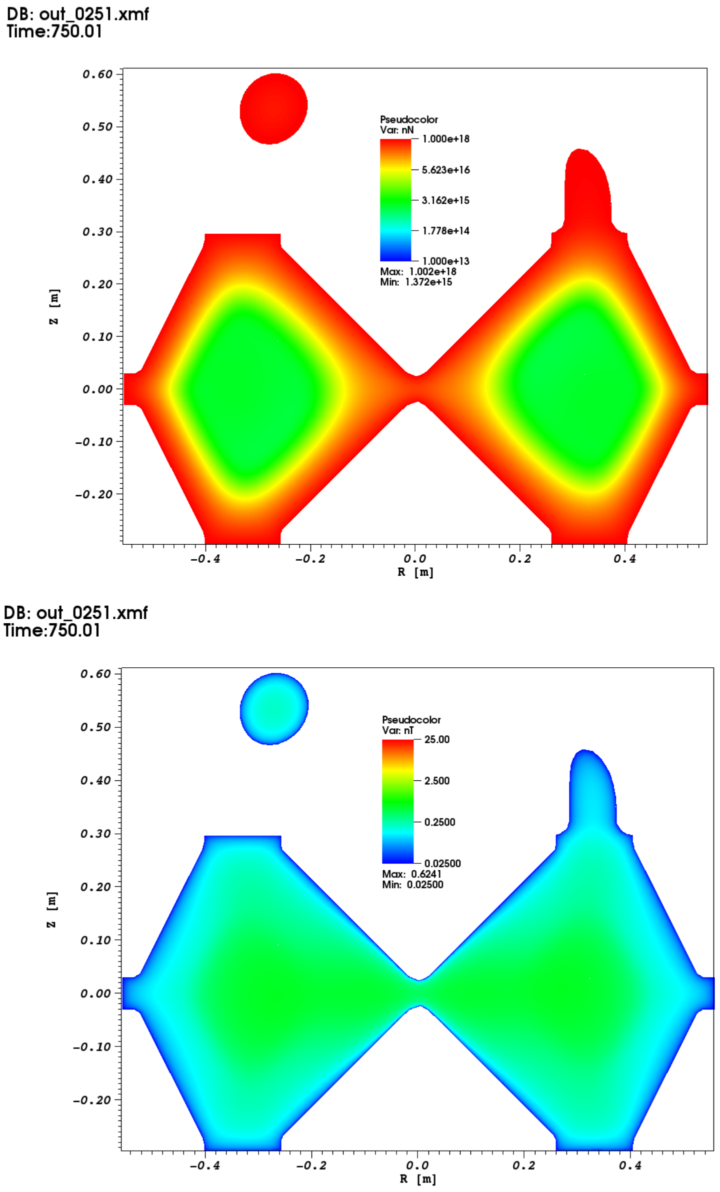

Figure 4.22: A poloidal cross-section plot of the neutral density (**Top**) and temperature (**Bottom**) at $t \approx 750\,\mu$s in the simulation. **Top**: Note the much higher minimum neutral densities observed at the end of decay $n_n \approx 1 \times 10^{15}$ m^{-3}. **Bottom**: Note the the maximum neutral temperature observed at this time point $T_n \approx 0.6$ eV, which is much cooler than at earlier times in the simulation.

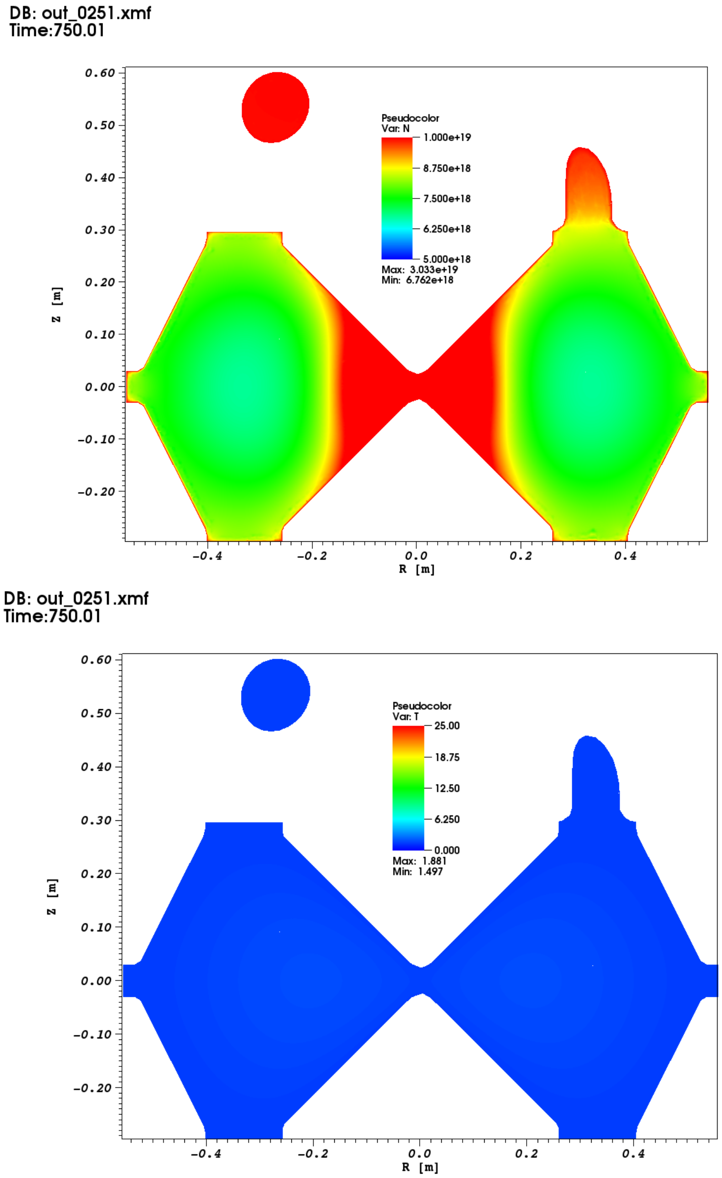

Figure 4.23: A poloidal cross-section plot of the plasma density (**Top**) and temperature (**Bottom**) at $t \approx 750\,\mu$s in the simulation. **Top**: Note the boundary condition dominated plasma density profile that is locally higher near the geometric axis. **Bottom**: Note the largely uniform, cool plasma temperature across the simulation domain when compared to early times in the simulation.

Fig. 4.1 is time shifted such that the end of the experimental data period aligns with the end of the simulation spheromak decay period. This provides a basis for comparison between the simulation and experimental discharges which otherwise have significantly different decay times t_{decay}. The result of this shift in time base of the experimental toroidal current trace for this simulation is shown in Fig. 4.24, which shows very good agreement in the key period of interest for validation purposes, but significant differences for the remainder of the simulation time period. The results from this simulation are summarized as follows. First, the simulation results consistently underpredict the neutral temperature when compared to TALIF measurements, as seen in Fig. 4.25. Additionally, the simulation does not capture the measured non-monotonic neutral temperature temporal profile. A comparison of the temporal evolution of the neutral density in shown in Fig. 4.26. Since temporal evolution measurements were all made at a depth $d = 11$ cm, it is clear that the simulation overpredicts the value of the neutral density at this TALIF measurement location when compared to experimental data. For spatial profile comparisons, Fig. 4.27 provides a similar result as for temporal evolution shown in Fig. 4.25 such that the simulation tends to underpredict the neutral temperature at the TALIF measurement locations $d = 11$ cm and 18 cm at the $t = 2.16$ ms equivalent time point in the simulation. Lastly, Fig. 4.28 shows both an overprediction of the neutral density at the shallower measurement depth $d = 11$ cm and a underprediction of the neutral depth at a measurement depth $d = 18$ cm. In short, the simulation predicts a much steeper neutral density gradient than observed from TALIF measurements.

The set of Figs. 4.29 – 4.33 show results from another simulation that uses the same simulation parameters presented in Tab. 4.1 except that the neutral density boundary condition is set lower to $n_n = 1 \times 10^{17}$ m^{-3}. Even with this change of neutral density at the boundary, the simulated and time base shifted experimental toroidal current traces still show good agreement, as seen in Fig. 4.29. Overall, this simulation follows the same trend as the previously discussed simulation with an underprediction of the neutral temperature when compared to experimental measurements, shown in Figs. 4.30 and 4.32. However, agreement

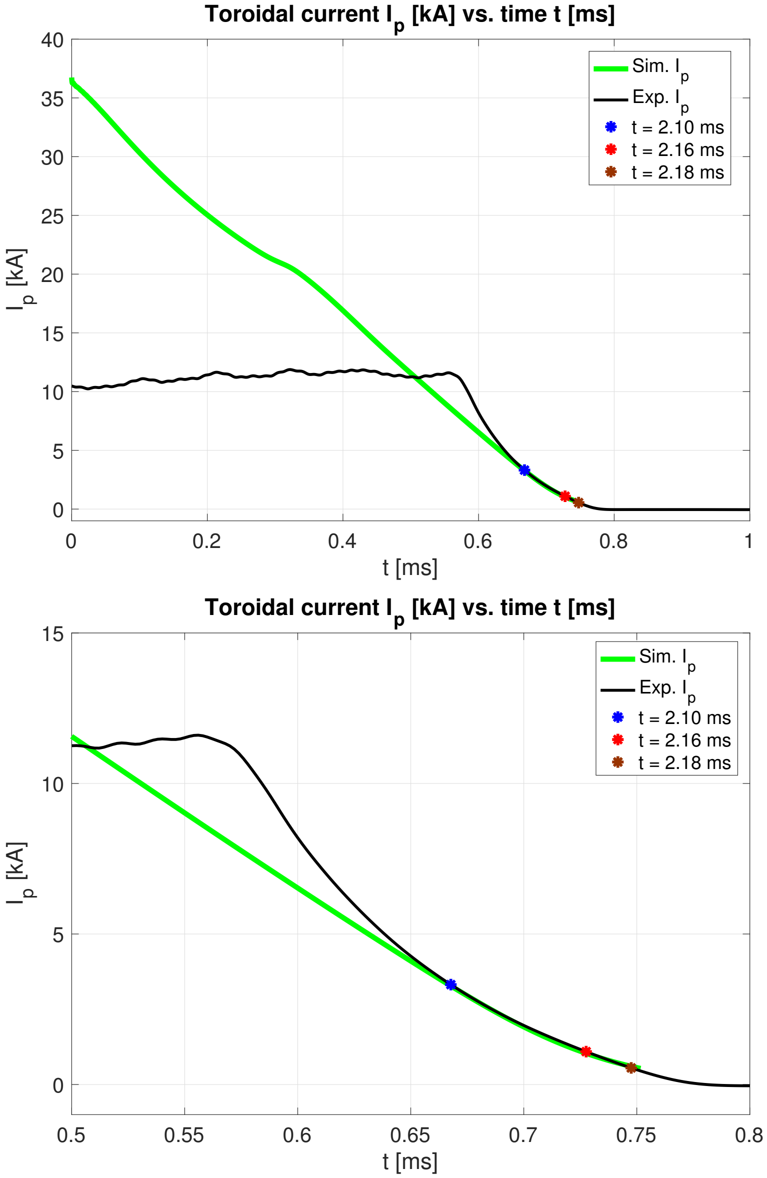

Figure 4.24: A comparison of the simulation and time base shifted experimental toroidal plasma current traces, with TALIF measurement times indicated at t = 2.10, 2.16, and 2.18 ms. **Top**: Note the significant difference between the simulation experimental toroidal plasma current over the majority of the simulation period, except towards the end of spheromak decay. **Bottom**: The toroidal current trace centered on the spheromak decay period. Note the good agreement observed between the simulation and experimental toroidal currents during the TALIF measurement times.

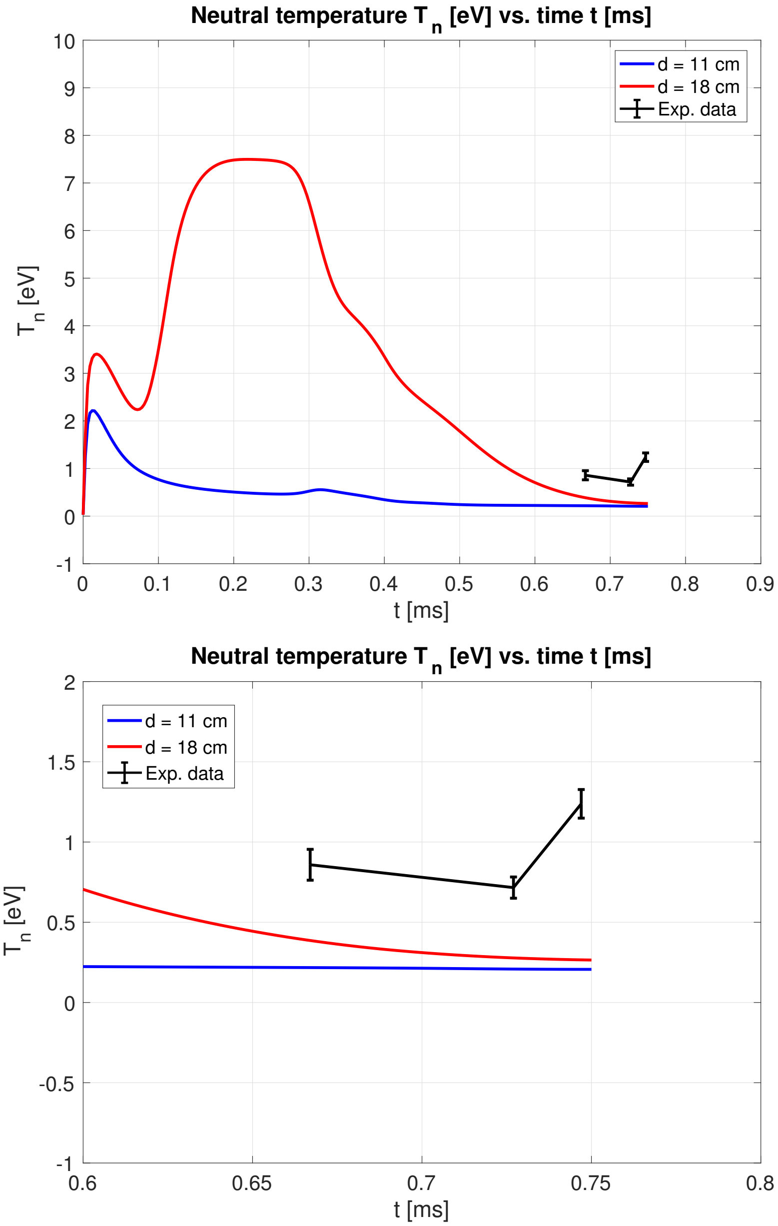

Figure 4.25: A comparison between the temporal evolution of the simulated neutral temperature and experimental TALIF measurements at $d = 11$ cm. **Top**: The simulated neutral temperature at depths of $d = 11$ and 18 cm over the spheromak decay period. Note the much warmer neutral temperatures observed closer to the spheromak core than at the shallower depth. **Bottom**: Note the underprediction of the neutral temperature by the simulation at all measurement time points at the end of spheromak decay.

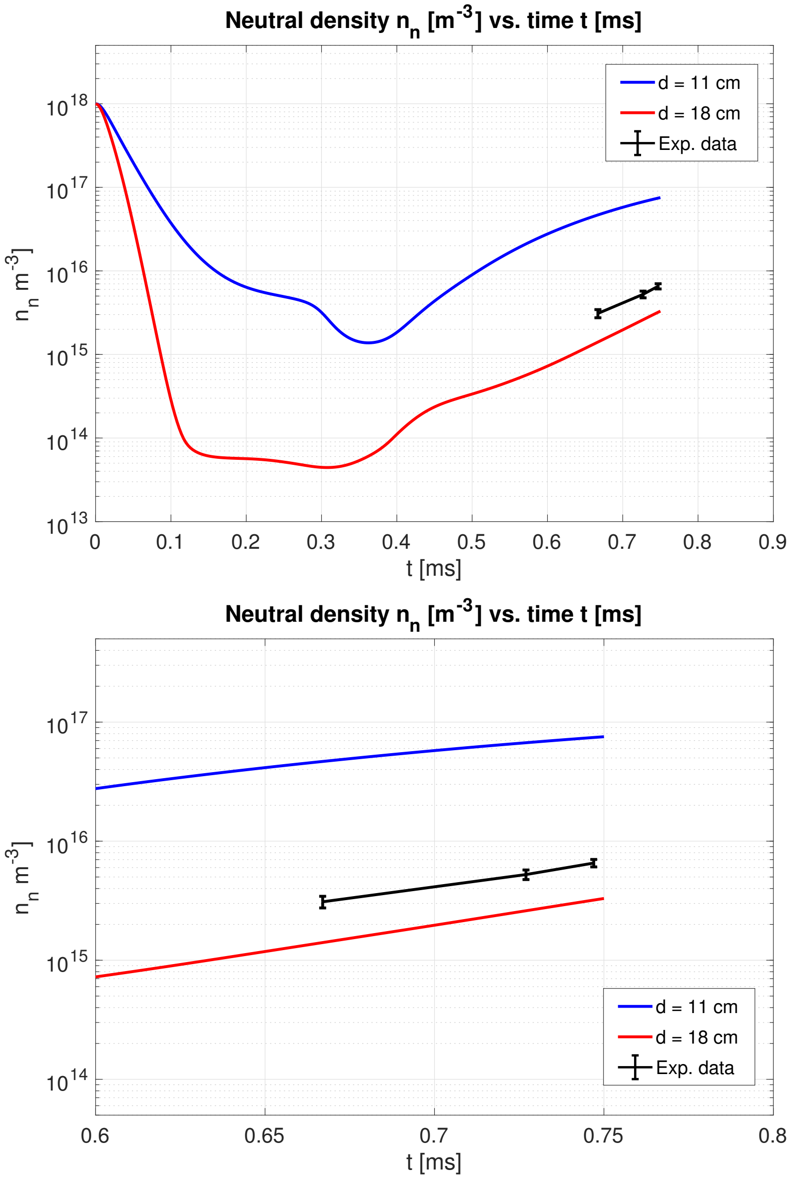

Figure 4.26: A comparison between the temporal evolution of the simulated neutral density and experimental TALIF measurements at $d = 11$ cm. **Top**: The simulated neutral density at depths of $d = 11$ and 18 cm over the spheromak decay period. Note the much lower neutral density observed closer to the spheromak core than at the shallower depth. **Bottom**: Note the overprediction of the neutral density by the simulation at all measurement time points at a depth $d = 11$ cm at the end of spheromak decay.

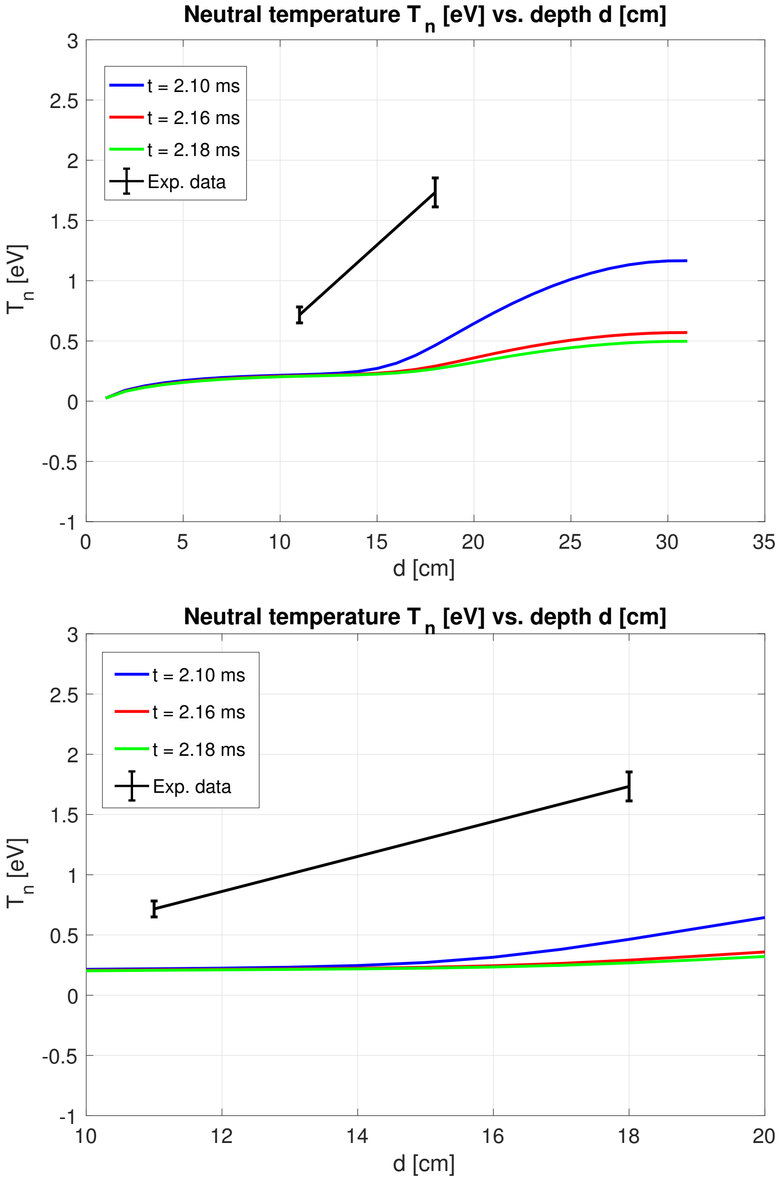

Figure 4.27: A comparison between the simulated neutral temperature spatial profile and experimental TALIF measurements at $t = 2.16$ ms. **Top**: The simulated neutral temperature at equivalent time points $t = 2.10$, 2.16 and 2.18 ms. **Bottom**: Note the underprediction of the simulated neutral temperature at both TALIF measurement depths $d = 11$ and 18 cm.

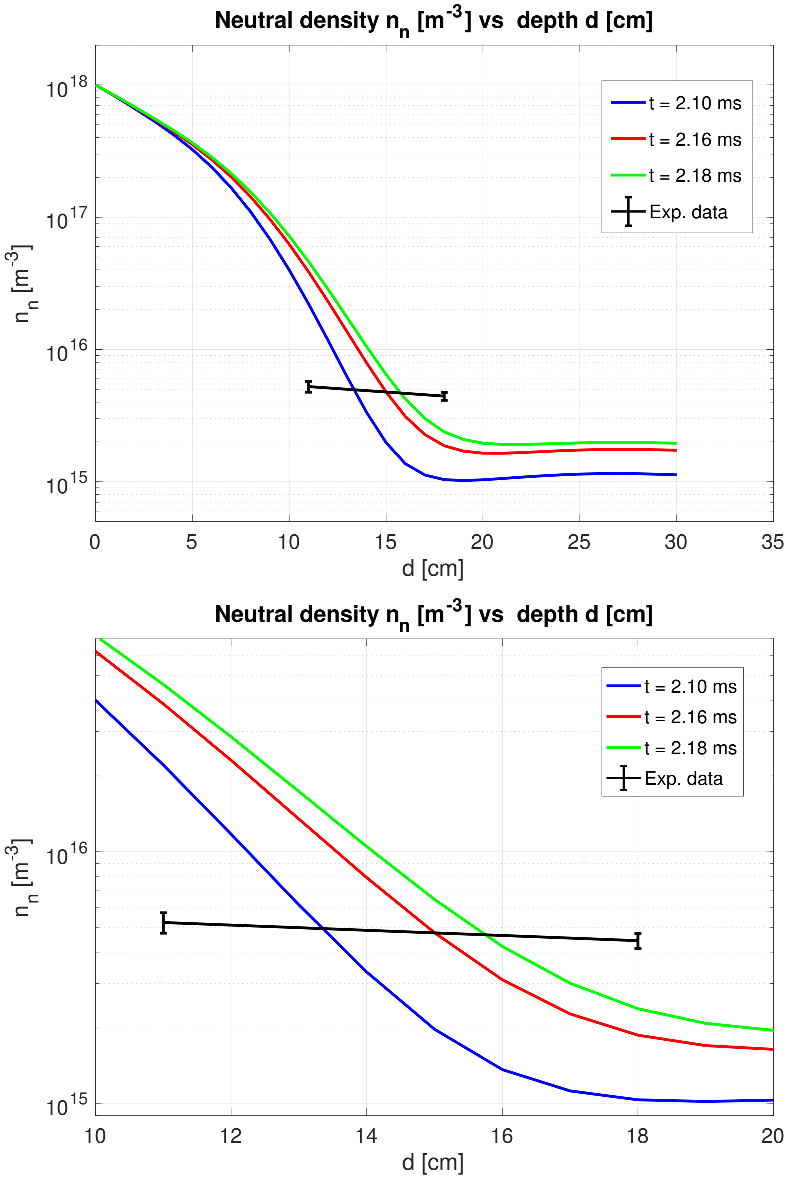

Figure 4.28: A comparison between the simulated neutral density spatial profile and experimental TALIF measurements at $t = 2.16$ ms. **Top**: The simulated neutral temperature at equivalent time points $t = 2.10$, 2.16 and 2.18 ms compared to experimental measurements. **Bottom**: Note the significantly steeper neutral density gradient observed in the simulation when compared to the experimental profile. The simulation tends to overpredict the neutral density at $d = 11$ cm, whereas it underpredicts the neutral density at $d = 18$ cm.

between simulated neutral density and experimental measurements is improved from this reduction of neutral density at the boundary. As seen in Fig. 4.31, the temporal evolution of the simulated neutral density agrees quite well with experimental measurements at all relevant time points at a measurement depth $d = 11$ cm, though there is still a slight overprediction of the neutral density when compared to experimental data. When considering neutral density spatial profiles, Fig. 4.33 similarly exhibits improved agreement with the experimental measurement at a depth $d = 11$ cm at $t = 2.16$ ms. However, a similar underprediction of the neutral density by the simulation is observed at a measurement depth $d = 18$ cm when compared to experimental data.

Two additional simulations were performed that use the same neutral density boundary conditions $n_n = 1 \times 10^{18}$ m^{-3} and $n_n = 1 \times 10^{17}$ m^{-3} as previously discussed simulations, but applied a lower plasma temperature boundary condition $T = 0.75$ eV instead of $T = 1.5$ eV. This modification in plasma temperature boundary condition was made in an effort to improve agreement between simulations and experimental data. The results from simulations performed with a neutral density boundary condition $n_n = 1 \times 10^{18}$ m^{-3} are provided in Figs. 4.34 – 4.38, whereas the results with a boundary neutral density $n_n = 1 \times 10^{17}$ m^{-3} are shown in Figs. 4.39 – 4.43. Both of these simulations exhibited good agreement between with experimental toroidal current traces during the TALIF measurement time interval, which is readily seen in Fig. 4.34 and Fig. 4.39, providing a continued basis for comparison between simulation and experimental results. Overall, the reduction in the boundary plasma temperature tends to worsen agreement between simulation and experimental results. As seen in Fig. 4.35 and Fig. 4.37, the lower boundary plasma temperature has led to overall lower neutral temperatures when compared to results shown in Figs. 4.25, 4.27, 4.30, and 4.32. Thus, this modification to the plasma temperature boundary condition has worsened the underprediction of the neutral temperature when compared to experimental measurements. For neutral density comparisons, a similar trend is observed in Fig. 4.38 such that simulations overpredict the neutral density at a depth $d = 11$ cm and underpredict the neutral density at a depth $d = 18$ cm, much like previously presented results. But, when using a

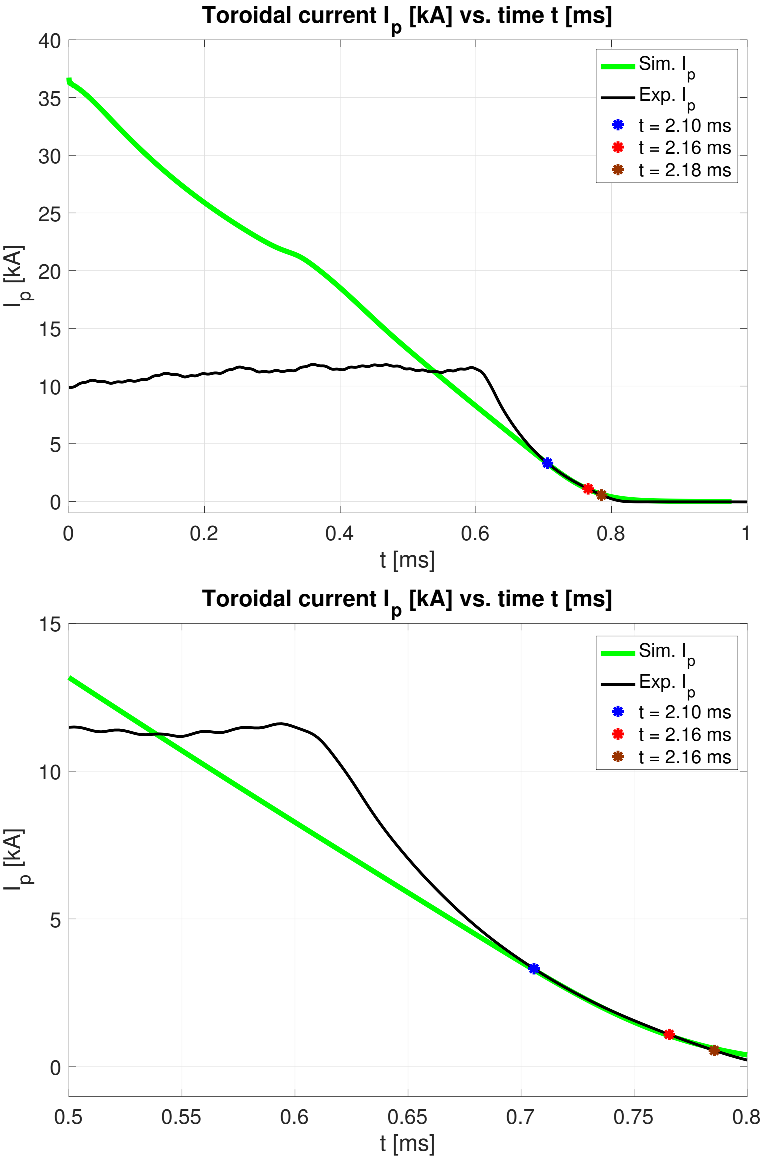

Figure 4.29: A comparison of the simulation and time base shifted experimental toroidal plasma current traces, with TALIF measurement times indicated at t = 2.10, 2.16, and 2.18 ms. Note the good agreement observed between the simulation and experimental toroidal currents during the TALIF measurement times, similarly to the simulation results shown in Fig. 4.24.

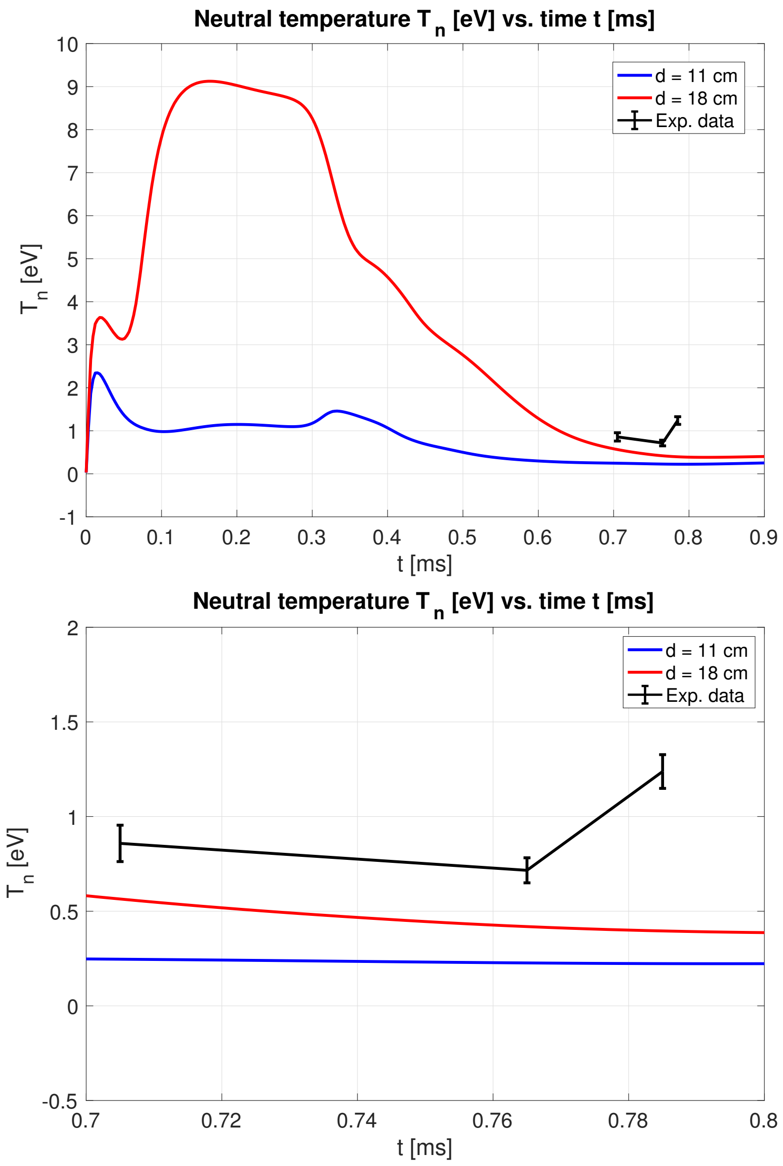

Figure 4.30: A comparison between the temporal evolution of the simulated neutral temperature and experimental TALIF measurements at $d = 11$ cm. **Top**: The simulated neutral temperature at depths of $d = 11$ and 18 cm over the spheromak decay period. Note the higher maximum neutral temperatures observed when compared to Fig. 4.25 due to CX reactions with an overall higher temperature spheromak plasma. **Bottom**: Note the continued underprediction of the neutral temperature by the simulation at all measurement time points at the end of spheromak decay.

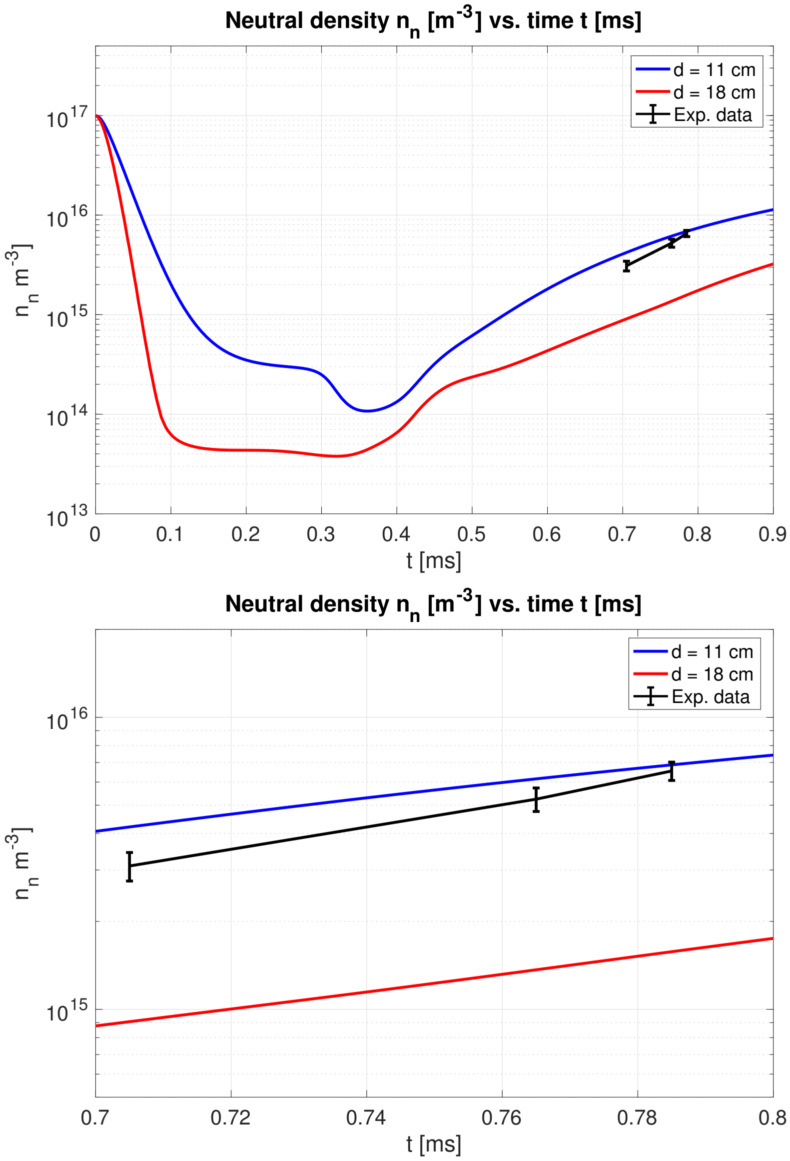

Figure 4.31: A comparison between the temporal evolution of the simulated neutral density and experimental TALIF measurements at $d = 11$ cm. **Top**: The simulated neutral density at depths of $d = 11$ and 18 cm over the spheromak decay period. **Bottom**: Note the improved agreement between simulation and experimental data at the TALIF measurement depth $d = 11$ cm, albeit the simulation slightly overpredicts the neutral density at all TALIF measurement times.

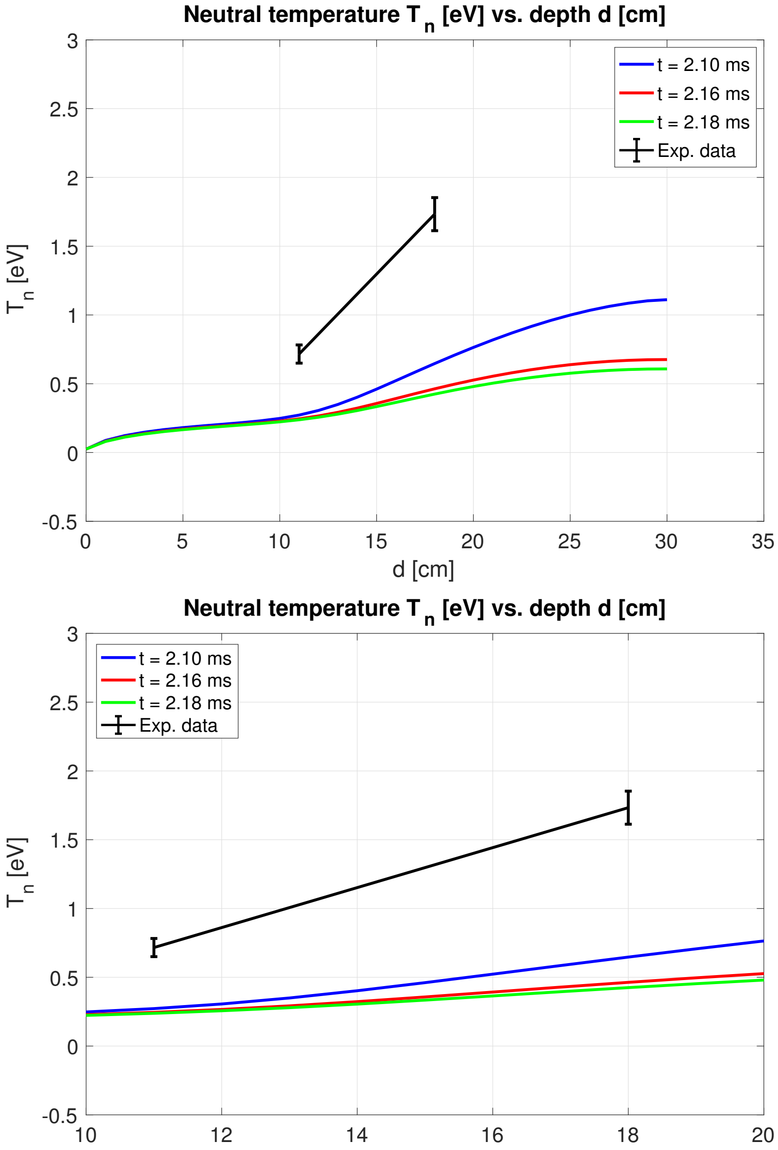

Figure 4.32: A comparison between the simulated neutral temperature spatial profile and experimental TALIF measurements at $t = 2.16$ ms. **Top**: The simulated neutral temperature at equivalent time points $t = 2.10$, 2.16 and 2.18 ms compared to experimental data. **Bottom**: Note the underprediction of the simulated neutral temperature at both TALIF measurement depths $d = 11$ and $d = 18$ cm.

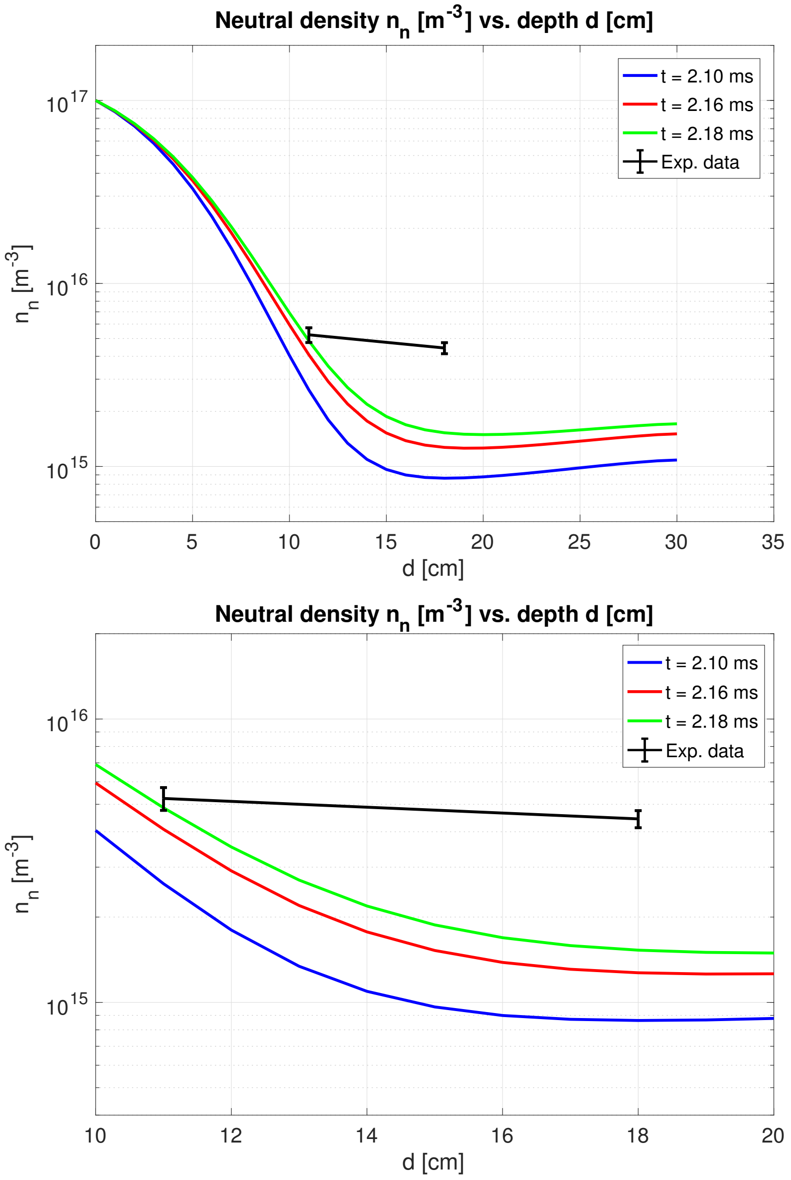

Figure 4.33: A comparison between the simulated neutral density spatial profile and experimental TALIF measurements at $t = 2.16$ ms. **Top**: The simulated neutral temperature at equivalent time points $t = 2.10$, 2.16 and 2.18 ms compared to experimental measurements. **Bottom**: Note the improved agreement between simulation and experimental data at the shallower measurement depth $d = 11$ cm, but a continued underprediction of the neutral density at a measurement depth $d = 18$ cm when compared to experimental measurements.

boundary neutral density $n_n = 1 \times 10^{17}$ m^{-3}, Fig. 4.43 shows the best agreement between experimental data and simulation occurring at a depth $d = 18$ cm, whereas the best agreement for an higher plasma temperature boundary condition $T = 1.5$ eV was observed at $d = 11$ cm in Fig. 4.33. Instead, this simulation tends to overpredict the neutral density at the shallower measurement depth $d = 11$ cm when compared to experimental data, which leads the worsened temporal agreement observed in Fig. 4.41.

Results from two additional simulations are provided in Figs. 4.44 – 4.53. The first simulation uses the simulation parameters listed in Tab. 4.2. The most significant change of chosen boundary conditions from previous results is a much higher neutral temperature boundary condition is assumed to determine whether it leads to improved agreement with experimental measurements. In Fig. 4.44, good agreement is observed between the simulation and experimental toroidal current traces during the time interval in which TALIF measurements were made, which is similar to previously presented results. This simulation exhibits improved agreement between the simulated neutral temperature and experimental measurements, as seen in Fig. 4.45 and 4.47 when compared to previously presented results. However, the simulation still exhibits an underprediction of the neutral temperature when compared to experimental measurements. However, this improved agreement in neutral temperatures appears to have come at the expense of worsened agreement in neutral densities. It is clear in Fig. 4.46 that the increase in neutral temperature boundary value has led to a substantial overprediction of the neutral density at the TALIF measurement depth $d = 11$ cm. This disagreement can be attributed to a greater penetration of neutrals into the core spheromak confinement region, as seen in Fig. 4.48. At both of the TALIF measurement locations at $t = 2.16$ ms, the simulation overpredicts the neutral density, though agreement is better at a depth $d = 18$ cm.

The next simulation presented makes use of the same choice of boundary conditions listed in Tab. 4.2 except that the boundary neutral density $n_n = 1 \times 10^{17}$ m^{-3}. Similar good agreement between the simulation and experimental toroidal current traces during the TALIF measurement time interval is observed, as seen in Fig. 4.49. Similarly to the previous

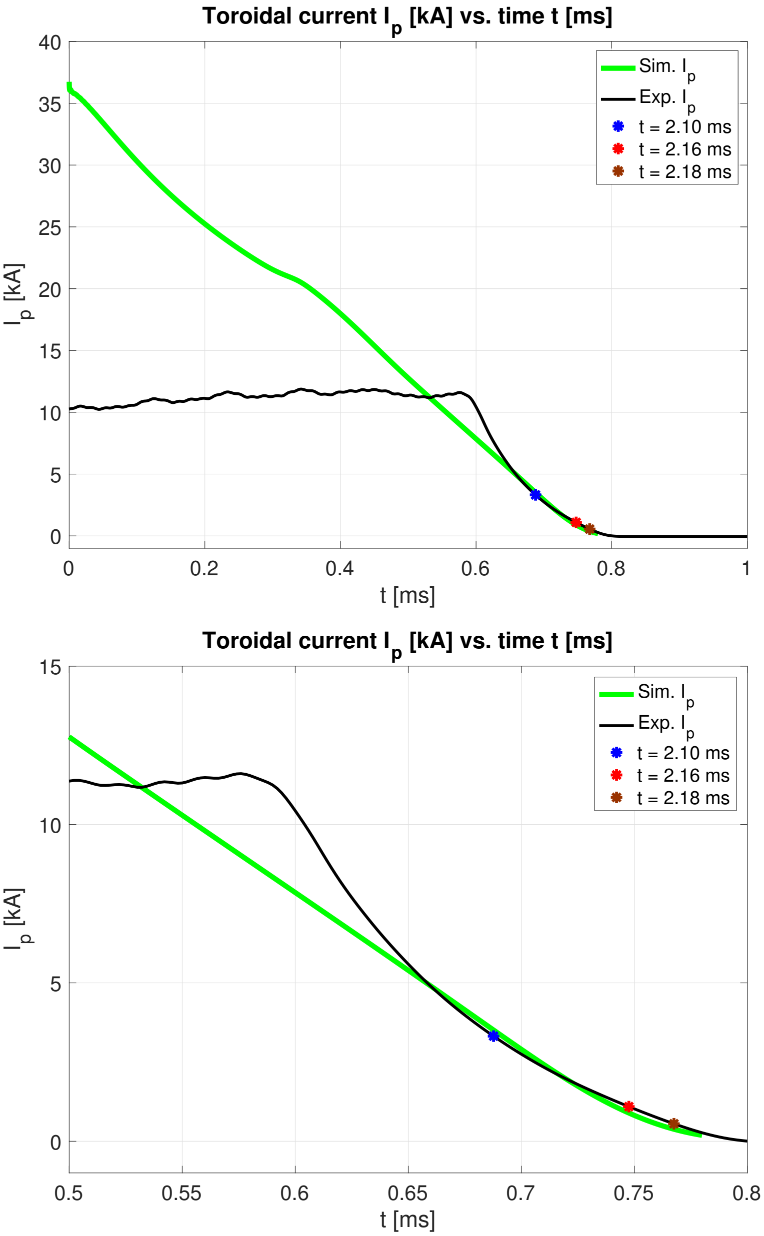

Figure 4.34: A comparison of the simulation and time base shifted experimental toroidal plasma current traces, with TALIF measurement times indicated at t = 2.10, 2.16, and 2.18 ms. Note the good agreement observed between the simulation and experimental toroidal currents during the TALIF measurement times, similarly to the simulation results shown in Fig. 4.24 and Fig. 4.29.

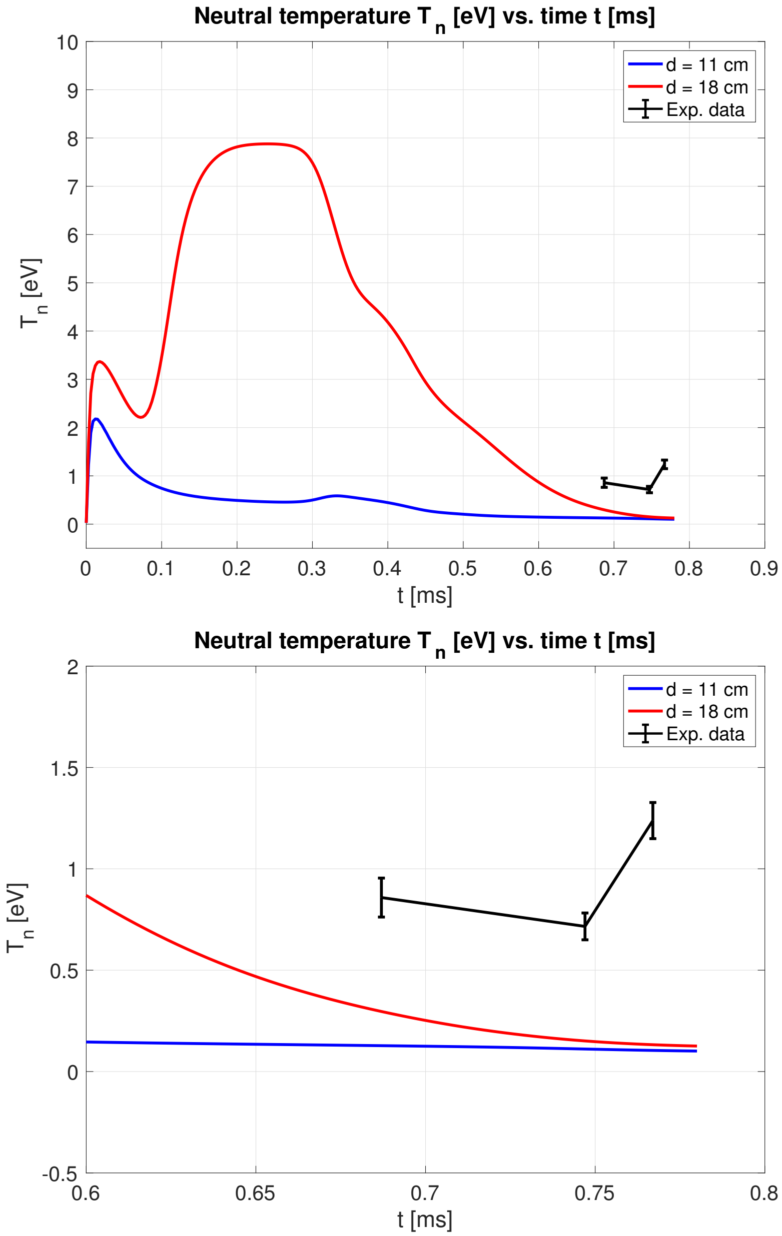

Figure 4.35: A comparison between the temporal evolution of the simulated neutral temperature and and experimental TALIF measurements at $d = 11$ cm. **Top**: The simulated neutral temperature at depths of $d = 11$ and 18 cm over the spheromak decay period. **Bottom**: Note the worsened underprediction of the neutral temperature by the simulation at all measurement time points at the end of spheromak decay due to a decreased boundary plasma temperature.

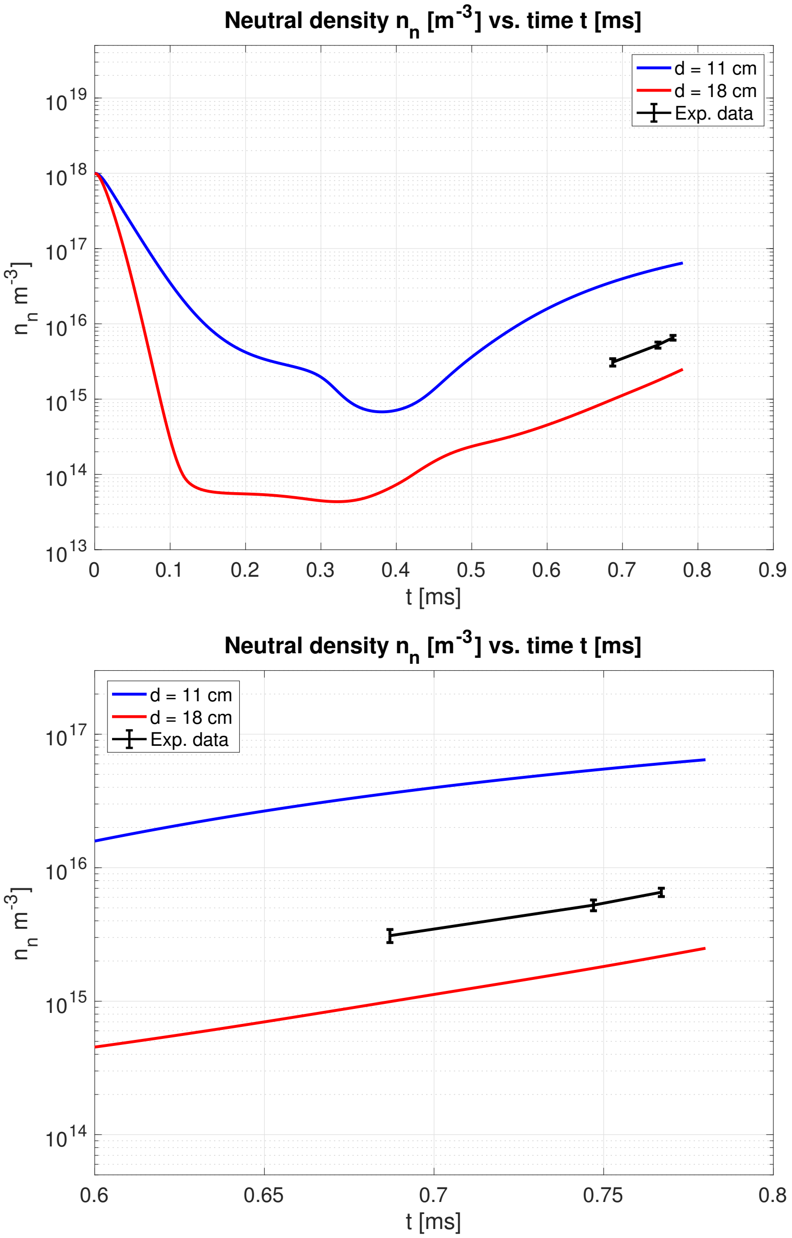

Figure 4.36: A comparison between the simulated neutral density temporal evolution and experimental TALIF measurements at $d = 11$ cm. **Top**: The simulated neutral density at depths of $d = 11$ and 18 cm over the duration simulation spheromak decay. **Bottom**: Note the overprediction of the neutral density at $d = 11$ cm when compared to experimental measurements, similarly to Fig. 4.26.

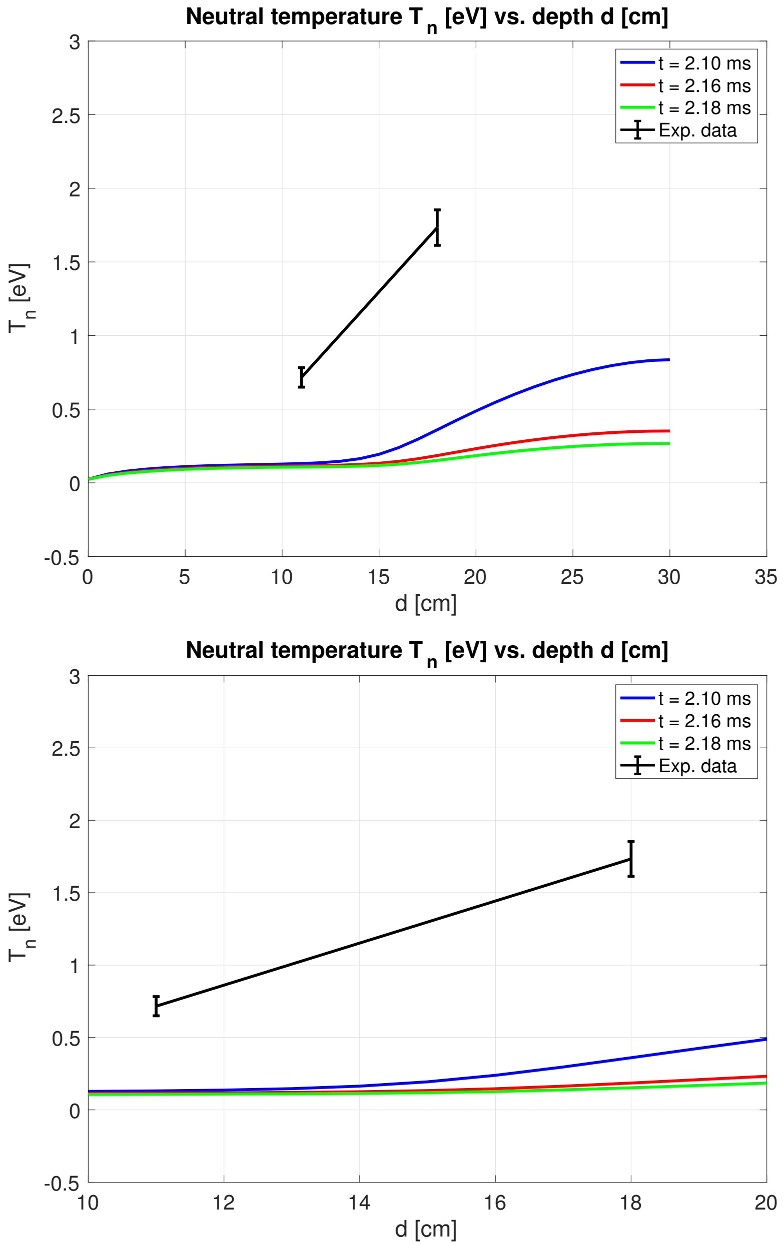

Figure 4.37: A comparison between the simulated neutral temperature spatial profile and experimental TALIF measurements at $t = 2.16$ ms. **Top**: The simulated neutral temperature at equivalent time points $t = 2.10$, 2.16 and 2.18 ms. **Bottom**: Note the worsened underprediction of the simulated neutral temperature at both TALIF measurement depths $d = 11$ and $d = 18$ cm when compared to Fig. 4.27.

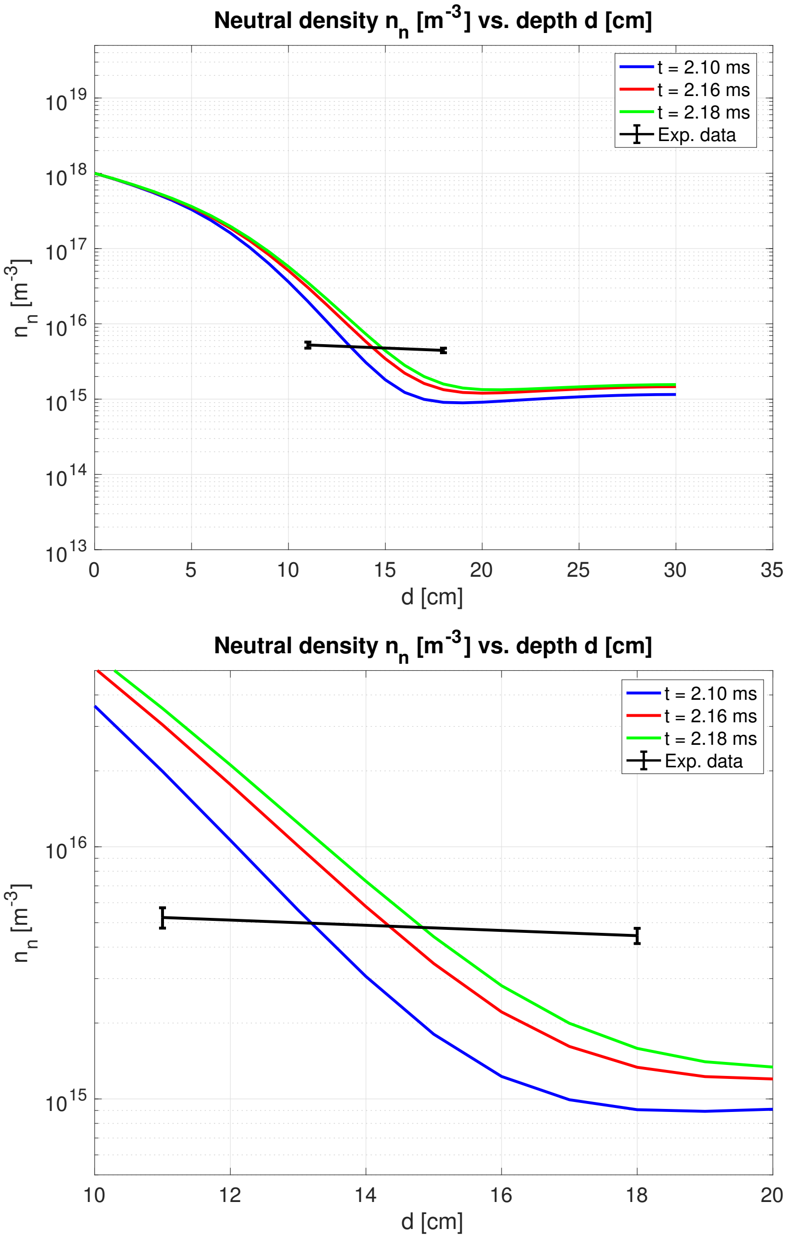

Figure 4.38: A comparison between the simulated neutral density spatial profile and experimental TALIF measurements at $t = 2.16$ ms. **Top**: The simulated neutral temperature at equivalent time points $t = 2.10$, 2.16 and 2.18 ms compared to experimental measurements. **Bottom**: Note the significantly steeper neutral density gradient observed in the simulation when compared to the experimental profile, much like Fig. 4.28. The simulation tends to overpredict the neutral density at $d = 11$ cm, whereas it underpredicts the neutral density at $d = 18$ cm.

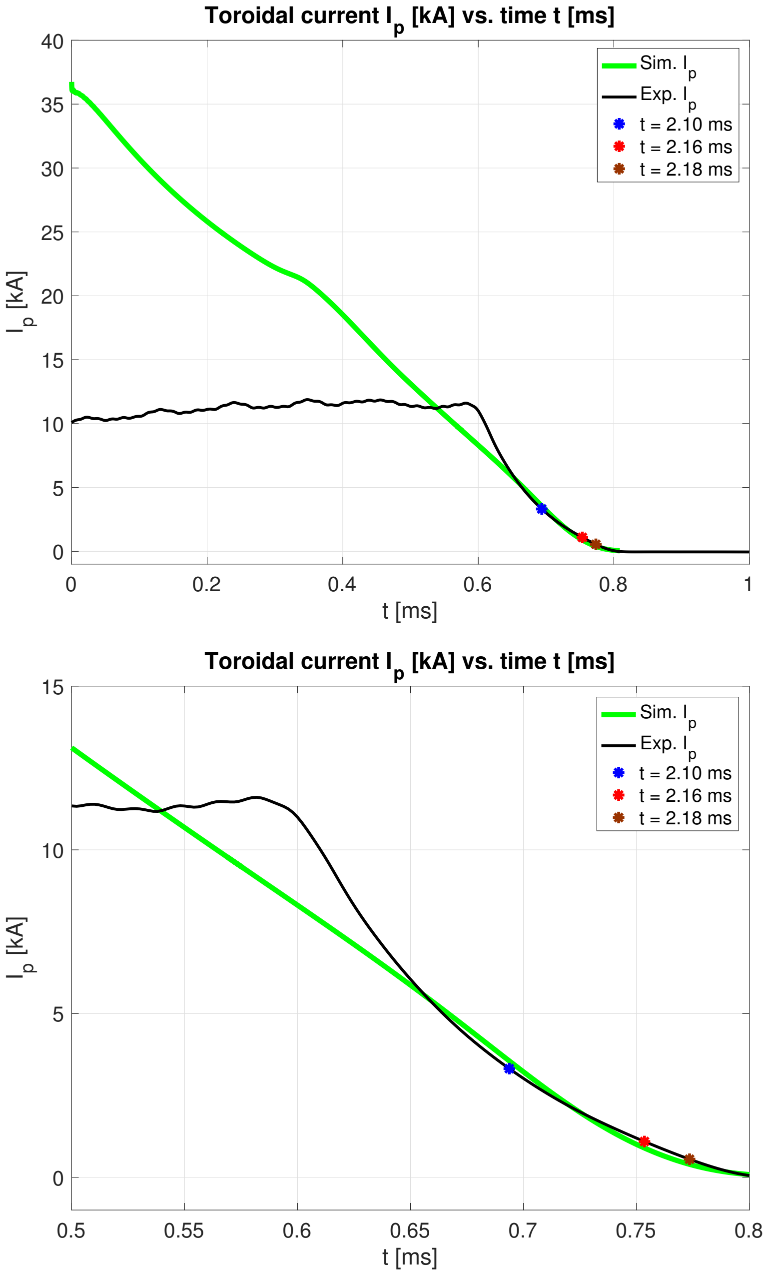

Figure 4.39: A comparison of the simulation and time base shifted experimental toroidal plasma current traces, with TALIF measurement times indicated at t = 2.10, 2.16, and 2.18 ms. Note the good agreement observed between the simulation and experimental toroidal currents during the TALIF measurement times, similarly to the simulation results shown in Fig. 4.24, 4.29, and 4.34.

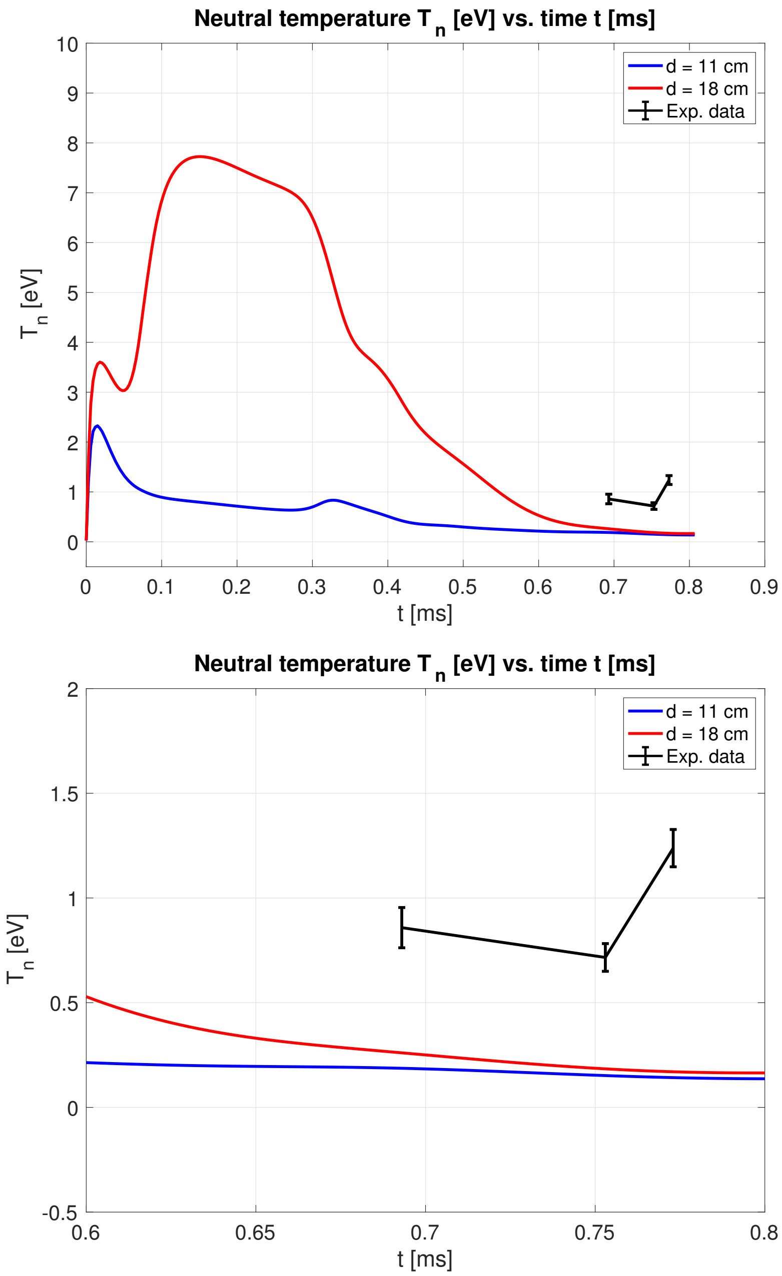

Figure 4.40: A comparison between the temporal evolution of the simulated neutral temperature and experimental TALIF measurements at $d = 11$ cm. **Top**: The simulated neutral temperature at depths of $d = 11$ and 18 cm over spheromak decay period. **Bottom**: Note the worsened underprediction of the neutral temperature by the simulation at all measurement time points at the end of spheromak decay due to the decreased boundary plasma temperature when compared to Fig. 4.30.

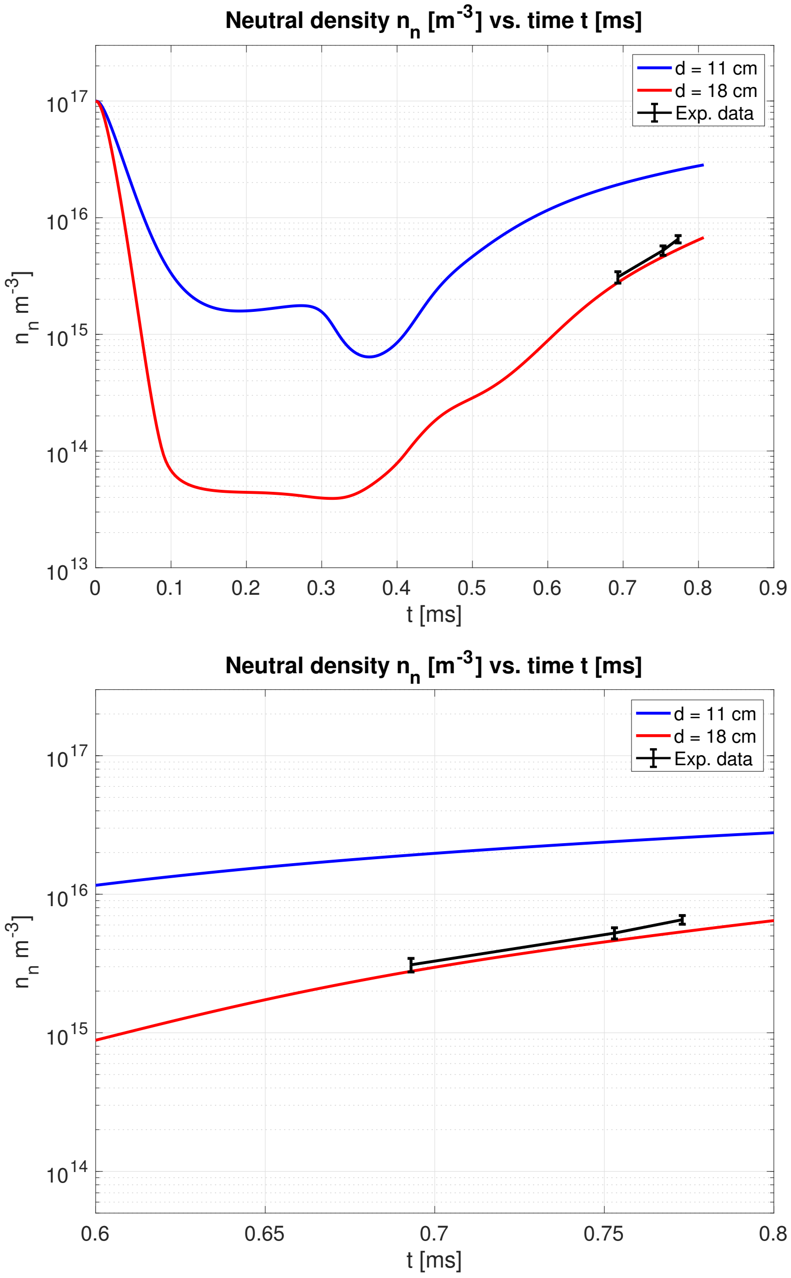

Figure 4.41: A comparison between the temporal evolution of the simulated neutral density and experimental TALIF measurements at $d = 11$ cm. **Top**: The simulated neutral density at depths of $d = 11$ and 18 cm over the spheromak decay period. **Bottom**: Note the consistent overprediction of the neutral density at $d = 11$ cm when compared to experimental measurements, similarly to Fig. 4.31.

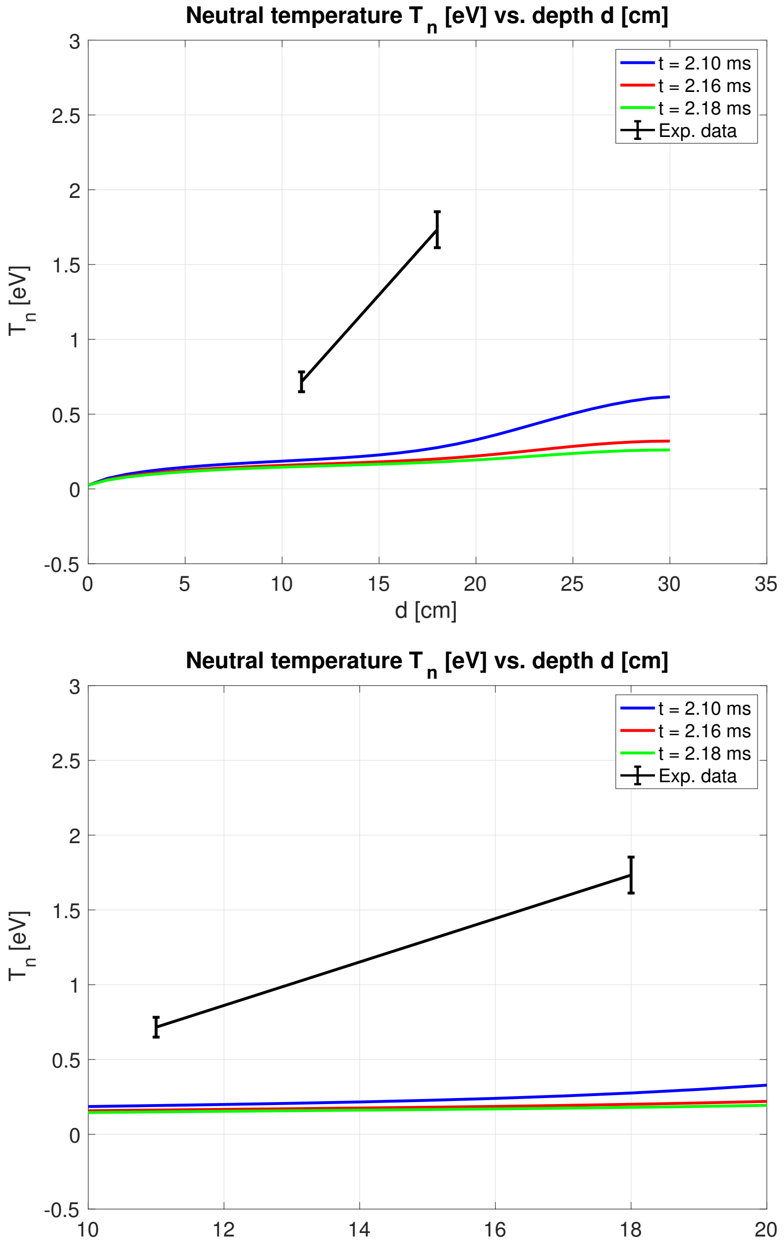

Figure 4.42: A comparison between the simulated neutral temperature spatial profile and experimental TALIF measurements at $t = 2.16$ ms. **Top**: The simulated neutral temperature at equivalent time points $t = 2.10$, 2.16 and 2.18 ms. **Bottom**: Note the worsened underprediction of the simulated neutral temperature at both TALIF measurement depths $d = 11$ and $d = 18$ cm when compared to Fig. 4.27.

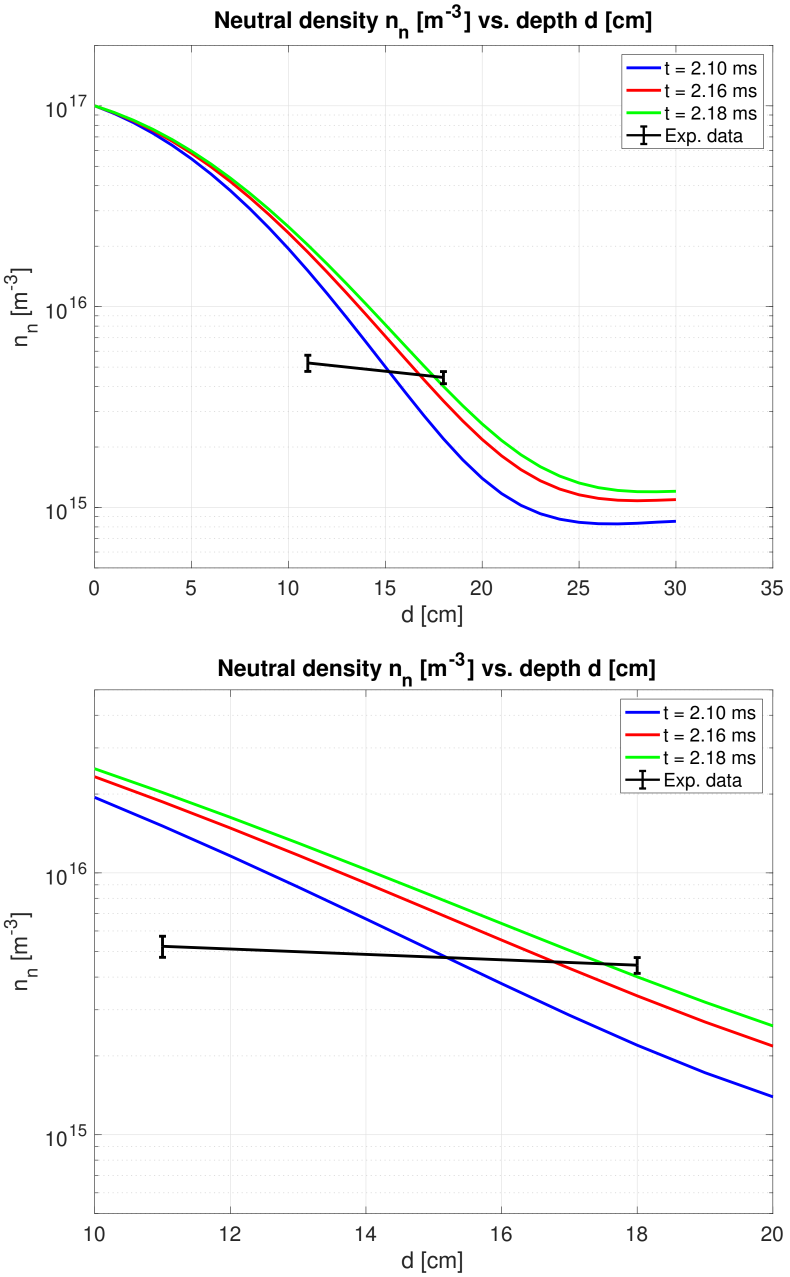

Figure 4.43: A comparison between the simulated neutral density spatial profile and experimental TALIF measurements at $t = 2.16$ ms. **Top**: The simulated neutral temperature at equivalent time points $t = 2.10$, 2.16 and 2.18 ms compared to experimental measurements. **Bottom**: Note the significantly steeper neutral density gradient observed in the simulation when compared to the experimental profile, much like Fig. 4.33. Better agreement is observed at $d = 18$ cm for this simulation whereas it was observed at $d = 11$ cm in Fig. 4.33.

Parameter	Symbol	Value	Units
Plasma density	n	1×10^{19}	m^{-3}
Neutral density	n_n	1×10^{18}	m^{-3}
Plasma temperature	T	1	eV
Neutral temperature	T_n	0.5	eV
Plasma viscosity	ν	400	m^2/s
Neutral viscosity	ν_n	400	m^2/s
Plasma diffusivity	D	1	m^2/s
Neutral diffusivity	D_n	1	m^2/s

Table 4.2: Table of representative simulation parameters for decaying spheromak plasma-neutral simulations with PSI-Tet for comparison with TALIF experimental measurements.

discussed simulation, the improved agreement for both the temporal and spatial neutral temperature profiles is observed in Figs. 4.50 – 4.52, though there the underprediction of the neutral temperature by the simulation is still maintained. Due to the lower neutral density boundary condition, improved agreement is observed between simulation and experimental results, as observed in Figs. 4.51 and 4.53. In particular, fairly good agreement is observed at a measurement depth $d = 11$ cm, but the simulation tends to unpredict the density at a depth $d = 18$ cm as shown in Fig. 4.53.

The last two simulations presented in this section are provided in Figs. 4.54 – 4.58 and Figs. 4.59 – 4.63. These simulations make use of the simulation parameters provided in Tab. 4.3. The parameter being varied in this simulation is that of both the plasma and neutral temperature boundary condition. In these two simulations, the plasma and neutral temperatures are set to be the same value at the boundary, inline with expectations if the majority of edge recycled neutral particles are generated via prompt backscattering instead of

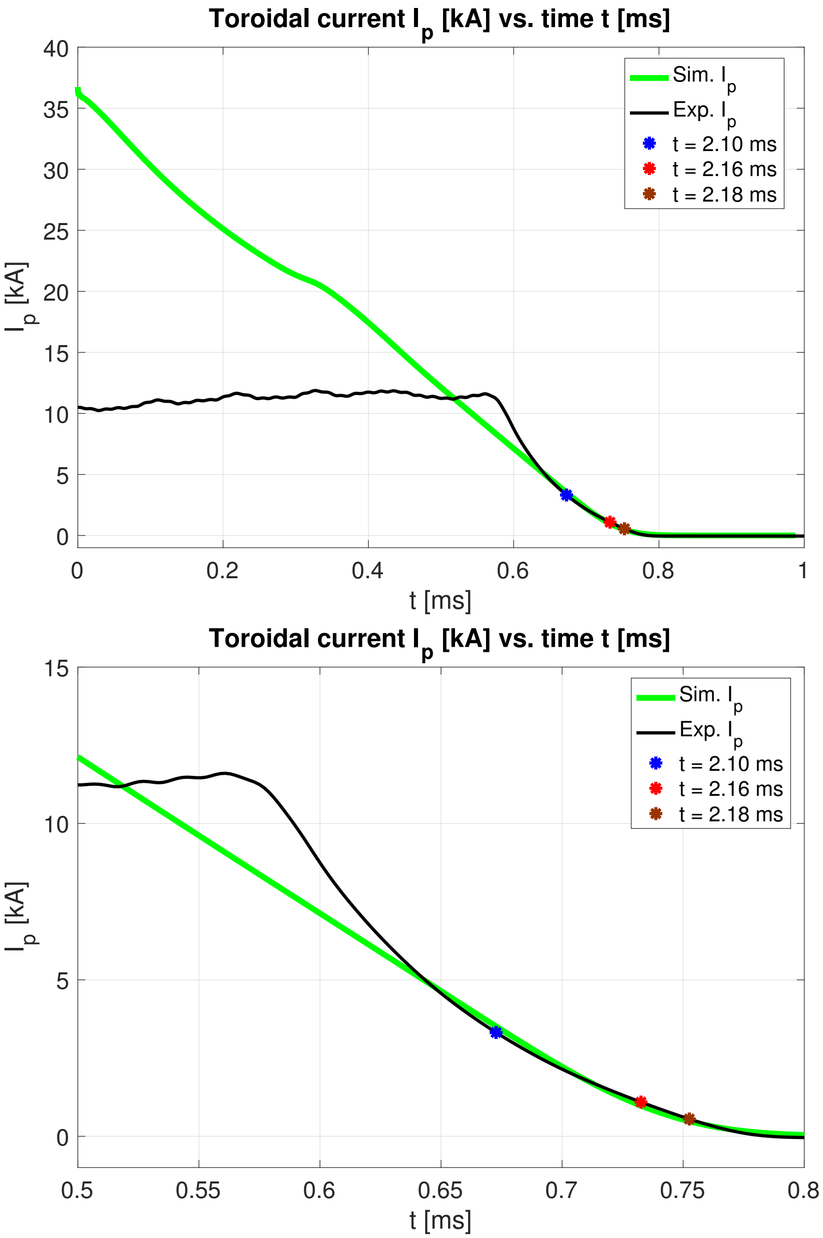

Figure 4.44: A comparison of the simulation and time base shifted experimental toroidal plasma current traces, with TALIF measurement times indicated at t = 2.10, 2.16, and 2.18 ms. Note the good agreement observed between the simulation and experimental toroidal currents during the TALIF measurement times.

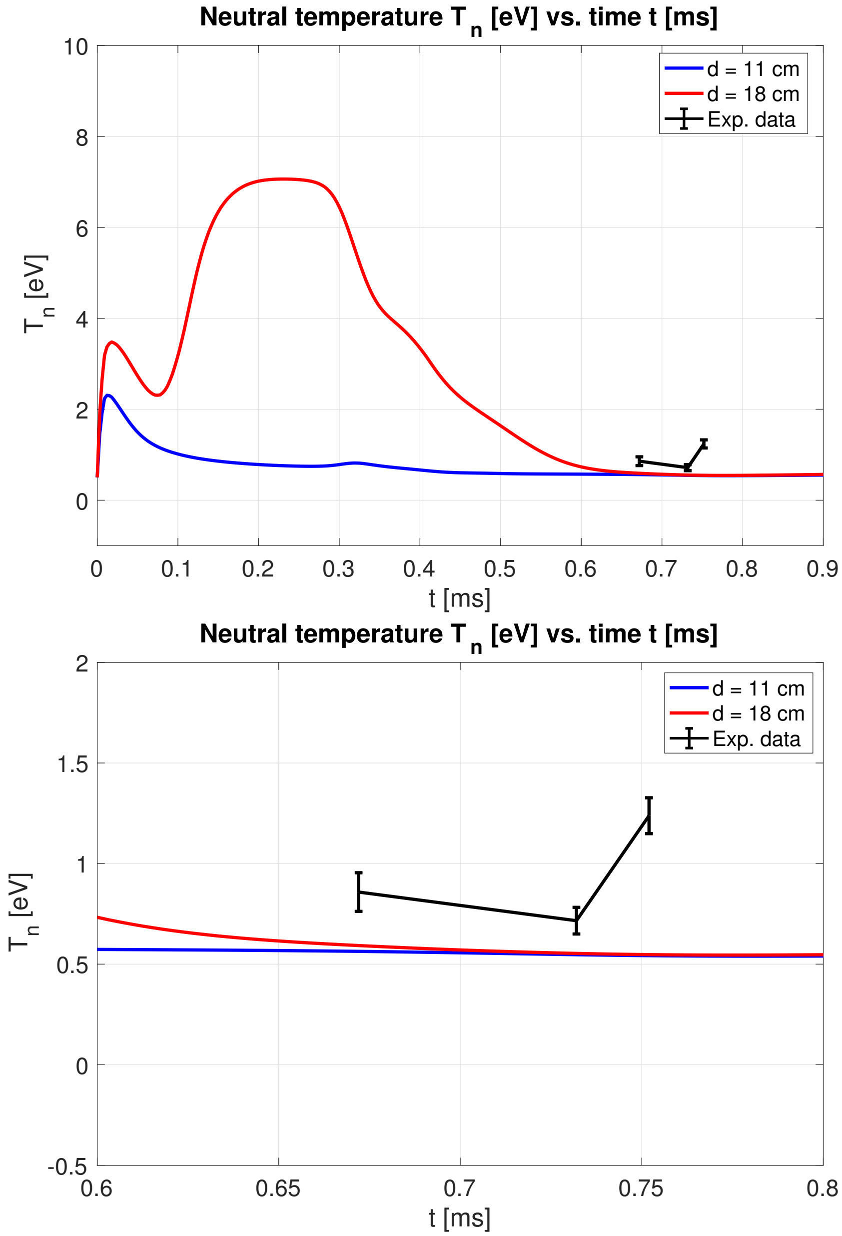

Figure 4.45: A comparison between the temporal evolution of the simulated neutral temperature and experimental TALIF measurements at $d = 11$ cm. **Top**: The simulated neutral temperature at depths of $d = 11$ and 18 cm over spheromak decay period. **Bottom**: Note the improved agreement of the neutral temperature by the simulation at all measurement time points at the end of spheromak decay due to the increased boundary neutral temperature.

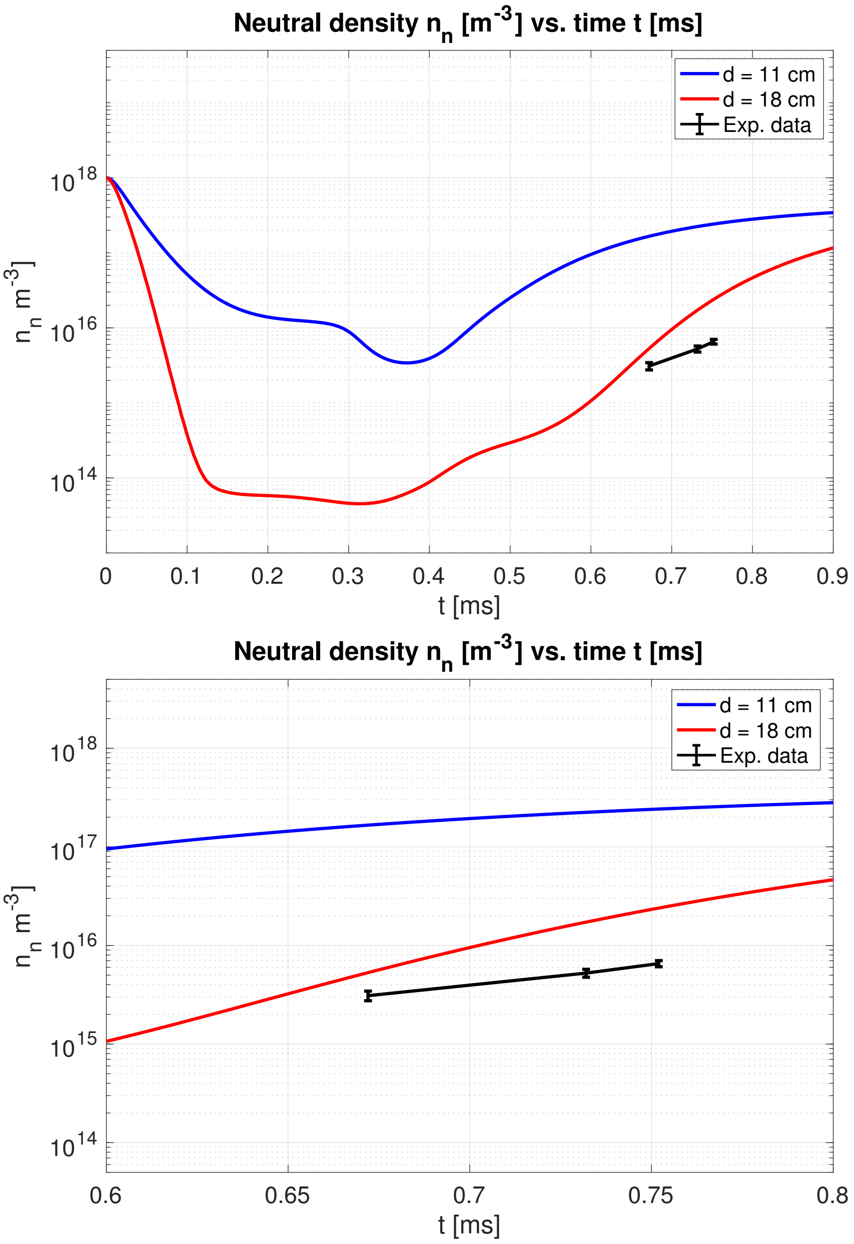

Figure 4.46: A comparison between the temporal evolution of the simulated neutral density and experimental TALIF measurements at $d = 11$ cm. **Top**: The simulated neutral density at depths of $d = 11$ and 18 cm over the spheromak decay period. **Bottom**: Note the severe overprediction of the neutral density at $d = 11$ cm when compared to experimental measurements.

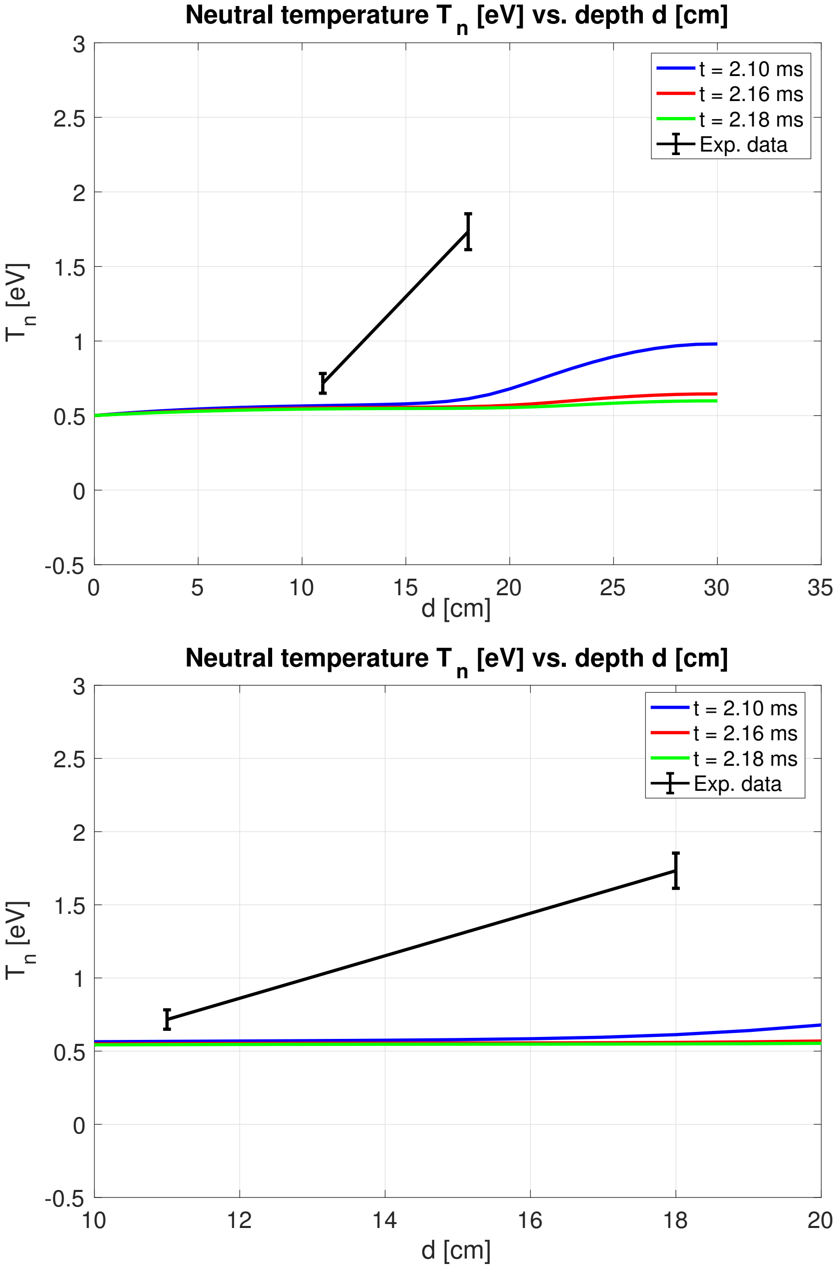

Figure 4.47: A comparison between the simulated neutral temperature spatial profile and experimental TALIF measurements at $t = 2.16$ ms. **Top**: The simulated neutral temperature at equivalent time points $t = 2.10$, 2.16 and 2.18 ms. **Bottom**: Note the improved agreement, albeit maintained underprediction of the simulated neutral temperature at both TALIF measurement depths $d = 11$ and $d = 18$ cm.

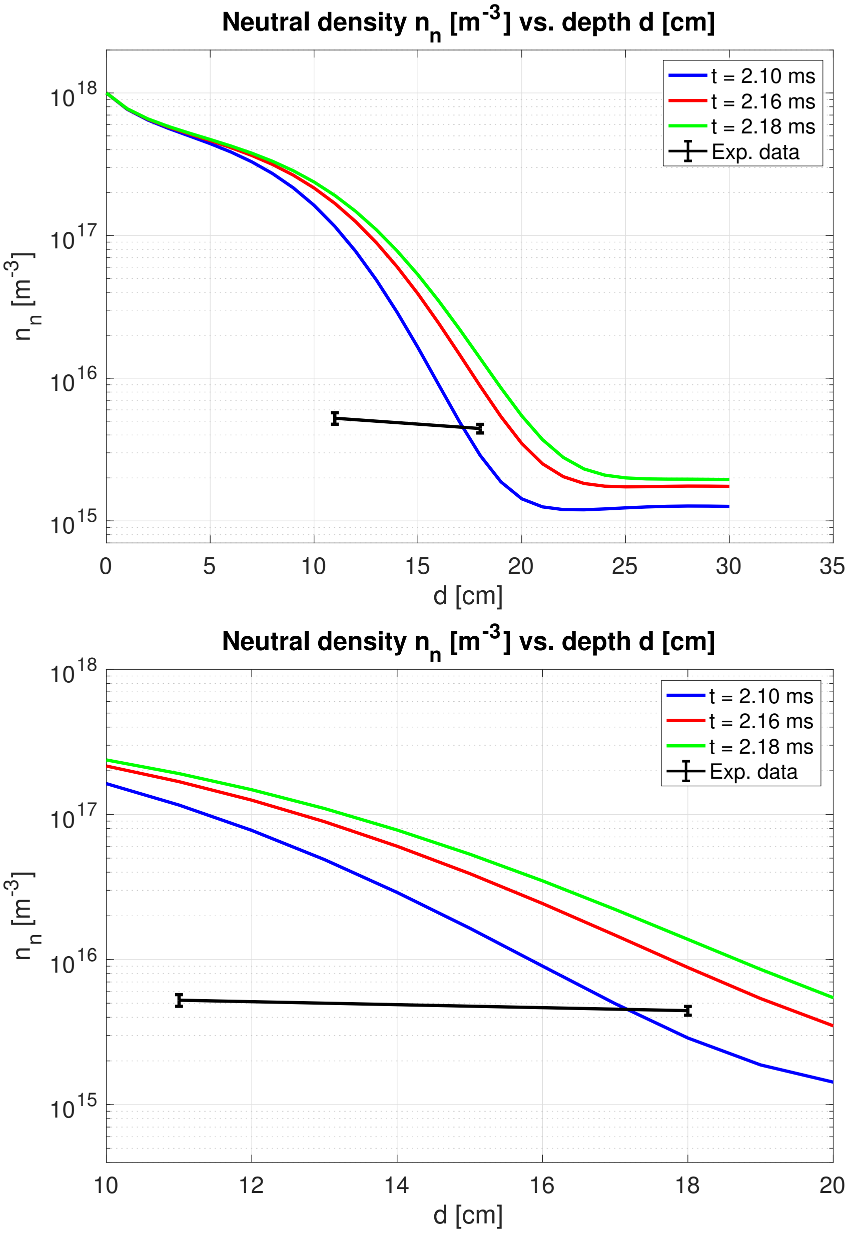

Figure 4.48: A comparison between the simulated neutral density spatial profile and experimental TALIF measurements at $t = 2.16$ ms. **Top**: The simulated neutral temperature at equivalent time points $t = 2.10$, 2.16 and 2.18 ms compared to experimental measurements. **Bottom**: Note the consistent overprediction of the simulated neutral density at both TALIF measurement depths. The overprediction is especially severe at the shallower measurement depth $d = 11$ cm.

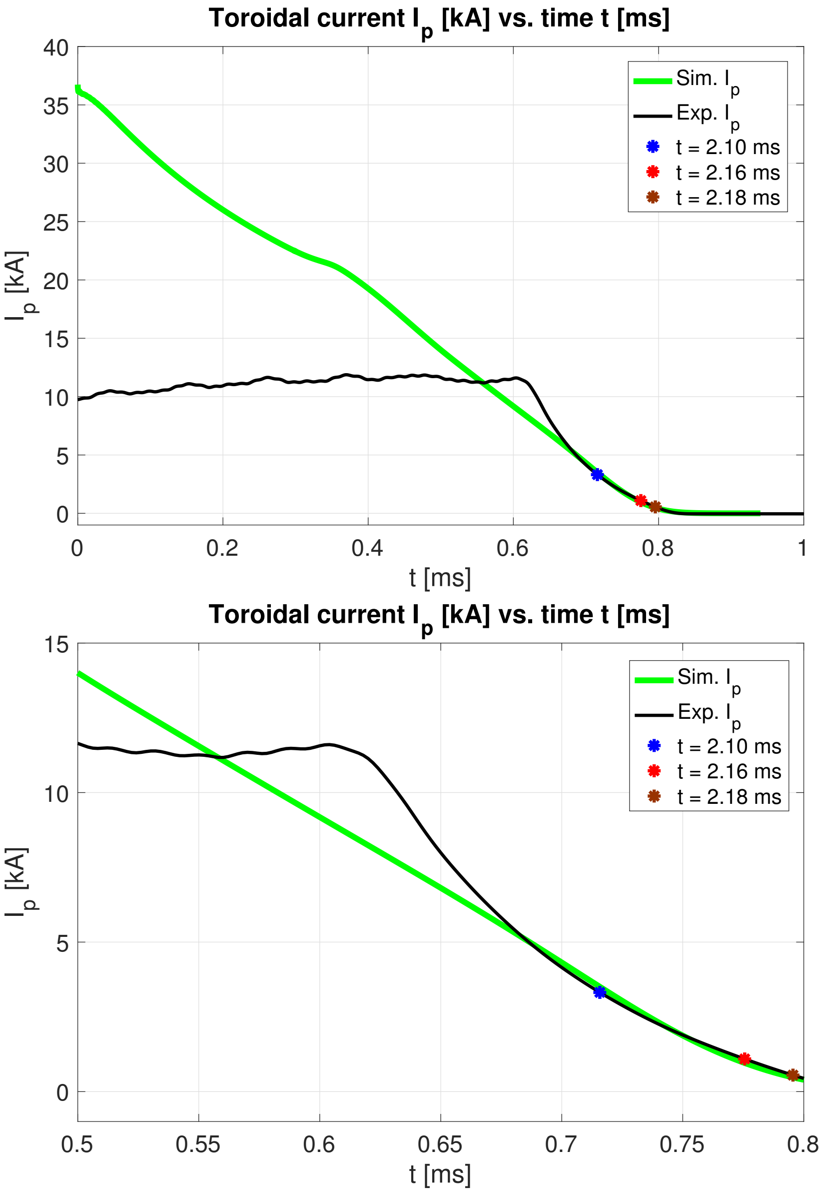

Figure 4.49: A comparison of the simulation and time base shifted experimental toroidal plasma current traces, with TALIF measurement times indicated at t = 2.10, 2.16, and 2.18 ms. Note the good agreement observed between the simulation and experimental toroidal currents during the TALIF measurement times.

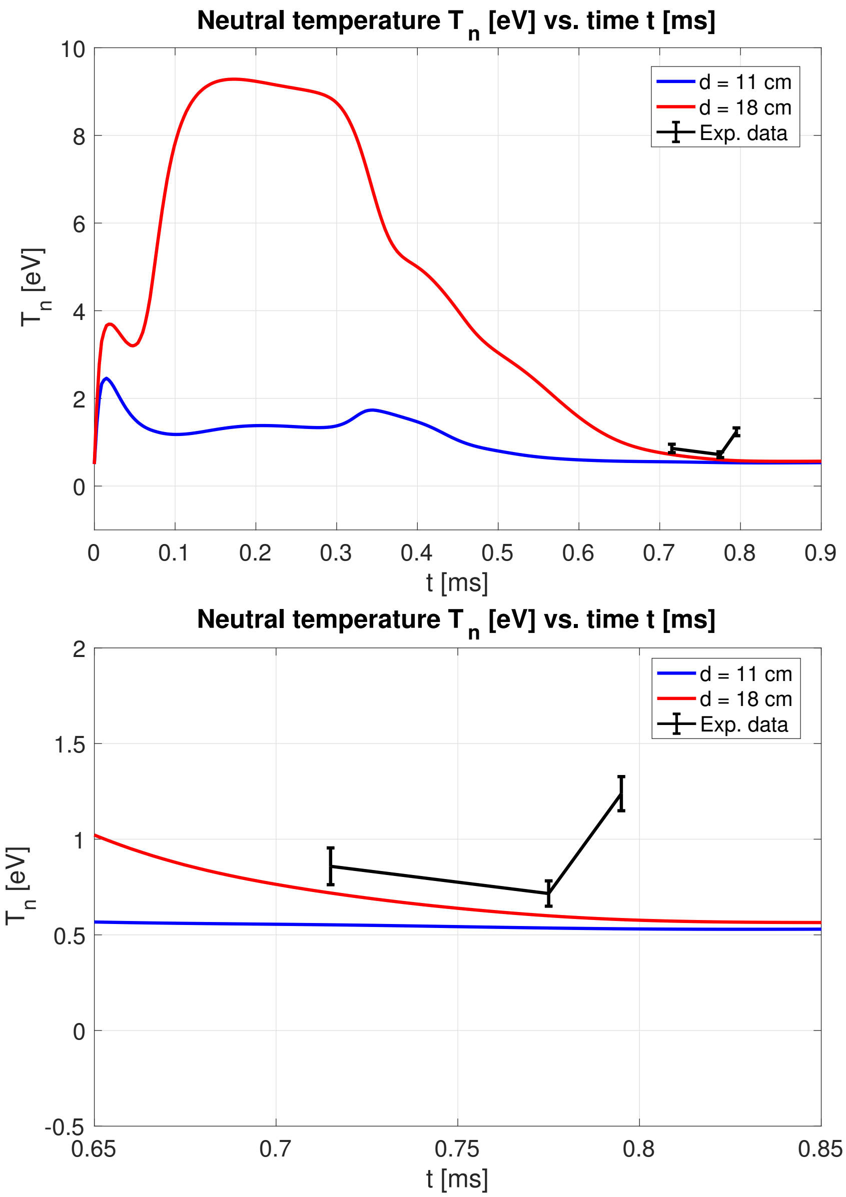

Figure 4.50: A comparison between the temporal evolution of the simulated neutral temperature and experimental TALIF measurements at $d = 11$ cm. **Top**: The simulated neutral temperature at depths of $d = 11$ and 18 cm over spheromak decay period. **Bottom**: Note the improved agreement of the neutral temperature by the simulation at all measurement time points at the end of spheromak decay due to the increased boundary neutral temperature.

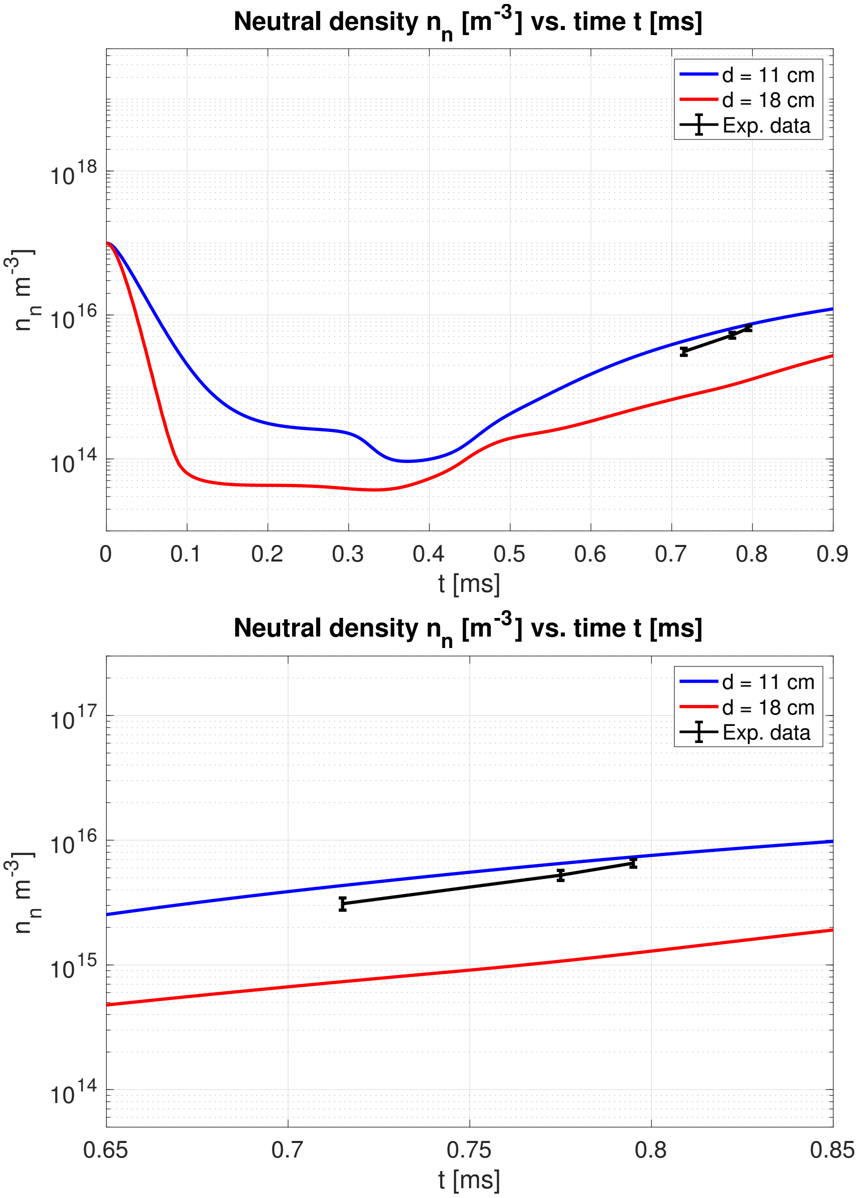

Figure 4.51: A comparison between the temporal evolution of the simulated neutral density and experimental TALIF measurements at $d = 11$ cm. **Top**: The simulated neutral density at depths of $d = 11$ and 18 cm over the spheromak decay period. **Bottom**: Note the improved agreement of the neutral density at $d = 11$ cm, consistent with previous simulations with this neutral density boundary condition.

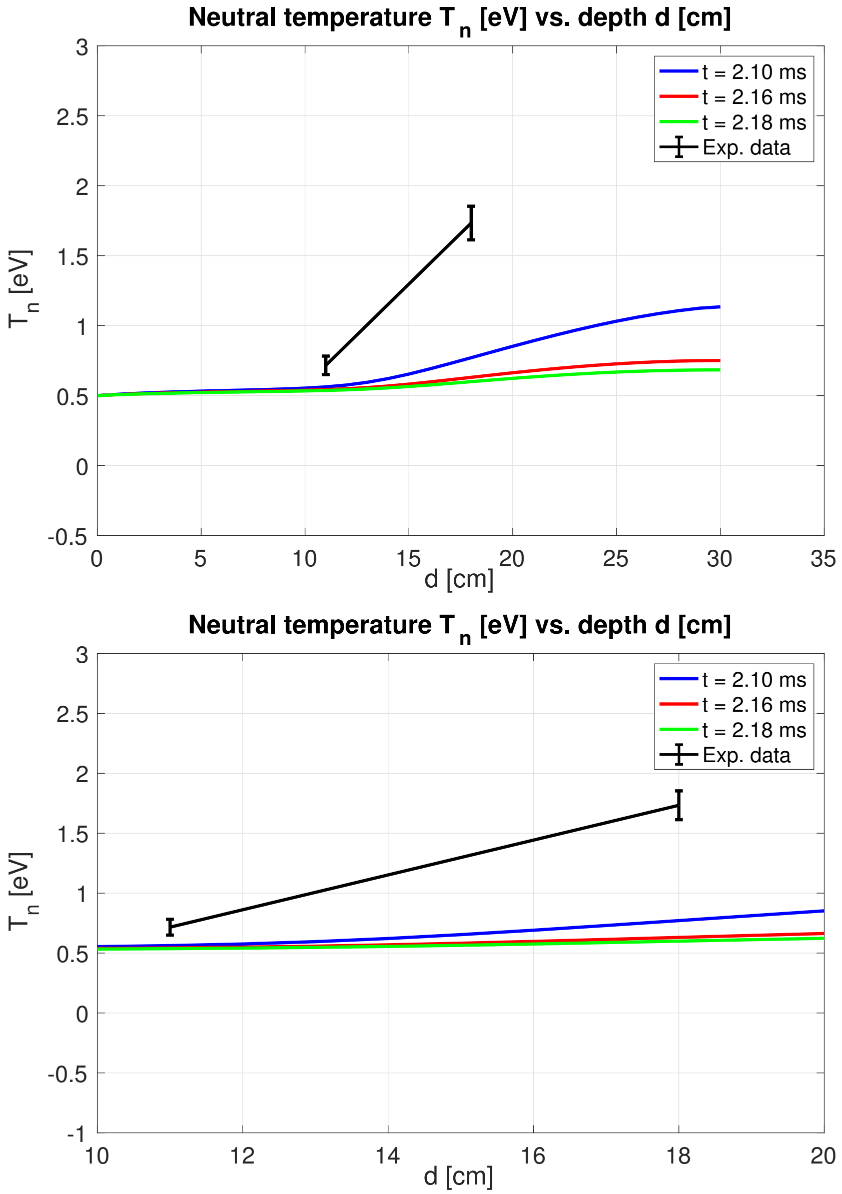

Figure 4.52: A comparison between the simulated neutral temperature spatial profile and experimental TALIF measurements at $t = 2.16$ ms. **Top**: The simulated neutral temperature at equivalent time points $t = 2.10$, 2.16 and 2.18 ms. **Bottom**: Note the improved agreement much like Fig. 4.47, albeit with the similar underprediction of the simulated neutral temperature at both TALIF measurement depths $d = 11$ and $d = 18$ cm.

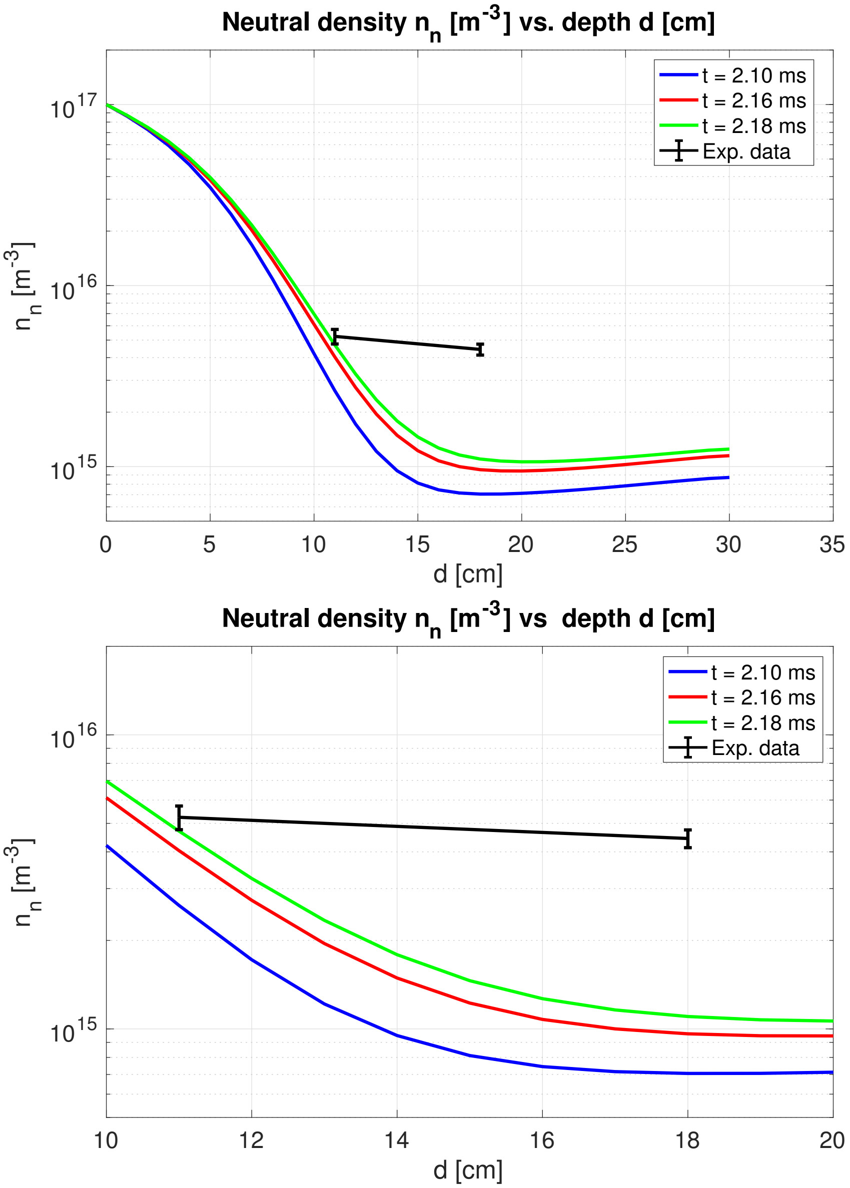

Figure 4.53: A comparison between the simulated neutral density spatial profile and experimental TALIF measurements at t = 2.16 ms. **Top**: The simulated neutral temperature at equivalent time points t = 2.10, 2.16 and 2.18 ms compared to experimental measurements. **Bottom**: Note the improved agreement of the neutral density at a measurement depth $d = 11$ cm, but a similar underprediction of the simulated neutral density at a depth d = 18 cm in line with previously present simulations with this neutral density boundary condition.

Parameter	Symbol	Value	Units
Plasma density	n	1×10^{19}	m^{-3}
Neutral density	n_n	1×10^{17}	m^{-3}
Plasma temperature	T	1 - 1.5	eV
Neutral temperature	T_n	1 - 1.5	eV
Plasma viscosity	ν	400	m^2/s
Neutral viscosity	ν_n	400	m^2/s
Plasma diffusivity	D	1	m^2/s
Neutral diffusivity	D_n	1	m^2/s

Table 4.3: Table of representative simulation parameters for decaying spheromak plasma-neutral simulations with PSI-Tet for comparison with TALIF experimental measurements.

thermal desorption from the wall as lower temperature, diatomic molecules. Additionally, a neutral density boundary condition $n_n = 1 \times 10^{17}$ m^{-3} is chosen for both of these simulations, which is consistent with a recycling fraction $f_{re} < 1$ for the considered simple sheath model.

Similarly to results presented previously, good agreement is observed between the simulation and experimental toroidal current traces during the period of comparison with TALIF measurements, as shown in Fig. 4.54. Using the chosen boundary condition temperatures of $T = T_n = 1$ eV has led to an improvement in agreement for both the spatial and temporal variation of the neutral temperature. In particular, this simulation is the first discussed that exhibits an overprediction of the neutral temperature at a TALIF measurement depth of any kind, specifically, $d = 11$ cm shown in Fig. 4.57. In short, the higher neutral temperature boundary condition has raised the floor of the neutral temperature throughout the domain to a sufficient level to exhibit better agreement with neutral temperature measurements. When comparing neutral densities, the simulation tends to agree best at a depth $d = 11$ cm, whereas it tends to underpredict the neutral density at a measurement depth $d = 18$ cm. The simulation still maintains a overall steeper neutral density gradient within the TALIF measurement domain $d = 11 - 18$ cm than measured.

The last simulation presented in this section makes use of the upper end of the temperature boundary condition ranges shown in Tab. 4.3 such that $T = T_n = 1.5$ eV. In line with all simulations presented in this section, but provided here for completeness, the simulation and experimental toroidal current traces exhibit good agreement during the TALIF measurement comparison period, shown in Fig. 4.59. However, the usage of this high of neutral and plasma boundary temperatures had led to worsened agreement compared to Figs. 4.55 – 4.58. In short, the simulation tends to overpredict the neutral temperature when compared to measurements, as shown in Fig. 4.60 and 4.62, albeit relatively good agreement is observed at a depth $d = 18$ cm in Fig. 4.62. Additionally, this choice of boundary conditions leads to a worsening overprediction of the neutral density, as seen in Fig. 4.61. In line with many of the previously presented results, the simulation tends to overpredict the neutral density at a depth $d = 11$ cm whereas it underpredicts the depth $d = 18$ cm when viewing the spatial profile in Fig. 4.63. The implications of these validation comparisons will be discussed in detail in the next Chapter.

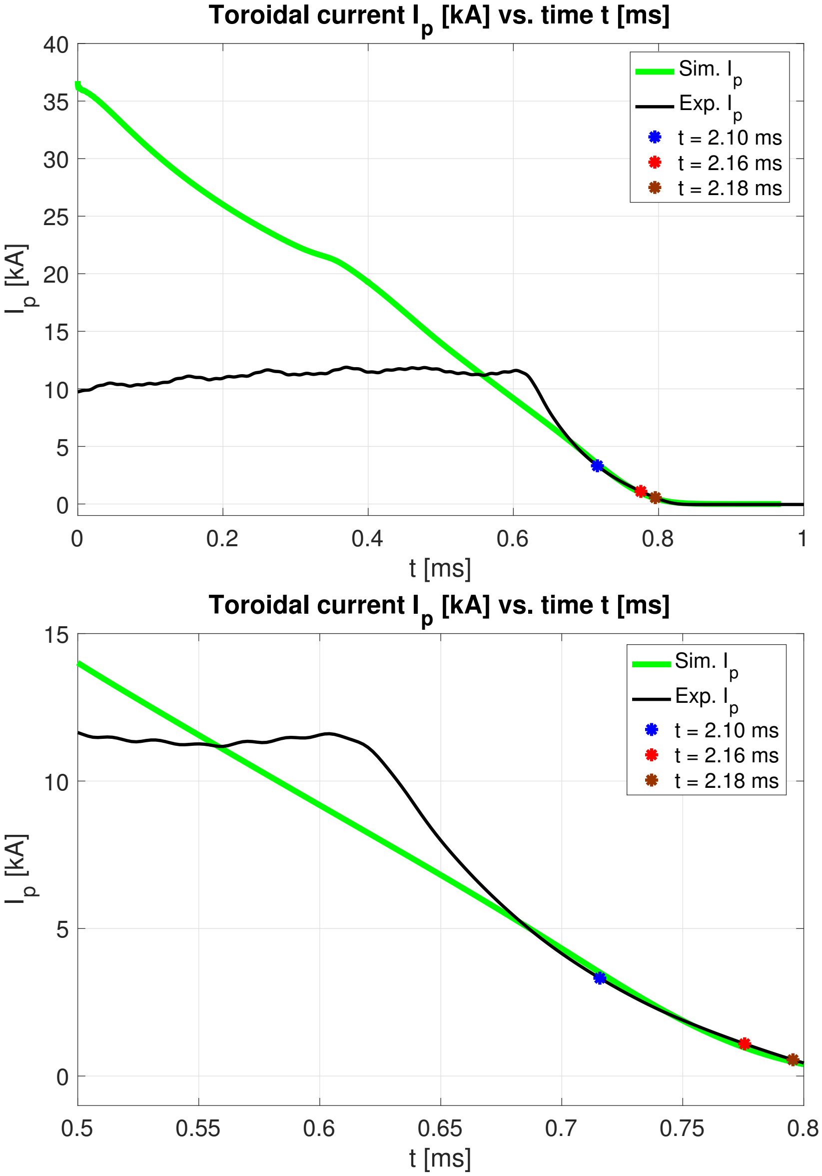

Figure 4.54: A comparison of the simulation and time base shifted experimental toroidal plasma current traces, with TALIF measurement times indicated at t = 2.10, 2.16, and 2.18 ms. Note the good agreement observed between the simulation and experimental toroidal currents during the TALIF measurement times.

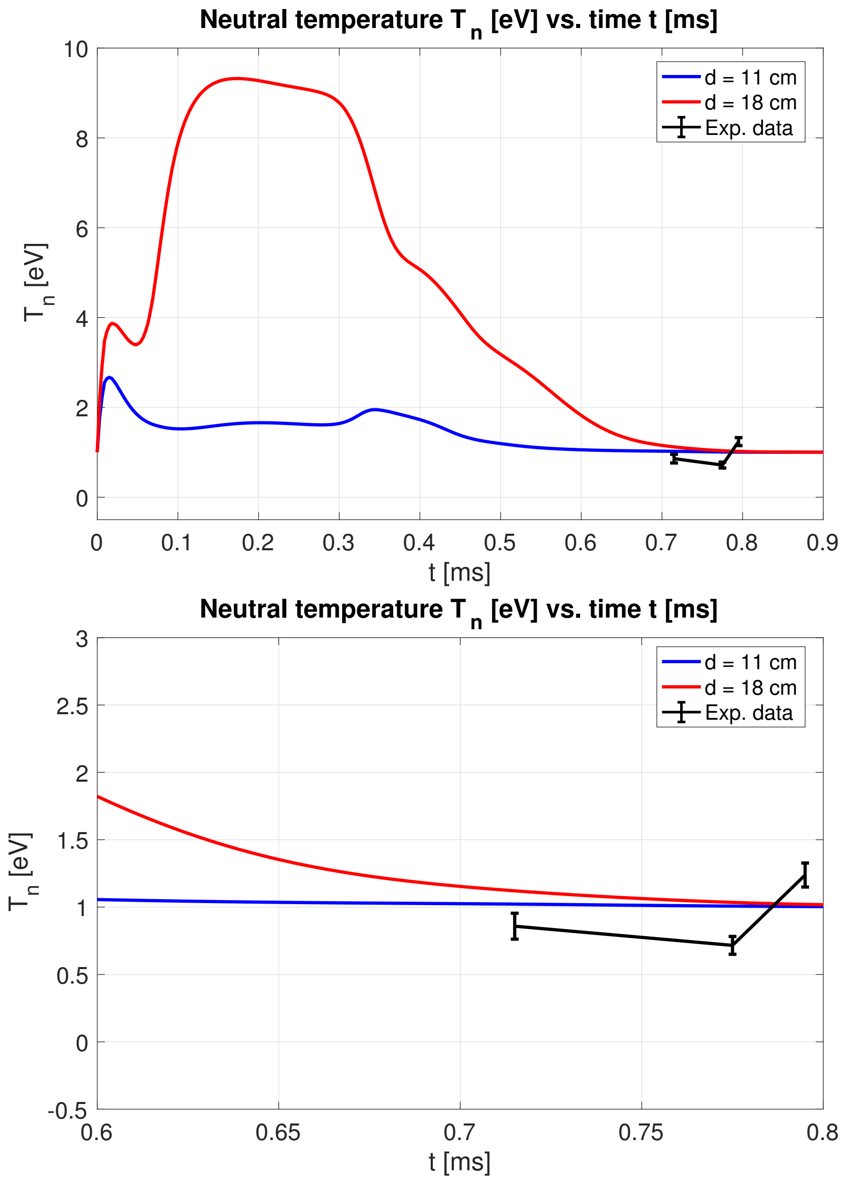

Figure 4.55: A comparison between the temporal evolution of the simulated neutral temperature and experimental TALIF measurements at $d = 11$ cm. **Top**: The simulated neutral temperature at depths of $d = 11$ and 18 cm over spheromak decay period. **Bottom**: Note the best neutral temperature agreement of presented results thus far at all measurement time points at the end of spheromak decay with this set of boundary conditions.

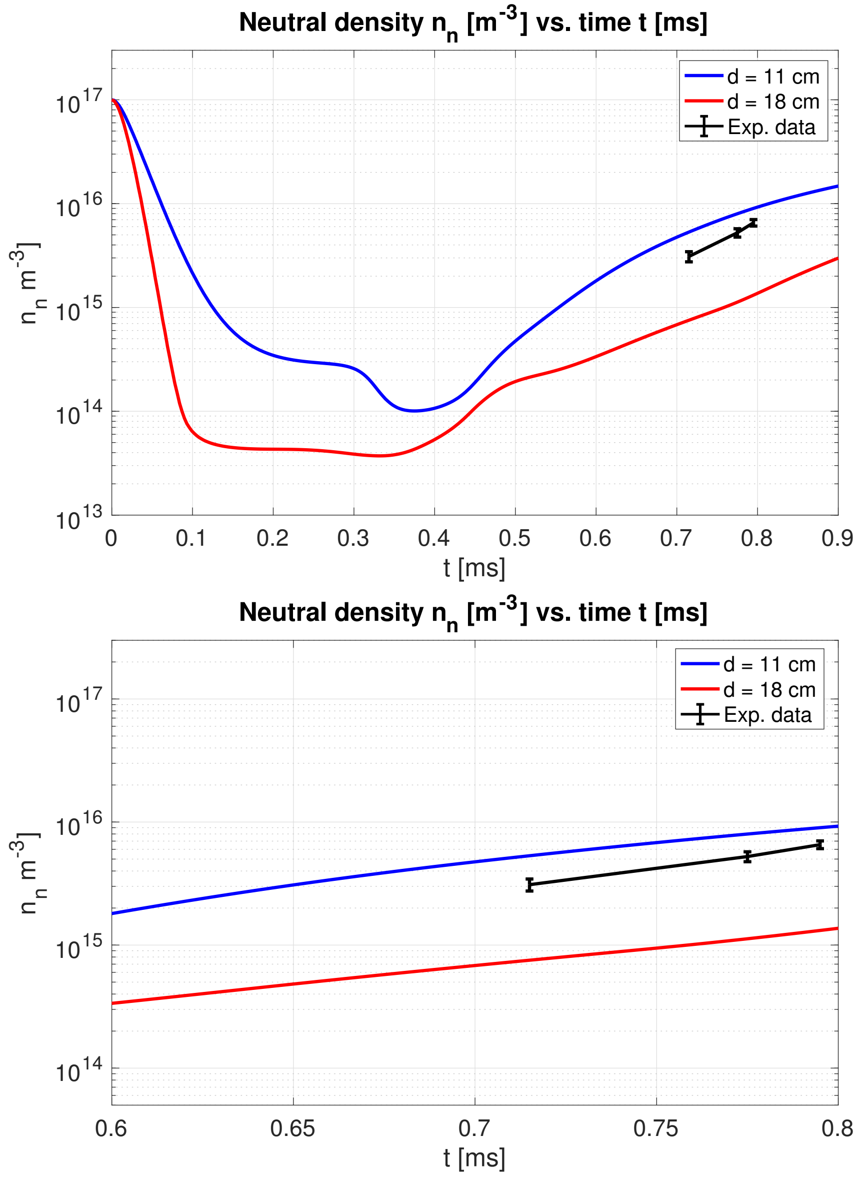

Figure 4.56: A comparison between the temporal evolution of the simulated neutral density and experimental TALIF measurements at $d = 11$ cm. **Top**: The simulated neutral density at depths of $d = 11$ and 18 cm over the spheromak decay period. **Bottom**: Note the slight overprediction of the neutral density at $d = 11$ cm, though agreement is overall fairly good with this chosen set of boundary conditions.

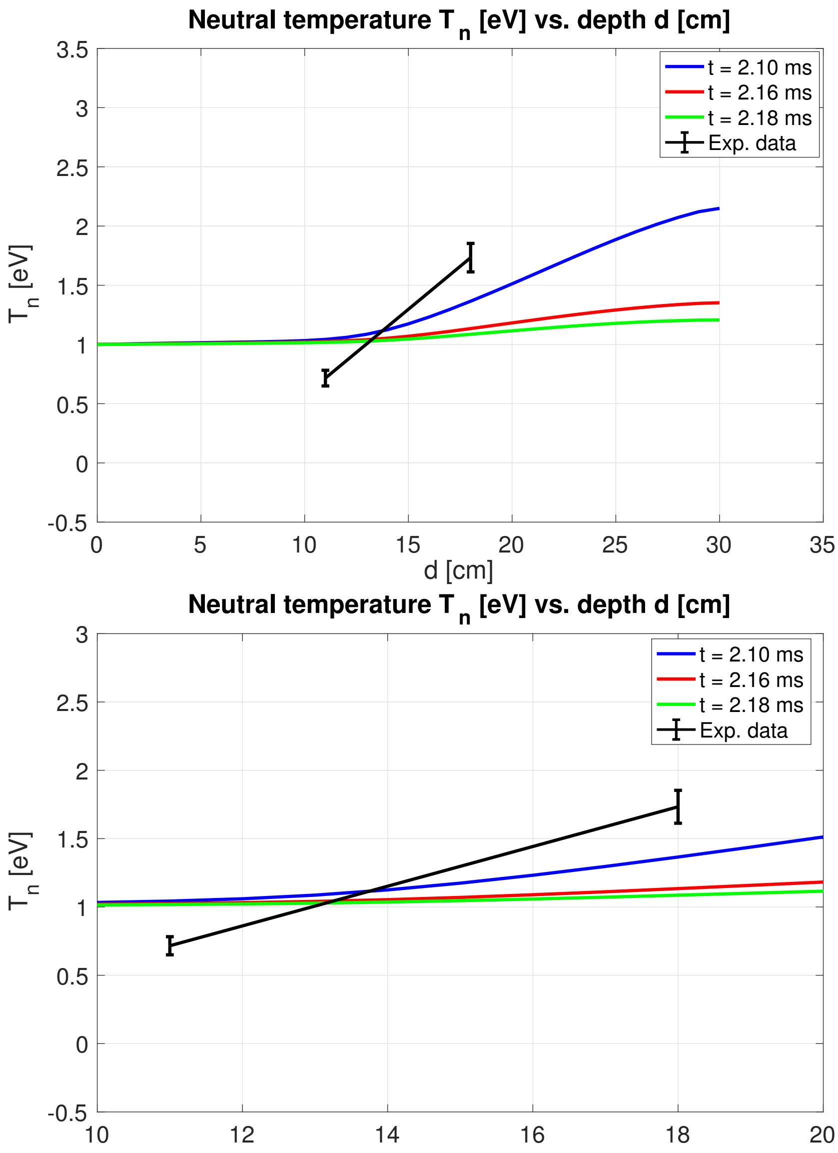

Figure 4.57: A comparison between the simulated neutral temperature spatial profile and experimental TALIF measurements at $t = 2.16$ ms. **Top**: The simulated neutral temperature at equivalent time points $t = 2.10$, 2.16 and 2.18 ms. **Bottom**: Note the improved agreement between simulation and experimental results. However, the simulation overpredicts the neutral temperature at $d = 11$ cm whereas it underpredicts the temperature at $d = 18$ cm.

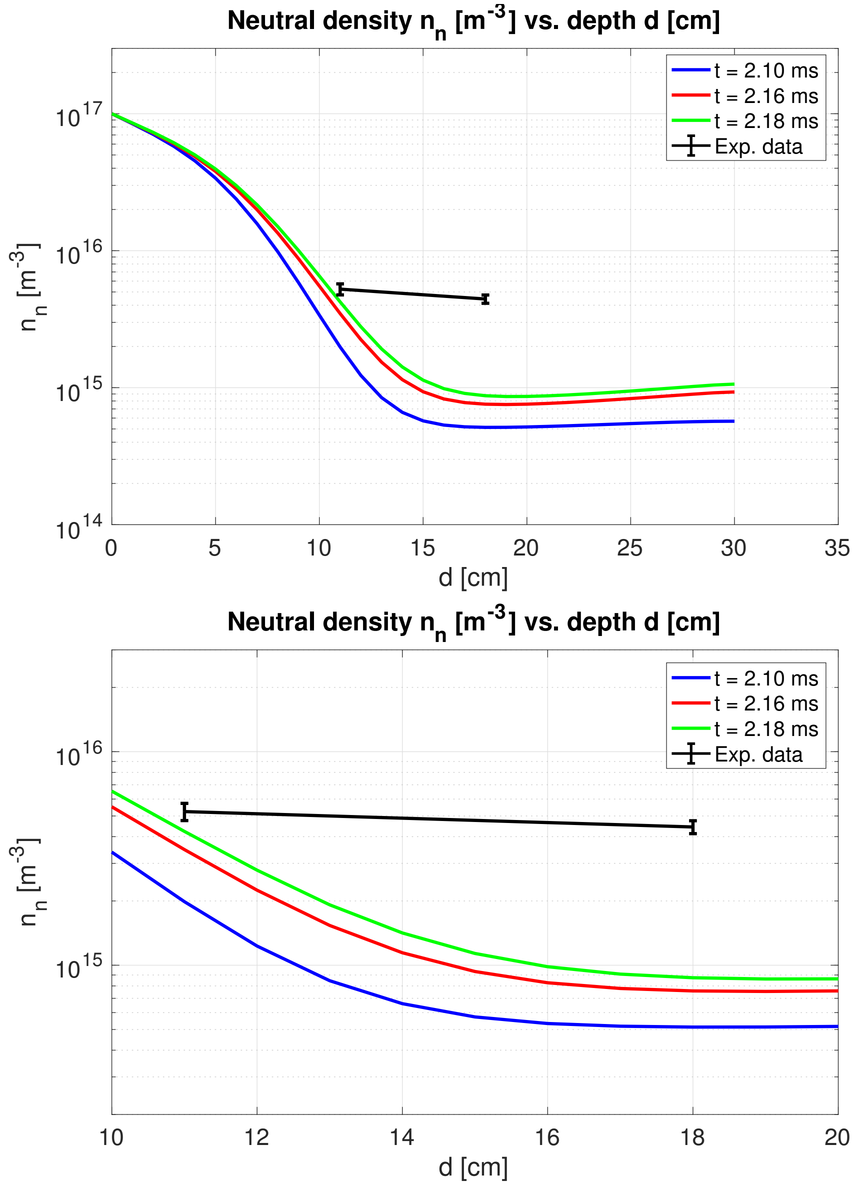

Figure 4.58: A comparison between the simulated neutral density spatial profile and experimental TALIF measurements at $t = 2.16$ ms. **Top**: The simulated neutral temperature at equivalent time points $t = 2.10$, 2.16 and 2.18 ms compared to experimental measurements. **Bottom**: Note the relatively good agreement of the neutral density at a measurement depth $d = 11$ cm, but a similar underprediction of the simulated neutral density at a depth $d = 18$ cm in line with previously presented simulations with this neutral density boundary condition.

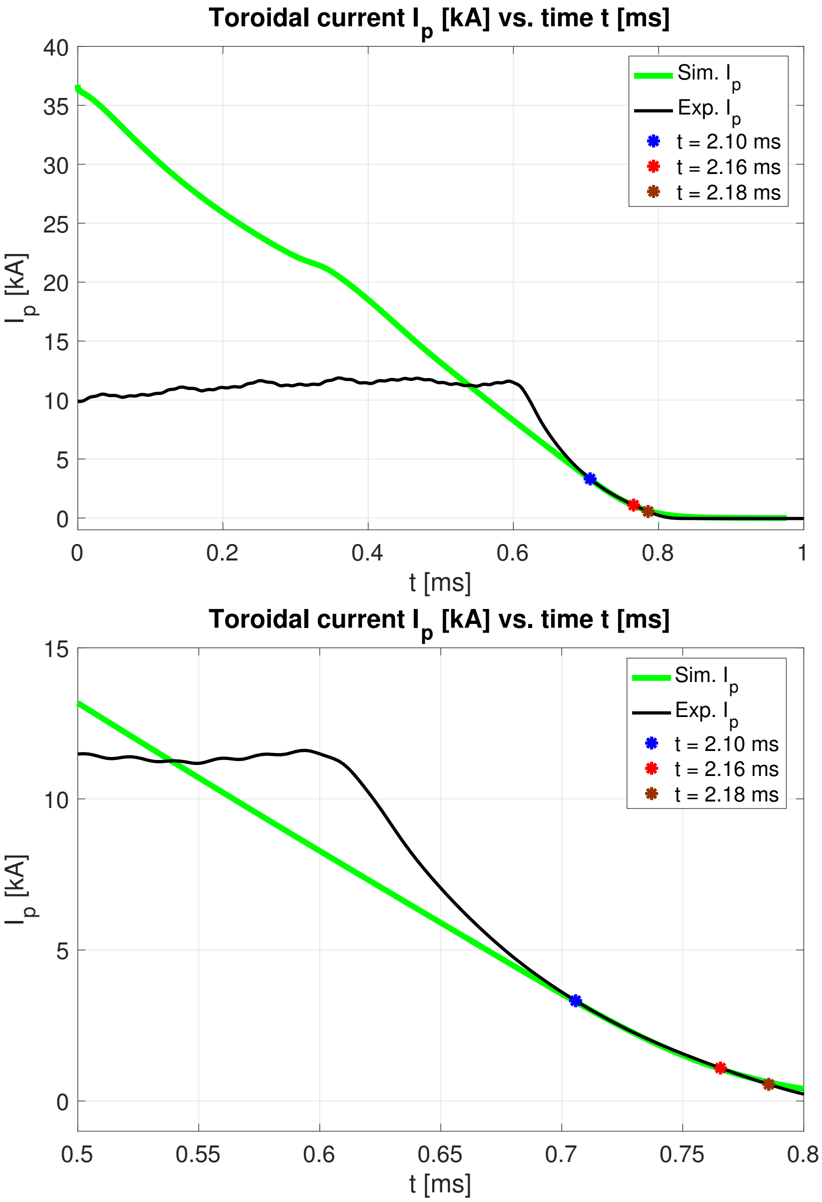

Figure 4.59: A comparison of the simulation and time base shifted experimental toroidal plasma current traces, with TALIF measurement times indicated at t = 2.10, 2.16, and 2.18 ms. Note the good agreement observed between the simulation and experimental toroidal currents during the TALIF measurement times.

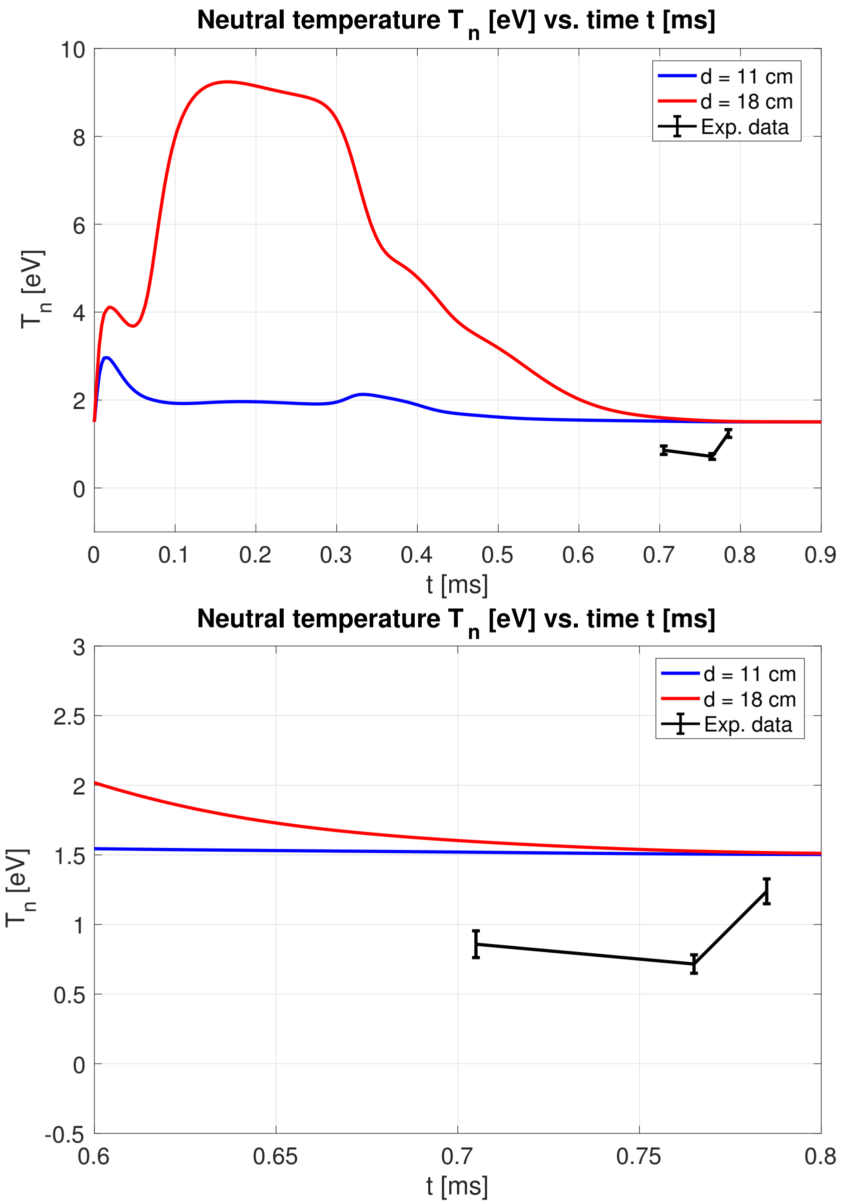

Figure 4.60: A comparison between the temporal evolution of the simulated neutral temperature and experimental TALIF measurements at $d = 11$ cm. **Top**: The simulated neutral temperature at depths of $d = 11$ and 18 cm over spheromak decay period. **Bottom**: Note the overprediction of the neutral temperature when compared to experimental measurements due to the higher neutral temperature boundary condition.

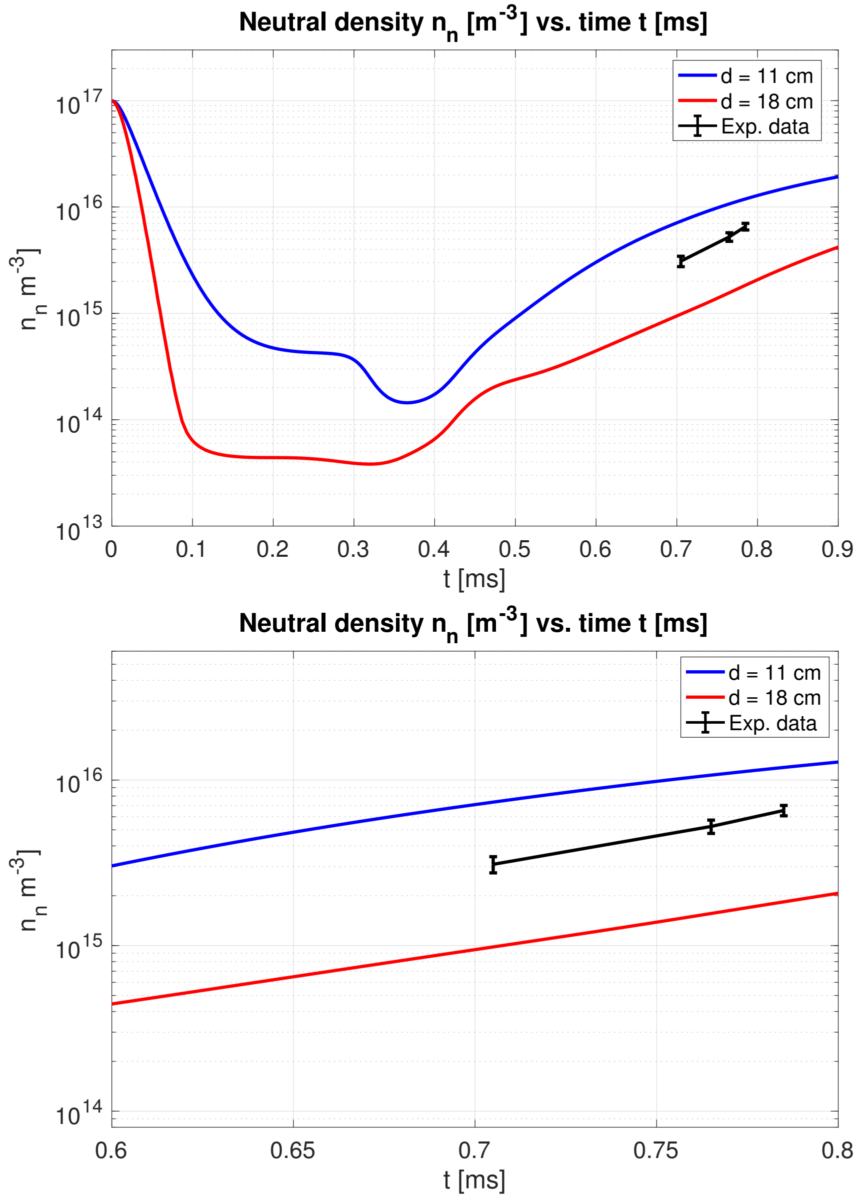

Figure 4.61: A comparison between the temporal evolution of the simulated neutral density and experimental TALIF measurements at $d = 11$ cm. **Top**: The simulated neutral density at depths of $d = 11$ and 18 cm over the spheromak decay period. **Bottom**: Note the worsened overprediction of the neutral density at $d = 11$ cm when compared to Fig. 4.56.

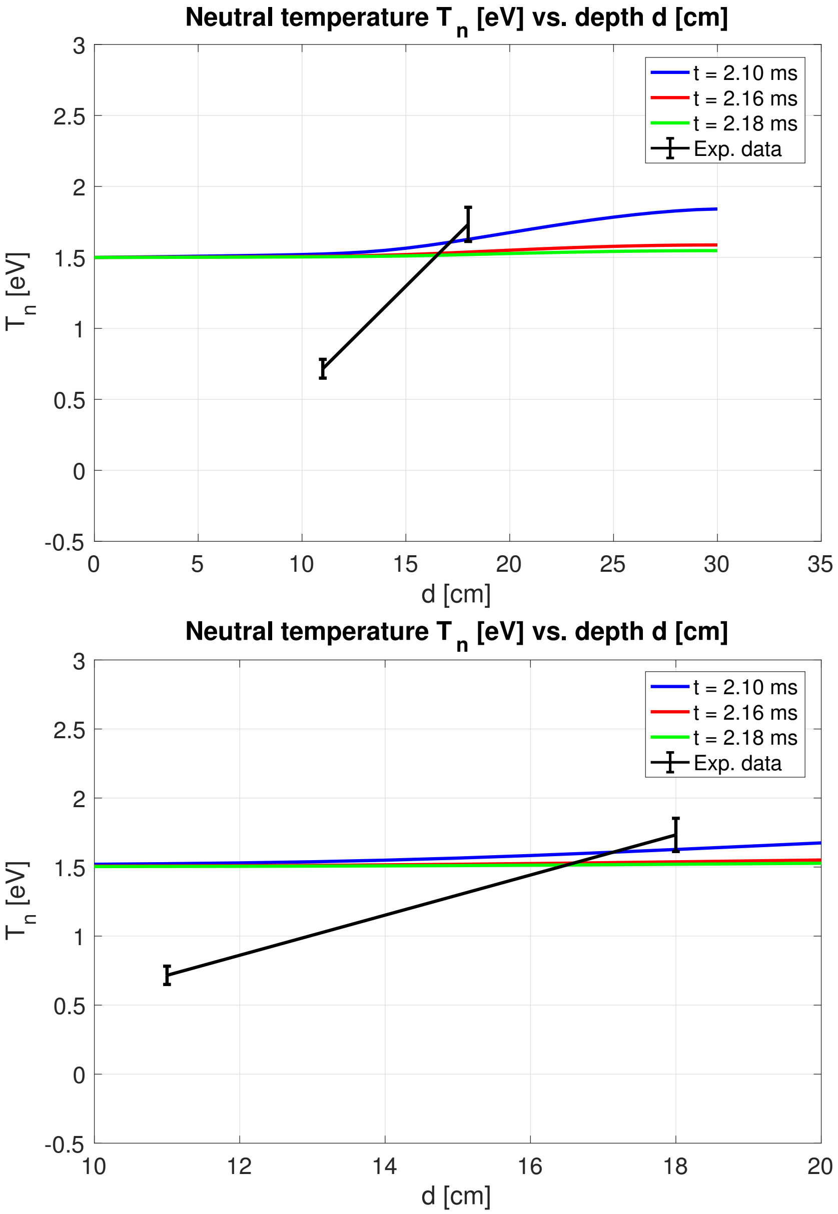

Figure 4.62: A comparison between the simulated neutral temperature spatial profile and experimental TALIF measurements at $t = 2.16$ ms. **Top**: The simulated neutral temperature at equivalent time points $t = 2.10$, 2.16 and 2.18 ms. **Bottom**: Note the improved agreement between simulation and experimental results at a depth $d = 18$ cm. However, the simulation overpredicts the neutral temperature at $d = 11$ cm.

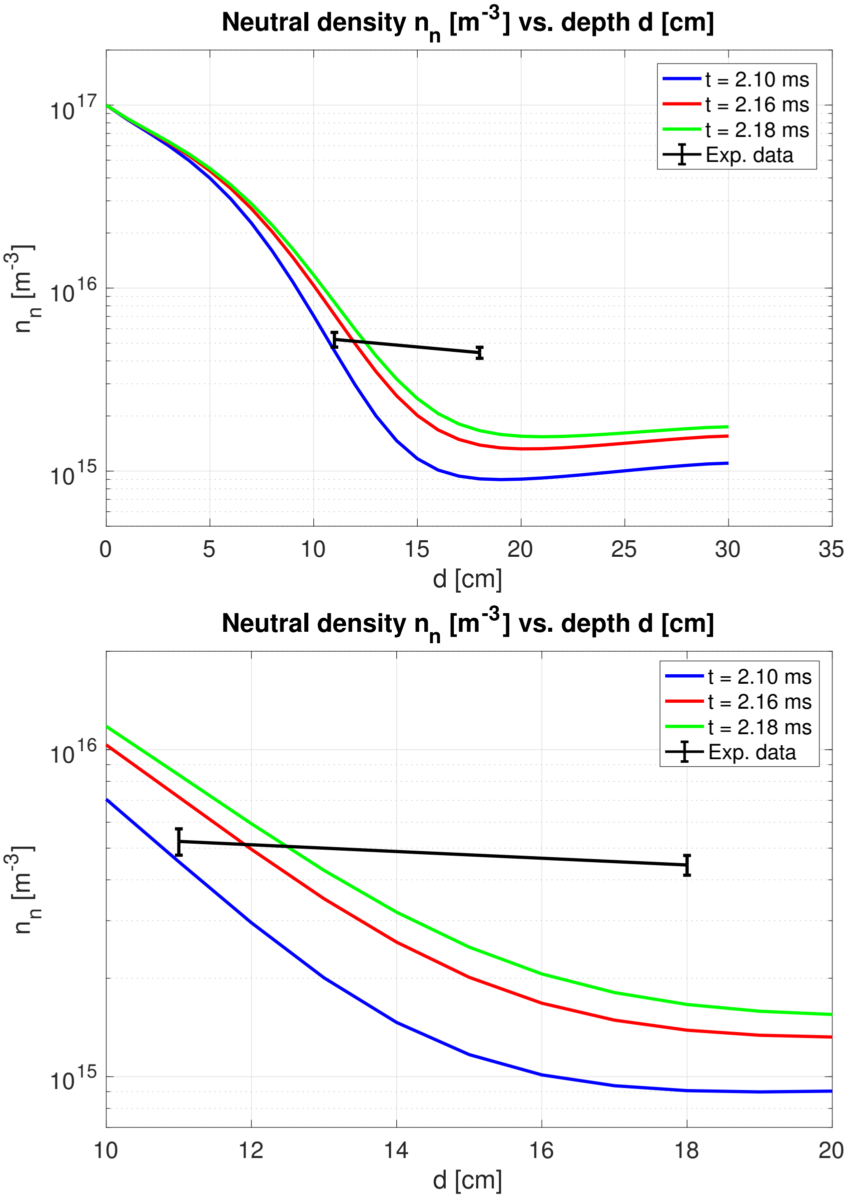

Figure 4.63: A comparison between the simulated neutral density spatial profile and experimental TALIF measurements at $t = 2.16$ ms. **Top**: The simulated neutral temperature at equivalent time points $t = 2.10$, 2.16 and 2.18 ms compared to experimental measurements. **Bottom**: Note the overprediction of the neutral density at a measurement depth $d = 11$ cm and a continued underprediction of the simulated neutral density at a depth $d = 18$ cm.

Chapter 5

DISCUSSION

5.1 TALIF neutral density and temperature measurements

As discussed in the previous Chapter, non-zero TALIF measurements of the monatomic, ground state deuterium neutral density and temperature in HIT-SI3 spheromak plasmas were only obtained during spheromak decay. Measurement attempts during the driven phase of the discharge yielded null results, manifesting as no statistically significant PMT voltage signals above noise levels, much like seen in Fig. 3.4(a). Nevertheless, non-zero TALIF measurements acquired during spheromak decay provide valuable insight into the characteristics of this neutral species in HIT-SI3 spheromak plasmas.

Both the temporal and spatial evolution of the monatomic, ground state neutral density is shown in Fig. 4.2 and Fig. 4.4, respectively. A monotonically increasing neutral density during spheromak decay is observed in Fig. 4.2 at the TALIF measurement depth $d = 11$ cm. This result is expected due to the anticipated influx of neutral particles from the plasma-material interface due to edge recycling and a relatively cool spheromak plasma near the end of life that is unable to fully counteract this influx via EI reactions. Experimentally, one would expect that as spheromak decay continues, plasma constituents will recombine into neutral atoms and/or molecules, inline with this experimental observation towards the end of spheromak decay. The neutral density spatial profile is observed to be relatively flat between measurement depths $d = 11 - 18$ cm with a relatively low number density $n_n \approx 5 \times 10^{15}$ m^{-3} observed even at the end of spheromak decay at $t = 2.16$ ms, as seen in Fig. 4.4. This result suggests a high ionization fraction $f_{ion} \geq 99.99\%$ when considering far-infrared (FIR) interferometer electron density measurements $n \approx 1 - 2 \times 10^{19}$ m^{-3} towards the end of spheromak decay. This ionization fraction assumes that a significant majority of neutral particles present in the system are monatomic, ground state deuterium atoms. If instead there is a significant population of diatomic, deuterium molecules present towards the end of spheromak decay, the TALIF diagnostic is incapable of measuring this population. This possibility will be discussed in detail in subsequent sections as a primary motivation for the addition of a diatomic, deuterium neutral fluid into the plasma-neutral model implemented in PSI-Tet.

At a measurement depth $d = 11$ cm, neutral temperatures $T_n \approx 0.7 - 1.3$ eV are observed during $t = 2.10 - 2.18$ ms, as seen in Fig. 4.3. Note the observed increase in the neutral temperature between $t = 2.16 - 2.18$ ms. This result is somewhat surprising since one may expect the neutral temperature to monotonically decrease in time during spheromak decay as the plasma cools. A possible explanation for this result is the loss of magnetic confinement towards the end of decay. At a measurement time $t = 2.18$ ms the toroidal plasma current $I_p \approx 0.6$ kA as seen in Fig. 4.1. It is possible that this small toroidal current and correspondingly weak poloidal magnetic field responsible for confinement of plasma pressure, the nearly complete decay of the toroidal current at this time leads to loss of thermal energy previously confined within the core spheromak region. The transient presence of warmer plasma at the TALIF measurement location may lead to localized, higher neutral temperature measurements at $t = 2.18$ ms when compared to earlier measurement times. The neutral temperature spatial profile shown in Fig. 4.5 shows an increasing neutral temperature as one proceeds from a measurement depth $d = 11$ to 18 cm. This result is likely due to the anticipated higher plasma temperatures near the spheromak core region when compared to measurement locations closer to the plasma-material interface.

These experimental results have multiple implications for the understanding of plasma-neutral dynamics in HIT-SI3 spheromak plasmas. Due to the low neutral density $n_n \approx 5 \times 10^{15}$ m^{-3} measured during spheromak decay, a likely reason TALIF measurement attempts during the higher plasma current, helicity injector driven phase of the spheromak discharge yielded null results is that the neutral density is below the detectable threshold ($\approx 2 \times 10^{14}$ m^{-3}) of the TALIF diagnostic [64] during this period of operation. Beyond the aforementioned limitations of the TALIF diagnostic being insensitive to diatomic deuterium molecules, the measurement depths where non-zero TALIF measurements were made may also explain a high ionization fraction even towards the end of spheromak decay. In short, it was only possible to attempt measurement to a minimum depth $d = 2$ cm of the wall due to laser power loading issues on optical viewports shown in Fig. 3.1. Measurements at this shallowest depth were only attempted during the driven phase of the discharge due to collaboration time constraints and yielded only null results. It is likely that if these measurements at shallower depths in the confinement chamber were attempted during spheromak decay, higher neutral densities than those measured during this work would be found due to the closer proximity of the measurement location to the source of edge recycled neutral particles at the plasma-material interface. The current lack of information in both the plasma and neutral parameters near the edge of the confinement chamber motivates the acquisition of additional data to better quantify these parameters in HIT-SI3 spheromak plasmas. As will be discussed in subsequent sections, this information is much needed to physically motivated the choice of boundary conditions for MHD plasma-neutral fluid simulations with PSI-Tet.

5.2 *Simulations of plasma-neutral dynamics in the HIT-SI3 experiment*

5.2.1 Impact of stabilizing artificial diffusion

When initially attempting to validate plasma-neutral simulations with TALIF neutral density and temperature measurements in HIT-SI3, significantly larger neutral densities were calculated at the TALIF measurement locations not only at comparable times during spheromak decay but throughout the entirety of the simulation for particular choices of boundary conditions. In particular, for simulations with relatively high neutral densities at the wall (i.e. $n_n \geq 1 \times 10^{18}$ m^{-3}) calculated neutral densities were much higher than TALIF measurements during the entirety of spheromak decay. Though there is uncertainty over the choice of boundary conditions as discussed previously, a consistently high calculation of neutral density at the TALIF measurement locations for many early simulations motivated further exploration into other potential sources for this disagreement.

One potential source of this disagreement is the impact of artificial diffusion used to stabilize the plasma and neutral density advances, shown in Eqs. 3.8 – 3.9 and reproduced below for convenience.

$$\frac{\partial n}{\partial t} + \nabla \cdot (n\vec{v}) = \Gamma_i^{ion} - \Gamma_n^{rec} + D\nabla^2 n$$

$$\frac{\partial n_n}{\partial t} + \nabla \cdot (n_n\vec{v}_n) = -\Gamma_i^{ion} + \Gamma_n^{rec} + D_n\nabla^2 n_n$$

The rightmost term in both density evolution equations is the artificial (i.e. non-physical) diffusion term added to the MHD plasma-neutral fluid model implemented in PSI-Tet. Fundamentally, the addition of these diffusive terms to the continuity equations results in two convection-diffusion transport equations, which can readily be seen by expanding the density advance equations as follows,

$$\frac{\partial n}{\partial t} + n(\nabla \cdot \vec{v}) + \vec{v} \cdot \nabla n = \Gamma_i^{ion} - \Gamma_n^{rec} + \nabla \cdot (D\nabla n)$$

$$\frac{\partial n_n}{\partial t} + n_n(\nabla \cdot \vec{v_n}) + \vec{v_n} \cdot \nabla n_n = -\Gamma_i^{ion} + \Gamma_n^{rec} + \nabla \cdot (D_n\nabla n_n)$$

In many fluid systems, incompressible flow conditions apply such that the velocity vector field cannot support a non-zero divergence (i.e. $\nabla \cdot \vec{v}_\alpha = 0$). However, compressible flow is permitted in the MHD plasma-neutral fluid model (i.e.!$\nabla \cdot \vec{v}_\alpha \neq 0$), and so must be retained for physical consistency. To compare the relative importance of the convective and diffusive terms in both the plasma and neutral density advances, one can take the ratio of convective and diffusive terms for each fluid, as shown in Eq. 5.1 and Eq. 5.2. A value of R or R_n much greater than 1 would indicate a convection dominated system, whereas a value much less than 1 would suggest a diffusion dominated system.

$$R = \frac{n(\nabla \cdot \vec{v}) + \vec{v} \cdot \nabla n}{\nabla \cdot (D\nabla n)} \tag{5.1}$$

$$R_n = \frac{n_n(\nabla \cdot \vec{v_n}) + \vec{v_n} \cdot \nabla n_n}{\nabla \cdot (D_n\nabla n_n)} \tag{5.2}$$

When discretizing a simulation domain for use with a finite element method (FEM) solver like PSI-Tet, the smallest characteristic length scale that one can resolve in the simulation is set by the mesh element size L_m. Using this length scale L_m and Eqs. 5.1 – 5.2 while only considering convective terms driven by density gradients (e.g. $\vec{v}_\alpha \cdot \nabla n_\alpha$), the Péclet number for mass transfer can be defined, expressed in Eqs. 5.3 – 5.4.

$$Pe \approx \frac{vL_m}{D} \tag{5.3}$$

$$Pe_n \approx \frac{v_n L_m}{D_n} \tag{5.4}$$

The Péclet number is a unitless quantity that details the relative importance of convective to diffusive terms in any convective-diffusion transport equation of interest over a characteristic scale length, in this case the mesh element size L_m. It has been observed that while using a characteristic scale length of the finite element size L_m, numerical instabilities are often observed when $Pe \gtrsim 1$ [75]. Thus, for fixed characteristic velocities in a system, if it becomes necessary to decrease the Péclet number to enable a numerically stable simulation the diffusion coefficient D_α can be increased and/or the mesh resolution can be increased to correspondingly decrease the characteristic finite element size L_m. Of course, for physical accuracy it is preferable to reduce the size of the artificial diffusion coefficient but this comes with the cost of greater computational expense when performing calculations with a higher resolution mesh (i.e. a larger number of finite elements within a given simulation domain).

For decaying spheromak simulations in HIT-SI3, it is found that numerical instabilities halt simulations unless the neutral diffusion coefficient D_n was increased to a particular value for a given mesh resolution. However, it is desired to reduce the size of D_n for more physically accurate results, especially since this term is a suspected source for the aforementioned disagreement between simulations and experimental results. Thus, it was necessary to progressively increase the mesh resolution to reduce characteristic finite element mesh size L_m to allow for numerically stable runs with smaller neutral diffusion coefficients D_n. Ultimately, it is desired to observe convergence such that numerically stable runs are possible without artificial diffusion terms significantly impacting computed solutions.

The results of this mesh resolution scan with decreasing values for the neutral diffusion coefficient D_n are shown in Fig. 5.3. Computed neutral density profiles along a chord from the wall to the magnetic axis ($d \approx 30$ cm) that include the TALIF measurement locations at depths $d = 11$ cm and $d = 18$ cm are plotted at similar simulation times during which the steepest neutral density gradients are observed. These profiles are calculated using identical initial and boundary conditions for the simulation while only changing the value of D_n. Note the significant impact the artificial neutral diffusion term in Eq. 3.9 has on calculated neutral density profiles in Fig. 5.3. A reduction of the neutral diffusion coefficient from $D_n = 100$ m^2/s to $D_n = 20$ m^2/s reduces the core neutral density at d = 30 cm by nearly three orders of magnitude. This large of an impact from an artificial term on solutions is highly undesirable for making meaningful comparisons to experimental data.

The mesh resolution is increased in tandem with reductions in the neutral diffusion coefficient until convergence is observed, defined as the value of artificial neutral diffusion coefficient that ensures the neutral diffusion term is no longer significantly impacting the solution. The results from these low neutral diffusion simulations are shown in Fig. 5.4. At values of $D_n \leq 1$ m^2/s, convergence is observed since no significant change in the neutral density profile is observed as the value of the coefficient is decreased below $D_n = 1$ m^2/s.

Thus, for all simulations performed and compared to TALIF neutral measurements in this work, a neutral diffusion coefficient $D_n = 1$ m^2/s is used to ensure this artificial term is not having a significant impact on computed solutions. Unfortunately, enabling numerically stable runs with $D_n = 1$ m^2/s resulted in significantly increased computational expense with a much higher resolution mesh (i.e. ≈ 4 times the number of elements as the original HIT-SI3 mesh). A comparison between the lower resolution and higher resolution tetrahedral meshes is shown in Fig. 5.1. Nevertheless, running with higher mesh resolution and corresponding lower value of the neutral diffusivity coefficient allows for more physically accurate for comparison to TALIF neutral density and temperature measurements. Correspondingly, if disagreement between simulation and experiment is still observed, it is likely due to a deficiency in the physical model, an issue with its implementation, and/or poorly chosen boundary conditions.

It should be noted that convergence is observed for decaying spheromak simulations for

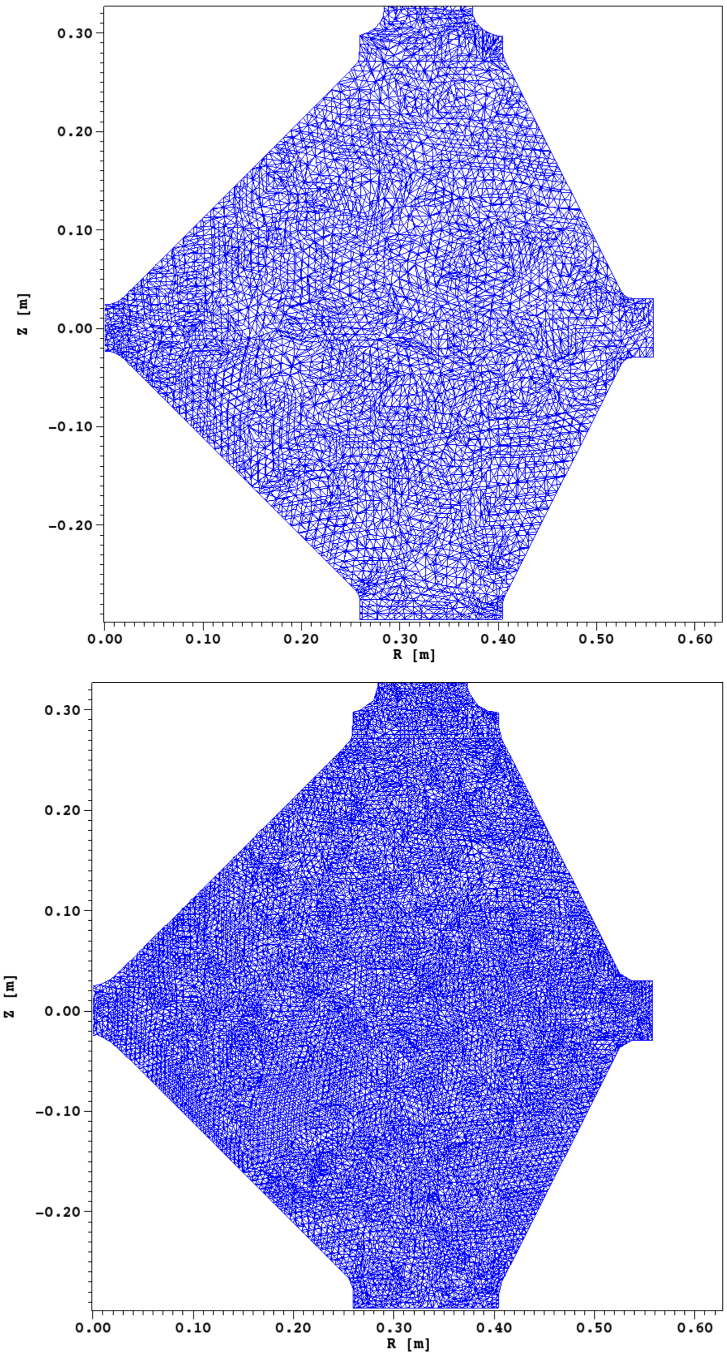

Figure 5.1: A comparison of low resolution (top) and high resolution (bottom) tetrahedral meshes used for plasma-neutral PSI-Tet simulations. Note the higher-resolution mesh was required to enable numerically-stable runs with $D_n \leq 1$ m^2/s.

a particular set of initial and boundary conditions. In particular, the neutral density was chosen to be the same as the plasma density at the boundary (i.e. $n = n_n = 1 \times 10^{19}$ m^{-3}) to generate large neutral density gradients, which correspondingly produce significant neutral flows via the $-\nabla p_n$ term in Eq. 3.11 from edge region into the core spheromak region. An example of the observed neutral flows and neutral pressure gradients in these simulations is provided as Fig. 5.2. As a result, if simulations are performed that produce even larger neutral density gradients and corresponding neutral flows, it may become necessary to perform calculations with even higher-resolution meshes to allow for numerically-stable simulations while ensuring artificial diffusion is not significantly impacting solutions since a lower value of neutral diffusion coefficient D_n will likely be required. However, as seen in Fig. 5.4, numerically stable decaying spheromak simulations have been successfully performed with a minimum neutral diffusion coefficient $D_n = 0.2$ m^2/s while using the higher-resolution mesh shown in Fig. 5.1, providing an avenue for future work should lower values of the neutral diffusion coefficient be needed.

As a subject of future work specifically on the topic of the impact of artificial diffusion on calculations, alternative approaches to stabilizing the density advances could be pursued that may result in more physically-accurate results and reduction of the computational expense of simulations. First, the artificial diffusion coefficient is currently applied isotropically throughout the simulation domain. For numerical stability, when considering the defined Péclet numbers in Eqs. 5.3 and 5.4, only in regions with significant convective transport are large artificial diffusivity coefficients required. Thus, in regions with significant neutral flows more artificial diffusion will be required than in other regions where the convective terms are not as large. Though the size of the diffusion term is dependent on both the diffusion coefficient and the size of the density gradient as seen in Eqs. 3.8 and 3.9, a lower diffusion coefficient in regions were convective transport is lesser may still allow for numerically stable runs. By imposing the artificial diffusion coefficient anisotropically, it becomes possible to target areas of concern more precisely while reducing non-physical impacts elsewhere.

In an effort to reduce computational expense of simulations, it would be worthwhile to

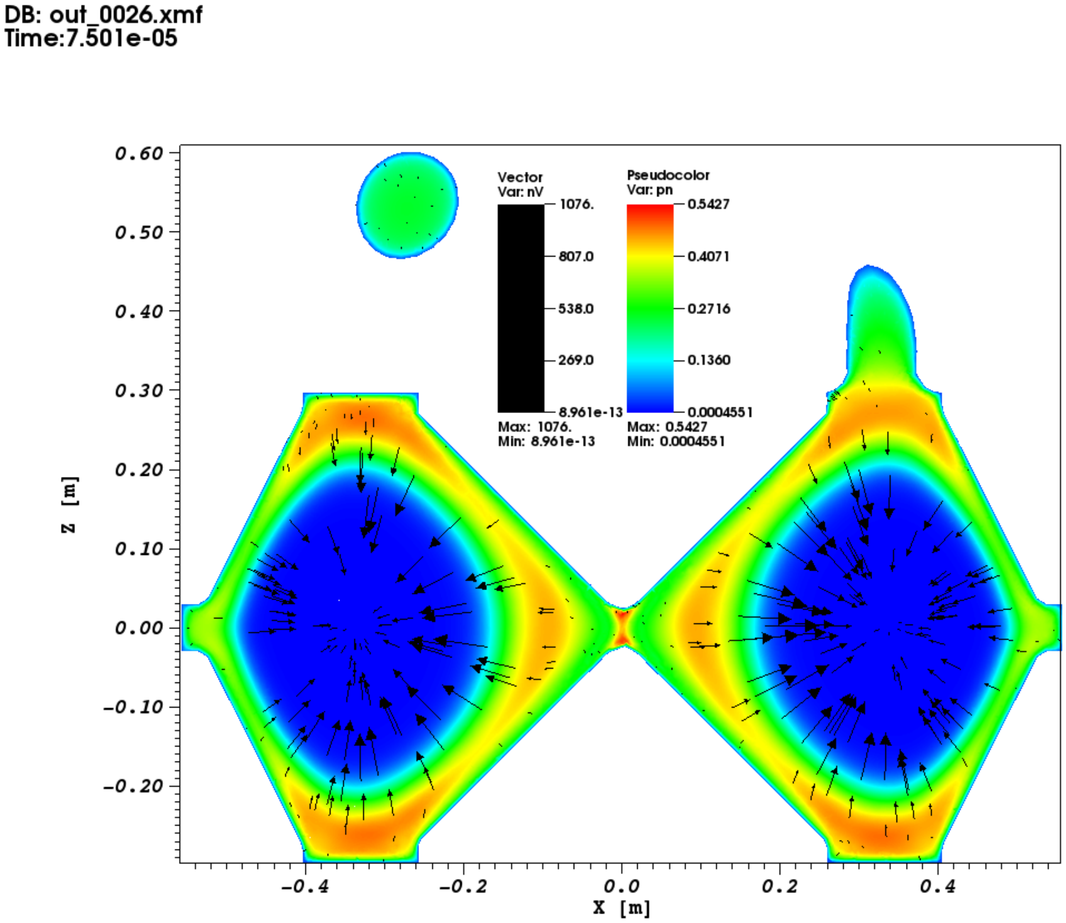

Figure 5.2: Calculated neutral velocity v_n [m/s] and neutral pressure $p_n = n_n T_n$ [Pa] in a decaying spheromak simulation. Note the inward minor radially directed neutral flow down the observed neutral pressure gradients at this time point in the simulation period. This provides a continuous source of neutral particles from the edge region into the core spheromak confinement region during the simulation, much like would be expected from edge recycling.

pursue adaptive mesh refinement. In short, for a given value of artificial diffusion coefficient, higher resolutions are only required in regions where the convective transport terms are large compared to the diffusive terms. In only increasing the resolution of the mesh in a subset of the simulation domain, it may be possible to reduce the computational expense of the simulation by not increasing the number of elements as significantly as was done for this work. Coupling anisotropic artificial diffusion coefficients and adaptive mesh confinement may allow for more physically accurate simulations to be performed while reducing overall computational expense when compared to the computational efforts presented in this work.

5.2.2 Impact of chosen boundary conditions

SRIM simulations of PMI interface

Calculations performed with the SRIM code have motivated the view that the majority of incident ions on the aluminum oxide plasma-material interface in HIT-SI3 will be implanted into the insulating plasma-facing coating. These implanted ions will subsequently recombine into diatomic molecules and thermalize with the wall. Should these diatomic molecules be desorbed from the wall during a HIT-SI3 discharge, they will re-enter the plasma region as cold, neutral molecules and likely be subsequently dissociated and ionized via various processes such as those shown in Fig. 2.3. In short, these calculations motivate the viewpoint that most neutral particles being produced from edge recycling in HIT-SI3 are molecular in form and relatively cold compared to the edge plasma temperature.

SRIM calculations suggest a natural division of promptly backscattered from absorbed/desorbed neutral particles based on their kinetic energies when they re-enter the plasma confinement volume. SRIM calculations suggest that promptly backscattered neutral atoms re-enter the confinement volume with approximately the same kinetic energy as they entered the sheath entrance. On the other hand, desorbed molecules from the plasma-material interface will have much lower kinetic energies as they re-enter the plasma confinement volume since they have thermalized with the relatively cool plasma facing wall. This difference in

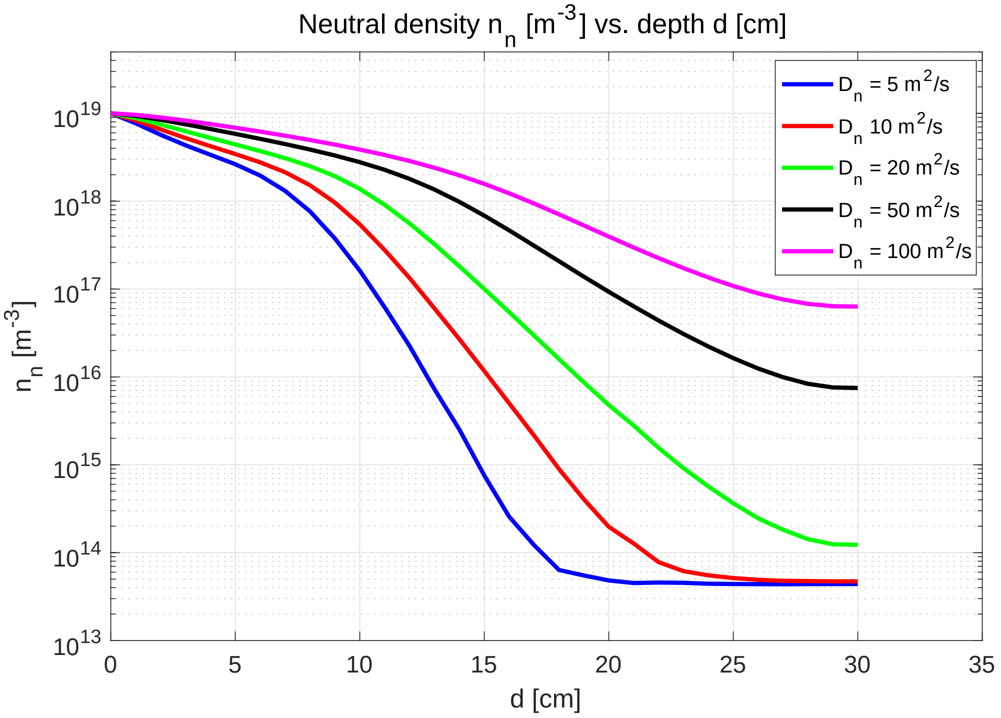

Figure 5.3: Calculated neutral density spatial profiles when the maximum neutral density gradients are observed with varying neutral diffusion coefficients. Note the significant impact decreasing the neutral diffusion coefficient D_n has on calculated neutral density profiles. Decreasing D_n can change the calculated neutral density at a given location by orders of magnitude. Reducing the nonphysical impact of artificial diffusion is critical for performing meaningful comparisons to experimental TALIF measurements.

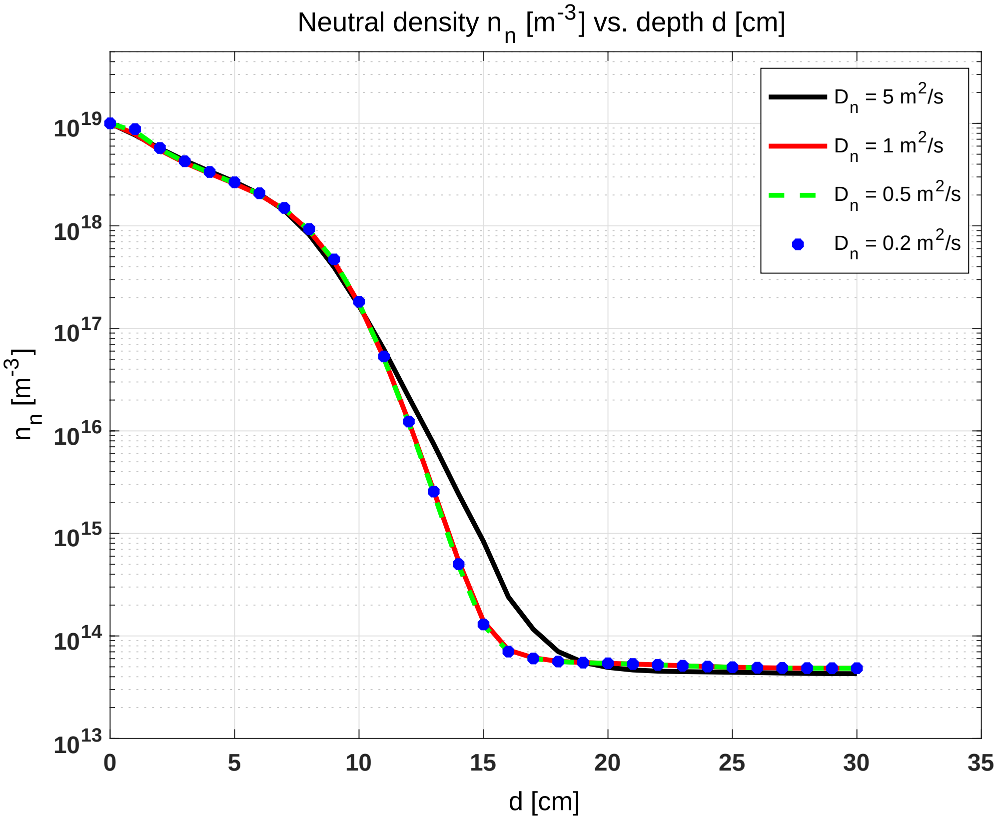

Figure 5.4: Calculated neutral density profiles at similar times when maximum neutral density gradients are observed while using progressively smaller neutral diffusion coefficients. Note that convergence is observed when using $D_n \leq 1$ m^2/s for these simulations. From this result, all simulations performed for comparisons to TALIF measurements use plasma and neutral diffusion coefficients $D = D_n = 1$ m^2/s.

kinetic energies will lead to deeper penetration of promptly backscattered neutral particles before they undergo a plasma-neutral reaction when compared to wall thermalized, desorbed deuterium molecules.

Returning to the expressions provided in the previous Chapter, under the $f_{re} = 1$ assumption, Eq. 3.35 applies, and is reproduced below for convenience,

$$\Gamma_i|_{SE} = \Gamma_n|_{SE}$$

It is clear from SRIM results that both promptly backscattered and desorbed thermal neutrals may compose the neutral mass flux $\Gamma_n|_{SE}$ out of the sheath entrance back into the bulk plasma region, and each species with different characteristic kinetic energies. For a chosen sheath entrance plasma temperature, SRIM calculations suggest the appropriate sheath entrance neutral temperature for promptly backscattered particles is approximately the same as the sheath entrance plasma temperature. This neutral temperature boundary condition is quite different than for desorbed deuterium molecules that have thermalized with the wall, which have much lower velocities exiting the sheath region than promptly backscattered neutral atoms.

To appropriately account for the differences between both types of edge recycled neutral particles, it would be best to treat promptly backscattered and desorbed, wall-thermalized neutral particles as separate neutral fluids. This will entail the addition of a molecular fluid to the existing plasma-neutral model. However, for this work a single monatomic, deuterium neutral fluid is maintained for the plasma-neutral model implemented in PSI-Tet. Lastly, it is noted from these SRIM calculations that the majority of edge recycled neutral particles in HIT-SI3 will be desorbed from the wall, which thus motivates a relatively cool neutral temperature boundary condition for PSI-Tet simulations.

Impact of neutral boundary conditions on decaying spheromak simulations

To quantify the impact of chosen boundary conditions on decaying spheromak simulations to compare with TALIF measurements, a series of simulations were performed that fix plasma fluid boundary conditions while allowing the neutral fluid boundary conditions to vary.

First, to assess the impact of the neutral density boundary condition, simulations are performed with the plasma density fixed at the boundary at $n = 1 \times 10^{19}$ m^{-3} while the neutral density at the boundary is varied within the range $n_n \in (1 \times 10^{17}\,\mathrm{m}^{-3}, 1 \times 10^{19}\,\mathrm{m}^{-3})$. The plasma temperature boundary value is held at $T = 1.5$ eV and the neutral temperature boundary value is held at $T_n = 0.025$ eV. No-slip boundary conditions are imposed on both the plasma and neutral fluids at the boundary, consistent with other decaying spheromak simulations presented in this work. Profiles are plotted at similar times during spheromak decay, which is defined as the time when the maximum level of neutral depletion is observed prior to the beginning of the $n = 2$ kink mode described in previous sections.

The results of these simulations are provided in Figs. 5.5 – 5.10. Note the significant variations observed between computed profiles along a TALIF chord at a given time in the simulation. As seen in Fig. 5.5, a higher fixed neutral density at the boundary tends to increase the plasma density within the core confinement region due to the consistent presence of a large source of neutrals to convert into plasma via EI reactions. However, a relatively weak impact of the neutral density boundary condition on the plasma density profile is observed within the core confinement region (i.e. $d \gtrapprox 10$ cm). In Fig. 5.6, calculated neutral density profiles are plotted as a function of depth into the HIT-SI3 confinement chamber. Note the significant variation in the neutral density profiles with changing neutral density boundary conditions. As the neutral density boundary value decreases, the location of the steep neutral density gradient tends to shift closer to the wall, resulting in a larger volume of relatively low neutral densities within the core confinement region. The calculated plasma and neutral temperature profiles are shown in Fig. 5.13 and Fig. 5.14, respectively. With decreasing neutral densities at the wall, higher maximum plasma and neutral temperatures are observed. Additionally, a transition from a cool, wall-dominated neutral temperature region to a warmer, core-dominated neutral temperature region is observed in Fig. 5.14. The location of the transition between these two regions tends to shift outward towards the wall as the neutral density is decreased at the boundary in tandem with the aforementioned transition between the high neutral density region near plasma edge and the low neutral density region within the spheromak core. Lastly, the plasma pressure and neutral pressure profiles are shown in Fig. 5.9 and Fig. 5.10, respectively. The maximum plasma pressure tends to increase with larger neutral density at the wall, which is primarily driven by increases in the plasma density when running with high neutral density boundary values. A steep neutral pressure gradient is observed which is primarily driven by a significant reduction of the neutral density within the spheromak core region compared to its boundary value. The location of the steep neutral pressure gradient tends to shift closer to the wall as the neutral density at the boundary decreases, which is primarily driven by changes in the neutral density profile seen in Fig. 5.6.

Second, to determine the impact of neutral temperature boundary conditions on solutions, simulations are performed with the plasma and neutral densities equal and fixed at the boundary $n = n_n = 1 \times 10^{19}$ m^{-3} and with the plasma temperature held at $T = 1.5\,\text{eV}$ at the boundary. The neutral temperature is varied within the range $T_n \in (0.025\,\text{eV}, 3\,\text{eV})$. No-slip boundary conditions are imposed on both the plasma and neutral fluids at the boundary, as is the case for all decaying spheromak simulations presented in this work. Profiles are plotted at similar times during spheromak decay, which again is defined as the time when the maximum level of depletion is observed prior to the beginning of the $n = 2$ kink mode.

The results from these simulations are shown in Figs. 5.11 – 5.16. The plasma and neutral density profiles are plotted in Fig. 5.11 and Fig. 5.12, respectively. It is clear in Fig. 5.12 that an increased neutral temperature boundary condition results in greater neutral penetration into the core confinement region. With a large source of neutral particles at the boundary capable of penetrating further into the confinement region, this provides a significant plasma source term from EI reactions. An impact of this large plasma source term is seen in Fig. 5.11, which shows progressively higher plasma densities within the core confinement region with increasing neutral temperature at the boundary. Additionally, Fig. 5.11 shows non-monotonic plasma density profiles that are peaked mid-minor radius instead of near the magnetic axis at a depth $d \approx 30$ cm. The observed maximum in the plasma density profile tends to decrease and shift towards the boundary as the neutral temperature decreases at the wall, which is primarily driven by changes in the neutral density profile. The impact of changing the neutral temperature boundary condition on the temperature profiles of each species is shown in Fig. 5.13 and Fig. 5.14. Note the interesting impacts changing the neutral temperature boundary condition has on these profiles. First, increasing the neutral temperature at the boundary tends to decrease the maximum plasma and neutral temperatures observed. It is clear a larger influx of relatively cool neutral particles from the edge with increased neutral temperatures at the boundary tends to suppress the temperature of both fluids. The temperature profiles for both fluids exhibit a region near the wall that is relatively cool and with small temperature gradients which then transitions into a higher temperature core region. The location of a significant plasma temperature gradient tends to shift inward from the wall toward the core region with increasing neutral temperature at the boundary, which is consistent with deeper penetration of relatively cool neutral particle that suppress plasma and neutral temperatures. Additionally, the maximum neutral temperature gradient tends to decrease with increasing neutral temperatures at the boundary, and the location of any appreciable neutral temperature gradient moves inward toward the core confinement region as the neutral temperatures at the boundary increases.

Lastly, the plasma and neutral pressure profiles are shown in Fig. 5.15 and Fig. 5.16, respectively. An increase in the maximum plasma pressure is observed in Fig. 5.15 as the neutral temperature at the boundary increases, but with a reduction in volume of the higher plasma pressure core region. Also, as seen in Fig. 5.16, since the neutral density is being held constant at the boundary in these simulations, higher neutral temperatures at the boundary cause the neutral pressure to increase at the boundary as well. This larger neutral pressure with increasing neutral temperatures at the boundary produces increasingly larger neutral pressure gradients that drive significant ∇p_n flows, as seen in Eq. 3.11. The larger inflow of relatively cool neutral particles into the core confinement region is the primary driver behind increased neutral penetration with progressively higher neutral temperature boundary values.

These simulation results provide insight into the impact of the choice of neutral density and temperature boundary conditions on decaying spheromak simulations for comparisons to TALIF measurements. First, as an expected result, decreasing the neutral density at the boundary tends to reduce the presence of neutrals throughout the simulation volume. Lower neutral densities throughout the simulation volume tends to reduce plasma energy losses from EI reactions, resulting in higher plasma temperatures. These higher temperature plasmas undergo CX reactions with neutrals which result in higher neutral temperatures within the core confinement region. Second, an interesting result from these simulations is that an increase in neutral temperature at the boundary tends to increase neutral density throughout the simulation volume, which tends to suppress the maximum plasma temperatures observed during the simulation. Also, the influx of relatively cool neutrals from the boundary tends to suppress the maximum neutral temperature as well. Thus, these results suggest that the most preferable set of boundary conditions to reduce the impact of neutrals on core plasma parameters is relatively cool, low density neutral boundary conditions.

5.2.3 Agreement between TALIF measurements and simulation

Validation results exhibit differing levels of agreement between experimental data and simulations that are strongly dependent on the choice of boundary conditions. In all simulations good agreement is observed between the experimental and simulated toroidal current traces towards the end of spheromak decay. For comparisons during spheromak decay, simulation times are chosen with comparable amplitudes of toroidal current to experimental discharges when TALIF measurements are made. In particular, simulation time points during spheromak decay when the toroidal current $I_p \approx 3.5, 1.2, \text{and}\, 0.6$ kA are chosen for comparison to TALIF data at the experimental time points t = 2.10, 2.16, and 2.18 ms.

It is argued the best agreement between experimental neutral measurements and simulations is shown in Figs. 4.54 – 4.58. Parameters used for this calculation are provided in Tab. 4.3. Of particular importance, this simulation makes use of equal plasma and neutral temperatures boundary values $T = T_n = 1$ eV. This choice of boundary temperature for both species allows for the best observed agreement with neutral temperature measurements,

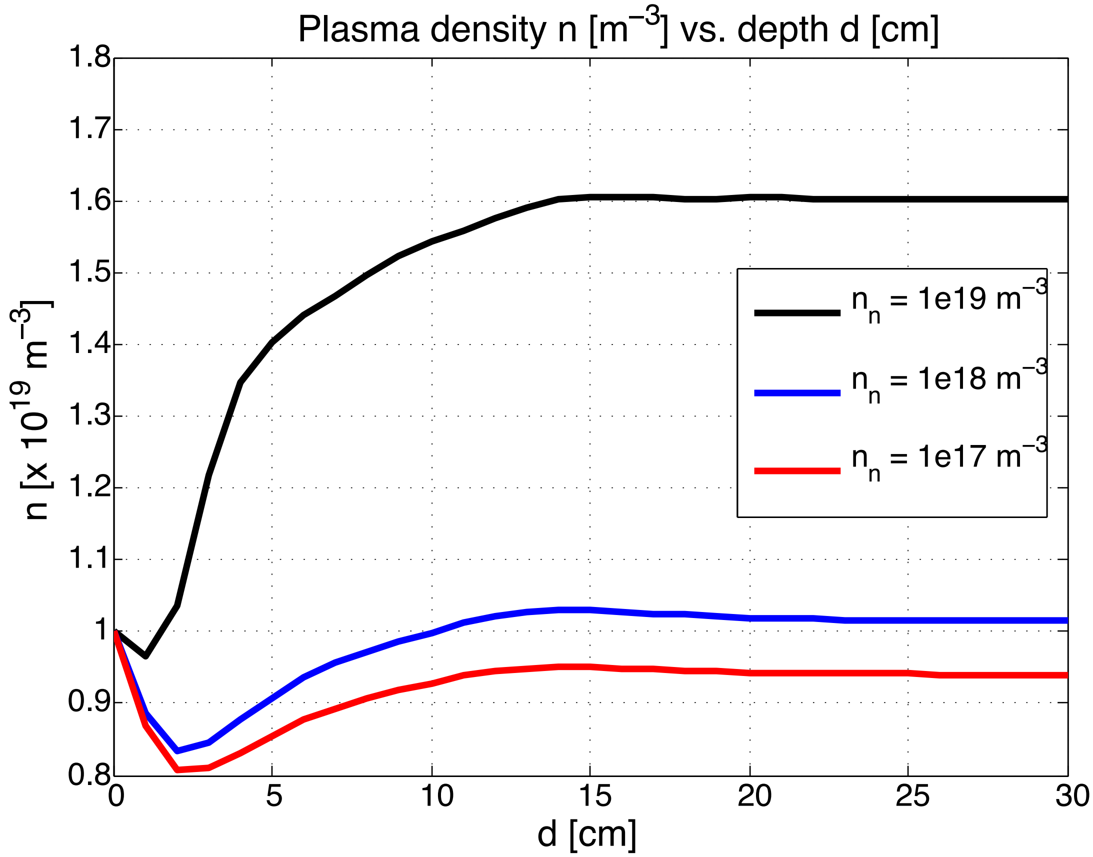

Figure 5.5: Calculated plasma density profiles as a function of varying the neutral density at the boundary. Note the impact of the neutral density boundary condition on the plasma density profile, which within the core spheromak region $d \gtrapprox 10$ cm has a weak spatial dependence.

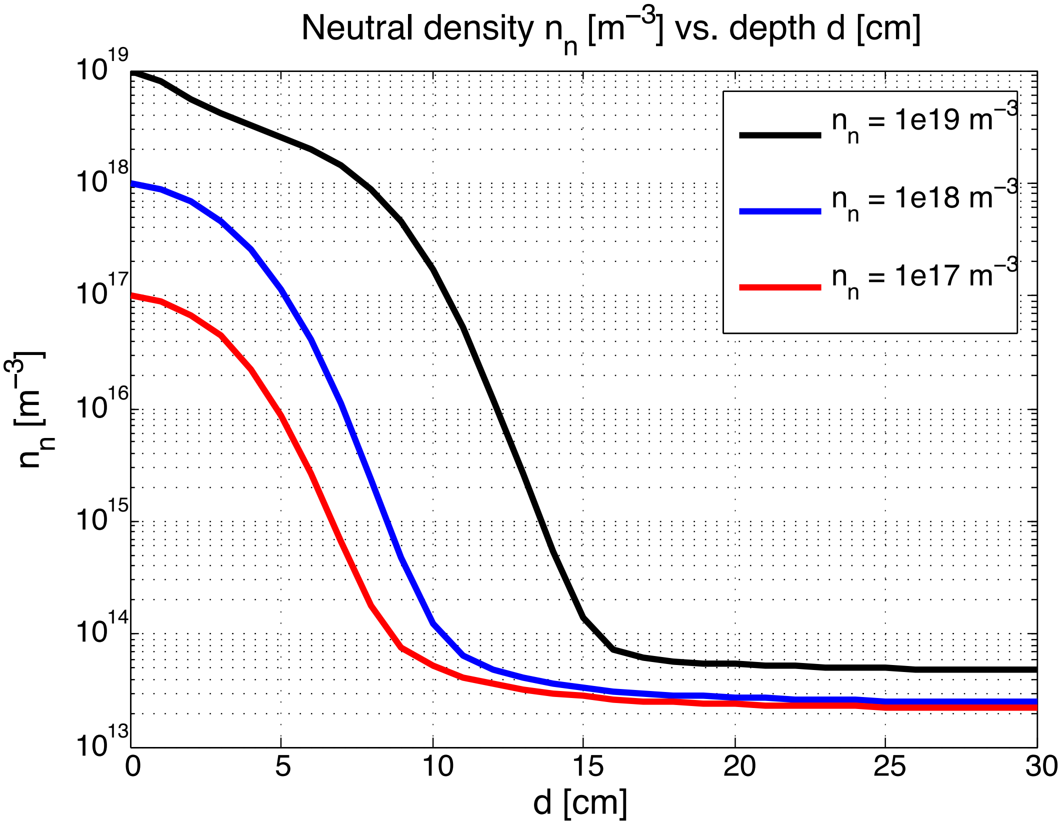

Figure 5.6: Calculated neutral density profiles as a function of varying the neutral density at the boundary. Note the impact of the neutral density boundary condition on the neutral density profile. A steep neutral density gradient is observed in all simulations, with the interior plateau value being reached at shallower depths d within the confinement chamber.

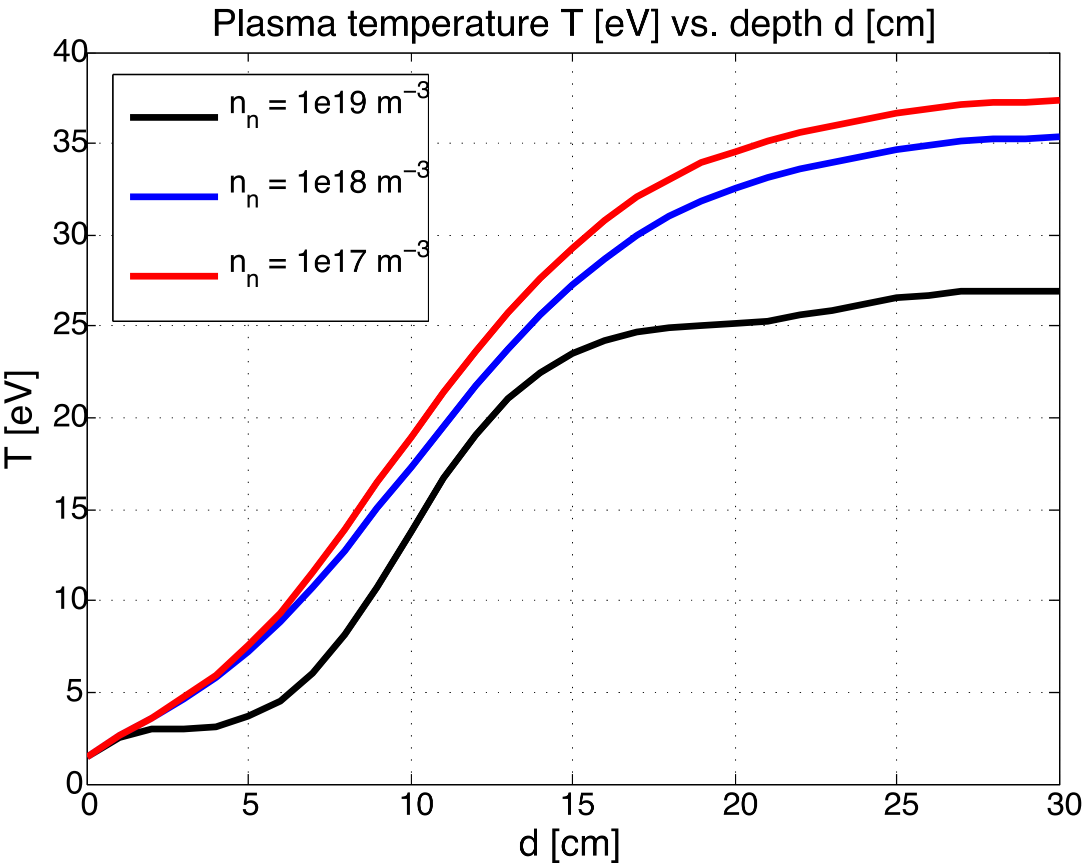

Figure 5.7: Calculated plasma temperature profiles as a function of varying the neutral density at the boundary. Note the impact of the neutral density boundary condition on the plasma temperature profile. Decreasing the neutral density at the wall tends to yield a larger volume of increasingly warm plasma within the core confinement region.

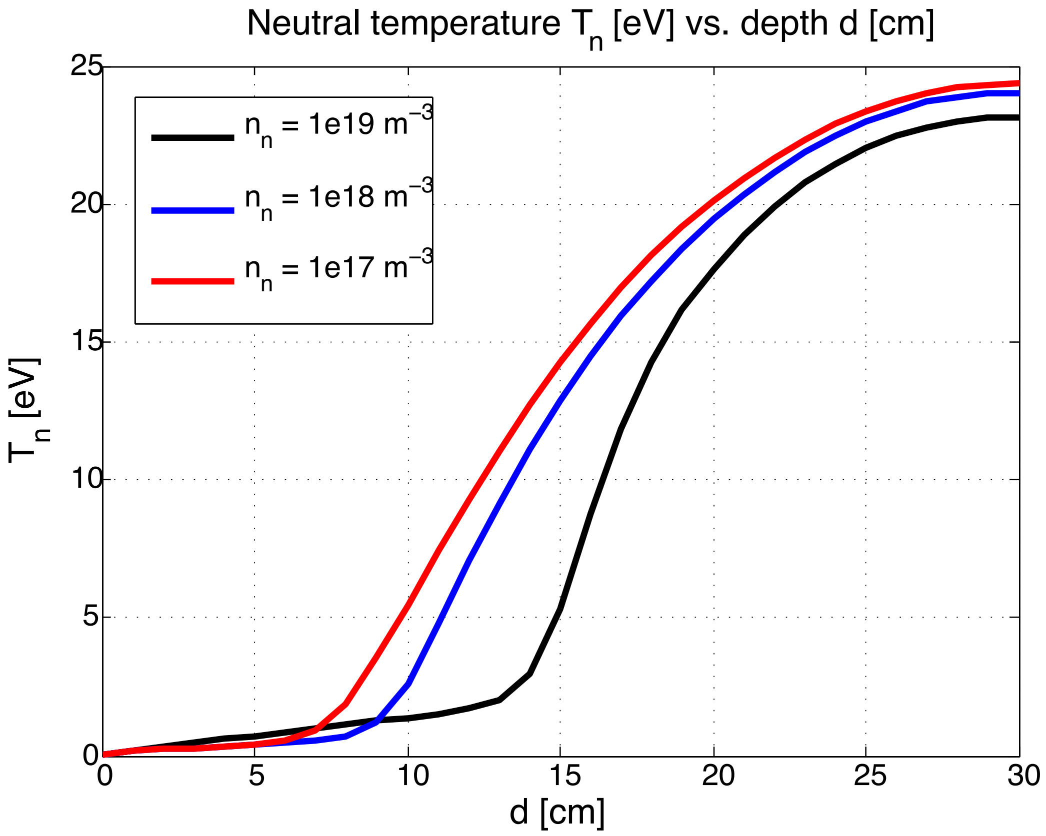

Figure 5.8: Calculated neutral temperature profiles as a function of varying the neutral density at the boundary. Note the impact of the neutral density boundary condition on the neutral temperature profile. Decreasing the neutral density at the wall yields a larger volume of increasingly warm neutrals within the interior region of the confinement volume via CX reactions with warm plasma ions.

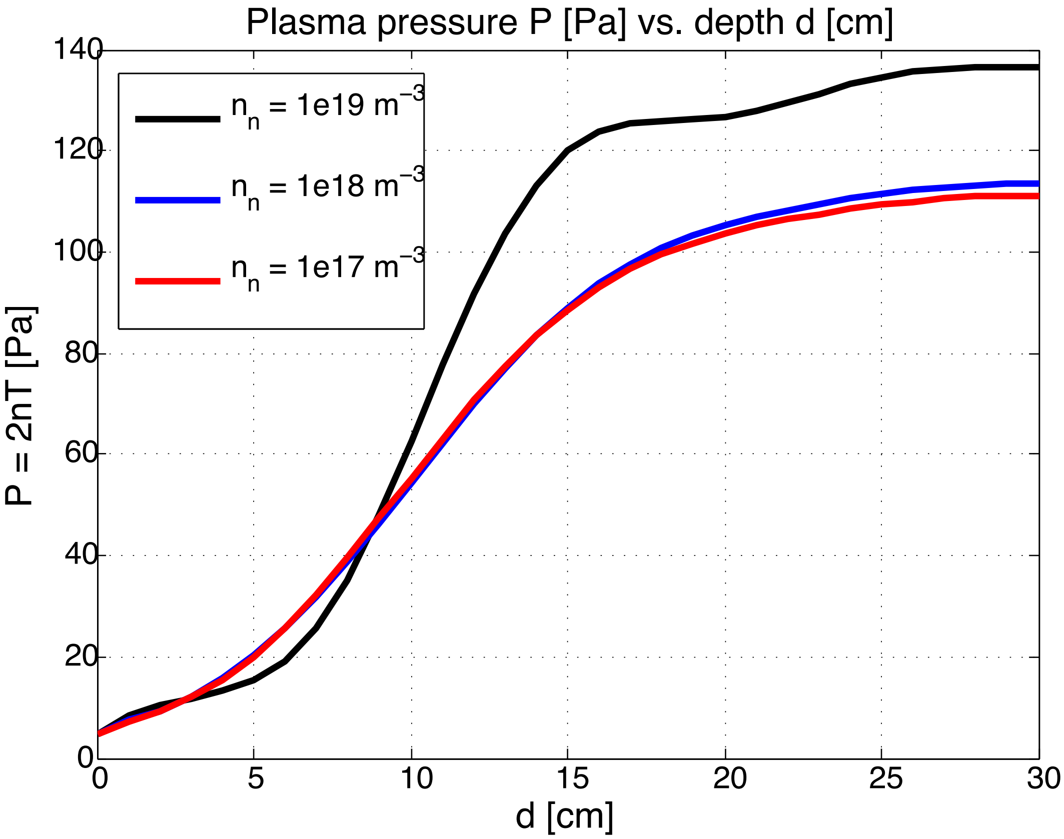

Figure 5.9: Calculated plasma pressure profiles as a function of varying the neutral density at the boundary. Note the impact of the neutral density boundary condition on the plasma pressure profile. Decreasing the neutral density at the wall tends to lessen the suppression of the plasma pressure near the edge, but also tends reduces the maximum plasma pressure reached in the core.

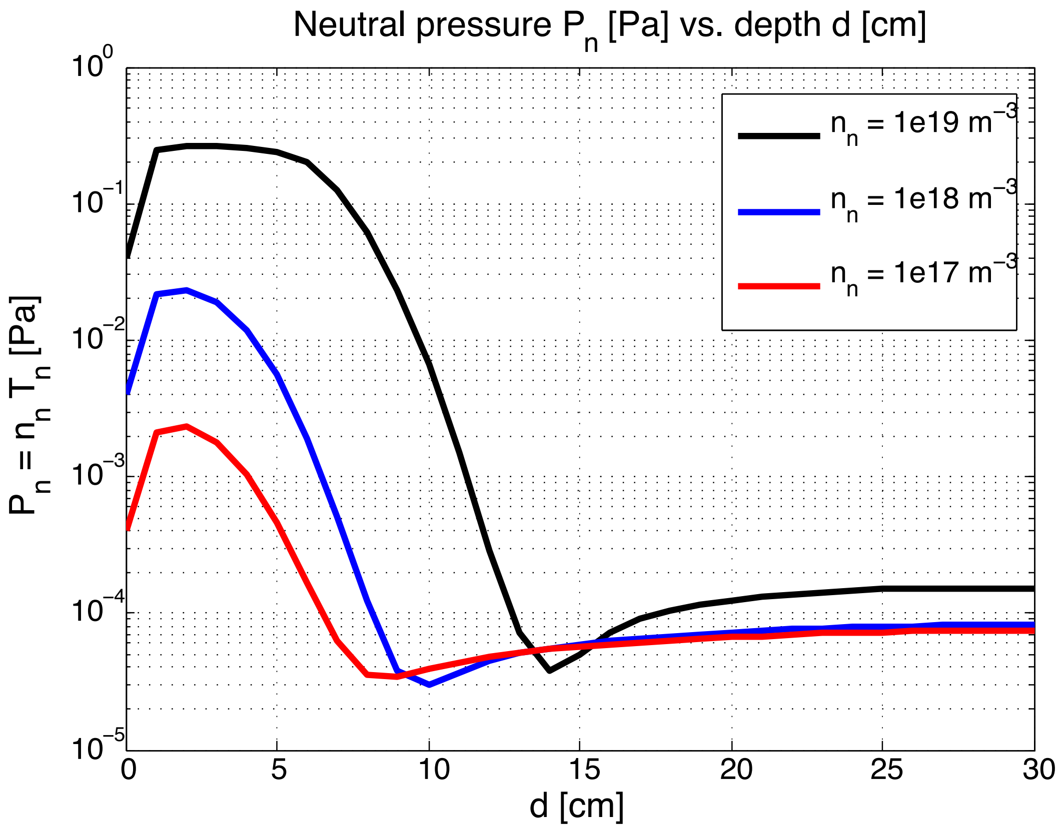

Figure 5.10: Calculated neutral pressure profiles as a function of varying the neutral density at the boundary. Note the impact of the neutral density boundary condition on the neutral pressure profile. A large neutral pressure gradient is observed in all simulations tried, primarily driven by significant neutral density gradients observed in Fig. 5.6. Additionally, a decreasing neutral density boundary condition tends to shift the location of the steep neutral pressure gradient closer to the boundary.

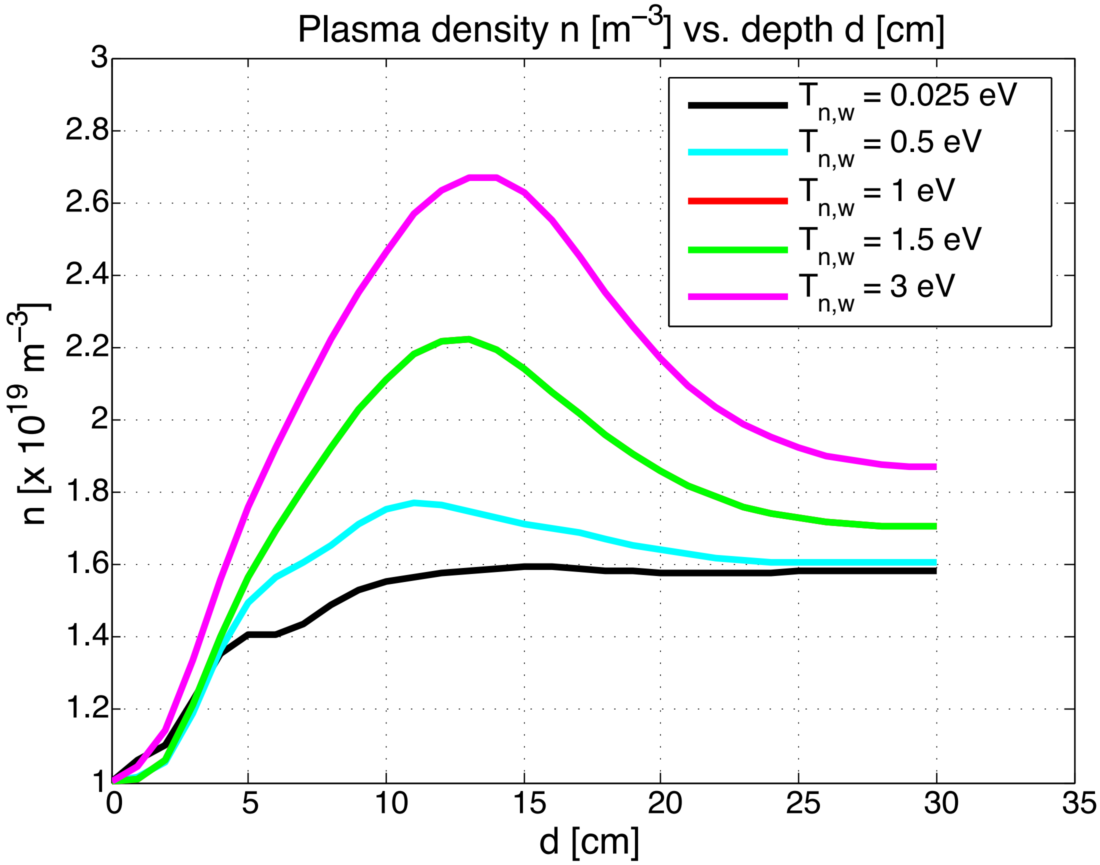

Figure 5.11: Calculated plasma density profiles as a function of varying the neutral temperature at the boundary. Note the impact of the neutral temperature boundary condition on the plasma density profile. A higher edge neutral temperature at the wall tends to increase the maximum plasma density observed. Additionally, the maximum plasma density appears mid-minor radius instead of near the magnetic axis at a depth $d \approx 30$ cm.

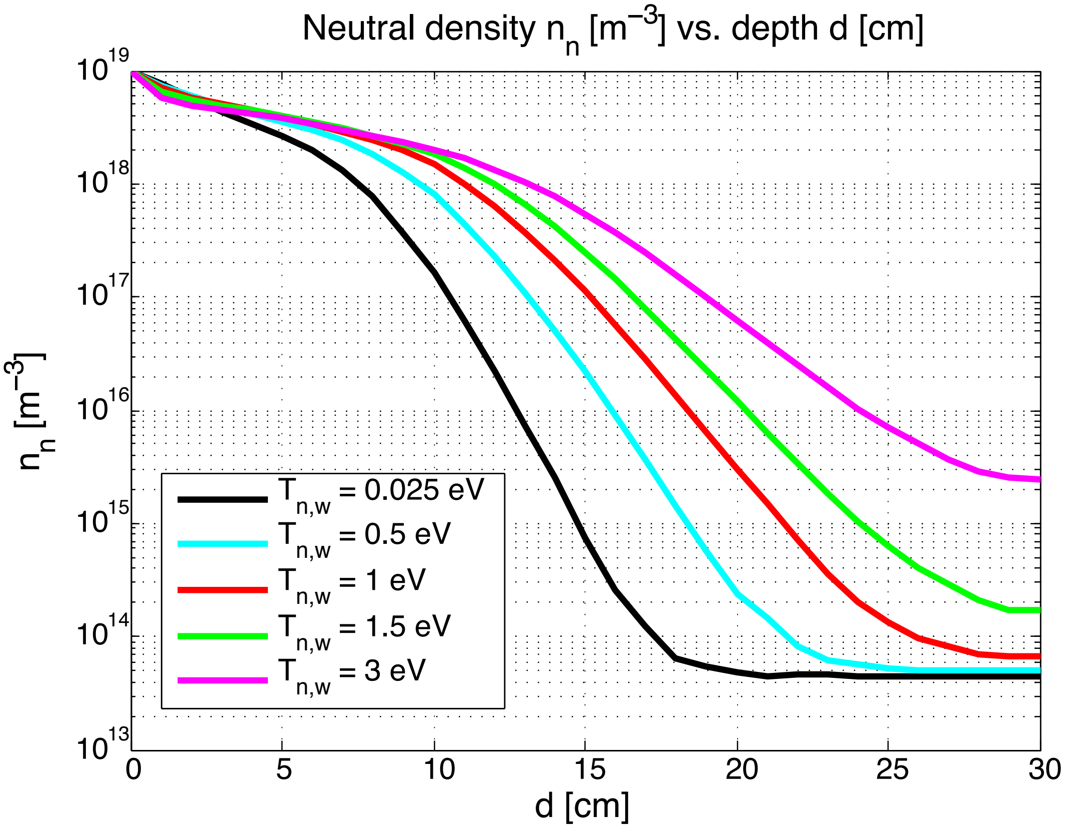

Figure 5.12: Calculated neutral density profiles as a function of varying the neutral temperature at the boundary. Note the impact of the neutral temperature boundary condition on the neutral density profile. Increasing the neutral temperature at the boundary tends to result in a greater penetration of neutrals into the core confinement region, providing a larger EI plasma source term that leads to the observed plasma density profiles in Fig. 5.11.

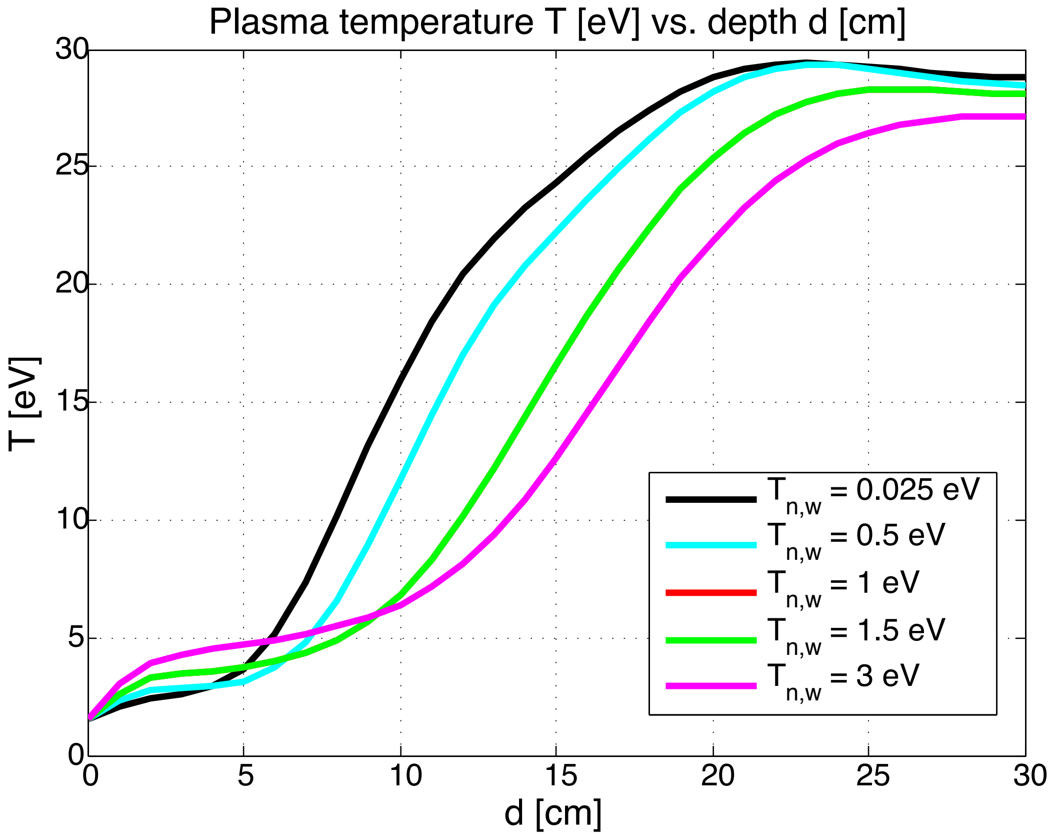

Figure 5.13: Calculated plasma temperature profiles as a function of varying the neutral temperature at the boundary. Note the impact of the neutral temperature boundary condition on the plasma temperature profile. The increased neutral penetration into the core confinement region as edge neutral temperature increases tends to suppress the plasma temperature profile over a larger volume when compared to cooler neutral temperature boundary conditions. Interestingly, warmer neutral boundary conditions lead to overall cooler plasma temperatures.

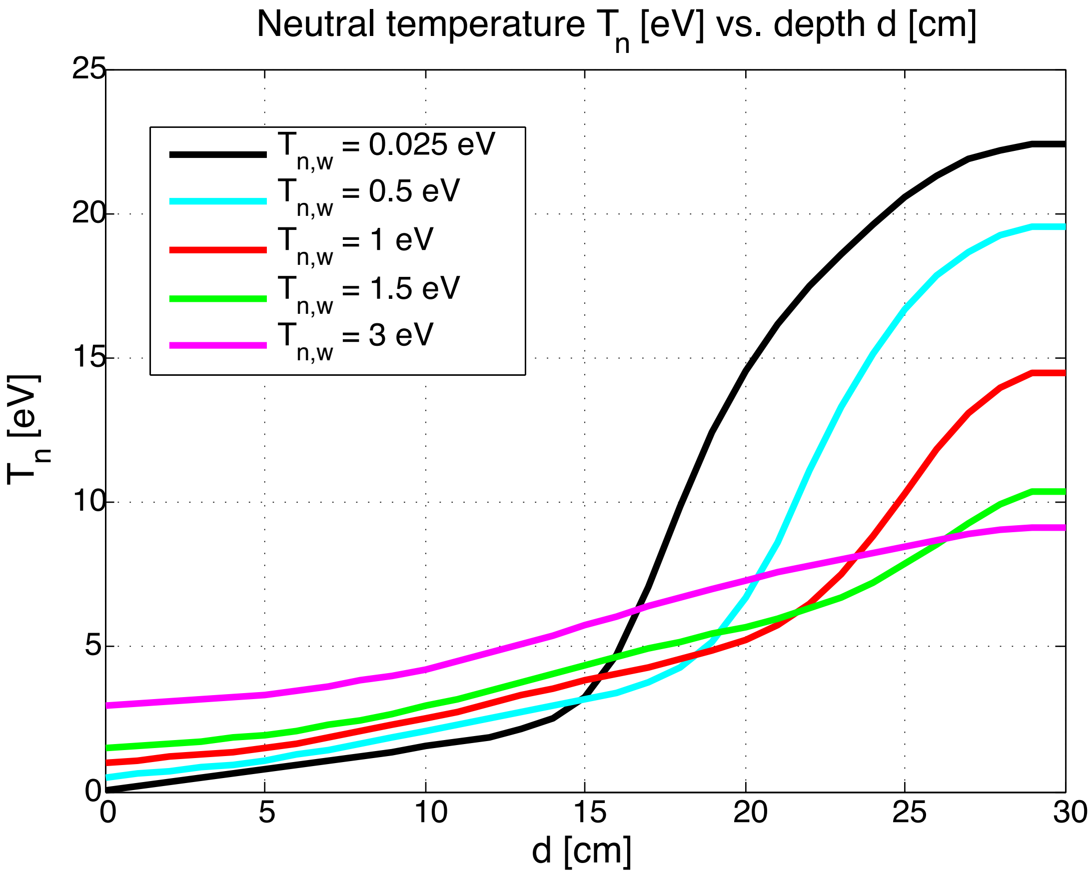

Figure 5.14: Calculated neutral temperature profiles as a function of varying the neutral temperature at the boundary. Note the impact of the neutral temperature boundary condition on the neutral temperature profile. The increased neutral penetration into the core confinement region as edge neutral temperature increases tends to reduce the maximum neutral temperature observed. The larger density of relatively cool neutrals in the core confinement region also results in lower maximum plasma temperatures as well as shown in Fig. 5.13.

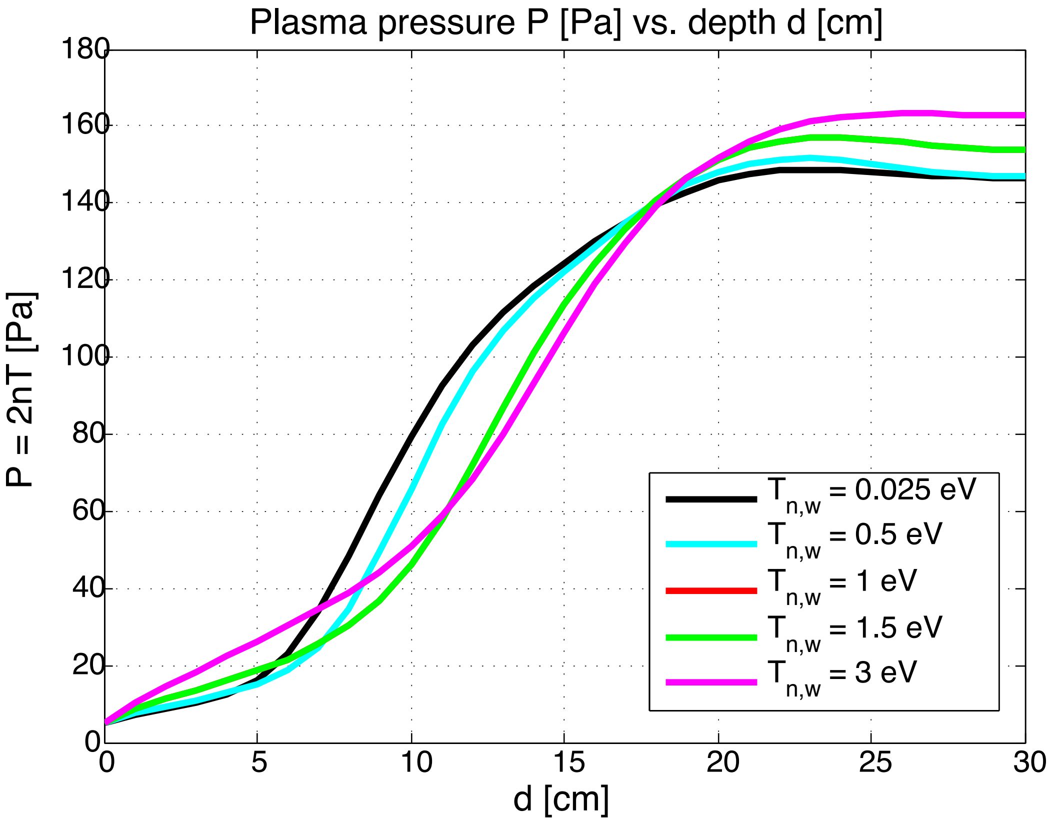

Figure 5.15: Calculated plasma pressure profiles as a function of varying the neutral temperature at the boundary. Note the impact of the neutral temperature boundary condition on the plasma pressure profile. Overall, the plasma pressure profiles do not vary significantly with changes in the neutral temperature boundary condition within the scanned range; however, the steepest plasma pressure gradients tend to move towards the core confinement region as the edge neutral temperature is increased. Additionally, higher boundary neutral temperatures tend to increase the maximum plasma pressure observed.

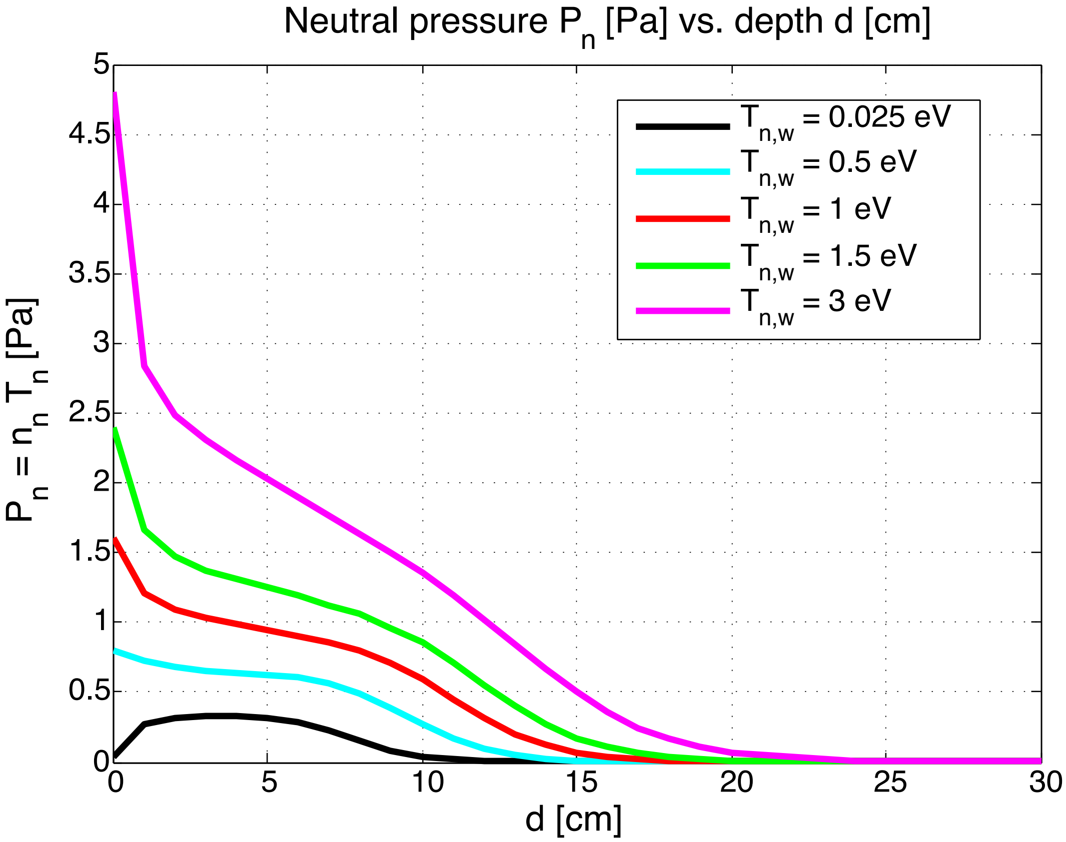

Figure 5.16: Calculated neutral pressure profiles as a function of varying the neutral temperature at the boundary. Note the impact of the neutral temperature boundary condition on the neutral pressure profile. Since the neutral density at the boundary is held constant for these simulations, increasing the boundary neutral temperature provides a corresponding increase in the neutral pressure at the boundary. It is clear the observed neutral pressure gradient becomes larger as the edge neutral temperature increases, which generates a larger $\nabla(p_n)$ flow expressed in Eq. 3.11 into the core confinement region. This larger neutral flow results in a higher neutral density throughout the simulation volume as seen in Fig. 5.12

.

shown in Fig. 4.55 and 4.57, while still maintaining decent agreement with the temporal evolution of the neutral density shown in Fig. 4.56. Results from other validation comparisons, such as those presented in Fig. 4.51 exhibit even better agreement with the temporal evolution of the neutral density at the TALIF measurement depth $d = 11$ cm. However, this improved agreement comes at the expense of worsened agreement with neutral temperature measurements, with a consistent underprediction of the neutral temperature by the simulation due to the choice of lower neutral temperature boundary conditions. Lastly, this simulation maintains the underprediction of the neutral density at a measurement depth $d = 18$ cm as seen in Fig. 4.58.

There are multiple implications from the observed level of agreement between experimental measurements and calculations making use of simulation parameters provided in Tab. 4.3. First, the best agreement between experimental neutral density measurements and simulations is found while using a neutral density boundary value $n_n = 1 \times 10^{17}$ m^{-3}. Revisiting SRIM simulation results and discussion and the simple sheath model in previous sections, this result may lend support to a plasma-facing wall that provides net pumping during the discharge, such that the recycling fraction $f_{re} < 1$. Net pumping during a discharge would correspondingly lead to a smaller influx of edge recycled neutral particles and a lower neutral density at the sheath entrance that is being used as the boundary value of the Extended-MHD simulation domain. It is surprising that significant pumping could still persist while operating in PDC mode that is used to produce many repeatable discharges for TALIF measurements. However, it is certainly possible that some amount of outgassing may occur during the inter-shot period while operating in PDC mode, or that steady-state recycling conditions are not reached during a discharge time $t = 2$ ms regardless of wall conditions. It should be noted that though the lower neutral density boundary condition produces the best agreement with experimental data, discrepancies still persist. As observed in the Fig. 4.58, the simulation tends to underpredict the neutral density at a depth $d = 18$ cm, whereas agreement is improved at a depth $d = 11$ cm. In general, steeper neutral density gradients are calculated within the measurement depth range $d = 11 - 18$ cm than is supported by measurements. Instead, a relatively flat spatial profile is observed experimentally, as seen in Fig. 4.4.

The observation that a lower neutral density boundary value improves agreement between simulations and experimental data is complicated by a second observation that the usage of relatively warm plasma and neutral temperature boundary conditions improves agreement with experimental measurements. At the end of spheromak decay during which non-zero TALIF measurements were made, toroidal currents $I_p < 3.5$ kA result in relatively modest poloidal magnetic fields that are responsible for thermal confinement. With limited magnetic confinement towards the end of spheromak decay, relatively low plasma temperatures and modest temperature gradients are observed, as shown in Fig. 4.57. Effectively, these temperatures converge to their boundary value within the depth range $d = 11-18$ cm, which is chosen to be relatively close to TALIF measurement values. The assumption that $T = T_n = 1$ eV at the boundary to produce relatively good agreement between simulations and experimental data has multiple implications for SRIM PMI calculations and sheath models discussed in previous sections. First, having the plasma and neutral boundary temperatures equal supports a view in which a sheath-accelerated ion is promptly backscattered from the aluminum oxide plasma-material interface with a significant fraction of its incident kinetic energy. In particular, the elastic scattering efficiency of sheath-accelerated deuterium ions impacting aluminum oxide provides a promptly backscattered energy fraction $f_e \approx 36.5\%$ that nearly cancels with the increase in the incident ion energy from sheath acceleration. Thus, assuming the dominant recycling method as prompt backscattering of sheath-accelerated ions supports the chosen boundary condition $T \approx T_n$ used in this simulation. However, this conclusion seemingly contradicts SRIM results that suggest a significant majority of incident ions implant themselves into the aluminum oxide target while assuming zero surface roughness. Non-zero surface roughness is expected in an experimental system and tends to decrease the prompt backscattering fraction from plasma-material interfaces below the zero surface roughness fraction. In short, SRIM results suggest that the majority of edge recycled neutral particles should be born as wall-thermalized diatomic molecules after being implanted, re-combining and thermalizing with the wall rather than as promptly backscattered, energetic monatomic atoms, which is observed in other magnetic fusion experiments [73].

An alternative explanation that may help reconcile this apparent discrepancy in results may instead be a common limitation of both the TALIF diagnostic system and the implemented plasma-neutral model in PSI-Tet: the presence diatomic deuterium molecules. In particular, the TALIF diagnostic system is insensitive to diatomic molecules and only measures monatomic, ground state deuterium atoms present in HIT-SI3 spheromak plasmas [62]. Similarly, the currently implemented plasma-neutral model in PSI-Tet only includes a single monatomic, deuterium neutral fluid with no tracking of excited states. Though comparisons between simulation and experimental results are well substantiated since both are considering a monatomic deuterium neutral species, it may be possible that there are significantly more neutral particles present in the system that exist in molecular form and/or in excited energy states. Especially towards the end of spheromak decay when plasma temperatures are relatively low and near boundary values, as seen in Fig. 4.23, many thermally desorbed diatomic molecules may not fully dissociated and ionized and instead could persist in a molecular and/or excited state.

The possible presence of diatomic molecules is especially important due to its impact on the choice of boundary conditions for xMHD plasma-neutral fluid simulations. If there are both monatomic and diatomic neutral particles generated from edge recycling with differing characteristic velocities at birth and excitation/ionization pathways, such a physical system would require much more sophisticated sheath, edge recycling, and dynamic plasma-neutral models than considered for this work. In particular, if monatomic and diatomic neutral particles are treated as separate fluids, a substantially lower monatomic neutral density boundary condition may be appropriate since the majority of edge recycled neutrals should reenter into the simulation domain as diatomic molecules. Thus, as a suggestion for future work, the currently implemented plasma-neutral model should likely be expanded into a three-fluid (plasma-monatomic-diatomic) neutral model for deuterium plasmas to more accurately capture plasma-neutral dynamics occurring in most plasma physics and fusion experiments. Ideally simulation results using an expanded, three-fluid plasma-netural model would be directly compared with experimental measurements of both the monatomic and diatomic neutral species in HIT-SI3 plasmas. This topic will be discussed in more detail in the next section.

However, prior to expanding the plasma-neutral model in PSI-Tet to include a diatomic neutral species, it should be noted that all simulation results shown in this work make use of fixed-boundary conditions, which can be modified in pursuit of improving agreement between simulations and experimental measurements. The variations in the choice of boundary conditions for this work has been focused on the density and temperature of both fluids since they are the quantities that TALIF diagnostic system measured that were non-zero. No appreciable bulk neutral flows were observed experimentally with the TALIF diagnostic system. As a result, zero-velocity boundary conditions for both species were used for all simulations presented, motivated by plasma-only simulations with PSI-Tet that made use of similar velocity boundary conditions [51]. However, as a suggestion for future work, introducing non-zero velocity boundary conditions and assessing the impact of varying plasma and neutral viscosity coefficients and models should be explored to determine whether such modifications improve agreement with experimental results and simulations.

In conclusion, the validation results presented in this section are promising, even though significant discrepancies persist. Within these discrepancies are opportunities for future work with the intent to ameliorate them. Collection of additional data concerning the composition of neutral particles in the HIT-SI3 experiment, improved physically motivated choices of boundary conditions, and improvements and/or enhancements of the plasma-neutral model all provide exciting avenues to pursue as a subject of future work.

Chapter 6

FUTURE WORK

6.1 Including diatomic molecules in plasma-neutral model

The plasma-neutral model currently implemented in PSI-Tet makes use of an MHD model for the plasma fluid and a single, ground state, monatomic neutral fluid [50]. Both excited and molecular species are not included in the current plasma-neutral formulation, but an effective ionization potential $\phi_{ion} \approx 33$ eV is used to capture the additional plasma energy losses during incomplete ionization events in a hydrogenic plasma. This model is used for all plasma-neutral simulations presented in this work, but it is argued that results from this work motivate the addition of a molecular neutral fluid for hydrogenic plasmas to more accurately capture plasma-neutral dynamics of interest in the HIT-SI3 experiment. Of course, it is also possible to introduce additional fluid species into the model as desired. For example, it may be desired to track particular excited states of interest instead of only considering ground state neutral species. However, it should be noted that each additional species with separate evolution equations will increase the complexity of the plasma-neutral model. Expanding the plasma-neutral model beyond its current scope necessarily relies on acquiring sufficient data to validate collisional operators and functional closures.

As discussed in previous sections, there are two main categories of neutral particles generated via edge recycling at a plasma-material interface: prompt backscattering and absorption/desorption, as shown in Fig. 2.2. Both previous literature [36] and results from SRIM calculations detail a natural division between edge recycled neutral particles generated via either method based on their characteristic kinetic energies re-entering the plasma confinement region, and for hydrogenic plasmas, being in either atomic or molecular form. In particular for hydrogenic plasmas, promptly-backscattered neutral particles tend to be energetic, monatomic neutral atoms capable of penetrating far into the plasma before an EI or CX plasma-neutral reaction occurs. On the other hand, sheath-accelerated ions that are implanted into the Al_2O_3 plasma-material interface in HIT-SI3 will tend to recombine into diatomic, deuterium molecules and thermalize with the wall. Correspondingly, when these wall-thermalized neutral particles are desorbed back into the plasma confinement chamber via edge recycling, they have much lower characteristic velocities than promptly backscattered neutral species. Both the lower velocities at birth and the different plasma-molecular reaction pathways result in different penetration lengths and plasma energy losses than monatomic neutral atoms.

After either species of edge recycled neutral particles re-enter the plasma confinement region, the potential plasma-neutral reaction pathways are diverse. The current plasma-neutral model captures key reactions of interest between a monatomic deuterium species and plasma constituents, such as resonant charge exchange with plasma ions and electron-impact ionization while with plasma electrons. However, the potential plasma-neutral reaction pathways for molecular deuterium interacting with plasma ions and electrons is complex and varied, as shown with a few example reactions in Fig. 2.3. Of course, it not suggested to attempt to capture all potential reaction pathways with a plasma-neutral fluid model as it will quickly become intractable. Instead, it is suggested to first expand the model to include three fluids: 1) an MHD plasma fluid, 2) a monatomic deuterium neutral fluid and 3) a diatomic deuterium neutral fluid. This new plasma-neutral model formulation can be derived in a similar fashion as presented in Appendix A starting with a four fluid formulation (i.e. plasma ions, plasma electrons, monatomic atoms, diatomic molecules) and subsequently formulate a three-fluid model using the typical MHD plasma assumptions and taking asymptotic limits. Performing the derivation in this fashion necessarily provides the four-fluid formulation that separates plasma ions and electrons should a two-fluid plasma model be desired over a single-fluid MHD plasma model.

Formulating a plasma-neutral model that includes a diatomic, deuterium fluid will necessarily require the identification of all plasma-neutral reaction pathways of interest and isolating the dominant reactions to include in a reduced model. Subsequently, it will be necessary to follow the process in Ref. [50] of calculating collision operators and velocity moments of the Boltzmann equation, shown in Eq. 2.1, with the addition of a new molecular species. In short, this new formulation will include the electron-impact ionization, resonant charge exchange, and radiative recombination reactions included in the current plasma-neutral model, but will include new coupling and reaction terms for all species primarily driven by the addition of molecular dissociation that can produce both monatomic neutral and plasma species depending on the particular reaction pathway, such as the examples shown in Fig. 2.3.

Ultimately, provided with a plasma-neutral model that includes diatomic, deuterium molecules, this model should first be verified and then validated with experimental measurements of the plasma, monatomic neutral, and diatomic neutral species in an experimental system of interest. Measurements of relevant characteristics of these species, especially in the edge region of any plasma physics experiment, will be critical for quantifying the validity of this physical model capturing plasma-neutral dynamics entirely within a fluid framework.

6.2 Continuing analysis on impact of boundary conditions

The plasma-neutral simulations of decaying spheromak configurations that are the focus of this work make use of zero-velocity boundary conditions. Fixed boundary conditions are also used for the density and temperature of both species at the boundary; however, these values were varied in pursuit of improved agreement with experimental TALIF measurements. It is argued an expanded exploration of the impact of chosen boundary conditions on plasma-neutral simulations should be undertaken as a subject of future work. As has been emphasized in this work, it is preferable to physically motivate the choice of boundary conditions as much as possible using available data and theoretical models. Otherwise, it is difficult to determine whether a particular physical model accurately captures a physical system of interest or if observed levels of agreement are coincidental and the result of unreasonable choices of boundary conditions. Of course, since physical models and/or experimental data used to physically motivate the choice of boundary conditions are likely incomplete, it is possible to overconstrain the choice of boundary conditions to what is defined as reasonable for a given physical model and experimental data set. In short, it is most important to gather as much meaningful data as possible to provide a rich data set for comparisons to both physical models and simulations.

With this qualification on physically motivating the choice of boundary conditions, it is suggested to expand the scope of study of the impact of chosen boundary conditions on simulation results by first allowing for non-zero normal velocities for both species at the sheath entrance, which is used as the boundary of the xMHD simulation domain. Revisiting the control volume shown in Fig. 3.7 and the functional expressions for the flux of ions and neutrals at the sheath entrance in Eqs. 3.37 - 3.38, these functional expressions assume a saturation of the Bohm criterion such that the incident ions enter the sheath region at their sound speed [36]. Similarly, it is assumed that neutrals exit the sheath region at their sound speed as well. Thus, as a first exploration of the impact of non-zero normal velocities entering and exiting the sheath entrance, one may set the plasma velocity at the boundary $v = c_s\hat{n}$ where $\hat{n}$ is a outwardly pointing normal vector on the surface of the simulation domain. Similarly, one can set $v_n = c_{s,n}(-\hat{n})$ for the neutral fluid at the sheath entrance. The value of each of these velocities should be self-consistently set by the choice of plasma and neutral temperatures at the boundary.

Additionally, the exploration of non-zero normal velocity boundary conditions for plasma-neutral simulations would allow for more physically-informed boundary conditions should a new molecular fluid be added to the plasma-neutral model, as described in the previous section. The natural division between promptly-backscattered monatomic atoms and thermally desorbed molecules provides motivation to independently set self-consistent boundary conditions for the density, temperature, and normal velocities for both neutral species independently from one another. This set of boundary conditions will likely produce better agreement with experimental measurements while also being more physically informed.

Lastly, more sophisticated models for the sheath region should be explored beyond the simple Bohm model used in this work [36]. The model used in this work assumes an unmagnetized, quasineutral, thermalized ($T_i \approx T_e$) bulk plasma interacting with a solid plasma-material interface electrostatically. With the introduction of magnetic fields, plasma ions and electrons are subject to the Lorentz force that constrains charged particle trajectories perpendicular to the magnetic field direction. Correspondingly, plasma magnetization tends to reduce perpendicular transport of charge particles across magnetic fields while not having a significant impact on transport parallel to the magnetic field direction. Accounting for the effect of plasma magnetization on charged particle transport may be important for setting the incoming plasma flux into the sheath region, which is subsequently acted on by the electrostatic sheath potential. However, before pursuing a more sophisticated sheath model that includes the effects of magnetic fields on plasma species, it is important to construct a physical picture of the edge plasma and sheath region that accurately accounts for characteristic scale lengths in a given experimental system. In particular, the main sheath region is on the order of a Debye length, whereas the pre-sheath region is on the order of ten Debye lengths as shown in Fig. 2.1. Depending on the magnetic field strength and characteristic velocities of charged particles in the edge plasma region of an experimental system, the size of gyroradii may either justify a unmagnetized view of the sheath region, when electron (and ion) gyroradii are significantly larger than the sheath region, or a more complicated model that accounts for gyromotion that occurs on the scale of the sheath and presheath region. Different models described in [36] provide progressively more complicated edge plasma models that could be used for a given experimental system of interest as appropriate for characteristic plasma parameters.

6.3 Driven HIT-SI and HIT-SI3 plasma-neutral simulations

The focus of this work is on performing comparisons between TALIF neutral measurements and plasma-neutral simulations in the HIT-SI3 experiment. Since non-zero TALIF measurements were only made during spheromak decay, performing decaying spheromak simulations was the primary focus on this work. However, it is desired to perform plasma-neutral simulations of the driven phase of a HIT-SI3 discharge when the fully-inductive, non-axisymmetric helicity injectors are forming and sustaining spheromak configurations against resistive decay. Acquiring non-zero data during the driven phase of the discharge is highly desirable to enable comparisons to plasma-neutral simulations of this time period.

It is also desired to simulate localized gas injection in the helicity injector assemblies, which could be achieved by using mixed boundary conditions. For example, a locally higher neutral density boundary condition with a set inflow velocity could be used to mimic gas injection from the high-speed puff valves on the experimental system. Also, including localized pumping of neutrals out of the diagnostic midplane holes and pumping cans on HIT-SI3 into a surge volume is desired to better capture the experimental system. The flexibility of the PSI-Tet framework enables the capability of simulating the full, three-dimensional simulation domain or just mimicking the effects of localized pumping by using locally lower neutral density boundary conditions, for example. Ultimately, in pursuing a choice of boundary conditions and parameters for a simulation that is sufficiently representative of the physical system, a validated computational tool can provide insights into optimizing the performance of an experimental system of interest. In particular, this computational tool should now be used to optimize sustained spheromak performance in the current experimental apparatus. After additional development and refinement, this computational tool could also be used to predicatively optimize the performance of future experiments that hope to demonstrate favorable scaling towards higher temperature, fusion-relevant sustained spheromak plasma conditions.

BIBLIOGRAPHY

[1] Intergovernmental Panel on Climate Change. Climate Change 2014: Synthesis Report, 2015.

[2] United Nations. Paris Agreement, 2015.

[3] United Nations. Kyoto Protocol to the United Nations Framework Convention on Climate Change, 1998.

[4] V. Ramanathan and Y. Feng. Air pollution, greenhouse gases and climate change: Global and regional perspectives. *Atmospheric Environment*, 43:37–50, 2009.

[5] M. Kampa and E. Castanas. Human health effects of air pollution. *151*, pages 362–367, 2008.

[6] J. Fenger. Air pollution in the last 50 years – From local to global. *Atmospheric Environment*, 43:13–22, 2009.

[7] B. Brunekreef. Air pollution and health. *The Lancet*, 360, October 2002.

[8] U.S. Energy Information Administration. International Energy Outlook 2017, September 2017.

[9] P. Denholm, E. Ela, B. Kirby, and M. Milligan. The Role of Energy Storage with Renewable Electricity Generation. Technical Report NREL/TP-6A2-47187, National Renewable Energy Laboratory, January 2010.

[10] Seattle City Light. Fuel Mix: How Seattle City Light electricity is generated, 2013. http://www.seattle.gov/light/FuelMix/.

[11] Z.S. Hartwig and Y.A. Podpaly. Magnetic Fusion Energy Formulary, February 2014. http://www.psfc.mit.edu/research/MFEFormulary/.

[12] J. Freidberg. *Plasma Physics and Fusion Energy.* Cambridge University Press, 2007.

[13] J. Wesson. *Tokamaks.* Oxford University Press, fourth edition, 2011.

[14] ITER Communication. ITER Council endores updated project schedule, https://www.iter.org/newsline/-/2588, November 2016.

[15] J. Freidberg. *Ideal MHD.* Cambridge University Press, 2014.

[16] D.A. Sutherland, et al. The dynomak: An advanced spheromak reactor concept with imposed-dynamo current drive and next generation nuclear power technologies. *Fusion Eng. Des.*, 89(4):412–425, 2014.

[17] ITER Organization. Facts & Figures. https://www.iter.org/factsfigures.

[18] Max Planck Institute for Plasma Physics. Wendelstein W7-X Stellarator. http://www.ipp.mpg.de/16900/w7x.

[19] P.M. Bellan. *Spheromaks: A Practical Application of Magnetohydrodynamic Dynamos and Plasma Self-Organization.* Imperial College Press, 2000.

[20] J.B. Taylor. Relaxation of Toroidal Plasma and Generation of Reverse Magnetic Fields. *Physical Review Letters*, 33(19), November 1974.

[21] Mitchell A. Berger. Introduction to magnetic helicity. *Plasma Phys. Control. Fusion*, 41:B167–B175, 1999.

[22] J.M. Finn and T.M. Antonsen Jr. Comments on Plasma Physics and Controlled Fusion. *Comments Plasma Phys. Controlled Fusion*, 9, 1985.

[23] Mitchell A. Berger and George B. Field. The topological properties of magnetic helicity. *J. Fluid Mech.*, 147:133–148, 1984.

[24] T.R. Jarboe, B.A. Nelson, and D.A. Sutherland. A mechanism for the dynamo terms to sustain closed-flux current, including helicity balance, by driving current which crosses the magnetic field. *Phys. Plasmas*, 22(072503), 2015.

[25] Thomas R Jarboe. Review of spheromak research. *Plasma Phys. Control. Fusion*, 36:945–990, 1994.

[26] B.S. Victor, et al. Sustained spheromaks with ideal n = 1 kink stability and pressure confinement. *Phys. Plasmas*, 21(082504), 2014.

[27] T.R. Jarboe, et al. Imposed-dynamo current drive. *Nucl. Fusion*, 52(083017), 2012.

[28] T.G. Cowling. The magnetic fields of sunspots. *Mon. Notices Roy. Astron. Soc.*, 94:39–48, 1933.

[29] B. Hudson, et al. Energy confinement and magnetic field generation in the SSPX spheromak. *Physics of Plasmas*, 15(056112), 2008.

[30] A.C. Hossack. *A Study of Ion Dynamics in HIT-SI Using Ion-Doppler Spectroscopy.* PhD thesis, University of Washington, 2015.

[31] A.C. Hossack, et al. Plasma response to sustainment with imposed-dynamo current drive in HIT-SI and HIT-SI3. *Nucl. Fusion*, 57(076026), 2017.

[32] A.C. Hossack, et al. Reduction of plasma density in the Helicity Injected Torus with Steady Inductance experiment by using a helicon pre-ionization source. *Rev. Sci. Instrum.*, 84(103506), 2013.

[33] C. Day, D. Murdoch, and R. Pearce. The vacuum systems of ITER. *Vacuum*, 83(773-778), 2008.

[34] B. Pegourie, et al. Supersonic gas injection on Tore Supra. *Journal of Nuclear Materials*, 313-316:539–542, 2003.

[35] S.L. Milora, W.A. Houlberg, L.L. Lengyel, and V. Mertens. Pellet Fuelling. *Nucl. Fusion*, 35(6):657–754, 1995.

[36] P.C. Stangeby. *The Plasma Boundary of Magnetic Fusion Devices.* Taylor & Francis Group, 2000.

[37] R.J. Goldston and P.H. Rutherford. *Introduction to Plasma Physics.* Taylor & Francis Group, 1995.

[38] E.T. Meier. *Modeling Plasmas with Strong Anisotropy, Neutral Fluid Effects, and Open Boundaries.* PhD thesis, University of Washington, 2011.

[39] D. Brunner, et al. Surface heat flux feedback controlled impurity seeding experiments with Alcator C-Mod's high-Z vertical target plate divertor: performance, limitations and implications for fusion power reactors. *Nucl. Fusion*, 57(086030), 2017.

[40] R. J. Fonck, A.T. Ramsey, and R.V. Yelle. Multichannel grazing-incidence spectrometer for plasma impurity diagnosis: SPRED. *Applied Optics*, 12:2115–2123, 1982.

[41] A.S. Kukushkin, et al. The key role of SOLPS modeling. *Fusion Eng. Des.*, 86(12):2865–2873, 2011.

[42] A. Yu. Pigarov, et al. Multi-fluid transport code modeling of time-dependent recycling in ELMy H-Mode. *Phys. Plasmas*, 21(062514), 2014.

[43] S. Wiesen, et al. The new SOLPS-ITER code package. *Jou. Nuc. Materials*, 463:480–484, 2015.

[44] R. Simonini, et al. Models and Numerics in the Multi-Fluid 2-D Edge Plasma Code EDGE2D/U. *Contrib. Plasma Phys.*, 34(2-3):368–373, 1993.

[45] C. Guillemaut, et al. Influence of atomic physics on EDGE2D-EIRENE simulations of JET divertor detachment with carbon and beryllium/tungsten plasma-facing components. *Nucl. Fusion*, 54(9), 2014.

[46] D. Harting, et al. Validating the 3D edge code EMC3-EIRENE against 2D simulations with EDGE2D-EIRENE for JET single null configurations. *Jou. Nuc. Materials*, 415(1):S540–S544, 2011.

[47] Y. Feng, et al. Recent Improvements in the EMC3-EIRENE Code. *Contrib. Plasma Phys.*, 54(4-6):426–431, 2014.

[48] V.A. Izzo. A numerical investigation of the effects of impurity penetration depth on disruption mitigation by massive high-pressure gas jet. *Nucl. Fusion*, 46(5):541–547, 2006.

[49] V.A. Izzo, et al. Magnetohydrodynamic simulations of massive gas injection into Alcator C-Mod and DIII-D Plasmas. *Phys. Plasmas*, 15(5), 2008.

[50] E.T. Meier and U. Shumlak. A general nonlinear fluid model for reacting plasma-neutral mixtures. *Phys. Plasmas*, 19(072503), 2012.

[51] C.J. Hansen. *MHD Modeling in Complex 3D Geometries: Towards Predictive Simulation of SIHI Current Drive.* PhD thesis, University of Washington, 2014.

[52] C. Hansen, et al. Simulation of injector dynamics during steady inductive helicity injection current drive in the HIT-SI experiment. *Phys. Plasmas*, 22(042505), 2015.

[53] C. Hansen, et al. Numerical studies and metric development for validation of magnetohydrodynamic models on the HIT-SI experiment. *Phys. Plasmas*, 22(056105), 2015.

[54] K. Morgan. *Finite-beta simulations of HIT-SI and HIT-SI3 using the NIMROD code.* PhD thesis, University of Washington, 2018.

[55] R.D. Hazeltine, et al. Analytical calculation of neutral transport and its effect on ions. *Nucl. Fusion*, 32(1), 1992.

[56] P. Helander and S.I. Krasheninnikov and P.J. Catto. Fluid equations for a partially ionized plasma. *Phys. Plasmas*, 1(10):3174–3180, 1994.

[57] P.J. Catto. A short mean-free path, coupled neutral-ion transport description of a tokamak edge plasma. *Phys. Plasmas*, 1(6):1936–1943, 1994.

[58] G.P. Zank. Interaction of solar wind with the local interstellar medium: a theoretical perspective. *Space Science Reviews*, 89(3-4):413–688, 1999.

[59] S.I. Braginskii. Transport processes in a plasma. *In M.A. Leontovich, editor, Reviews of Plasma Physics*, 1:205–311, 1965.

[60] A.S. Kukushkin, et al. Effect of neutral transport on ITER divetor performance. *Nucl. Fusion*, 45(7), 2005.

[61] A. Loarte, et al. Chapter 4: Power and particle control. *Nucl. Fusion*, 47:S203–S263, 2007.

[62] R.M. Magee, et al. A two photon absorption laser induced fluorescence diagnostic for fusion plasmas. *Rev. Sci. Instrum.*, 83(10D701), 2012.

[63] T. Kajiwara, et al. Application of two-photon-excited laser-induced fluorescence to atomic hydrogen measurements in the edge region of high-temperature plasmas. *Rev. Sci. Instrum.*, 62:2345–2349, 1991.

[64] D. Elliott, et al. Two-photon LIF on the HIT-SI experiment: Absolute density and temperature measurements of deuterium neutrals. *Rev. Sci. Instrum.*, 2016.

[65] M.G.H. Boogaarts, et al. Quantitative two-photon laser-induced fluorescence measurements of atomic hydrogen densities, temperatures, and velocities in an expanding thermal plasma. *73*, 2002.

[66] J. Bokor, et al. Two-photon excitation of the n = 3 level in h and d atoms. *Phys. Rev. A*, 24(612), 1981.

[67] K. Niemi, et al. Absolute calibration of atomic density measurements by laser-induced fluorescence spectroscopy with two-photon excitation. *J. Phys. D: Applied Physics*, 34:2330–2335, 2001.

[68] Stephen Jardin. *Computational Methods in Plasma Physics.* CRC Press, 2010.

[69] Youcef Saad and Martin H. Schultz. Gmres: A generalized minimal residual algorithm for solving nonsymmetric linear systems. *SIAM J. Sci. Stat. Comput.*, 7(3), 1986.

[70] M. Greenwald. Verification and validation for magnetic fusion. *Phys. Plasmas*, 17(058101), 2010.

[71] William L. Oberkampf and Christopher J. Roy. *Verification and Validation in Scientific Computing.* Cambridge University Press, 2010.

[72] J. Ziegler. SRIM and TRIM, http://www.srim.org/.

[73] E.M. Hollmann, et al. Spectroscopic measurement of atomic and molecular deuterium fluxes in the DIII-D plasma edge. *Plasma Phys. Control. Fusion*, 48:1165–1180, 2006.

[74] D.P. Stotler, et al. Midplane neutral density profiles in the national spherical torus experiment. *Phys. Plasmas*, 22(082506), 2015.

[75] Fabrice Schlegel. Understanding Stabilization Methods, https://www.comsol.com/blogs/understanding-stabilization-methods/.

Appendix A

TWO-FLUID (PLASMA-NEUTRAL) MODEL DERIVATION

This section details the derivation of two-fluid (plasma-neutral) model from the starting three-fluid (electron-ion-neutral) model provided in [50] by taking appropriate asymptotic limits to derive an MHD plasma model and applying other assumptions as required.

To derive an MHD plasma model, we take various asymptotic limits when considered separate evolution equations for both the ion and electron fluids. First, we elect to neglect electron mass such that $m_e \to 0$ while assuming electron inertia plays a small role in the system when compared to the inertia of ion fluid. Additionally, it is assume that vacuum permittivity $\epsilon_o \to 0$, restricting the model to low frequency dynamics. From Gauss' Law, $\epsilon_o \nabla \cdot \vec{E} = \rho_c = 0$, which leads to quasineutral plasma such that $\rho_c = Zen_i - en_e = 0$. A hydrogenic plasma (i.e. $Z = 1$) is assumed for this implementation, which can be easily modified by allowing for $Z > 1$. Additionally, it is assumed that the only neutral particles present in the system have approximately the same mass as the plasma species $m_i = m_n$, such that the only neutral particles we include in the implemented model are monatomic deuterium atoms while still neglecting the electron mass. Lastly, we introduce the definition of current density $\vec{J} \equiv ne(\vec{v_i} - \vec{v_e}) = ne(\vec{v} - \vec{v_e})$ where $\vec{v_i} \equiv \vec{v}$. Though similar derivations have been presented in [38] and [50], the strong form expressions derived in this section will be specifically structured for implementation in the PSI-Tet code after weak formulations are calculated in Appendix B.

Density evolution

Starting from the three-fluid equations provided in [50], the separate density evolution equations for ion, electron and neutral are provided in Eqs. A.1 - A.3.

$$\frac{\partial n_i}{\partial t} + \nabla \cdot (n_i \vec{v_i}) = \Gamma_i^{ion} - \Gamma_n^{rec} \tag{A.1}$$

$$\frac{\partial n_e}{\partial t} + \nabla \cdot (n_e \vec{v_e}) = \Gamma_i^{ion} - \Gamma_n^{rec} \tag{A.2}$$

$$\frac{\partial n_n}{\partial t} + \nabla \cdot (n_n \vec{v_n}) = \Gamma_n^{rec} - \Gamma_i^{ion} \tag{A.3}$$

Applying the asymptotic assumption of $\epsilon_o \rightarrow 0$ yields the condition of quasineutrality, such that for a hydrogenic plasma $n_i = n_e \equiv n$. From inspection, it is only necessary to evolve the density of one plasma species since the density of one plasma species is equal to the density of the other plasma species in a quasineutral, hydrogenic plasma. Thus, the two-fluid (plasma-neutral) continuity equations while using the definition $\vec{v_i} \equiv \vec{v}$ are provided in Eqs. A.4-A.5.

$$\frac{\partial n}{\partial t} + \nabla \cdot (n \vec{v}) = \Gamma_i^{ion} - \Gamma_n^{rec} \tag{A.4}$$

$$\frac{\partial n_n}{\partial t} + \nabla \cdot (n_n \vec{v_n}) = \Gamma_n^{rec} - \Gamma_i^{ion} \tag{A.5}$$

Momentum evolution

The three-fluid momentum evolution equations for each species is provided in Eqs. A.6 - A.8.

$$\frac{\partial}{\partial t}(m_i n_i \vec{v_i}) + \nabla \cdot (m_i n_i \vec{v_i}\vec{v_i} + \mathbf{P_i}) = q_i n_i(\vec{E} + \vec{v_i} \times \vec{B}) + \vec{R}_i^{ie} + \vec{R}_i^{in} + \Gamma_i^{ion} m_i \vec{v_n} \tag{A.6}$$
$$- \Gamma_n^{rec} m_i \vec{v_i} + \Gamma^{cx} m_i (\vec{v_n} - \vec{v_i}) + \vec{R}_{in}^{cx} - \vec{R}_{ni}^{cx}$$

$$\frac{\partial}{\partial t}(m_e n_e \vec{v_e}) + \nabla \cdot (m_e n_e \vec{v_e}\vec{v_e} + \mathbf{P_e}) = -q_e n_e(\vec{E} + \vec{v_e} \times \vec{B}) - \vec{R}_i^{ie} + \vec{R}_e^{en} \tag{A.7}$$
$$+ \Gamma_i^{ion} m_e \vec{v_n} - \Gamma_n^{rec} m_e \vec{v_e}$$

$$\frac{\partial}{\partial t}(m_n n_n \vec{v_n}) + \nabla \cdot (m_n n_n \vec{v_n}\vec{v_n} + \mathbf{P_n}) = -\vec{R}_i^{in} - \vec{R}_e^{en} + \Gamma_n^{rec}(m_i\vec{v_i} + m_e\vec{v_e}) \tag{A.8}$$
$$- \Gamma_i^{ion} m_n \vec{v_n} + \Gamma^{cx} m_i(\vec{v_i} - \vec{v_n}) - \vec{R}_{in}^{cx} + \vec{R}_{ni}^{cx}$$

The MHD plasma momentum evolution equation is derived while considering the separate momentum evolution equations for the ions and electrons provided in Eq. A.6 and Eq. A.7, respectively. First, the ion and electron momentum equations are summed as follows,

$$\frac{\partial}{\partial t}(m_i n_i \vec{v_i}) + \frac{\partial}{\partial t}(m_e n_e \vec{v_e}) + \nabla \cdot (m_i n_i \vec{v_i}\vec{v_i} + \mathbf{P_i}) + \nabla \cdot (m_e n_e \vec{v_e}\vec{v_e} + \mathbf{P_e}) \tag{A.9}$$
$$= q_i n_i(\vec{E} + \vec{v}_i \times \vec{B}) + \vec{R}_i^{ie} + \vec{R}_i^{in} + \Gamma_i^{ion} m_i \vec{v}_n - \Gamma_n^{rec} m_i \vec{v}_i + \Gamma^{cx} m_i(\vec{v}_n - \vec{v}_i) + \vec{R}_{in}^{cx} - \vec{R}_{ni}^{cx}$$
$$- q_e n_e(\vec{E} + \vec{v}_e \times \vec{B}) - \vec{R}_i^{ie} + \vec{R}_e^{en} + \Gamma_i^{ion} m_e \vec{v}_n - \Gamma_n^{rec} m_e \vec{v}_e$$

We define the following to simplify mathematical expression,

$$m_i n \vec{v}\vec{v} + \mathbf{P} = \sum_{\alpha=i,e} (m_\alpha n \vec{v_\alpha}\vec{v_\alpha} + \mathbf{P}_\alpha)$$

where α denotes either the ion or electron species parameters. Using this expression and substituting into Eq. A.9 yields the following

$$\frac{\partial}{\partial t}(m_i n_i \vec{v_i}) + \frac{\partial}{\partial t}(m_e n_e \vec{v_e}) + \nabla \cdot (m_i n \vec{v}\vec{v} + \mathbf{P}) = (q_i n_i - q_e n_e)\vec{E} \tag{A.10}$$
$$+ (q_i n_i \vec{v_i} - q_e n_e \vec{v_e}) \times \vec{B} + \vec{R}_i^{in} + \vec{R}_e^{en} + \Gamma_i^{ion} \vec{v}_n (m_i + m_e) - \Gamma_n^{rec}(m_i \vec{v_i} + m_e \vec{v_e})$$
$$+ \Gamma^{cx} m_i(\vec{v}_n - \vec{v}_i) + \vec{R}_{in}^{cx} - \vec{R}_{ni}^{cx}$$

Using earlier definitions, the previous expression can be simplified into the following form,

$$\frac{\partial}{\partial t}(m_i n \vec{v}) + \nabla \cdot (m_i n \vec{v}\vec{v} + \mathbf{P}) = \vec{J} \times \vec{B} + \vec{R}_i^{in} + \vec{R}_e^{en} + \Gamma_i^{ion} m_i \vec{v_n} - \Gamma_n^{rec} m_i \vec{v} \tag{A.11}$$
$$+ \Gamma^{cx} m_i(\vec{v_n} - \vec{v}) + \vec{R}_{in}^{cx} - \vec{R}_{ni}^{cx}$$

For implementation into the PSI-Tet code, it is desired to isolate velocity evolution since velocity is the fundamental quantity of interest to evolve in PSI-Tet for this portion of the model; mass density is already evolved in the continuity portion of the model. The velocity advance can be isolated by noting that, from the chain rule

$$\frac{\partial}{\partial t}(m_i n \vec{v}) = m_i[n\frac{\partial \vec{v}}{\partial t} + \vec{v}\frac{\partial n}{\partial t}] \tag{A.12}$$

and from relevant vector identities that

$$\nabla \cdot (m_i n\vec{v}\vec{v}) = m_i[(\nabla \cdot (n\vec{v}))\vec{v} + (n\vec{v} \cdot \nabla)\vec{v}] \tag{A.13}$$

and substitute into the simplified expression above to yield

$$nm_i[\frac{\partial \vec{v}}{\partial t} + \vec{v} \cdot \nabla\vec{v}] = -\nabla \cdot \mathbf{P} + \vec{J} \times \vec{B} + \vec{R}_i^{in} + \vec{R}_e^{en} + \Gamma_i^{ion} m_i(\vec{v}_n - \vec{v}) \tag{A.14}$$
$$+ \Gamma^{cx} m_i(\vec{v}_n - \vec{v}) + \vec{R}_{in}^{cx} - \vec{R}_{ni}^{cx}$$

where plasma continuity has been used to simplify the express, such that $\frac{\partial n}{\partial t} + \nabla \cdot (n\vec{v}) = \Gamma_i^{ion} - \Gamma_n^{rec}$. Lastly, the assumption that plasma-neutral frictional terms are small in plasmas that are just a few percent ionized [37] is used to neglect the $\vec{R}_i^{in}$and $\vec{R}_e^{en}$ terms, and use the defined quantity $\rho \equiv nm_i$ to write the MHD momentum equation as follows,

$$\rho[\frac{\partial \vec{v}}{\partial t} + \vec{v} \cdot \nabla\vec{v}] = -\nabla \cdot \mathbf{P} + \vec{J} \times \vec{B} + \Gamma_i^{ion} m_i(\vec{v}_n - \vec{v}) + \Gamma^{cx} m_i(\vec{v}_n - \vec{v}) + \vec{R}_{in}^{cx} - \vec{R}_{ni}^{cx} \tag{A.15}$$

Lastly, expanding the plasma fluid pressure tensor as $\mathbf{P} = (p_i + p_e)\mathbf{I} + \mathbf{\Pi}$, assuming that $T_i = T_e = T$ and quasineutrality $n_i = n_e \equiv n$, we find plasma pressure $p = p_i + p_e = nT_i + nT_e = 2nT$. Using this form of plasma pressure, we find the final strong form version of the MHD momentum equation of interest

$$\rho\left[\frac{\partial \vec{v}}{\partial t} + \vec{v} \cdot \nabla\vec{v}\right] = \vec{J} \times \vec{B} - \nabla(2nT) - \nabla \cdot \mathbf{\Pi} + \Gamma_i^{ion} m_i(\vec{v}_n - \vec{v}) \tag{A.16}$$
$$+ \Gamma^{cx} m_i(\vec{v}_n - \vec{v}) + \vec{R}_{in}^{cx} - \vec{R}_{ni}^{cx}$$

With the desired velocity evolution equation derived from the two-fluid (electron-ion) fluid equations in Eq. A.17, neutral velocity evolution is isolated in a similar fashion as the plasma velocity. Using the same vector identities and the chain rule, starting with Eq. A.8, we can derive an expression for neutral velocity evolution to be

$$m_n n_n \frac{\partial \vec{v_n}}{\partial t} + n_n m_n \vec{v_n} \cdot \nabla\vec{v_n} = -\nabla \cdot \mathbf{P_n} - \vec{R}_i^{in} - \vec{R}_e^{en} + \Gamma_n^{rec} m_i(\vec{v} - \vec{v_n}) \tag{A.17}$$
$$+ \Gamma^{cx} m_i(\vec{v} - \vec{v_n}) + \vec{R}_{ni}^{cx} - \vec{R}_{in}^{cx}$$

Lastly, applying the same assumption that $\vec{R}_i^{in}$and $\vec{R}_e^{en}$ are negligible in fairly well ionized plasmas [37], and $\rho_n = n_n m_n \approx n_n m_i$, the neutral velocity strong form equation reduces to the desired form,

$$\rho_n[\frac{\partial \vec{v_n}}{\partial t} + \vec{v_n} \cdot \nabla \vec{v_n}] = -\nabla(n_n T_n) - \nabla \cdot \mathbf{\Pi_n} + \Gamma_n^{rec} m_i(\vec{v} - \vec{v_n}) + \Gamma^{cx} m_i(\vec{v} - \vec{v_n}) \tag{A.18}$$
$$+ \vec{R}_{ni}^{cx} - \vec{R}_{in}^{cx}$$

Energy evolution

Starting from the three fluid (i.e. ion-electron-neutral) energy evolution equations from [50], reproduced below,

$$\frac{\partial \epsilon_i}{\partial t} + \nabla \cdot (\epsilon_i \vec{v}_i + \vec{v}_i \cdot \mathbf{P_i} + \vec{h}_i) = \vec{v}_i \cdot (q_i n_i \vec{E} + \vec{R}_i^{ie} + \vec{R}_i^{in}) + Q_i^{ie} + Q_i^{in} \tag{A.19}$$
$$+ \frac{m_i}{m_n}(\Gamma_i^{ion} \frac{1}{2} m_n v_n^2 + Q_n^{ion}) - \Gamma_n^{rec} \frac{1}{2} m_i v_i^2 - Q_i^{rec} + \Gamma^{cx} \frac{1}{2} m_i (v_n^2 - v_i^2)$$
$$+ \vec{v}_n \cdot \vec{R}_{in}^{cx} - \vec{v}_i \cdot \vec{R}_{ni}^{cx} + Q_{in}^{cx} - Q_{ni}^{cx}$$

$$\frac{\partial \epsilon_e}{\partial t} + \nabla \cdot (\epsilon_e \vec{v_e} + \vec{v_e} \cdot \mathbf{P_e} + \vec{h}_e) = \vec{v_e} \cdot (-q_e n_e \vec{E} - \vec{R}_i^{ie} + \vec{R}_e^{en}) + Q_e^{ie} + Q_e^{en} \tag{A.20}$$
$$+ \frac{m_e}{m_n}(\Gamma_i^{ion} \frac{1}{2} m_n v_n^2 + Q_n^{ion}) - \Gamma_i^{ion} \phi_{ion} - \Gamma_n^{rec} \frac{1}{2} m_e v_e^2 - Q_e^{rec}$$

$$\frac{\partial \epsilon_n}{\partial t} + \nabla \cdot (\epsilon_n \vec{v}_n + \vec{v}_n \cdot \mathbf{P_n} + \vec{h}_n) = -\vec{v}_n \cdot (\vec{R}_i^{in} + \vec{R}_e^{en}) + Q_n^{in} + Q_n^{en} \tag{A.21}$$
$$+ \Gamma_n^{rec}(\frac{1}{2} m_i v_i^2 + \frac{1}{2} m_e v_e^2) + Q_i^{rec} + Q_e^{rec} - (\Gamma_i^{ion} \frac{1}{2} m_n v_n^2 + Q_n^{ion}) + \Gamma^{cx} \frac{1}{2} m_i (v_i^2 - v_n^2)$$
$$+ \vec{v}_i \cdot \vec{R}_{ni}^{cx} - \vec{v}_n \cdot \vec{R}_{in}^{cx} + Q_{ni}^{cx} - Q_{in}^{cx}$$

where $\epsilon_\alpha \equiv m_\alpha n_\alpha v_\alpha^2/2 + p_\alpha/(\gamma - 1)$ is the total fluid energy density of species α. Q_i^{ie} and Q_e^{ie} are scattering collisional heat exchange terms provided by Braginskii as Q_{ie} and Q_{ei}, respectively [59]. $Q_{i/n}^{in}$ and $Q_{e/n}^{en}$ represent the same type of heat exchange due to ion-neutral and electron-neutral collisions, respectively. The species heat flux is $\vec{h}_\alpha$ which is defined with an appropriate closure.

From the three-fluid equations presented above, it is desired to first derive the MHD energy evolution equation for the plasma fluid. We first start by summing the ion and electron energy equations in the same fashion as deriving the MHD momentum evolution equation. The result is as follows,

$$\frac{\partial(\epsilon_i+\epsilon_e)}{\partial t}+\nabla\cdot(\epsilon_i\vec{v}_i+\vec{v}_i\cdot\mathbf{P_i}+\vec{h}_i)+\nabla\cdot(\epsilon_e\vec{v}_e+\vec{v}_e\cdot\mathbf{P_e}+\vec{h}_e)$$
$$=\vec{v}_i\cdot(q_in_i\vec{E}+\vec{R}_i^{ie}+\vec{R}_i^{in})+Q_i^{ie}+Q_i^{in}+\frac{m_i}{m_n}(\Gamma_i^{ion}\frac{1}{2}m_nv_n^2+Q_n^{ion})-\Gamma_n^{rec}\frac{1}{2}m_iv_i^2-Q_i^{rec}$$
$$+\Gamma^{cx}\frac{1}{2}m_i(v_n^2-v_i^2)+\vec{v}_n\cdot\vec{R}_{in}^{cx}-\vec{v}_i\cdot\vec{R}_{ni}^{cx}+Q_{in}^{cx}-Q_{ni}^{cx}+\vec{v}_e\cdot(-q_en_e\vec{E}-\vec{R}_i^{ie}+\vec{R}_e^{en})$$
$$+Q_e^{ie}+Q_e^{en}+\frac{m_e}{m_n}(\Gamma_i^{ion}\frac{1}{2}m_nv_n^2+Q_n^{ion})-\Gamma_i^{ion}\phi_{ion}-\Gamma_n^{rec}\frac{1}{2}m_ev_e^2-Q_e^{rec}$$

We define $\epsilon\equiv\epsilon_i+\epsilon_e=(p_i+p_e)/(\gamma-1)+(m_in_iv_i^2+m_en_ev_e^2)/2$ and use the following notation for simplification,

$$\epsilon\vec{v}+\vec{v}\cdot\mathbf{P}+\vec{h}=\sum_{\alpha=i,e}(\epsilon_\alpha\vec{v}_\alpha+\vec{v}_\alpha\cdot\mathbf{P}_\alpha+\vec{h}_\alpha) \tag{A.22}$$

Using these definitions, we can rewrite the sum of total fluid energy density of both the ion and electron species as follows

$$\frac{\partial\epsilon}{\partial t}+\nabla\cdot(\epsilon\vec{v}+\vec{v}\cdot\mathbf{P}+\vec{h})=(q_in_i\vec{v}_i-q_en_e\vec{v}_e)\cdot\vec{E}+(\vec{v}_i-\vec{v}_e)\cdot\vec{R}_i^{ie}+\vec{v}_i\cdot\vec{R}_i^{in}+\vec{v}_e\cdot\vec{R}_e^{en}$$
$$+Q_i^{ie}+Q_e^{ie}+Q_i^{in}+Q_e^{en}+\frac{m_i}{m_n}(\Gamma_i^{ion}\frac{1}{2}m_nv_n^2+Q_n^{ion})+\frac{m_e}{m_n}(\Gamma_i^{ion}\frac{1}{2}m_nv_n^2+Q_n^{ion})$$
$$-\Gamma_n^{rec}(\frac{1}{2}m_iv_i^2+\frac{1}{2}m_ev_e^2)-\Gamma_i^{ion}\phi_{ion}-Q_i^{rec}-Q_e^{rec}+\Gamma^{cx}\frac{1}{2}m_i(v_n^2-v_i^2)+\vec{v}_n\cdot\vec{R}_{in}^{cx}-\vec{v}_i\cdot\vec{R}_{ni}^{cx}$$
$$+Q_{in}^{cx}-Q_{ni}^{cx}$$

Using the MHD asymptotic limit $m_e\to0$ and other definition $\rho\approx n_im_i$, a few simplifications worth noting are found. First, the sum of the total energy densities ϵ is as follows,

$$\epsilon=\epsilon_i+\epsilon_e=(p_i+p_e)/(\gamma-1)+(m_in_iv_i^2+m_en_ev_e^2)/2$$
$$=(p_i+p_e)/(\gamma-1)+mn_iv_i^2/2=(p_i+p_e)/(\gamma-1)+\rho v_i^2/2$$

Simplifying further using MHD variables defined previously,

$$\epsilon=(p_i+p_e)/(\gamma-1)+\rho v^2/2=p/(\gamma-1)+\rho v^2/2 \tag{A.23}$$

Furthermore, the combined ion-electron energy evolution equation reduces to, after rearrangement,

$$\begin{aligned}\frac{\partial\epsilon}{\partial t} + \nabla\cdot(\epsilon\vec{v} + \vec{v}\cdot\mathbf{P} + \vec{h}) &= \vec{J}\cdot\vec{E} + (\vec{v}-\vec{v}_e)\cdot\vec{R}_i^{ie} + \vec{v}\cdot\vec{R}_i^{in} + \vec{v}_e\cdot\vec{R}_e^{en} + Q_i^{ie} + Q_e^{ie} \\ &+ Q_i^{in} + Q_e^{en} + \Gamma_i^{ion}(\frac{1}{2}m_i v_n^2 - \phi_{ion}) + Q_n^{ion} - \Gamma_n^{rec}(\frac{1}{2}m_i v^2) - Q_i^{rec} - Q_e^{rec} + \Gamma^{cx}\frac{1}{2}m_i(v_n^2 - v^2) \\ &+ \vec{v}_n\cdot\vec{R}_{in}^{cx} - \vec{v}\cdot\vec{R}_{ni}^{cx} + Q_{in}^{cx} - Q_{ni}^{cx}\end{aligned} \tag{A.24}$$

Lastly, one further simplification made by Meier [50] is used for this work, $(\vec{v}-\vec{v_e})\cdot\vec{R}_i^{ie} - (Q_i^{ie}+Q_e^{ie}) = 0$ as suggested by Braginskii in [59]. Using this assumption, the above equation further reduces to,

$$\begin{aligned}\frac{\partial\epsilon}{\partial t} + \nabla\cdot(\epsilon\vec{v} + \vec{v}\cdot\mathbf{P} + \vec{h}) &= \vec{J}\cdot\vec{E} + \vec{v}\cdot\vec{R}_i^{in} + \vec{v_e}\cdot\vec{R}_e^{en} + Q_i^{in} + Q_e^{en} \\ &+ \Gamma_i^{ion}(\frac{1}{2}m_i v_n^2 - \phi_{ion}) + Q_n^{ion} - \Gamma_n^{rec}(\frac{1}{2}m_i v^2) - Q_i^{rec} - Q_e^{rec} + \Gamma^{cx}\frac{1}{2}m_i(v_n^2 - v^2) \\ &+ \vec{v}_n\cdot\vec{R}_{in}^{cx} - \vec{v}\cdot\vec{R}_{ni}^{cx} + Q_{in}^{cx} - Q_{ni}^{cx}\end{aligned} \tag{A.25}$$

which is the MHD total energy evolution equation. As a reminder, this evolution equation is for the total fluid energy density, which is the sum of the thermal pressure p and dynamic pressure $\frac{1}{2}\rho v^2$. We evolve separate equations for density (continuity), and velocity (momentum), and thus the variables for dynamic pressure are fully defined by other equations in the model. The thermal pressure, p is written as $p = p_i + p_e$, which is just $p = nT + nT = 2nT$ since this model assumes $T_i = T_e$ and from quasineutrality $n_i = n_e = n$. Density evolution is defined by the continuity equation, but as of yet, there is not a relationship that exclusively describes the evolution of plasma temperature. Thus, it is desired for implementation into PSI-Tet to isolate thermal pressure p evolution from total energy evolution, and then isolate temperature evolution from thermal pressure evolution.

First, in an effort to ultimately isolate temperature evolution from thermal energy evolution, the MHD kinetic energy evolution equation must be derived so that it can be removed from the total energy evolution equation. Using the MHD plasma momentum equation derived previously, the kinetic energy evolution equation can be found by taking the scalar product of the plasma momentum equation with the plasma velocity $\vec{v}$, as follows,

$$\vec{v}\cdot[\frac{\partial}{\partial t}(\rho\vec{v})+\nabla\cdot(\rho\vec{v}\vec{v}+\mathbf{P})=\vec{J}\times\vec{B}+\vec{R}_i^{in}+\vec{R}_e^{en}+\Gamma_i^{ion}m_i\vec{v_n}-\Gamma_n^{rec}m_i\vec{v} \tag{A.26}$$
$$+\Gamma^{cx}m_i(\vec{v_n}-\vec{v})+\vec{R}_{in}^{cx}-\vec{R}_{ni}^{cx}]$$

Making use of the following expansions,

$$\vec{v}\cdot\frac{\partial}{\partial t}(\rho\vec{v})=\frac{\partial}{\partial t}\left(\frac{1}{2}\rho v^2\right)+m_i\frac{1}{2}v^2\frac{\partial n}{\partial t} \tag{A.27}$$
$$\vec{v}\cdot(\nabla\cdot(\rho\vec{v}\vec{v}))=\nabla\cdot\left(\frac{1}{2}m_in\vec{v}v^2\right)+\frac{1}{2}m_iv^2\nabla\cdot(n\vec{v}) \tag{A.28}$$

we expand the previous equation as follows,

$$\frac{\partial}{\partial t}(\frac{1}{2}\rho v^2)+m_i\frac{1}{2}v^2\frac{\partial n}{\partial t}+\nabla\cdot\left(\frac{1}{2}m_in\vec{v}v^2\right)+\frac{1}{2}m_iv^2\nabla\cdot(n\vec{v})+\vec{v}\cdot(\nabla\cdot\mathbf{P})= \tag{A.29}$$
$$\vec{v}\cdot(\vec{J}\times\vec{B})+\vec{v}\cdot\vec{R}_i^{in}+\vec{v}\cdot\vec{R}_e^{en}+\Gamma_i^{ion}m_i\vec{v}\cdot\vec{v_n}-\Gamma_n^{rec}m_iv^2+\Gamma^{cx}m_i(\vec{v}\cdot\vec{v_n}-v^2)$$
$$+\vec{v}\cdot\vec{R}_{in}^{cx}-\vec{v}\cdot\vec{R}_{ni}^{cx}$$

Substituting in plasma continuity derived in a previous section $\frac{\partial n}{\partial t}+\nabla\cdot(n\vec{v})=\Gamma_i^{ion}-\Gamma_n^{rec}$, we find that

$$\frac{\partial}{\partial t}(\frac{1}{2}\rho v^2)+\nabla\cdot\left(\frac{1}{2}m_in\vec{v}v^2\right)=-\vec{v}\cdot(\nabla\cdot\mathbf{P})+\vec{v}\cdot(\vec{J}\times\vec{B}) \tag{A.30}$$
$$+\vec{v}\cdot(\vec{R}_i^{in}+\vec{R}_e^{en}+\vec{R}_{in}^{cx}-\vec{R}_{ni}^{cx})+\Gamma_i^{ion}m_i\left(\vec{v}\cdot\vec{v_n}-\frac{v^2}{2}\right)-\Gamma_n^{rec}m_i\frac{1}{2}v^2+\Gamma^{cx}m_i(\vec{v}\cdot\vec{v_n}-v^2)$$

which is desired form of this equation. Now that kinetic energy, or in other words, dynamic pressure evolution has been derived from the plasma momentum equation, this expression can be used to isolate pressure evolution within the total energy evolution equation.

Starting with the MHD total energy evolution equation, we intend to first isolate thermal pressure evolution. We note that $\epsilon=p/(\gamma-1)+\rho v^2/2$ where $p=p_i+p_e$. Substituting in the expanded form of ϵ into the complete MHD energy evolution in Eq. A.25, we find the following

$$\frac{\partial}{\partial t}\left(\frac{p}{\gamma-1}\right)+\nabla\cdot\left(\frac{p\vec{v}}{\gamma-1}\right)+\frac{\partial}{\partial t}\left(\frac{1}{2}\rho v^2\right)+\nabla\cdot\left(\frac{1}{2}\rho\vec{v}v^2\right)=-\nabla\cdot(\vec{v}\cdot\mathbf{P}+\vec{h})+\vec{J}\cdot\vec{E}$$
$$+\vec{v}\cdot\vec{R}_i^{in}+\vec{v_e}\cdot\vec{R}_e^{en}+Q_i^{in}+Q_e^{en}+\Gamma_i^{ion}\left(\frac{1}{2}m_i v_n^2-\phi_{ion}\right)+Q_n^{ion}-\Gamma_n^{rec}\left(\frac{1}{2}m_i v^2\right)-Q_i^{rec}-Q_e^{rec}$$
$$+\Gamma^{cx}\frac{1}{2}m_i(v_n^2-v^2)+\vec{v_n}\cdot\vec{R}_{in}^{cx}-\vec{v}\cdot\vec{R}_{ni}^{cx}+Q_{in}^{cx}-Q_{ni}^{cx}$$

Substituting the expression for plasma kinetic energy evolution found before, we find that

$$\frac{\partial}{\partial t}\left(\frac{p}{\gamma-1}\right)+\nabla\cdot\left(\frac{p\vec{v}}{\gamma-1}\right)+\nabla\cdot(\vec{v}\cdot\mathbf{P}+\vec{h})=\vec{v}\cdot(\nabla\cdot\mathbf{P})+\vec{J}\cdot\vec{E}-\vec{v}\cdot(\vec{J}\times\vec{B}) \tag{A.31}$$
$$+(\vec{v}_e-\vec{v})\cdot\vec{R}_e^{en}+(\vec{v}_n-\vec{v})\cdot\vec{R}_{in}^{cx}+\Gamma_i^{ion}\left(\frac{1}{2}m_i v_n^2-m_i\vec{v}\cdot\vec{v}_n+m_i\frac{v^2}{2}-\phi_{ion}\right)$$
$$+\Gamma^{cx}m_i\left(\frac{v_n^2}{2}-\vec{v}\cdot\vec{v}_n+\frac{v^2}{2}\right)+Q_i^{in}+Q_e^{en}+Q_n^{ion}-Q_i^{rec}-Q_e^{rec}+Q_{in}^{cx}-Q_{ni}^{cx}$$

To be consistent with previous assumptions that frictional terms between plasma and neutral fluids are small in reasonably well ionized plasmas [37], we can reduce the energy equation as follows,

$$\frac{\partial}{\partial t}\left(\frac{p}{\gamma-1}\right)+\nabla\cdot\left(\frac{p\vec{v}}{\gamma-1}\right)+\nabla\cdot(\vec{v}\cdot\mathbf{P}+\vec{h})=\vec{v}\cdot(\nabla\cdot\mathbf{P})+\vec{J}\cdot\vec{E}-\vec{v}\cdot(\vec{J}\times\vec{B}) \tag{A.32}$$
$$+(\vec{v}_n-\vec{v})\cdot\vec{R}_{in}^{cx}+\Gamma_i^{ion}\left(\frac{1}{2}m_i v_n^2-m_i\vec{v}\cdot\vec{v}_n+m_i\frac{v^2}{2}-\phi_{ion}\right)+\Gamma^{cx}m_i\left(\frac{v_n^2}{2}-\vec{v}\cdot\vec{v}_n+\frac{v^2}{2}\right)$$
$$+Q_n^{ion}-Q_i^{rec}-Q_e^{rec}+Q_{in}^{cx}-Q_{ni}^{cx}$$

Introducing Generalized Ohm's Law from the electron momentum equation to express the electric field $\vec{E}$ in terms of other quantities of interest as follows,

$$\vec{E}=-\vec{v}\times\vec{B}+\frac{1}{nq}(\vec{J}\times\vec{B}-\nabla\cdot\mathbf{P_e}-\vec{R}_i^{ie}+\vec{R}_e^{en})$$

Again we neglect $\vec{R}_e^{en}$ in line with previous assumptions of a fairly well ionized plasma.

Substituting this expression for the electric field $\vec{E}$, we find

$$\begin{aligned}&\frac{\partial}{\partial t}\left(\frac{p}{\gamma-1}\right)+\nabla\cdot\left(\frac{p\vec{v}}{\gamma-1}\right)+\nabla\cdot(\vec{v}\cdot\mathbf{P}+\vec{h})=\vec{v}\cdot(\nabla\cdot\mathbf{P})\\&+\vec{J}\cdot\left[-\vec{v}\times\vec{B}+\frac{1}{nq}(\vec{J}\times\vec{B}-\nabla\cdot\mathbf{P_e}-\vec{R}_i^{ie})\right]-\vec{v}\cdot(\vec{J}\times\vec{B})+(\vec{v_n}-\vec{v})\cdot\vec{R}_{in}^{cx}\\&+\Gamma_i^{ion}\left(\frac{1}{2}m_i v_n^2-m_i\vec{v}\cdot\vec{v_n}+m_i\frac{v^2}{2}-\phi_{ion}\right)+\Gamma^{cx}m_i\left(\frac{v_n^2}{2}-\vec{v}\cdot\vec{v_n}+\frac{v^2}{2}\right)+Q_n^{ion}-Q_i^{rec}\\&-Q_e^{rec}+Q_{in}^{cx}-Q_{ni}^{cx}\end{aligned}\tag{A.33}$$

Using triple product rules and orthogonality to simplify further, the $\vec{J}\cdot\vec{E}$ term only provides a diamagnetic (i.e. electron pressure), resistive, and Lorentz term, the last of which cancels with the already present term $-\vec{v}\cdot(\vec{J}\times\vec{B})$, we find that

$$\begin{aligned}&\frac{\partial}{\partial t}\left(\frac{p}{\gamma-1}\right)+\nabla\cdot\left(\frac{p\vec{v}}{\gamma-1}\right)+\nabla\cdot(\vec{v}\cdot\mathbf{P}+\vec{h})=\vec{v}\cdot(\nabla\cdot\mathbf{P})-\frac{\vec{J}}{nq}\cdot(\nabla\cdot\mathbf{P_e})\\&-\frac{\vec{J}}{nq}\cdot\vec{R}_i^{ie}+(\vec{v_n}-\vec{v})\cdot\vec{R}_{in}^{cx}+\Gamma_i^{ion}\left(\frac{1}{2}m_i v_n^2-m_i\vec{v}\cdot\vec{v_n}+m_i\frac{v^2}{2}-\phi_{ion}\right)\\&+\Gamma^{cx}m_i\left(\frac{v_n^2}{2}-\vec{v}\cdot\vec{v_n}+\frac{v^2}{2}\right)+Q_n^{ion}-Q_i^{rec}-Q_e^{rec}+Q_{in}^{cx}-Q_{ni}^{cx}\end{aligned}\tag{A.34}$$

Using the definitions that $\vec{R}_i^{ie}\equiv -nq\eta\vec{J}$ and $\mathbf{P_e}=p_e\mathbf{I}+\mathbf{\Pi_e}\approx p_e\mathbf{I}$ since $\mathbf{\Pi_i}$ is the dominant anisotropic pressure tensor term, we have

$$\begin{aligned}&\frac{\partial}{\partial t}\left(\frac{p}{\gamma-1}\right)+\nabla\cdot\left(\frac{p\vec{v}}{\gamma-1}\right)+\nabla\cdot(\vec{v}\cdot\mathbf{P}+\vec{h})=\vec{v}\cdot(\nabla\cdot\mathbf{P})-\frac{\vec{J}}{nq}\cdot(\nabla p_e)+\eta j^2\\&+(\vec{v}_n-\vec{v})\cdot\vec{R}_{in}^{cx}+\Gamma_i^{ion}\left(\frac{1}{2}m_i v_n^2-m_i\vec{v}\cdot\vec{v}_n+m_i\frac{v^2}{2}-\phi_{ion}\right)+\Gamma^{cx}m_i\left(\frac{v_n^2}{2}-\vec{v}\cdot\vec{v}_n+\frac{v^2}{2}\right)\\&+Q_n^{ion}-Q_i^{rec}-Q_e^{rec}+Q_{in}^{cx}-Q_{ni}^{cx}\end{aligned}\tag{A.35}$$

which is the pressure evolution equation form of interest.

With plasma pressure evolution isolated from total plasma energy density evolution, the desired temperature evolution equation can be isolated. We continue to use the assumption that $p=p_i+p_e=n_iT_i+n_eT_e=2nT$. Substituting $p=2nT$ into plasma pressure evolution equation, we find that

$$
\begin{aligned}
&\frac{\partial}{\partial t}\left(\frac{2nT}{\gamma-1}\right)+\nabla\cdot\left(\frac{2nT\vec{v}}{\gamma-1}\right)+\nabla\cdot(\vec{v}\cdot\mathbf{P}+\vec{h})=\vec{v}\cdot(\nabla\cdot\mathbf{P})-\frac{\vec{J}}{nq}\cdot(\nabla p_e)+\eta j^2 \\
&+(\vec{v}_n-\vec{v})\cdot\vec{R}_{in}^{cx}+\Gamma_i^{ion}\left(\frac{1}{2}m_i v_n^2-m_i\vec{v}\cdot\vec{v}_n+m_i\frac{v^2}{2}-\phi_{ion}\right)+\Gamma^{cx}m_i\left(\frac{v_n^2}{2}-\vec{v}\cdot\vec{v}_n+\frac{v^2}{2}\right) \\
&+Q_n^{ion}-Q_i^{rec}-Q_e^{rec}+Q_{in}^{cx}-Q_{ni}^{cx}
\end{aligned}
\tag{A.36}
$$

Using the chain rule for the time derivative and vector identities for the flux term, we arrive at the following expression for the first two terms in the equation above,

$$
\begin{aligned}
&\frac{\partial}{\partial t}\left(\frac{2nT}{\gamma-1}\right)+\nabla\cdot\left(\frac{2nT\vec{v}}{\gamma-1}\right)=\frac{2}{\gamma-1}\left(n\frac{\partial T}{\partial t}+T\frac{\partial n}{\partial t}\right)+(n\vec{v})\cdot\nabla\left(\frac{2T}{\gamma-1}\right)+\frac{2T}{\gamma-1}\nabla\cdot(n\vec{v}) \\
&=\frac{2n}{\gamma-1}\frac{\partial T}{\partial t}+(n\vec{v})\cdot\nabla\left(\frac{2T}{\gamma-1}\right)+\frac{2T}{\gamma-1}\left[\frac{\partial n}{\partial t}+\nabla\cdot(n\vec{v})\right]
\end{aligned}
$$

Substituting in the MHD plasma continuity equation, we find that

$$
\begin{aligned}
&\frac{2n}{\gamma-1}\left[\frac{\partial T}{\partial t}+\vec{v}\cdot\nabla T\right]+\frac{2T}{\gamma-1}[\Gamma_i^{ion}-\Gamma_n^{rec}]+\nabla\cdot(\vec{v}\cdot\mathbf{P}+\vec{h})=\vec{v}\cdot(\nabla\cdot\mathbf{P}) \\
&-\frac{\vec{J}}{nq}\cdot(\nabla p_e)+\eta j^2+(\vec{v}_n-\vec{v})\cdot\vec{R}_{in}^{cx}+\Gamma_i^{ion}\left(\frac{1}{2}m_i v_n^2-m_i\vec{v}\cdot\vec{v}_n+m_i\frac{v^2}{2}-\phi_{ion}\right) \\
&+\Gamma^{cx}m_i\left(\frac{v_n^2}{2}-\vec{v}\cdot\vec{v}_n+\frac{v^2}{2}\right)+Q_n^{ion}-Q_i^{rec}-Q_e^{rec}+Q_{in}^{cx}-Q_{ni}^{cx}
\end{aligned}
\tag{A.37}
$$

Lastly, using the definition that $\mathbf{P}:\nabla\vec{v}\equiv\nabla\cdot(\vec{v}\cdot\mathbf{P})-\vec{v}\cdot(\nabla\cdot\mathbf{P})$ while also expanding the pressure tensor, we find the temperature evolution equation form of interest,

$$
\begin{aligned}
&\frac{n}{\gamma-1}\left[\frac{\partial T}{\partial t}+\vec{v}\cdot\nabla T\right]=-nT\nabla\cdot\vec{v}-\nabla\cdot\vec{h}+\frac{S}{2}+\frac{1}{2}\Big[(\vec{v}_n-\vec{v})\cdot\vec{R}_{in}^{cx} \\
&+(\Gamma_i^{ion}+\Gamma^{cx})\frac{m_i}{2}(\vec{v}-\vec{v}_n)^2-\Gamma_i^{ion}\left(\phi_{ion}+\frac{2T}{\gamma-1}\right)+\Gamma_n^{rec}\frac{2T}{\gamma-1}+Q_n^{ion}-Q_i^{rec}-Q_e^{rec} \\
&+Q_{in}^{cx}-Q_{ni}^{cx}]
\end{aligned}
\tag{A.38}
$$

where $S=\eta j^2-\mathbf{\Pi}:\nabla\vec{v}$. With the plasma temperature evolution equation isolated, the same process is carried out with the neutral temperature evolution equation. The final result from this process in the desired form of interest is as follows

$$\frac{n_n}{\gamma - 1}\left[\frac{\partial T_n}{\partial t} + \vec{v}_n \cdot \nabla T_n\right] = -n_n T_n \nabla \cdot \vec{v}_n - \mathbf{\Pi_n} : \nabla \vec{v}_n - \nabla \cdot \vec{h}_n \tag{A.39}$$

$$+ (\Gamma_n^{rec} + \Gamma^{cx})\frac{m_i}{2}(\vec{v} - \vec{v}_n)^2 - (\Gamma_n^{rec} - \Gamma_i^{ion})\frac{T_n}{\gamma - 1} + (\vec{v} - \vec{v}_n) \cdot \vec{R}_{ni}^{cx} + Q_i^{rec} + Q_e^{rec}$$

$$- Q_n^{ion} + Q_{ni}^{cx} - Q_{in}^{cx}$$

Appendix B

WEAK FORMULATION DERIVATION OF PLASMA-NEUTRAL MODEL

B.1 Crank-Nicholson Scheme

Note that $+ \rightarrow (k+1)$ and $- \rightarrow (k-1)$, forward and backward in time, respectively. Define a metric M where $M^{+} = M^{-}$defines a time step. The metric is given using the advancing quantity of interest, via

$$\frac{\partial U}{\partial t} = F\left(U, x, t, \frac{\partial U}{\partial x}, ...\right)$$

$$\frac{U^{n+1} - U^{n}}{\Delta t} = \frac{1}{2}\left[F^{n+1}\left(U, x, t, \frac{\partial U}{\partial x}, ...\right) + F^{n}\left(U, x, t, \frac{\partial U}{\partial x}, ...\right)\right]$$

$$M^{\pm} = U^{\pm} \mp \frac{\Delta t}{2} F^{\pm}\left(U, x, t, \frac{\partial U}{\partial x}, ...\right)$$

B.1.1 Density advance

Physical equations

The plasma continuity equation including the effects from the introduction of a neutral fluid is given by Eq. 3.8 and is reproduced below for convenience,

$$\frac{\partial n}{\partial t} + \nabla \cdot (n\vec{v}) = \Gamma^{ion} - \Gamma^{rec} = n_e n_n \left\langle \sigma_{ion} \nu_e \right\rangle - n_i n_e \left\langle \sigma_{rec} \nu_e \right\rangle$$

Assuming $n_i = n_e = n$ in MHD limit, the above expression can be simplified to,

$$\frac{\partial n}{\partial t} + \nabla \cdot (n\vec{v}) = n n_n \left\langle \sigma_{ion} \nu_e \right\rangle - n^2 \left\langle \sigma_{rec} \nu_e \right\rangle$$

Define $c_{rec} \equiv \left\langle \sigma_{rec} \nu_e \right\rangle$ and $c_{ion} \equiv \left\langle \sigma_{ion} \nu_e \right\rangle$, and rearrange into desired equation form,

$$\frac{\partial n}{\partial t} = -\nabla \cdot (n\vec{v}) + n n_n c_{ion} - n^2 c_{rec}$$

The neutral continuity equation including the effects from interactions with the plasma fluid is given by Eq. 3.9 and is reproduced below for convenience,

$$\frac{\partial n_n}{\partial t} + \nabla \cdot (n_n \vec{v}) = -\Gamma^{ion} + \Gamma^{rec} = n_e n_n \langle \sigma_{ion} \nu_e \rangle - n_i n_e \langle \sigma_{rec} \nu_e \rangle$$

Assuming $n_i = n_e = n$ in the MHD limit and using aforementioned definitions of reaction rates, the equation of interest for the neutral density advance is as follows

$$\frac{\partial n_n}{\partial t} = -\nabla \cdot (n_n \vec{v_n}) - n n_n c_{ion} + n^2 c_{rec}$$

Numerical equations

It is necessary to add artificial diffusion to stabilize density advection. Thus, the strong form continuity equation for numerical simulations is as follows for both the plasma and neutral fluids

$$\frac{\partial n}{\partial t} = -\nabla \cdot (n \vec{v}) + n n_n c_{ion} - n^2 c_{rec} + D \nabla^2 n$$
$$\frac{\partial n_n}{\partial t} = -\nabla \cdot (n_n \vec{v_n}) - n n_n c_{ion} + D_n \nabla^2 n_n$$

Nonlinear metrics

The nonlinear metrics required for the Crank-Nicholson scheme are given by

$$M_n^{\pm} = n^{\pm} \mp \frac{\Delta t}{2}(-\nabla \cdot (n \vec{v}) + n n_n c_{ion} - n^2 c_{rec} + D \nabla^2 n)$$
$$M_{n_n}^{\pm} = n_n^{\pm} \mp \frac{\Delta t}{2}(-\nabla \cdot (n_n \vec{v_n}) - n n_n c_{ion} + n^2 c_{rec} + D_n \nabla^2 n_n)$$

Expanding in a finite element basis, where ϕ_n^T is the test function set for plasma density, we obtain the nonlinear metric form of interest,

$$M_n^{\pm} = \int \left(\phi_n^T \left(n^{\pm} \mp \frac{\Delta t}{2} \left[-\nabla \cdot (n \vec{v}) + n n_n c_{ion} - n^2 c_{rec} \right] \right) \pm D \frac{\Delta t}{2} \nabla \phi_n^T \cdot \nabla n^{\pm} \right) dV$$
$$+ \int_{\partial \Omega} D \frac{\Delta t}{2} \phi_n^T \nabla n^{\pm} \cdot d\vec{S}$$

Expanding in a finite element basis, where $\phi_{n_n}^T$ is the test function set for neutral density, we obtain the nonlinear metric weak formulation of interest,

$$M_{n_n}^{\pm} = \int \left(\phi_{n_n}^T \left(n_n^{\pm} \mp \frac{\Delta t}{2} \left[-\nabla \cdot (n_n \vec{v_n}) - n n_n c_{ion} + n^2 c_{rec} \right] \right) \pm D_n \frac{\Delta t}{2} \nabla \phi_{n_n}^T \cdot \nabla n_n^{\pm} \right) dV$$
$$+ \int_{\partial\Omega} D_n \frac{\Delta t}{2} \phi_{n_n}^T \nabla n_n^{\pm} \cdot d\vec{S}$$

B.1.2 Velocity advance

Physical equations

The plasma and neutral momentum equations including the effects from the introduction of a neutral fluid is provided in Eqs. 3.10 - 3.11 and are reproduced below for convenience,

$$\rho \left[\frac{\partial \vec{v}}{\partial t} + \vec{v} \cdot \nabla v \right] = \vec{J} \times \vec{B} - \nabla(2nT) - \nabla \cdot \mathbf{\Pi} + \Gamma_i^{ion} m_i (\vec{v}_n - \vec{v}) + \Gamma^{cx} m_i (\vec{v}_n - \vec{v}) \tag{B.1}$$
$$+ \vec{R}_{in}^{cx} - \vec{R}_{ni}^{cx}$$
$$\rho_n \left[\frac{\partial \vec{v}_n}{\partial t} + \vec{v}_n \cdot \nabla \vec{v}_n \right] = -\nabla(n_n T_n) - \nabla \cdot \mathbf{\Pi_n} + \Gamma_n^{rec} m_i (\vec{v} - \vec{v}_n) + \Gamma^{cx} m_i (\vec{v} - \vec{v}_n) \tag{B.2}$$
$$+ \vec{R}_{ni}^{cx} - \vec{R}_{in}^{cx}$$

Numerical equations

Isolating the temporal derivative of both the plasma and neutral velocities (i.e. $\frac{\partial v}{\partial t}$ and $\frac{\partial v_n}{\partial t}$), one finds the expressions in the form of interest for the derivation of the nonlinear metrics to be implemented in PSI-Tet,

$$\frac{\partial \vec{v}}{\partial t} = -\vec{v} \cdot \nabla \vec{v} + \frac{1}{\rho} \Big[\vec{J} \times \vec{B} - \nabla(2nT) - \nabla \cdot \mathbf{\Pi} + \Gamma_i^{ion} m_i (\vec{v}_n - \vec{v}) + \Gamma^{cx} m_i (\vec{v}_n - \vec{v}) \tag{B.3}$$
$$+ \vec{R}_{in}^{cx} - \vec{R}_{ni}^{cx} \Big]$$
$$\frac{\partial \vec{v}_n}{\partial t} = -\vec{v}_n \cdot \nabla \vec{v}_n + \frac{1}{\rho_n} [-\nabla(n_n T_n) - \nabla \cdot \mathbf{\Pi_n} + \Gamma_n^{rec} m_i (\vec{v} - \vec{v}_n) + \Gamma^{cx} m_i (\vec{v} - \vec{v}_n) \tag{B.4}$$
$$+ \vec{R}_{ni}^{cx} - \vec{R}_{in}^{cx} \Big]$$

Nonlinear Metrics

The strong form expressions of the nonlinear metric for the Crank-Nicolson scheme for the velocity advances are as follows

$$\begin{aligned}&M_v^{\pm} = \vec{v}^{\pm} \mp \frac{\Delta t}{2}\left[-\vec{v}^{\pm} \cdot \nabla \vec{v}^{\pm} - \frac{1}{\rho^{\pm}}\Big(\vec{j}^{\pm} \times \vec{B}^{\pm} - \nabla(2n^{\pm}T^{\pm}) - \nabla \cdot \mathbf{\Pi}^{\pm} + \Gamma_i^{ion} m_i(\vec{v}_n^{\pm} - \vec{v}^{\pm})\right.\\ &\left.+\Gamma^{cx} m_i(\vec{v}_n^{\pm} - \vec{v}^{\pm}) + \vec{R}_{in}^{cx} - \vec{R}_{ni}^{cx}\Big)\right]\end{aligned}$$

$$\begin{aligned}&M_{v_n}^{\pm} = \vec{v}_n^{\pm} \mp \frac{\Delta t}{2}\Bigg[-\vec{v}_n^{\pm} \cdot \nabla \vec{v}_n^{\pm} - \frac{1}{\rho_n^{\pm}}\big(-\nabla(n_n^{\pm}T_n^{\pm}) - \nabla \cdot \mathbf{\Pi_n}^{\pm} + \Gamma_n^{rec} m_i(\vec{v}^{\pm} - \vec{v}_n^{\pm})\\ &+\Gamma^{cx} m_i(\vec{v}^{\pm} - \vec{v}_n^{\pm}) + \vec{R}_{ni}^{cx} - \vec{R}_{in}^{cx}\Big)\Bigg]\end{aligned}$$

Expanding in a finite element basis, where ϕ_v^T and $\phi_{v_n}^T$ are the test function sets for plasma and neutral velocity advances, respectively, the desired weak formulation of the nonlinear metric is obtained,

$$\begin{aligned}&M_v^{\pm} = \int_{\Omega} \phi_v^T \cdot \Bigg(\vec{v}^{\pm} \mp \frac{\Delta t}{2}\Bigg[-\vec{v}^{\pm} \cdot \nabla \vec{v}^{\pm} - \frac{1}{\rho^{\pm}}\Big(\vec{j}^{\pm} \times \vec{B}^{\pm} - \nabla(2n^{\pm}T^{\pm}) - \nabla \cdot \mathbf{\Pi}^{\pm}\\ &+\Gamma_i^{ion} m_i(\vec{v}_n^{\pm} - \vec{v}^{\pm}) + \Gamma^{cx} m_i(\vec{v}_n^{\pm} - \vec{v}^{\pm}) + \vec{R}_{in}^{cx} - \vec{R}_{ni}^{cx}\Big)\Bigg]\Bigg)\, dV\end{aligned}$$

$$\begin{aligned}&M_{v_n}^{\pm} = \int_{\Omega} \phi_{v_n}^T \cdot \Bigg(\vec{v}_n^{\pm} \mp \frac{\Delta t}{2}\Bigg[-\vec{v}_n^{\pm} \cdot \nabla \vec{v}_n^{\pm} - \frac{1}{\rho_n^{\pm}}\big(-\nabla(n_n^{\pm}T_n^{\pm}) - \nabla \cdot \mathbf{\Pi_n}^{\pm} + \Gamma_n^{rec} m_i(\vec{v}^{\pm} - \vec{v}_n^{\pm})\\ &+\Gamma^{cx} m_i(\vec{v}^{\pm} - \vec{v}_n^{\pm}) + \vec{R}_{ni}^{cx} - \vec{R}_{in}^{cx}\Big)\Bigg]\Bigg)\, dV\end{aligned}$$

B.1.3 Temperature advance

Physical equations

The temperature evolution equations expressed in Eqs. 3.12 - 3.13 for the plasma-neutral model are reproduced below,

$$\frac{n}{\gamma-1}\left[\frac{\partial T}{\partial t}+\vec{v}\cdot\nabla T\right]=-nT\nabla\cdot\vec{v}-\nabla\cdot\vec{q}+\frac{1}{2}\left(\eta\vec{J}^2-\mathbf{\Pi}:\nabla\vec{v}\right)$$
$$+\frac{1}{2}\left[(\vec{v}_n-\vec{v})\cdot\vec{R}_{in}^{cx}+(\Gamma_i^{ion}+\Gamma^{cx})\frac{m_i}{2}(\vec{v}-\vec{v}_n)^2-\Gamma_i^{ion}\left(\phi_{ion}+\frac{2T}{\gamma-1}\right)+\Gamma_n^{rec}\left(\frac{2T}{\gamma-1}\right)\right.$$
$$\left.+Q_n^{ion}-Q_i^{rec}+Q_{in}^{cx}-Q_{ni}^{cx}\right]$$

$$\frac{n_n}{\gamma-1}\left[\frac{\partial T_n}{\partial t}+\vec{v}_n\cdot\nabla T_n\right]=-n_nT_n\nabla\cdot\vec{v}_n-\nabla\cdot\vec{q}_n-\mathbf{\Pi_n}:\nabla\vec{v}_n+(\vec{v}-\vec{v}_n)\cdot\vec{R}_{ni}^{cx}$$
$$+(\Gamma_n^{rec}+\Gamma^{cx})\frac{m_i}{2}(\vec{v}-\vec{v}_n)^2-(\Gamma_n^{rec}-\Gamma_i^{ion})\left(\frac{T_n}{\gamma-1}\right)+Q_i^{rec}-Q_n^{ion}+Q_{ni}^{cx}-Q_{in}^{cx}$$

Numerical equations

Isolating the temporal derivative of both the plasma and neutral temperatures (i.e. $\frac{\partial T}{\partial t}$ and $\frac{\partial T_n}{\partial t}$), one finds the expressions in the form of interest for derivation of the nonlinear metrics to be implemented in PSI-Tet,

$$\frac{\partial T}{\partial t}=-\vec{v}\cdot\nabla T+\frac{\gamma-1}{n}\left(-nT\nabla\cdot\vec{v}-\nabla\cdot\vec{q}+\frac{1}{2}\left(\eta\vec{J}^2-\mathbf{\Pi}:\nabla\vec{v}\right)\right.$$
$$+\frac{1}{2}\left[(\vec{v}_n-\vec{v})\cdot\vec{R}_{in}^{cx}+(\Gamma_i^{ion}+\Gamma^{cx})\frac{m_i}{2}(\vec{v}-\vec{v}_n)^2-\Gamma_i^{ion}\left(\phi_{ion}+\frac{2T}{\gamma-1}\right)+\Gamma_n^{rec}\left(\frac{2T}{\gamma-1}\right)\right.$$
$$\left.\left.+Q_n^{ion}-Q_i^{rec}+Q_{in}^{cx}-Q_{ni}^{cx}\right]\right)$$

$$\frac{\partial T_n}{\partial t}=-\vec{v}_n\cdot\nabla T_n+\frac{\gamma-1}{n_n}\left(-n_nT_n\nabla\cdot\vec{v}_n-\nabla\cdot\vec{q}_n-\mathbf{\Pi_n}:\nabla\vec{v}_n+(\vec{v}-\vec{v}_n)\cdot\vec{R}_{ni}^{cx}\right.$$
$$\left.+(\Gamma_n^{rec}+\Gamma^{cx})\frac{m_i}{2}(\vec{v}-\vec{v}_n)^2-(\Gamma_n^{rec}-\Gamma_i^{ion})\left(\frac{T_n}{\gamma-1}\right)+Q_i^{rec}-Q_n^{ion}+Q_{ni}^{cx}-Q_{in}^{cx}\right)$$

Nonlinear metrics

The strong form expression of the nonlinear metric for the Crank-Nicolson scheme for the plasma temperature advance is as follows,

$$
\begin{aligned}
M_T^{\pm} = T^{\pm} \mp \frac{\Delta t}{2} \Bigg[& -\vec{v}^{\pm} \cdot \nabla T^{\pm} + \frac{\gamma - 1}{n^{\pm}} \Bigg(-n^{\pm} T^{\pm} \nabla \cdot \vec{v}^{\pm} - \nabla \cdot \vec{q}^{\pm} + \frac{1}{2} \Big(\eta(\vec{J}^2)^{\pm} - \mathbf{\Pi}^{\pm} : \nabla \vec{v}^{\pm} \Big) \\
& + \frac{1}{2} \Bigg[(\vec{v}_n^{\pm} - \vec{v}^{\pm}) \cdot (\vec{R}_{in}^{cx})^{\pm} + \big(\Gamma_i^{ion} + \Gamma^{cx} \big)^{\pm} \frac{m_i}{2} (\vec{v}^{\pm} - \vec{v}_n^{\pm})^2 - (\Gamma_i^{ion})^{\pm} \left(\phi_{ion} + \frac{2T^{\pm}}{\gamma - 1} \right) \\
& + (\Gamma_n^{rec})^{\pm} \left(\frac{2T^{\pm}}{\gamma - 1} \right) + (Q_n^{ion})^{\pm} - (Q_i^{rec})^{\pm} + (Q_{in}^{cx})^{\pm} - (Q_{ni}^{cx})^{\pm} \Bigg] \Bigg) \Bigg]
\end{aligned}
$$

This nonlinear metric is then converted into weak form using the test function ϕ_T^T to be implemented in the PSI-Tet code,

$$
\begin{aligned}
M_T^{\pm} = \int_{\Omega} \phi_T^T \Bigg(T^{\pm} \mp \frac{\Delta t}{2} \Bigg[& -\vec{v}^{\pm} \cdot \nabla T^{\pm} + \frac{\gamma - 1}{n^{\pm}} \Bigg(-n^{\pm} T^{\pm} \nabla \cdot \vec{v}^{\pm} - \nabla \cdot \vec{q}^{\pm} + \frac{1}{2} \Big(\eta(\vec{J}^2)^{\pm} - \mathbf{\Pi}^{\pm} : \nabla \vec{v}^{\pm} \Big) \\
& + \frac{1}{2} \Bigg[(\vec{v}_n^{\pm} - \vec{v}^{\pm}) \cdot (\vec{R}_{in}^{cx})^{\pm} + \big(\Gamma_i^{ion} + \Gamma^{cx} \big)^{\pm} \frac{m_i}{2} (\vec{v}^{\pm} - \vec{v}_n^{\pm})^2 - (\Gamma_i^{ion})^{\pm} \left(\phi_{ion} + \frac{2T^{\pm}}{\gamma - 1} \right) \\
& + (\Gamma_n^{rec})^{\pm} \left(\frac{2T^{\pm}}{\gamma - 1} \right) + (Q_n^{ion})^{\pm} - (Q_i^{rec})^{\pm} + (Q_{in}^{cx})^{\pm} - (Q_{ni}^{cx})^{\pm} \Bigg] \Bigg) \Bigg] \Bigg) \, dV
\end{aligned}
$$

Making use of the vector identity $\nabla \cdot (\psi \vec{A}) = \psi(\nabla \cdot \vec{A}) + \vec{A} \cdot \nabla \psi$, where ψ is a scalar and $\vec{A}$ is a vector and the divergence theorem, one can express the metric in the desired form for implementation in PSI-Tet as follows

$$
\begin{aligned}
M_T^{\pm} = \int_{\Omega} \Bigg[\phi_T^T \Bigg(T^{\pm} \mp \frac{\Delta t}{2} \Bigg[& -\vec{v}^{\pm} \cdot \nabla T^{\pm} + \frac{\gamma - 1}{n^{\pm}} \left(-n^{\pm} T^{\pm} \nabla \cdot \vec{v}^{\pm} + \vec{q}^{\pm} \cdot \frac{\nabla n^{\pm}}{n^{\pm}} \right) \\
& + \frac{\gamma - 1}{2n^{\pm}} \Big(\eta(\vec{J}^2)^{\pm} - \mathbf{\Pi}^{\pm} : \nabla \vec{v}^{\pm} \Big) + \frac{\gamma - 1}{2n^{\pm}} \Bigg[(\vec{v}_n^{\pm} - \vec{v}^{\pm}) \cdot (\vec{R}_{in}^{cx})^{\pm} + \big(\Gamma_i^{ion} + \Gamma^{cx} \big)^{\pm} \frac{m_i}{2} (\vec{v}^{\pm} - \vec{v}_n^{\pm})^2 \\
& - (\Gamma_i^{ion})^{\pm} \left(\phi_{ion} + \frac{2T^{\pm}}{\gamma - 1} \right) + (\Gamma_n^{rec})^{\pm} \left(\frac{2T^{\pm}}{\gamma - 1} \right) + (Q_n^{ion})^{\pm} - (Q_i^{rec})^{\pm} + (Q_{in}^{cx})^{\pm} - (Q_{ni}^{cx})^{\pm} \Bigg] \Bigg] \Bigg) \\
& \mp \frac{\Delta t(\gamma - 1)}{2n^{\pm}} \vec{q}^{\pm} \cdot \nabla \phi_T^T \Bigg] \, dV \mp \int_{\partial\Omega} \phi_T^T \frac{\Delta t(\gamma - 1)}{2n^{\pm}} \vec{q}^{\pm} \cdot \hat{n} \, dS
\end{aligned}
$$

The strong form expression of the nonlinear metric for the Crank-Nicolson scheme for the neutral temperature advance is as follows,

$$M_{T_n}^{\pm} = T_n^{\pm} \mp \frac{\Delta t}{2}\left[-\vec{v}_n^{\pm}\cdot\nabla T_n^{\pm} + \frac{\gamma-1}{n_n}\left(-n_n T_n \nabla\cdot\vec{v}_n - \nabla\cdot\vec{q}_n - \mathbf{\Pi_n} : \nabla\vec{v}_n + (\vec{v}-\vec{v}_n)\cdot\vec{R}_{ni}^{cx}\right.\right.$$
$$\left.\left. +(\Gamma_n^{rec}+\Gamma^{cx})\frac{m_i}{2}(\vec{v}-\vec{v}_n)^2 - (\Gamma_n^{rec}-\Gamma_i^{ion})\left(\frac{T_n}{\gamma-1}\right) + Q_i^{rec} - Q_n^{ion} + Q_{ni}^{cx} - Q_{in}^{cx}\right)\right]$$

Expanding in a finite element basis for the weak formulation of interest for implementing in PSI-Tet, the neutral temperature metric is as follows,

$$M_{T_n}^{\pm} = \int_{\Omega} \phi_{T_n}^{T}\left(T_n^{\pm} \mp \frac{\Delta t}{2}\left[-\vec{v}_n^{\pm}\cdot\nabla T_n^{\pm} + \frac{\gamma-1}{n_n}\left(-n_n T_n \nabla\cdot\vec{v}_n - \nabla\cdot\vec{q}_n - \mathbf{\Pi_n} : \nabla\vec{v}_n + (\vec{v}-\vec{v}_n)\cdot\vec{R}_{ni}^{cx}\right.\right.\right.$$
$$\left.\left.\left. +(\Gamma_n^{rec}+\Gamma^{cx})\frac{m_i}{2}(\vec{v}-\vec{v}_n)^2 - (\Gamma_n^{rec}-\Gamma_i^{ion})\left(\frac{T_n}{\gamma-1}\right) + Q_i^{rec} - Q_n^{ion} + Q_{ni}^{cx} - Q_{in}^{cx}\right)\right]\right) dV$$

Once again, making use of the vector identity $\nabla\cdot(\psi\vec{A}) = \psi(\nabla\cdot\vec{A}) + \vec{A}\cdot\nabla\psi$, where ψ is a scalar and $\vec{A}$ is a vector and the divergence theorem, one can express the metric in the desired form for implementation in PSI-Tet as follows,

$$M_{T_n}^{\pm} = \int_{\Omega}\left[\phi_{T_n}^{T}\left(T_n^{\pm} \mp \frac{\Delta t}{2}\left[-\vec{v}_n^{\pm}\cdot\nabla T_n^{\pm} + \frac{\gamma-1}{n_n}\left(-n_n T_n \nabla\cdot\vec{v}_n - \mathbf{\Pi_n} : \nabla\vec{v}_n + \vec{q}_n^{\pm}\cdot\frac{\nabla n_n^{\pm}}{n_n^{\pm}}\right.\right.\right.\right.$$
$$\left.\left.\left. +(\vec{v}-\vec{v}_n)\cdot\vec{R}_{ni}^{cx} + (\Gamma_n^{rec}+\Gamma^{cx})\frac{m_i}{2}(\vec{v}-\vec{v}_n)^2 - (\Gamma_n^{rec}-\Gamma_i^{ion})\left(\frac{T_n}{\gamma-1}\right) + Q_i^{rec} - Q_n^{ion} + Q_{ni}^{cx} - Q_{in}^{cx}\right)\right]\right)$$
$$\left. \mp\frac{\Delta t(\gamma-1)}{2n_n}\vec{q}_n\cdot\nabla\phi_{T_n}^{T}\right] dV \mp \int_{\partial\Omega}\frac{\Delta t(\gamma-1)}{2n_n^{\pm}}\vec{q}^{\pm}\cdot\hat{n}\, dS$$

B.2 Newton-Rhapson Method

B.2.1 Example Jacobians for density advances

An example calculation of the full Jacobians for the Newton-Rhapson method required to solve for next time step for the Crank-Nicholson time advance scheme for the plasma and neutral density advances is provided as follows. Define the Jacobian $J_{M_i,U_j} \equiv \frac{\partial M_i^{+}}{\partial U_j}$where M is the metric of interest and U is the composite system vector being differentiated with respect to.

Jacobian $(dn/dt)(n)$ (Self-coupling)

The self-coupling Jacobian is computed as follows,

$$\frac{\partial M_n^+}{\partial n} \equiv J_{n,n} = \frac{\partial}{\partial n}\left(n - \frac{\Delta t}{2}[-\nabla \cdot (n\vec{v}) - n^2 c_{rec} + n n_n c_{ion} + D\nabla \cdot \nabla n]\right)$$

$$J_{n,n} = \delta n - \frac{\Delta t}{2}[-\nabla \cdot (\delta n\vec{v}) - 2n\delta n c_{rec} + \delta n n_n c_{ion} + D\nabla \cdot \nabla \delta n]$$

And expanding in a finite element basis for weak formulation,

$$\frac{\partial M_n^+}{\partial n} \equiv J_{n,n} = \int \left(\phi_n^T \left(\delta n - \frac{\Delta t}{2}[-\nabla \cdot (\delta n\vec{v}) - 2n\delta n c_{rec} + \delta n n_n c_{ion}]\right) + D\frac{\Delta t}{2}\nabla \phi_n^T \cdot \nabla \delta n\right) dV$$

$$+ \int D\frac{\Delta t}{2}\phi_n^T \delta n \cdot d\vec{S}$$

Jacobian $(dn/dt)(n_n)$ (Neutral density coupling)

The neutral density coupling Jacobian is computed as follows,

$$\frac{\partial M_n^+}{\partial n_n} \equiv J_{n,n_n} = \frac{\partial}{\partial n_n}\left(n - \frac{\Delta t}{2}[-\nabla \cdot (n\vec{v}) - n^2 c_{rec} + n n_n c_{ion} + D\nabla \cdot \nabla n]\right)$$

$$J_{n,n_n} = -\frac{\Delta t}{2} n \delta n_n c_{ion}$$

And expanding in a finite element basis for weak formulation,

$$\frac{\partial M_n^+}{\partial n_n} \equiv J_{n,n_n} = \int \phi_n^T \left(-\frac{\Delta t}{2} n \delta n_n c_{ion}\right) dV$$

Jacobian $(dn/dt)(v)$ (Plasma velocity coupling)

The plasma velocity coupling Jacobian is computed as follows,

$$\frac{\partial M_n^+}{\partial v} \equiv J_{n,v} = \frac{\partial}{\partial v}\left(n - \frac{\Delta t}{2}[-\nabla \cdot (n\vec{v}) - n^2 c_{rec} + n n_n c_{ion} + D\nabla \cdot \nabla n]\right)$$

$$J_{n,v} = -\frac{\Delta t}{2}[-\nabla \cdot (n\delta\vec{v})]$$

And expanding in a finite element basis for weak formulation,

$$\frac{\partial M_n^+}{\partial v} \equiv J_{n,v} = \int \phi_n^T \left(-\frac{\Delta t}{2}[-\nabla \cdot (n\delta\vec{v})]\right) dV$$

Jacobian $(dn/dt)(T)$ (Plasma temperature coupling)

The plasma temperature coupling Jacobian is computed as follows,

$$\frac{\partial M_n^+}{\partial T} \equiv J_{n,T} = \frac{\partial}{\partial T}\left(n - \frac{\Delta t}{2}[-\nabla \cdot (n\vec{v}) - n^2 c_{rec} + n n_n c_{ion} + D\nabla \cdot \nabla n]\right)$$
$$J_{n,T} = n^2 \frac{\partial c_{rec}}{\partial T} - n n_n \frac{\partial c_{ion}}{\partial T}$$

And expanding in a finite element basis for weak formulation,

$$\frac{\partial M_n^+}{\partial T} \equiv J_{n,T} = \int \phi_n^T \frac{\Delta t}{2}\left[n^2 \frac{\partial c_{rec}}{\partial T} - n n_n \frac{\partial c_{ion}}{\partial T}\right] dV$$

Jacobian $(dn_n/dt)(n_n)$ (Self-coupling)

The neutral density self-coupling Jacobian is computed as follows,

$$\frac{\partial M_{n_n}^+}{\partial n_n} \equiv J_{n_n,n_n} = \frac{\partial}{\partial n_n}\left(n_n - \frac{\Delta t}{2}[-\nabla \cdot (n_n\vec{v_n}) + n^2 c_{rec} - n n_n c_{ion} + D_n\nabla \cdot \nabla n_n]\right)$$
$$J_{n_n,n_n} \equiv \delta n_n - \frac{\Delta t}{2}[-\nabla \cdot (\delta n_n \vec{v_n}) - n\delta n_n c_{ion}] + D_n \nabla \cdot \nabla \delta n_n$$

And expanding in a finite element basis for weak form,

$$\frac{\partial M_{n_n}^+}{\partial n_n} \equiv J_{n_n,n_n} = \int \left(\phi_{n_n}^T\left(\delta n_n - \frac{\Delta t}{2}[-\nabla \cdot (\delta n_n \vec{v_n}) - n\delta n_n c_{ion}]\right) + D_n \frac{\Delta t}{2} \nabla \phi_{n_n}^T \cdot \nabla \delta n_n\right) dV$$
$$+ \int D_n \frac{\Delta t}{2} \phi_{n_n}^T \nabla \delta n_n \cdot d\vec{S}$$

Jacobian $(dn_n/dt)(n)$ (Plasma density coupling)

The plasma density coupling Jacobian is computed as follows,

$$\frac{\partial M_{n_n}^+}{\partial n} \equiv J_{n_n,n} = \frac{\partial}{\partial n}\left(n_n - \frac{\Delta t}{2}[-\nabla \cdot (n_n\vec{v_n}) + n^2 c_{rec} - n n_n c_{ion} + D_n\nabla \cdot \nabla n_n]\right)$$
$$J_{n_n,n} = -\frac{\Delta t}{2}[2n\delta n c_{rec} - \delta n n_n c_{ion}] = \frac{\Delta t}{2}[\delta n n_n c_{ion} - 2n\delta n c_{rec}]$$

And expanding in a finite element basis for weak form,

$$\frac{\partial M_{n_n}^+}{\partial n} \equiv J_{n_n,n} = \int \phi_{n_n}^T \delta n \frac{\Delta t}{2}(n_n c_{ion} - 2n c_{rec})\, dV$$

Jacobian $(dn_n/dt)(v_n)$ (Neutral velocity coupling)

The neutral velocity coupling Jacobian is computed as follows,

$$\frac{\partial M_{n_n}^+}{\partial v_n} \equiv J_{n_n,v_n} = \frac{\partial}{\partial v_n}\left(n_n - \frac{\Delta t}{2}[-\nabla \cdot (n_n \vec{v_n}) + n^2 c_{rec} - n n_n c_{ion} + D_n \nabla \cdot \nabla n_n]\right)$$

$$J_{n,v} = -\frac{\Delta t}{2}[-\nabla \cdot (n_n \delta \vec{v_n})]$$

And expanding in a finite element basis for weak formulation,

$$\frac{\partial M_{n_n}^+}{\partial v_n} \equiv J_{n_n,v_n} = \int \phi_{n_n}^T \left(-\frac{\Delta t}{2}[-\nabla \cdot (n_n \delta \vec{v_n})]\right) dV$$

Jacobian $(dn_n/dt)(T)$ (Plasma temperature coupling)

The plasma temperature coupling Jacobian is computed as follows,

$$\frac{\partial M_{n_n}^+}{\partial T} \equiv J_{n_n,T} = \frac{\partial}{\partial T}\left(n_n - \frac{\Delta t}{2}[-\nabla \cdot (n_n \vec{v_n}) + n^2 c_{rec} - n n_n c_{ion} + D_n \nabla \cdot \nabla n_n]\right)$$

$$J_{n_n,T} = \frac{\Delta t}{2}\left[-n^2 \frac{\partial c_{rec}}{\partial T} + n n_n \frac{\partial c_{ion}}{\partial T}\right]$$

And expanding in a finite element basis for weak form,

$$\frac{\partial M_{n_n}^+}{\partial T} \equiv J_{n_n,T} = \int \phi_{n_n}^T \frac{\Delta t}{2}\left[-n^2 \frac{\partial c_{rec}}{\partial T} + n n_n \frac{\partial c_{ion}}{\partial T}\right] dV$$

Derivatives of ionization and recombination cross-sections

Using the reaction collision cross section approximations provided in Appendix C, the approximation for $\langle \sigma_{rec} \nu_e \rangle \equiv c_{rec}$ is given by

$$c_{rec} \approx 2.6 \times 10^{-19} \frac{Z^2}{T^{1/2}} \, [\mathrm{m}^3/\mathrm{s}]$$

where electron temperature T is in eV and Z is the proton number of ionized nuclei. We may need to use a more sophisticated model since this only can be relied on ±100% in a range of electron temperatures of 1 to 15 eV, but I'm using this for now since it's simple. The approximation for $\langle \sigma_{ion} \nu_e \rangle \equiv c_{ion}$ is given by

$$c_{ion} \approx A \times 10^{-6} \frac{(1 + P(\frac{\phi_{ion}}{T})^{1/2})}{X + \frac{\phi_{ion}}{T}} \left(\frac{\phi_{ion}}{T}\right)^K e^{-\frac{\phi_{ion}}{T}} \, [\mathrm{m}^3/\mathrm{s}]$$

where ionization potential $\phi_{ion}$and bombarding electron temperature T have the same units (eV), and A, P, X, K are coefficients tabulated for elements H through Ni. This formula is accurate to within 5% of recommended data for electron temperatures 1 to 20 keV, which is more robust for our purposes than the recombination reaction rate above.

$$\frac{\partial c_{rec}}{\partial T} = \frac{\partial}{\partial T}\left[2.6 \times 10^{-19}\frac{Z^2}{T^{1/2}}\right]$$

$$\frac{\partial c_{rec}}{\partial T} = -2.6 \times 10^{-19}\frac{1}{2}\frac{Z^2}{T^{3/2}}\delta T = -\frac{c_{rec}}{2T}\delta T$$

$$\frac{\partial c_{ion}}{\partial T} = \frac{\partial}{\partial T}\left[A \times 10^{-6}\frac{(1 + P(\frac{\phi_{ion}}{T})^{1/2})}{X + \frac{\phi_{ion}}{T}}\left(\frac{\phi_{ion}}{T}\right)^K e^{-\frac{\phi_{ion}}{T}}\right]$$

Define:

$$\alpha \equiv A \times 10^{-6}$$

$$\beta \equiv (1 + P(\frac{\phi_{ion}}{T})^{1/2})$$

$$\gamma \equiv (X + \frac{\phi_{ion}}{T})^{-1}$$

$$\Delta \equiv (\frac{\phi_{ion}}{T})^K$$

$$\epsilon \equiv e^{-\frac{\phi_{ion}}{T}}$$

The generalized chain rule provides the following expansion

$$\frac{\partial c_{ion}}{\partial T} = \alpha\frac{\partial}{\partial T}\left[\beta \cdot \gamma \cdot \Delta \cdot \epsilon\right] = \alpha[\frac{\partial \beta}{\partial T} \cdot \gamma \cdot \Delta \cdot \epsilon + \beta \cdot \frac{\partial \gamma}{\partial T} \cdot \Delta \cdot \epsilon + \beta \cdot \gamma \cdot \frac{\partial \delta}{\partial T} \cdot \epsilon + \beta \cdot \gamma \cdot \Delta \cdot \frac{\partial \epsilon}{\partial T}\right]$$

Define:

$$A \equiv \frac{\partial \beta}{\partial T} \cdot \gamma \cdot \Delta \cdot \epsilon$$

$$B \equiv \beta \cdot \frac{\partial \gamma}{\partial T} \cdot \Delta \cdot \epsilon$$

$$C \equiv \beta \cdot \gamma \cdot \frac{\partial \Delta}{\partial T} \cdot \epsilon$$

$$D \equiv \beta \cdot \gamma \cdot \Delta \cdot \frac{\partial \epsilon}{\partial T}$$

Thus, the partial derivative can be defined in terms of the above defined quantities,

$$\frac{\partial c_{ion}}{\partial T} = \alpha[A + B + C + D]$$

$$A \equiv \frac{\partial \beta}{\partial T} \cdot \gamma \cdot \Delta \cdot \epsilon = \frac{\partial}{\partial T}\left(1 + P\left(\frac{\phi_{ion}}{T}\right)^{1/2}\right) \cdot \gamma \cdot \Delta \cdot \epsilon = -\frac{P\phi_{ion}^{1/2}\delta T}{2T^{3/2}} \cdot \gamma \cdot \Delta \cdot \epsilon$$

$$A \equiv \frac{\partial \beta}{\partial T} \cdot \gamma \cdot \Delta \cdot \epsilon = -\frac{P}{2}\sqrt{\frac{\phi_{ion}}{T^3}}\delta T \frac{(\frac{\phi_{ion}}{T})^K}{X + \frac{\phi_{ion}}{T}} e^{-\frac{\phi_{ion}}{T}}$$

$$B \equiv \beta \cdot \frac{\partial \gamma}{\partial T} \cdot \Delta \cdot \epsilon = \beta \cdot \frac{\partial}{\partial T}(X + \frac{\phi_{ion}}{T})^{-1} \cdot \Delta \cdot \epsilon = \beta \cdot \frac{\phi_{ion}\delta T}{(XT + \phi_{ion})^2} \cdot \Delta \cdot \epsilon$$

$$B \equiv \beta \cdot \frac{\partial \gamma}{\partial T} \cdot \Delta \cdot \epsilon = \frac{\phi_{ion}^{K+1}(1 + P(\frac{\phi_{ion}}{T})^{1/2})e^{-\frac{\phi_{ion}}{T}}\delta T}{T^K(XT + \phi_{ion})^2}$$

$$C \equiv \beta \cdot \gamma \cdot \frac{\partial \Delta}{\partial T} \cdot \epsilon = \beta \cdot \gamma \cdot \frac{\partial}{\partial T}[(\frac{\phi_{ion}}{T})^K] \cdot \epsilon = \beta \cdot \gamma \cdot -\frac{K\phi_{ion}^K\delta T}{T^{K+1}} \cdot \epsilon$$

$$C \equiv \beta \cdot \gamma \cdot \frac{\partial \Delta}{\partial T} \cdot \epsilon = -\frac{K\phi_{ion}^K\delta T}{T^{K+1}} \cdot \frac{(1 + P(\frac{\phi_{ion}}{T})^{1/2})e^{-\frac{\phi_{ion}}{T}}}{X + \frac{\phi_{ion}}{T}}$$

$$D \equiv \beta \cdot \gamma \cdot \Delta \cdot \frac{\partial \epsilon}{\partial T} = \beta \cdot \gamma \cdot \Delta \cdot \frac{\partial}{\partial T}(e^{-\frac{\phi_{ion}}{T}}) = \beta \cdot \gamma \cdot \Delta \cdot \frac{\phi_{ion}e^{-\frac{\phi_{ion}}{T}}\delta T}{T^2}$$

$$D \equiv \beta \cdot \gamma \cdot \Delta \cdot \frac{\partial \epsilon}{\partial T} = \frac{(1 + P(\frac{\phi_{ion}}{T})^{1/2})}{X + \frac{\phi_{ion}}{T}}(\frac{\phi_{ion}}{T})^K \frac{\phi_{ion}e^{-\frac{\phi_{ion}}{T}}\delta T}{T^2}$$

Therefore, using the expression of $\partial c_{ion}/dT$ in terms of derived quantities,

$$\frac{\partial c_{ion}}{\partial T} = \alpha\frac{\partial}{\partial T}[\beta \cdot \gamma \cdot \Delta \cdot \epsilon] = \alpha[A + B + C + D]$$

$$\frac{\partial c_{ion}}{\partial T} = \alpha\left(-\frac{P}{2}\sqrt{\frac{\phi_{ion}}{T^3}}\delta T \frac{(\frac{\phi_{ion}}{T})^K}{X + \frac{\phi_{ion}}{T}} e^{-\frac{\phi_{ion}}{T}} + \frac{\phi_{ion}^{K+1}(1 + P(\frac{\phi_{ion}}{T})^{1/2})e^{-\frac{\phi_{ion}}{T}}\delta T}{T^K(XT + \phi_{ion})^2}\right.$$
$$\left.-\frac{K\phi_{ion}^K\delta T}{T^{K+1}} \cdot \frac{(1 + P(\frac{\phi_{ion}}{T})^{1/2})e^{-\frac{\phi_{ion}}{T}}}{X + \frac{\phi_{ion}}{T}} + \frac{(1 + P(\frac{\phi_{ion}}{T})^{1/2})}{X + \frac{\phi_{ion}}{T}}\left(\frac{\phi_{ion}}{T}\right)^K \frac{\phi_{ion}e^{-\frac{\phi_{ion}}{T}}\delta T}{T^2}\right)$$

And, simplifying,

$$\frac{\partial c_{ion}}{\partial T} = \alpha\delta T e^{-\frac{\phi_{ion}}{T}}\left(1 + P\left(\frac{\phi_{ion}}{T}\right)^{1/2}\right)$$
$$\left(-\frac{\frac{P}{2}\sqrt{\frac{\phi_{ion}}{T^3}}(\frac{\phi_{ion}}{T})^K}{(X + \frac{\phi_{ion}}{T})((1 + P(\frac{\phi_{ion}}{T})^{1/2})} + \frac{\phi_{ion}^{K+1}}{T^K(XT + \phi_{ion})^2} - \frac{\frac{K\phi_{ion}^K}{T^{K+1}}}{X + \frac{\phi_{ion}}{T}} + \frac{(\frac{\phi_{ion}}{T})^K\frac{\phi_{ion}}{T^2}}{X + \frac{\phi_{ion}}{T}}\right)$$

Note this is the complete calculation of the Jacobians for the Newton-Rhapson method for the plasma and neutral density advances. But, only reduced forms of the Jacobians for all advances are implemented into PSI-Tet since they still allow for efficient convergence with significantly reduced complexity. For example, the plasma temperature dependence of the ionization and recombination reaction rates is not included in the implemented Jacobians in PSI-Tet since they are very small terms compared to other Jacobian terms. Since the complexity of the exact Jacobians are extensive, it is desirable to implement only the dominant terms that enable efficient convergence of the Newton-Rhapson method, and is the philosophy used for the current implementation of the plasma-neutral model in PSI-Tet.

Appendix C

EXPANDED TERMS FOR QUICK REFERENCE

0th order moment definitions

0^{th} order moments are presented below for convenience. Note that relevant values are in SI units unless otherwise noted.

$$\Gamma_n^{ion} \equiv -n_e n_n \langle \sigma_{ion} v_e \rangle$$

$$\Gamma_i^{ion} = \Gamma_e^{ion} = -\Gamma_n^{ion}$$

$$\Gamma_i^{rec} \equiv -n_i n_e \langle \sigma_{rec} v_e \rangle$$

$$\Gamma_n^{rec} = -\Gamma_i^{rec} = -\Gamma_e^{rec}$$

$$\Gamma^{cx} \equiv \sigma_{cx}(V_{cx}) n_i n_n V_{cx}$$

1st order moment definitions

1^{st} order moments are presented below for convenience. Note that relevant values are in SI units unless otherwise noted.

$$\vec{R}_{in}^{cx} \approx -m_i \sigma_{cx}(V_{cx}) n_i n_n \vec{v}_{in} v_{Tn}^2 \left[4\left(\frac{4}{\pi} v_{Ti}^2 + v_{in}^2 \right) + \frac{9\pi}{4} v_{Tn}^2 \right]^{-1/2}$$

$$\vec{R}_{ni}^{cx} \approx m_i \sigma_{cx}(V_{cx}) n_i n_n \vec{v}_{in} v_{Ti}^2 \left[4\left(\frac{4}{\pi} v_{Tn}^2 + v_{in}^2 \right) + \frac{9\pi}{4} v_{Ti}^2 \right]^{-1/2}$$

2nd order moment definitions

2^{nd} order moments are presented below for convenience. Note that relevant values are in SI units unless otherwise noted.

$$Q_n^{ion} \equiv \Gamma_i^{ion} \frac{3}{2} k T_n$$
$$Q_i^{rec} \equiv \Gamma_n^{rec} \frac{3}{2} k T_i$$
$$Q_{in}^{cx} \approx \sigma_{cx}(V_{cx}) m_i n_i n_n \frac{3}{4} v_{Tn}^2 \sqrt{\frac{4}{\pi} v_{Ti}^2 + \frac{64}{9\pi} v_{Tn}^2 + v_{in}^2}$$
$$Q_{ni}^{cx} \approx \sigma_{cx}(V_{cx}) m_i n_i n_n \frac{3}{4} v_{Ti}^2 \sqrt{\frac{4}{\pi} v_{Tn}^2 + \frac{64}{9\pi} v_{Ti}^2 + v_{in}^2}$$

Global quantity definitions

Variable definitions for use in the zeroth, first, and second order moment definitions provided above and presented here for convenience.

Speeds

Functional forms of the charge exchange, plasma-neutral, and thermal velocities are given below.

$$V_{cx} \equiv \sqrt{\frac{4}{\pi} v_{Ti}^2 + \frac{4}{\pi} v_{Tn}^2 + v_{in}^2}$$
$$v_{in}^2 \equiv |\vec{v}_i - \vec{v}_n|^2; \vec{v}_{in} = \vec{v}_i - \vec{v}_n; v_{in} = |\vec{v}_{in}|$$
$$v_{T_i}^2 = \frac{\gamma k T_i}{m_i}; v_{T_n}^2 = \frac{\gamma k T_n}{m_n}$$

Cross-sections and reaction rates

Functional forms of the charge-exchange cross sections for monatomic deuterium atoms, and ionization/recombination reactions rates are provided below.

$$\sigma_{cx,D} = 1.09 \times 10^{-18} - 7.15 \times 10^{-20} \ln(V_{cx}) \, [\mathrm{m}^2]$$
$$c_{ion} \equiv \langle \sigma_{ion} v_e \rangle = c_{rec} \approx 2.6 \times 10^{-19} \frac{Z^2}{T^{1/2}} \, [\mathrm{m}^3/\mathrm{s}]$$

where electron temperature T is in eV and Z is the proton number of ionized nuclei.

$$c_{rec} \equiv \langle \sigma_{rec} v_e \rangle = c_{ion} \approx A \times 10^{-6} \frac{(1 + P(\frac{\phi_{ion}}{T})^{1/2})}{X + \frac{\phi_{ion}}{T}} \left(\frac{\phi_{ion}}{T} \right)^K e^{-\frac{\phi_{ion}}{T}} \; [\mathrm{m}^3/\mathrm{s}]$$

where ionization potential ϕ_{ion} and bombarding electron temperature T have the same units (eV), and A, P, X, K are coefficients tabulated for elements H through Ni. This formula is accurate to within 5% of recommended data for electron temperatures 1 to 20 keV, which is more robust for our purposes than the recombination reaction rate above.

Appendix D

PSI-TET PLASMA-NEUTRAL CODE

The current version of the plasma-neutral branch of PSI-Tet is titled “neutrals_floor” and is hosted on Github at `https://github.com/hansec/Psi-Framework/tree/neutrals_floor`. Note the currently implemented Jacobians referenced in Appendix C are located in file /physics/xmhd.F90 within the PSI-Tet source directory /src. Only the dominant terms are included in the implemented Jacobians that have a significant impact on convergence of the Newton-Rhapson method; other less important terms are omitted to reduce complexity of the implemented Jacobians.

VITA

Derek Aiden Sutherland
Bachelor of Science in Nuclear Science and Engineering and in Physics
Massachusetts Institute of Technology
June 2012

Doctor of Philosophy
University of Washington
August 2019